Bond Behaviour of Fibre Reinforced Polymer Strengthened Concrete Structures Using Advanced Composite Processing Techniques

A thesis submitted in fulfilment of the requirements for the degree of

Doctor of Philosophy

Seyed Ali Hadigheh

B.Sc. (Civil Eng.), M.Sc. Eng. (Struct.)

School of Civil, Environmental and Chemical Engineering

College of Science, Engineering and Health

RMIT University

June 2014

DECLARATION

I hereby declare that this thesis is my own work and that, to the best of my knowledge and belief, it reproduces no material previously published or written, nor material that has been accepted for the award of any other degree or diploma, except where due acknowledgement has been made in the text.

S. Ali Hadigheh

ACKNOWLEDGEMENTS

I would like to present my deepest gratitude and appreciation to my senior supervisor Dr. Rebecca Gravina for her valuable guidance and advice during the course of this research project. I would also like to thank my second supervisor, Professor Sujeeva Setunge for her support and encouragement.

A particular gratefulness is given to both Dr. Abbas Mohajerani and Dr. Sara Moridpour for their remarkable advice and guidance during my research.

This research project is supported by RMIT University International Research Scholarship and also technical and financial supports from industry partner, Inovas Pty Ltd, which are gratefully acknowledged. I wish to thank Dr. Laurence (Laurie) Walker, Dr. S.J. (Paul) Kim and Mr. Colin McCullough from Inovas Pty Ltd for their valuable technical supports and cooperation.

The assistance of laboratory staffs especially Mr. Pavel Ryjkov, Mr. Saravanan Mani, and Mr. Kevin Dung Le from Civil Eng. Department at RMIT University is appreciated. Also, the contribution of Mr. Rod Wilkie from Melbourne Testing Services Co. (MTS) and Mr. Dilhan Alexander from Sika Australia for providing the equipment for the tensile test and materials for pultrusion and wet lay-up techniques is acknowledged. In addition, the guidance of Mr. Amin Shadmani from Bestech Australia Pty Ltd regarding the application of strain gauges is appreciated.

My profound and eternal gratitude goes to my beloved parents whose their love and encouragement have been a great source of support to strive for success throughout my life. Also, my highest appreciation goes to my brother and sisters for their unconditional love and continuous help. It was my brother who inspired me to choose Civil Engineering as my subject and guided me through my career.

Last but not least, I wish to express my regards to all of my friends at RMIT University for their assistance and encouragements.

ABSTRACT

Fibre reinforced polymer (FRP) materials are widely used in strengthening of existing concrete structures. Several characteristics such as light weight, high stiffness-to-weight ratio, high resistance to environmental degradation, low cost, ease of installation and less interruption to structural features enable FRP composites to be considered as a proper strengthening technique for various structural elements. Based on advances in the production of epoxies and also considerable scientific research on the FRP-repaired systems, nowadays designers are not reluctant to suggest strengthening of structures with composite materials, since the first applications of FRP in civil engineering in the 1990s. However, the efficiency of FRP applications is governed by the performance of the bond between the FRP and the substrate. Although the interface behaviour in FRP bonded joints has been extensively studied, the characteristics of the bond are still not fully understood.

In the literature, the bond between the FRP and the concrete substrate has been studied typically for two commonly used processing techniques, that is the wet lay-up and pultruded laminate systems. However recent trends in the application of advanced processing techniques, which adopt a vacuum consolidation process with resin injection or heat with pre-impregnated laminates in order to improve the curing process and speed of application, necessitate further investigation on the bond behaviour between the FRP manufactured with these techniques and concrete. Vacuum or vacuum and heat are commonly used in marine and aerospace industries for the fabrication of fibre reinforced polymer (FRP) materials. However, the application of these techniques has received less consideration in strengthening of the structures.

The research presented in this thesis consists of experimental, analytical and numerical studies of the interface behaviour in adhesively bonded joints manufactured with common and new developed FRP processing methods. The wet lay-up and pultruded laminates are categorized as common, and vacuum assisted resin infusion (VARI) and heated vacuum bag only (HVBO) are considered as recently developed processing methods. The effect of the principal parameters on the interface behaviour is studied through several series of experiments. Local and global investigations of the interface indicate that through application of VARI and HVBO, a bond with high quality is achievable.

To monitor the bond characteristics during the experiments, a new single lap shear test set-up is developed and employed in this research. Results indicate that accurate and reliable results can be achieved in terms of interfacial responses using modified single lap shear test set-up.

Through the experimental program, the effect of the bondline thickness is specifically studied for different types of processing techniques. Investigation on the local and global bond parameters show that after a specific bondline thickness, load carrying capacity of the joint does not change. Therefore, a new concept, the optimum bondline thickness, is proposed and the load-bondline thickness relationships are adopted based on the nonlinear regression analysis of the experimental results.

Since in this research various techniques are compared and considering this fact that the fabrication method in these techniques is different therefore, the bond characteristics are scaled in a way that the comparison can be possible. This scaling factor here is called "*equalisation of the processing techniques*."

A new analytical approach is presented for determination of the interface behaviour in FRP-to-concrete bonded joints. Based on the boundary conditions, two methods (*Method A* and *Method B*) are proposed to predict the bond-slip relationships and interfacial fracture energy. *Method A* is developed based on the effective bond length and the fixity of the strain whilst *Method B* is expanded regarding the FRP length and the slip fixity condition at both ends of the bonded region. Since the models are derived solely based on boundary conditions of the joints, they can be applied to any type of the FRP processing technique. In addition, the interface characteristics are obtained from the value of the applied load at each stage and the properties of the materials which are available in most of the tests.

Comparison between the experimental and the analytical results of the maximum load carrying capacity, the strain, shear stress and slip profiles and also the fracture energy of the interface indicate that the proposed analytical methods are capable to predict the interfacial behaviour between the FRP and concrete substrates with satisfactory precision. Finally, considering the proper material constitutive laws, a finite element analysis is carried out and the outcomes are presented.

LIST OF PUBLICATIONS

Journal Papers:

1. Hadigheh, S. A., Gravina, R. J., Setunge, S. and Kim, S. J. (2015). "Bond characterization of adhesively bonded joints made with the resin infusion (RI) process." *International Journal of Adhesion & Adhesives*, 57(0), 13-21.
2. Hadigheh, S. A., Gravina, R. J. and Setunge, S. (2014). "Prediction of the bond-slip law in externally laminated concrete substrates by an analytical based nonlinear approach." *Materials and Design*, 10.1016/j.matdes.2014.10.061.
3. Hadigheh, S. A., Gravina, R. J. and Setunge, S. (2014). "Identification of the interfacial fracture mechanism in the FRP laminated substrates using a modified single lap shear test set-up." *Engineering Fracture Mechanics,* In Press.
4. Gravina, R. J., Hadigheh, S. A. and Setunge, S. (2014). "Interfacial bond strength of resin impregnated fibre reinforced polymer laminates bonded to concrete using vacuum and heat: Experimental study." *Australian Journal of Structural Engineering (AJSE)*, 15(2), 189-201.
5. Gravina, R. J., Hadigheh, S. A., Setunge, S. and Kim, S. J. (2013). "Application of heat/resin injection in the presence of vacuum for FRP attachments on the concrete substrate." *Applied Mechanics and Materials*, 438-439, 459-466.

Conference Papers:

1. Hadigheh, S. A. and Gravina, R. J. (2014). "Interfacial stress analysis of the adhesively bonded joints." 23rd Australasian Conference on the Mechanics of Structures and Materials (ACMSM23), Byron Bay, Australia.
2. Hadigheh, S. A., Gravina, R. J. and Setunge, S. (2014). "Numerical Modelling of the Interface between Concrete and FRP Composites." 1st International Conference on Infrastructure Failures and Consequences (ICIFC2014), Melbourne, Australia.

3. Gravina, R. J. and Hadigheh, S. A. (2014). "Bond behaviour between concrete and FRP materials processed with different processing techniques." International Workshop on Research to Reality: Promoting Fibre Composites in Civil Infrastructure, Australia, University of Southern Queensland (USQ).
4. Hadigheh, S. A., Gravina, R. J., Setunge, S. and Kim, S. J. (2013). "Effects of bondline thickness in externally bonded joints processed with vacuum assisted resin infusion." Proc. The Fourth Asia-Pacific Conference on FRP in Structures (APFIS 2013), Melbourne, Australia.
5. Gravina, R. J., Hadigheh, S. A. and Setunge, S. (2013). "Bond performance of FRP to concrete using vacuum and heat/resin injection." Proc. Concrete 2013, Gold Coast, Australia.
6. Hadigheh, S. A., Gravina, R. J. and Setunge, S. (2013). "Experimental and analytical identification of interfacial bond characteristics in adhesively bonded joints." Proc. The 11th international symposium on fiber reinforced polymers for reinforced concrete structures (FRPRCS11), Guimarães, Portugal.
7. Hadigheh, S. A., Gravina, R. J., Setunge, S. and Kim, S. J. (2012). "Experimental study on the bondline behavior between concrete and FRP materials", from Materials to Structures: Advancement through Innovation (ACMSM 22), Sydney, Australia, 505-511.
8. Hadigheh, S. A., Gravina, R. J. and Setunge, S. (2012). "Shear debonding of FRP plates from concrete surface: using modified single lap shear test set-up." The 6th International Composites Conference (ACUN-6), Melbourne, Australia, 175-80.
9. Hadigheh, S. A., Gravina, R. J. and Setunge, S. (2012). "Interfacial stress distribution of FRP-to-concrete joints using advanced composite processing techniques." Proc. The 6th International Conference on FRP Composites in Civil Engineering (CICE 2012), Rome, Italy.
10. Gravina, R. J., Hadigheh, S. A. and Setunge, S. (2012). "Bond and force transfer of FRP materials bonded to concrete using sitecure system." Proc. The Third Asia-Pacific Conference on FRP in Structures (APFIS 2012), Japan.

TABLE OF CONTENTS

LIST OF FIGURES

LIST OF TABLES

LIST OF SYMBOLS

A	Crack surface area (mm^2)
	Fitting coefficient
A_c	Cross sectional area of the concrete (mm^2)
A_e	Equivalent area (mm^2)
A_{frp}	Cross sectional area of the laminate (mm^2)
A_g	Equivalent area of the cross section (mm^2)
a	Distance from the loaded end of the FRP (mm)
	Crack length (mm)
c	Maximum aggregate size (mm)
D	Depth of intermediate crack debonding (mm)
	Scalar stiffness degradation variable
d_a	Maximum aggregate size (mm)
E_{adh}	Adhesive elastic modulus (MPa)
E_c	Modulus of elasticity of the concrete (MPa)
E_{crc}	Crack-closing stiffness
E_{fib}	Modulus of elasticity of fibre (GPa)
E_{frp}	FRP stiffness (GPa)
E_{pl}	Modulus of elasticity of the plate (GPa)
$E_{frp}t_{frp}$	FRP stiffness (GPa.mm)
E^*	Elasticity modulus of the fracture process zone (MPa)
F	Load applied to the sample from the actuator during the test (kN)
F_{int}	Initial load (kN)
F_{max}	Maximum applied load during the lap shear test (kN)
$\overline{F}_{\max}$	Mean value of maximum applied load (kN)
F_{ref}	Reference load vector (kN)
F_u	Ultimate load (kN)
$(FAW)_{ply}$	Fibre areal weight (mass per area per ply) (gr/m^2)
f'_c	Concrete characteristic compressive strength (MPa)
$f'_{c,28}$	Characteristic compressive strength of the concrete at the 28^{th} day after

	casting (MPa)
f'_{cm}	Mean value of concrete compressive strength (MPa)
$f'_{cm,SLS}$	Mean value of concrete compressive strength at the day of the modified single lap shear test (MPa)
f'_{cst}	Concrete surface tensile strength (MPa)
f'_{ct}	Concrete tensile strength (MPa)
$f_{ct,m}$	Mean value of concrete strength (MPa)
f_{frp}	FRP tensile strength (MPa)
f_{t0}	Mean value of concrete tensile strength (MPa)
G	Energy release rate
G_{adh}	Adhesives shear modulus (MPa)
G_c	Shear modulus of the concrete (MPa)
G_F	Interfacial fracture energy (antisymmetric in-plane shear mode) (N/mm)
G_f	Size-effect fracture energy (N/mm)
G_{lam}	Shear modulus of the FRP laminate (MPa)
h_{eff}	Thickness of the interfacial layer (mm)
K	Stress intensity factor
K^{el}	Degraded elasticity matrices
${K_0}^{el}$	Initial (undamaged) elasticity matrices
$\overline{k_d}$	Normalized descending stiffness
k_0	Initial stiffness
$\overline{k_0}$	Normalized initial stiffness
L_{eff}	Effective bond length (mm)
L_{frp} or L	FRP length (mm)
L_{per}	Length of the debonding failure plane (mm)
L_{tab}	Tab length (mm)
L_0	Initial transfer length (mm)
l_p	Length of tension-softening FPZ along the fictitious crack (mm)
n_{ply}	Number of plies per plate
S	Slip at the loaded end (mm)
S_{adh}	Adhesive shear strength (MPa)
S_{max}	Global slip at maximum load (mm)

S_u	Ultimate global slip (mm)
s	Local slip (mm)
s_f	Slip at the free end of the FRP (mm)
s_L	Local slip at the loaded end (mm)
s_l	Global slip at the loaded end (mm)
s_x	Local slip any location from the free end of the FRP (mm)
s_{ult}	Ultimate local slip value (mm)
s_0	Local slip at the maximum shear stress (mm)
T_{adh}	Tensile strength (MPa)
T_{fib}	Tensile strength of fibres (MPa)
T_g	Transitional temperature (°C)
t_{adh}	Adhesive thickness (mm)
t_{bl}	Bondline thickness (mm)
t_{cfib}	Carbon fibre thicknesses (mm)
t_{frp}	FRP thickness (mm)
t_{gfib}	Glass fibre thicknesses (mm)
t_{lam}	Laminate thickness (mm)
t_{pl}	Measured thickness of the plate (or coupon specimen) (mm)
t_{ply}	Thickness of each ply (mm)
t_{tab}	Tab thickness (mm)
x	Distance relative to the free end (mm)
U	Work of the external forces
$u_{c,x}$	Displacement of concrete at point x (mm)
$u_{frp,x}$	Displacement of the FRP at point x (mm)
V	Internal strain energy
V_f	Fibre volume fraction
W_c	Concrete width (mm)
W_{FRP}	FRP width (mm)
w	Maximum aggregate size (mm)
	Crack opening displacement (mm)
w_c or W_c	Critical value of the crack opening displacement (COD) of the fictitious crack
w_r	FRP-to-concrete width ratio (mm/mm)
α and β	Constants

β_w	Width ratio factor
γ	Specific surface energy of the elastic solid
γ_x	Shear strain of the adhesive
$\delta 1$	Displacement of the loaded end (mm)
$\delta 2$	Displacement of the back of the concrete block (mm)
$\varepsilon_{c,x}$	Strain in concrete at point x
ε_{cu}	Ultimate strain of the concrete
ε_{c0}	Concrete strain corresponding to f'_c
$\varepsilon_{frp,x}$	Strain of the FRP at point x
$\varepsilon_{frp,0}$	Ultimate strain of FRP
ε_t	Tensile strain
ε_t^{cr}	Cracking strain
ε_t^{pl}	Plastic strain
$\tilde{\varepsilon}^{pl}$	Equivalent plastic strains
ε_0	Strain value at the loaded end
ε_{50u}	Strain corresponding to the stress equal to 50% of the maximum concrete strength
ρ	Stiffness ratio of the FRP strip to the concrete block
ρ_{fib}	Density of the reinforcing fibre (gr/m^3)
ρ_{ply}	Density of each ply (gr/m^3)
σ_{f0}	Initial crack closure stress
$\sigma_{n,max}$	Maximum normal component at the plate end (MPa)
σ_t	Tensile stress (MPa)
σ_1	Principal tensile stress in concrete at the critical section (MPa)
$\tau_{a,max}$	Maximum shear components at the plate end (MPa)
$\tau_{int,x}$	Interfacial shear stress at point x (MPa)
τ_{max}	Maximum shear stress (MPa)
τ_{mean}	Mean value of shear stress (MPa)
$\tau_{\xi 0}$	Maximum shear stress prior to the initial cracking load (MPa)
υ	Poisson's ratio
υ_{fib}	Fibre volume fraction
φ_f	Aspect ratio of the interface failure plane
λ	Interface property factor (mm)

Ψ	Load proportionality factor
ψ	Fitting coefficient
ξ_0	Relative load level

CHAPTER 1

INTRODUCTION

1.1. Bond Behaviour of FRP Strengthened Concrete Structures

The application of fibre reinforced polymer (FRP) materials in strengthening of structures has increased over the last 10 years. Based on damages caused by several factors such as, environmental harshness, earthquakes, and/or structural changes, the need for strengthening of existing structures is inevitable. FRP as a sheet or laminate can be used in shear or flexural strengthening of beams, joints or slabs. In these conditions, the FRP contributes to carrying a proportion of the load applied to the member. Tensile stresses produced in the substrate are transferred to the FRP through the interfacial region. Therefore in order to achieve a desirable stress transmission system, adequate bond between adherends is required.

In shear and flexural members, bonded plates resist the interface shear and normal stresses which are transferred from the substrate. When FRP transverses a crack in the substrate, stress discontinuity in the vicinity of the crack induces stress concentration in the FRP. Such high stresses lead to debonding along the interface between concrete substrate and the FRP close to the bonded region. When debonding starts, mainly due to interface shear stresses, intermediate crack (IC) debonding occurs. IC debonding is referred to flexural intermediate crack debonding (FIC), critical diagonal crack debonding (CDC) or shear intermediate crack debonding (SIC) regarding the crack widening procedure (HB 305 2008). By increasing the load, the crack gradually propagates along the bondline and abates the bonded area until the entire FRP plate separates from the concrete with no further stress transfer.

Two processing techniques commonly used in the repair of concrete structures via bond of FRP onto the substrate are known as the pultrusion and wet lay-up systems. The pultruded FRP plate and wet lay-up systems both involve the curing of resins up to several days under ambient conditions to achieve full load capacity. Hence, advanced processing techniques for the application of FRP on structures that adopt a vacuum consolidation process with resin

injection or heat with pre-impregnated laminates to improve the curing process, and speed of application have been developed and implemented.

Vacuum assisted resin infusion (VARI) and heated vacuum bag only (HVBO) are among the new developed techniques through which high quality of the bond is achievable. In VARI, the impregnation of the fibres is carried out by the injection of the resin through a vacuum consolidated chamber. HVBO involves the application of the heat over the pre-impregnated fibres in the presence of the vacuum while the curing occurs on site by elevated temperature. Although the use of VARI and HVBO has been developed in the FRP application, the bond characteristics of the joints processed with these methods have not been investigated.

A large number of research has been conducted to investigate the effects of different parameters on the fracture mechanism in adhesively bonded joints. These factors are mainly; the height of the free concrete edge, loading offset, bonded length, FRP width, concrete compressive strength, and concrete composition. Despite the research already carried out (Bizindavyi and Neale 1999; Cao et al. 2007; Chen and Teng 2001; López-González et al. 2012; Mazzotti et al. 2008; Nakaba et al. 2001; Pan and Leung 2007; Seracino et al. 2007; Subramaniam et al. 2007; Yao et al. 2005), very little investigation has been done to study the effects of bondline thickness on the bond between FRP and concrete. This is mainly due to the difficulties in controlling the thickness of the bond.

In the majority of literature, the single lap shear test set-up has been adopted to investigate the bond performance. However, the scattered results of the experiments may be attributed to the test instrumentation and experimental set-ups (Dai et al. 2006; Liu and Wu 2012; Zhou et al. 2010). According to the fracture mechanism of the FRP/concrete interfaces, the slip value is small and any error in test set-up may lead to scattered results. Therefore, it is required to consider modified test set-ups in order to monitor the bond with higher precision and reduce the variation in the experimental results.

Several analytical approaches have been presented to gain a comprehensive understanding of the bond-slip constitutive law between FRP and concrete. However, the proposed models to date do not fully determine the interfacial behaviour. In particular, these models are developed based on specific types of joints hence the constitutive laws cannot be subjected to the FRP-to-concrete joints processed with different and especially new manufacturing techniques. Therefore, a comprehensive relationship is required to predict the bond behaviour between concrete substrate and the FRP materials fabricated with different processing techniques.

1.2. Scope of Research

The objective of this dissertation is to develop a fundamental understanding of the interface characteristics in the adhesively bonded joints. This research is carried out with focus on the application of different processing techniques. Considering this objective, the study consists of the following stages:

- To provide a comprehensive literature review about the interface behaviour of the adhesively bonded joints manufactured with different FRP processing techniques.
- To investigate the applicability of the existing models for prediction of the interface behaviour in FRP bonded joints.
- To develop a new test set-up in order to achieve more reliable results when the single lap shear tests are employed to investigate the bond behaviour.
- To study the interfacial behaviour of the FRP/concrete joints considering several FRP processing techniques.
- To address the effect of various parameters on the interface response of the FRP/concrete joints and to incorporate the findings into practical engineering applications.
- To develop efficient and sound analytical interface constitutive models to predict the bond behaviour of the joints manufactured with different processing methods.
- To simulate the interface behaviour in finite element software package by implementation of the material properties considering constitutive laws and modelling techniques.

1.3. Outline of the Dissertation

This dissertation is presented in six chapters and three appendices. The remaining five chapters are organized as follows:

Chapter 2 mainly provides information about different FRP processing techniques with the focus on the commonly used methods (e.g. wet lay-up and pultrusion) and also new techniques (e.g. VARI and prepreg). The possible failure modes in FRP strengthened structures are mentioned in the next section and finally existing bond tests and the effective factors on the interface behaviour are discussed in the last part of the chapter. This chapter also concerns modelling approaches of the interface in the adhesively bonded joints. These approaches are defined as empirical, elasticity and fracture mechanics-based models. The

advantages and limitations of such methods when predicting the debonding failure of the joints are highlighted. For better understanding, the basics of the fracture mechanics theory are stipulated in this chapter. In addition, the finite element simulation techniques of the FRP/concrete joints are discussed.

Chapter 3 presents the outline of the experiments which are carried out to investigate the interfacial behaviour between the concrete substrate and the FRP composites. Firstly, the methods of the tests are discussed and then a modified single lap shear test set-up is proposed. In addition, the implementation of several FRP processing techniques such as pultrusion, wet lay-up, heated vacuum bag only (HVBO) and vacuum assisted resin infusion (VARI) is introduced. In order to compare the characteristics of these processing techniques which have various properties, a specific criterion is required. This implementation is performed by a standard method for equalisation of the manufacturing techniques. Finally in the last part of the chapter, the properties of the materials used in this research are reported.

Chapter 4 presents the experimental results of the modified single lap shear tests. The sensitivity of the interface behaviour to material properties, specimen geometry, surface treatment and FRP processing techniques is also discussed.

Chapter 5 introduces a new analytical approach for determination of the bond behaviour between the FRP and concrete substrates. Considering fixity of the strain and the slip, two different sets of local bond-slip laws, called *Method A* and *Method B*, are presented, respectively. The first method (*Method A*) is developed based on the effective bond length and the fixidity of the strain values. However, when the effective bond length is unknown, *Method B* may be used. *Method B* is derived based on a more generic condition which involves the FRP bonded length instead of the effective bond length and also fixidity of the slip at both ends of the bonded region. The advantage of the proposed models is that the development of the models is carried out based on boundary conditions of the joints therefore, a more stable and accurate bond-slip relationship is achievable which can be applied to any type of the joint processed with different FRP manufacturing techniques. The ability of the proposed models to predict the interface response is studied by comparing the results of the modified single lap shear tests presented in Chapter 5 with the analytical model. In addition, final part of the chapter provides brief and essential information about the modelling of the interface in Abaqus finite element software.

Chapter 6 summarises the major outcomes of the research and provides recommendations for future works.

Finally, three appendices are included at the end of this thesis. Appendix A contains results of the tensile tests on the FRP composites utilized in this research. For convenience, all the graphs are displayed in the same scale through Chapters 4 and 5. Therefore for the clarity of the responses, Appendix B presents the results of the modified single lap shear tests in various scales. Two different models (*Method A* and *Method B*) are proposed in Chapter 5 to calculate the interface behaviour of the adhesively bonded joints. Appendix C provides a comparison between the two proposed models in determination of the bond characteristics. The structure of the thesis is briefly illustrated in Figure 1-1.

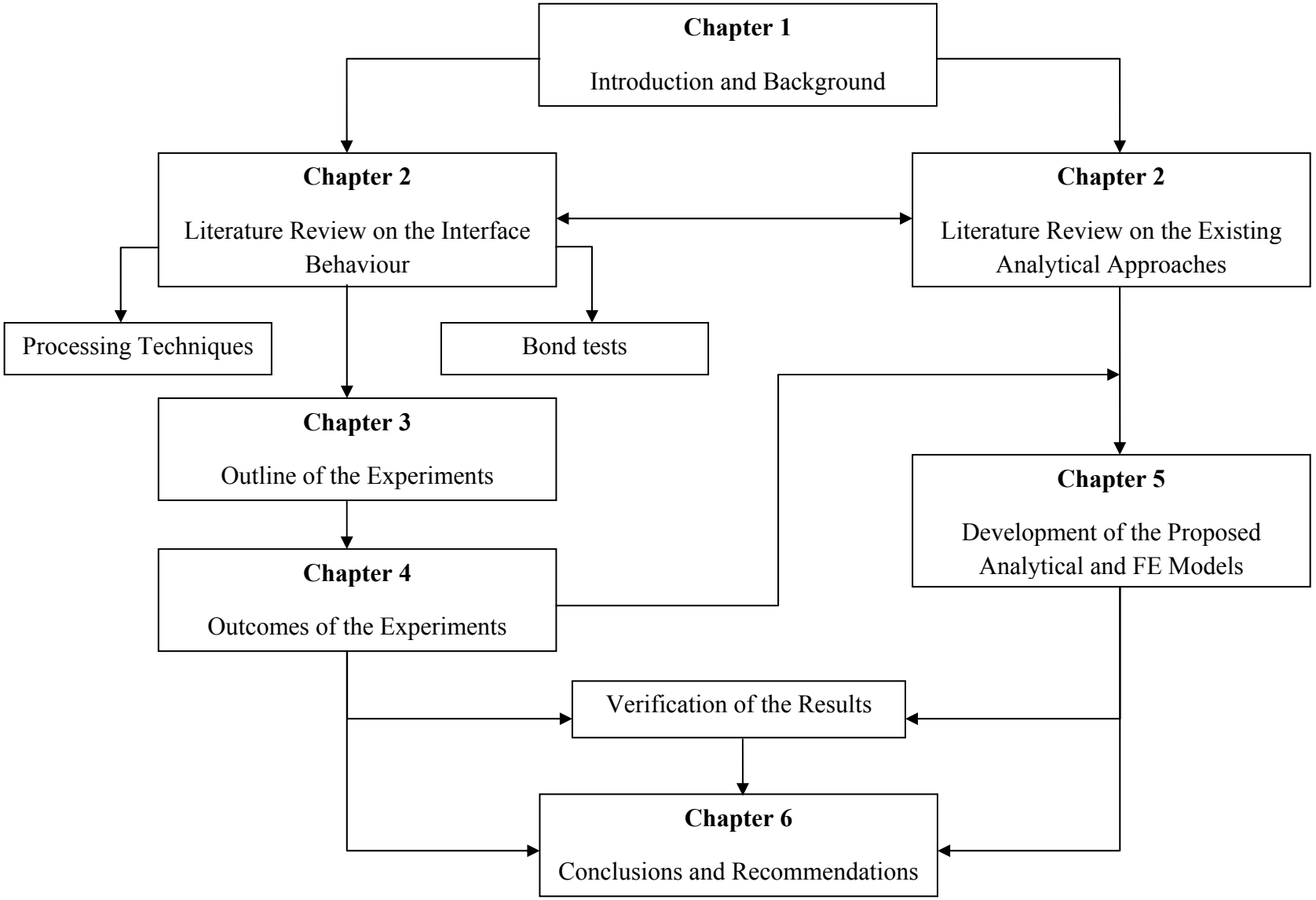

Figure 1-1. Outline of the dissertation.

CHAPTER 2

INTERFACIAL CHARACTERIZATION OF ADHESIVELY BONDED JOINTS

2.1. Introduction

Fibre Reinforced Polymeric (FRP) materials have been used in the construction industry over the last two decades (ACI 440.2R-08 2008; HB 305 2008). Based on damages caused by several factors such as, environmental effects, earthquakes, and/or structural changes, the need for strengthening of existing buildings is inevitable. Using composites for strengthening of concrete structures has far more benefits in comparison with the previous retrofitting strategies, such as; light-weight, high ratio of stiffness-to-weight, high resistance to environmental degradation, lower cost, ease of installation and less interruption to structural features (Karbhari and Zhao 2000).

Strengthening of concrete structures by FRP has shown some drawbacks due to immature debonding of the composite plate during external loading before the ultimate tensile capacity of the retrofitted member is reached. Hence, the interfacial behaviour between the FRP and the substrate is one of the most influential factors which has to be carefully considered during the strengthening process.

2.2. FRP Processing Techniques

2.2.1. Wet *Lay-up*

Since the 1940s, wet lay-up or hand lay-up has been widely used to manufacture fibre reinforced composites in the aerospace and marine industries. It is a flexible method, very cost-competitive with low capital outlay (Hollaway 1994), and easy to install (Bank 2006). Wide variety of components, with large and complex shapes, may be produced using wet lay-up process (Daken et al. 1994).

In this technique, the mould (or substrate) is treated by appropriate surface preparation (e.g. sand blasting, water jet blasting, grinding or etc.) and cleaned from the dust and debris. Fibres are cut into desired dimensions prior to installation. Most of the resins are provided in base and hardener parts and therefore they have to be mixed by hand or a mixer in the proportion recommended by the resin manufacturer. The first layer of resin which is applied on the mould is called *gel coat*. The resin is allowed to gel before application of the reinforcement. After the resin is draped with fibres, rollers are used to impregnate the fibres and brush out the excessive resin and trapped air. Alternate layers of resin and fibres can be laid on the mould to make thicker composites. In this method, the bond between fibres and resin and also composite with the mould are formed at the same time. Figure 2-1 illustrates the wet lay-up process.

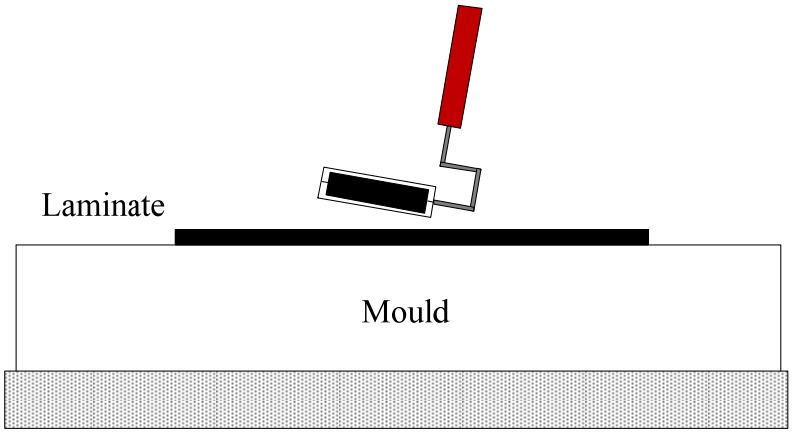

Figure 2-1. Wet lay-up technique.

2.2.2. Pultrusion

Pultrusion of composites was greatly considered immediately after Second World War. During the early stages, pultrusions were used to build fishing or ski poles and golf course flag staffs (ACI 440R-96 1996). Since the 1970s, the application of pultruded profiles has been considered as large-sized structural shapes in bridge and building construction. By the 1980s, standardization of pultruded I-shaped beams was commenced by some companies (Bakis et al. 2002). Pultruded profiles were utilised for construction of the primary load-bearing systems in industrial cooling tower structures.

The 1990s was a milestone for the pultrusion industry since a significant shift occurred in the application of pultruded profiles from non-structural to primary load carrying elements in bridge and building structures (Bakis et al. 2002). Since then, pultruded sections have been

used to construct different types of structures, such as bridges, cable trays, building systems, flooring support, pipe support, trusses and joints, wind blades and window frames. Today, the electrical, marine (Boyd et al. 2004), aeronautics (Carlone et al. 2007), automotive and wastewater industries utilise pultrusions due to their superiority in terms of product consistency and economy.

Pultrusion is a type of automated continuous moulding process in which the fibres are impregnated with resin by either drawing through a resin bath or injection of resin into the reinforcement. Resin bath may contain resin matrix, catalyst and additives. The fibres are pulled through forming guides in order to achieve designed mechanical properties and wipe off the excessive resin. The impregnated fibres form the final geometry by pulling into a heated die. The curing of resin occurs inside the die under controlled temperature which is produced by electrical heaters, hot oil or by steam. Depending on the section, the curing time is longer for complex and thick profiles. At the final stage, the cured profile is cut into desired length with cut off saws. Depending on the application of water during the cut, saws are divided into wet or dry cut saws. Figure 2-2 represents the typical process of the pultrusion technique.

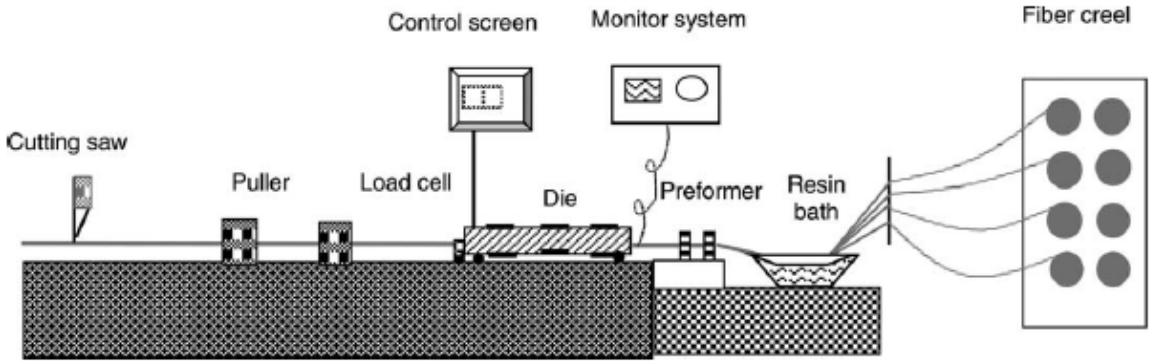

Figure 2-2. Pultrusion process (Zhu et al. 2004).

Different types of fibre can be used as reinforcement in pultrusion, such as roving, mats, fabrics, and braided preforms. Common types of resins used in pultrusion are polyester resins, vinyl ester resins, epoxy resins, and methacrylate vinyl ester resins. The selection of the resin depends on the design and application of the profile. Polyesters have good physical properties with competitive cost. Vinyl esters have sufficient resistance to corrosion and show higher mechanical properties in elevated temperatures. Where the impact and shear strength are concerns, vinyl ester is a good choice as resin for pultruded profiles. Epoxies show the highest physical properties and strength compare to the other types of resins.

Methacrylate vinyl esters have very low viscosity which offers good saturation during the pultrusion.

2.2.3. Vacuum Assisted Resin Infusion (VARI)

Although there are various processing techniques, the repair of concrete structures via bond of fibre reinforced polymer materials (FRP) onto the substrate is typically carried out by two commonly used methods, pultruded laminates or wet lay-up (or hand lay-up) systems. In the pultruded plate repair system, prefabricated plates are manufactured by the pultrusion method and bonded on the substrate by the epoxy adhesives. The wet lay-up method involves the impregnation of the unidirectional or weaved fibres by a low-viscosity epoxy adhesive using rollers or brushes. However, with the wide application of the composite materials in the strengthening of structures, new processing techniques with higher quality are necessary in order to achieve more reliable FRP repairing systems.

Whilst using vacuum assisted resin infusion (VARI), vacuum assisted resin transfer moulding (VARTM) and resin transfer moulding (RTM) are quite new in strengthening of structures, they have been used in marine, petroleum and composite manufacturing industries in a large scale. Application of these methods may lead to reduce production cost, make complex geometry with large components, produce composites with high fibre volume fraction and to improve the quality of the products (Teoh and Hsiao 2011).

With advances in the production of epoxies with longer gel time and improvements in vacuuming equipment and materials, the application of vacuum assisted resin infusion or resin transfer moulding is growing rapidly. In these methods, the reinforcement is placed on a rigid mould and covered with a layer of peel ply and flow medium. The whole system is isolated by another rigid mould while the vacuum is induced into the system. The vacuum distributes the resin over and inside of the reinforcement (Figure 2-3). During the process, the vacuum pressure is precisely monitored to avoid any noticeable changes which can cause a fault inside of the composite. Using vacuum results in production of components with better mechanical properties, lower porosity levels and accurate fibre management (Edwards 1998; Hayward and Harris 1990). The flow of the resin is improved using higher permeable flow medium both in the plane and transverse directions.

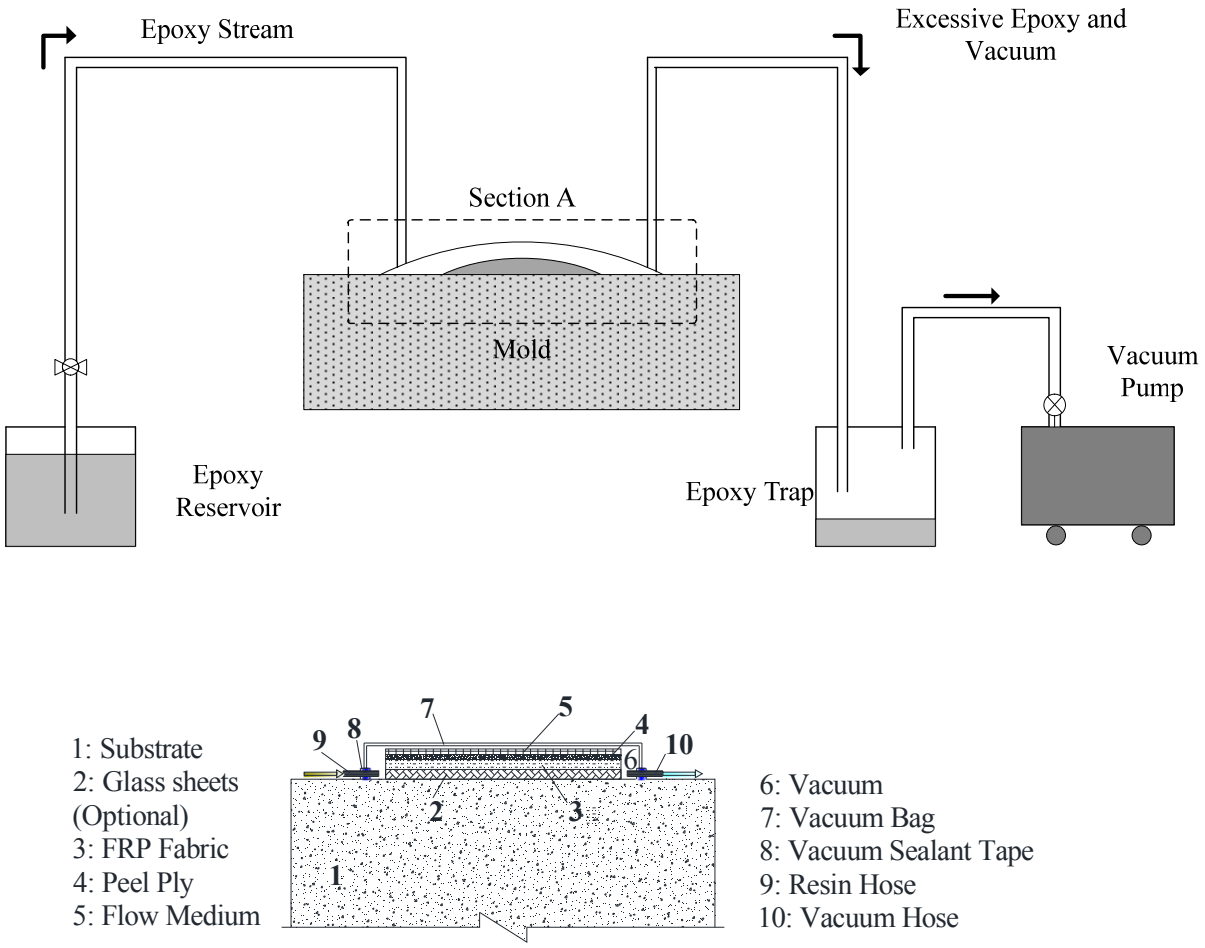

Figure 2-3. VARI application process.

In resin transfer moulding, the mould consists of two rigid parts while the vacuum assisted resin infusion is sealed with one rigid mould and a vacuum bag (Correia et al. 2005; Williams et al. 1996). Due to the thickness variation in complex components, high volume fraction is difficult to achieve using the RTM method. In addition, the clamping cost of both rigid moulds is not economically efficient (Gupta and Sundaram 2009; Tang et al. 2013). Therefore, resin transfer moulding is not used to produce complex components. In contrast, the advantage of using flexible vacuum bag in VARI (also called resin infusion under flexible tooling, *RIFT*) system facilitates making complex profiles with low cost. The vacuum bag is fixed to the mould using vacuum sealant tapes around the bag.

In the late 1940s, vacuum infusion moulding (later called Marco method) was used to manufacture boat hulls. Reinforcement is draped over the solid male mould and the female mould is used for consolidation and vacuum infusion. As well as the marine industry

(Chalmers 1991; Dodkins et al. 1994; Silva-Muñoz and Lopez-Anido 2009), the VARI and RTM techniques have been used widely in other fields such as aerospace for production of light weight profiles with low operation cost and increase of the payload (Alms et al. 2010; McIlhagger et al. 2000).

With successful use of resin transfer moulding (RTM) in composite manufacturing, several improvements have been done on the apparatus and material application. The vacuum is implemented in the process to achieve better composite quality, as it is attributed to the removal of moisture and impurities associated with production and also increased pressure difference between the mould and the epoxy (Hayward and Harris 1990).

From the material science and manufacturing point of view, several investigations have been carried out to study the efficiency of vacuum assisted resin injection method or resin transfer moulding in comparison to other commonly used processing techniques (Böger et al. 2008; Deka et al. 2009; Morales et al. 2010; Poodts et al. 2013; Zainuddin et al. 2010). Several research has been carried out to develop the applicability and fabrication of the fibres in terms of reducing the processing time in VARI system using different techniques such as preheating (Zhang et al. 2014).

Before the application of the vacuum assisted resin infusion (VARI) technique, the surface of the sample is to be cleaned to avoid any deficiency in bond between the FRP plates and the substrate. The dry plate preforms are placed on the mould (here, concrete) and fixed by applying the spray adhesive. Subsequently, the peel ply and the flow medium are placed on the plates. The flow (infusion) medium is used to aid the resin to be distributed and spread over the bond area. This medium is highly permeable with low resistance against resin flow and rigid enough to stand buckling under vacuum. To prevent the wastage of the resin, flow medium is cut about 10 cm less than the preformed plates close to the vacuum hose side. To take off the disposable parts, a peel ply layer is arranged between the flow medium and the vacuum bag. This peel ply layer (or release film) can prevent damages to the bond when the disposable parts are removed.

The whole system is then covered by a specific plastic bag in order to produce the vacuum condition during the VARI technique. The vacuum bag can be sealed all around the area by the vacuum sealant tapes (the double sticking tape). The inlet and outlet tubes are located at the start and the end of the mould to supply resin and remove air, respectively. The inlet tube is attached to the resin hose (or resin tank) and the outlet tube is connected to the vacuum hose (or vacuum pump). The outlet tube is opened and the vacuum applied to the system to settle the fabrics and plates and then the inlet tube is opened. The vacuum pulls the

resin down through the flow medium, plate preform and the interface between the FRP and the mould (substrate). Therefore, the epoxy can fast saturate the dry fibres and bond them together as well as to the substrate.

To ensure a sufficient quality and speed of fibre saturation, low viscose matrix resins with typical viscosity of 0.5-1.0 Pa.s are used (Lee and Wei 2000; Tang et al. 2013). When the resin covers all the area, the inlet tube (resin supply) is closed and the bonded area is kept under vacuum condition until the resin is cured in ambient temperature. The excessive resin is trapped in a resin trap tank prior to the vacuum pump. A schematic view of the vacuum assisted resin infusion is shown in Figure 2-4.

The vacuum pump produces a motive force based on the pressure differential between the inside and outside of the vacuum bag which distributes the resin over the entire mould. The presence of vacuum minimizes the formation of dry spot areas on the cured FRP which leads to the higher quality in composite. Therefore, the vacuum pressure has a great role on the performance of the VARI system. Although 8 to 10 ton/m^2 pressure is reasonable to produce the vacuum, based on the substrate porosity it is required to provide higher vacuum pressure. If sufficient pressure is not used, the composite may be of low fibre volume fraction with some unsaturated spots on the plates (McIlhagger et al. 2000). After curing, the disposable parts can be peeled off from the substrate.

Although through the resin infusion technique a good uniformity and compaction of the fibres is achievable, there are some concerns about the function of the resin. The resin, which is pulled down through the fibres, provides the bond between substrate and the fibres and simultaneously holds the fibres together as a composite. Normally in other processing techniques, the resin is applied to make the composite action of the fibres while the adhesive is placed between the composite and substrate. However, in resin infusion the adhesive part is eliminated which leads to the formation of fewer interfaces and exclusion of a more compliant layer. Considering the property changes of the adherents with time or temperature and also crack development at the interfaces, premature failure is expected in adhesively bonded joints processed with resin infusion technique (Karbhari and Zhao 2000).

(a)

(b)

(c)

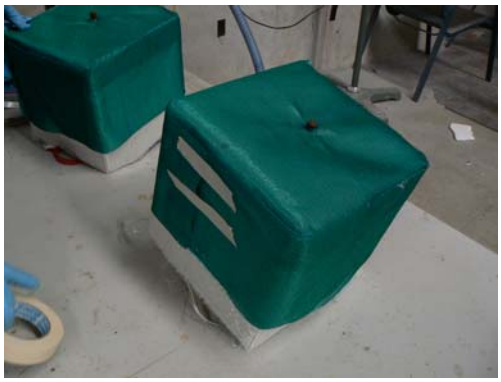

(d)

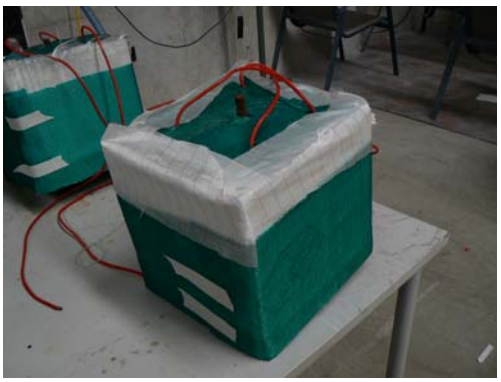

(e)

(f)

(g)

(h)

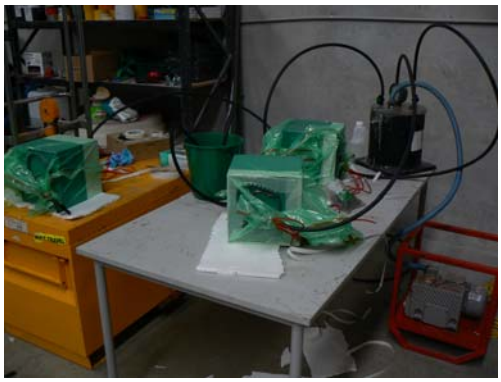
(i)

(j)

Figure 2-4. Vacuum assisted resin infusion process: (a) pre-cut FRP sheets, (b) placing sample, (c) wrapping sheets, (d) flow media, (e) release film, (f) vacuum bag, (g) seal the vacuum chamber, (h) vacuum pump, (i) resin container and (j) resin flow.

For aerospace structures, the void content in the composites is a primary issue and should be kept less than 1%. However, the void content in the components with thickness more than 6 mm which is processed with the VARI system was reported more than 1% (Gupta and Sundaram 2009). To overcome this problem, recently, the vacuum enhanced resin infusion technology (VERITy) is developed. In this method, the reinforcement is held under vacuum and the resin infused inside the tool cavity. The vacuum pressure is held even after the infusion has been completed until the fibres dry (Gupta and Sundaram 2009). To ensure that only the air is bled out of the cavity tool while the resin remains inside, a special breather is utilised.

The permeability of the fabrics, viscosity of the resin, and the required resin flow path are the primary parameters in the vacuum assisted resin transfer moulding (VARTM) system. The low permeability of the fabrics usually leads to creation of the resin starved regions on the composite structures when the VARTM method is applied (Alms et al. 2010). To minimise this effect, new manufacturing methods such as SCRIMP or VIPR have been proposed. In the Seemann's composite resin infusion moulding process (SCRIMP) (Seemann WH 1990), a distribution media is applied on the reinforcement to ease the resin flow which reduces the saturating time of the fibres.

The vacuum induced preform relaxation (VIPR) uses a small external vacuum chamber which is sealed to the flexible surface of the mould (e.g. vacuum bag) to make the vacuum condition above the preform (Alms et al. 2010). This process induces compressive forces on the fabrics and contributes to a better permeable system. When a sufficient amount of resin is infused into the system, the chamber is removed. Recent investigation showed that significant

and uniform mechanical properties can be achieved in composites using VIPR manufacturing technique with higher fibre volume fraction (Alms et al. 2010).

With the growth in application of the new methods in composite manufacturing, models are currently developed to address the mechanical and economical aspects of different manufacturing techniques (Bader 2002; Tapeinos et al. 2012). Using the Activity Based Costing (ABC) method (O'Guin 1991), cost estimation was performed on the carbon nanotube-based polymer composite samples manufactured by three different methods; vacuum assisted resin infusion (VARI), wet lay-up (or hand lay-up), and resin transfer moulding (RTM) (Tapeinos et al. 2012). RTM in this study can resemble the methods which consist of automatic and rigid moulding while wet lay-up indicates the manual manufacturing of the composites. In addition, VARI may be a representative of the processing methods with one rigid mould and a flexible vacuum bag. Considering the material, labour, energy and used assets costs, the relative estimated cost for different manufacturing systems to the wet lay-up system is reported in Figure 2-5(a) (Tapeinos et al. 2012).

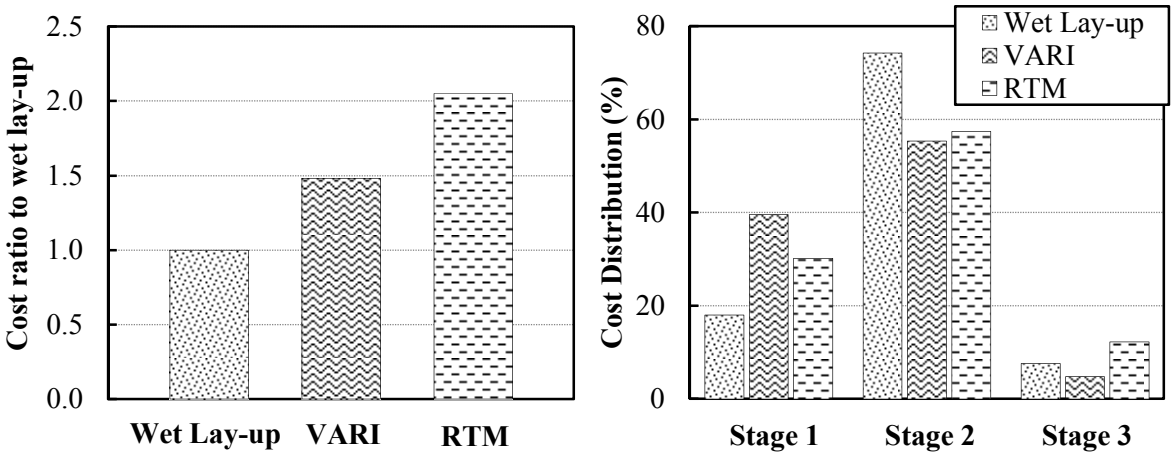

(a) (b)

Figure 2-5. Comparison between different manufacturing processes of a GFRP plate, (a) total cost, (b) cost distribution.

Wet lay-up method has the least manufacturing costs, following the VARI system and the most expensive method is the RTM process with almost doubled expenses in comparison with the wet lay-up process. The estimated cost is calculated for a GFRP plate with dimensions of 300 mm × 300 mm under laboratory conditions. In large scale manufacturing, the cost for VARI and RTM systems are more cost-efficient in comparison with the wet lay-up method (Brouwer et al. 2003; Kulshreshtha and Vasile 2002). It should be considered that

the attained quality and performance of the automated mechanisms (e.g. VARI or RTM) are higher than the wet lay-up technique (Sevkat and Brahimi 2011; Tapeinos et al. 2012) and in most cases, the quality cannot be compromised to cut the cost.

The distribution of the estimated cost of different stages of the manufacturing is presented in Figure 2-5(b) (Tapeinos et al. 2012). Stage 1 is the preparation step and involves the layer cut off, mould preparation, lay-up, and bagging process. In stage 2 (process stage), the costs of materials, preparation for processing, and curing are considered. For the last stage (stage 3), called post process, the cost is estimated based on the post curing of the composites, removal and cleaning of the equipment. According to Figure 2-5(b), wet lay-up has the least expensive preparation stage among the manufacturing techniques. This is mainly due to the lack of mould and bagging process. However during the process stage, wet lay-up is the most expensive method which is caused by the labour work and curing.

Although the use of VARI system is common in marine and aerospace industries, very little attention has been paid to the application of this system in the strengthening of the structures by FRP materials. Ease of the application of the vacuum assisted resin infusion process in large components and achieving high mechanical properties with low cost (Himmel and Bach 2006; Tapeinos et al. 2012; Zhou et al. 2013) make VARI a suitable method for structural strengthening of infrastructures with composite materials.

The successful application of the vacuum-injection system in shear strengthening of the reinforced concrete beams is compared with the hand lay-up method (Täljsten and Elfgren 2000). Results showed that the strength of the fractured beams can be restored to the same amount in an uncracked beam (Täljsten and Elfgren 2000). Vacuum bag curing was applied to bond the concrete to the shuttering in composite beams, consisted of fibre reinforced polymer materials and concrete (Canning et al. 1999). The resin injection method was able to satisfy the level of composite action in the composite beams.

The vacuum resin infusion is used in fabrication of FRP bridges for replacement of deteriorated structures, e.g. Bennett's Creek in US (Alampalli et al. 2000) and West Mill Bridge in Oxfordshire, UK. Significant strength was achieved for the replaced bridge through prototype and field proof tests applying a full-scale load as well as less construction time and cost effectiveness (Alampalli et al. 2002; Hejll et al. 2005). The successful application of the vacuum assisted resin infusion system in concrete-filled FRP tubes in strengthening of bridge structures (Dagher et al. 2012) and enhancement of the punching resistance of GFRP composite sandwich panels (Dawood et al. 2011) have been reported. In addition, recently the

application of the VARI technique is considered in production of the glass fibre reinforced polymer (GFRP) connectors in sandwich panels (Lameiras et al. 2013).

Despite these studies which focus on the overall structural response of the strengthened elements, the bond behaviour between the concrete and the FRP processed with VARI method has not been investigated. Therefore in the following chapters, the performance of the interface in adhesively bonded joints processed with VARI is compared with other commonly used methods.

2.2.4. Prepreg Processing Technique

Since the first introduction of composite materials in the aircraft industry, it was in 1980's that prep-impregnated (pre-preg) laminates were considered as a new speciality materials. Firstly, pre-pregs were used only for construction of the non-structural elements in aircrafts such as rotor blades, wing spars and tail fins. With technological advancements in composite manufacturing, the application of pre-preg laminates is growing in the aviation and aerospace industries in such a way that nowadays more than 50% of primary structures such as airframe, airfoil, and fuselag parts are made of pre-pregs (Bank 2006; Hayes et al. 2000).

With the successful application of pre-pregs in aeronautics (Drakonakis et al. 2013; Hayes et al. 2000; Kratz and Hubert 2013; Kumar et al. 2013; Morrison and Bader 1989; Witik et al. 2012), other industries such as wind turbines (Lukaszewicz et al. 2012; Monroy Aceves et al. 2012; Schubel 2012), sports equipment, machinery, tooling and pipeline (McGeorge et al. 2009) have been attempting to utilise these laminates as an alternative to the conventional materials.

Pre-preg laminates consist of fibres (unidirectional, woven fabric or multiaxials form) that have been pre-impregnated with resin and partially cured. Since the resin is pre-impregnated into the fibres, the working life with the laminates at ambient temperature is short. However, they can be stored in a cool area for a long period of time to extend the shelf-life of the composite. The tacky behaviour of the pre-pregs aids contractors to use the laminates overhead or in vertical applications. The ratio between resin and fibre in pre-preg laminates can be tailored by the manufacturer considering the aim of the strengthening. Regarding the high-fibre volume fraction (V_f), pre-preg laminates are used to produce high performance structures (Bader 2002). Figure 2-6 shows a carbon pre-preg laminate with protective covers.

Figure 2-6. Pre-preg laminates.

In terms of the matrix types, epoxy, phenolic, and bismaleimide are commonly used in pre-preg systems. Epoxies have an excellent mechanical performance, good environmental resistance and high toughness which enable them to be utilised in aerospace, marine, automotive, wind energy and building industries. On the other hand, phenolic and bismaleimide have good fire and high temperature resistances, respectively. Bismaleimide can stand temperatures up to 260°C with reliable mechanical characteristics.

From the first application of the pre-pregs, hand lay-up was the easiest way of pre-preg processing. This manual lay-up process can be used for any type of unidirectional and woven reinforcement. With growing application of pre-pregs in different industries, automated lay-up methods have been developing to overcome labour cost and lower quality of the laid pre-preg regarding the conventional hand lay-up. Automated Tape Laying (ATL) and Automated Fibre Placement (AFP) are the two main techniques currently employed.

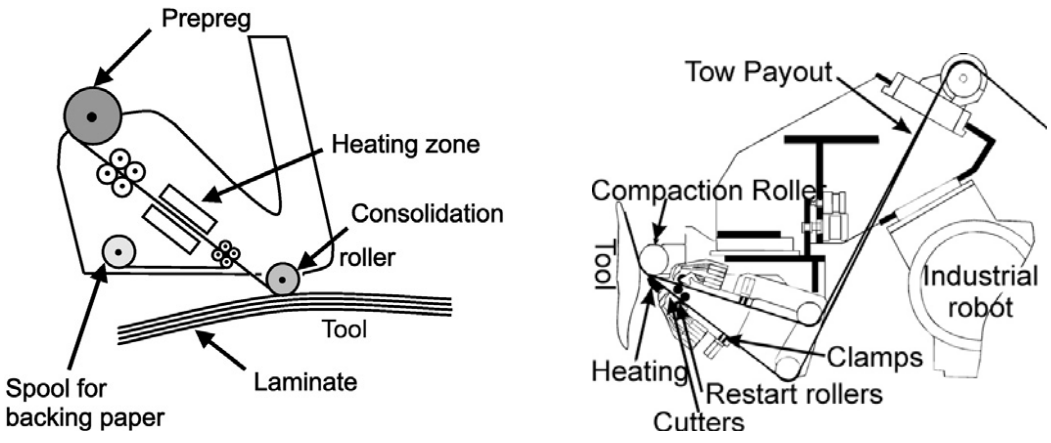

(a) (b)

Figure 2-7. Schematic view of (a) ATL head (Åström 1997), and (b) AFP head (DO 1997).

In Automated Tape Laying (ATL), the system applies a tape on the tool (Figure 2-7a) using a silicone roller. Then, the pre-preg is supplied on a cardboard core and held by a head. The pre-preg is attached on the tool with pressure which is applied through the end-effector. Meanwhile, the temperature is precisely controlled in front of the lay-up head or in the lay-up system in delivery (Lukaszewicz et al. 2012).

The lay-up process in AFP is quite similar as ATL (Figure 2-7b). The pre-preg is delivered from a creel cabinet to the head and then sent to the flexible compaction roller where heat and force are applied to the pre-preg. The main difference between ATL and AFP is the width of the pre-pregs which are applied. In ATL, single tape up to 300 mm wide is used, whereas in AFP, narrow tapes almost 6 mm wide are utilised (Lukaszewicz et al. 2013). Since AFP is mostly used to make complex parts, the productivity of this method is lower than ATL. By application of robotic systems, AFP may be more affordable than ATL system (Lukaszewicz et al. 2012).

Pre-preg laminates can be processed using autoclave, vacuum bag only (VBO), resin film infusion (RFI), pressure bag moulding, press moulding, or thermal expansion moulding. Autoclave is the most common manufacturing technique in aerospace industry for production of structural components with superior quality (Menta et al. 2013) and with high fibre volume (Bader 2002; Grunenfelder et al. 2013), low porosity (Cender et al. 2013; Tavares et al. 2010a) and controlled cure (Hollaway 1994). In this method, pre-impregnated fibres are laid on a single part mould either manually or automatically and covered by a vacuum bag to consolidate the laminates. Then, the component is loaded into a pressurized vessel, called autoclave chamber (Figure 2-8).

In general, pressure vessels are used as an autoclave to control the vacuum, pressure, and cure temperature cycles on the element. To minimize the trapped air or moisture and produce materials with high mechanical performance, high pressure is applied to the laminates in the autoclave during the process (Bader 2002; Davies et al. 2007). In order to lower the risk of runaway exotherm of the resin, uniform heating is required over the pre-pregs. Therefore, slow heating rate is applied in the autoclave process (Zhang et al. 2009).Since high pressures can be applied, thick sections with complex shapes can be made with the autoclave process.

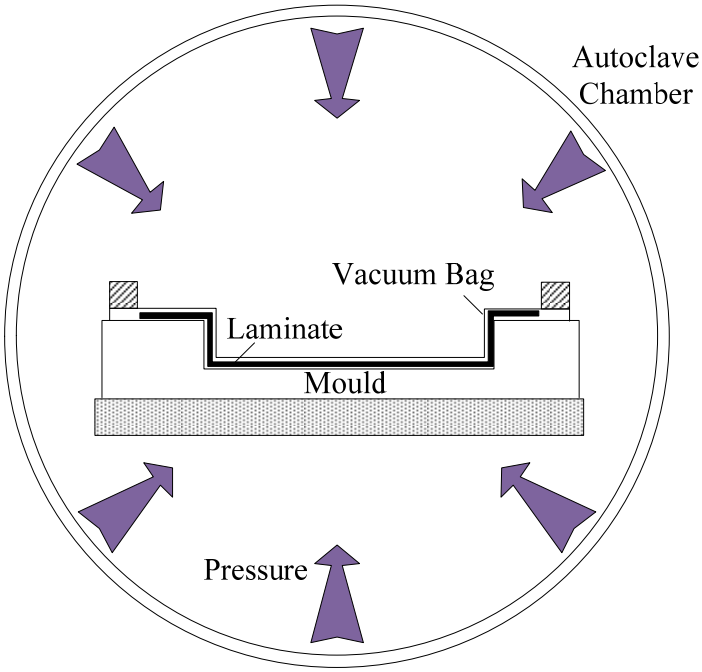

Figure 2-8. Autoclave process.

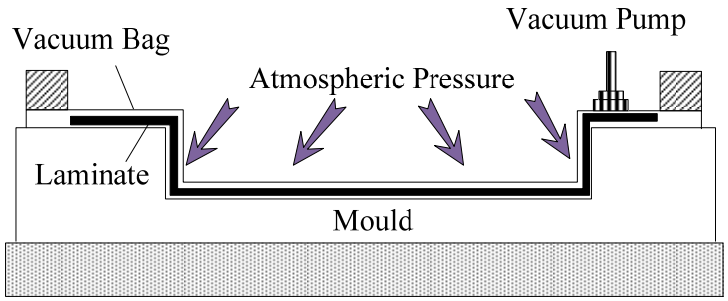

Figure 2-9. Vacuum bag only technique.

Although using the autoclave technique leads to high performance composites, the intensive labour requirements, high capital equipment, high operating cost, poor energy efficiency and slow curing heat-up rates have motivated industries to seek for new methods such as out-of-autoclave (OOA) or vacuum bag only (VBO) techniques for manufacturing of pre-preg laminates (Davies et al. 2007; Garschke et al. 2012; Hernández et al. 2011; Rider et al. 2011; Tavares et al. 2010a; Witik et al. 2012). Therefore, vacuum bag only process is becoming a viable alternative to autoclave method in pre-preg laminate manufacturing (Centea and Hubert 2012; Kratz and Hubert 2011).

In VBO, the reinforcement is laid on a mould and sealed with a flexible vacuum bag. The air is evacuated from the bag which provides consolidation pressure over the lay-ups (Figure 2-9). The assembly may be placed in an oven to cure the resin. The reaction of the chemicals

and curing are carried out under the vacuum bag which allows removing air and volatiles from the laminate surface.

Vacuum bagging technique may be used for fabrication of complex shapes with large components. It is generally suitable for manufacturing of the sandwich panels (Hollaway 1994). The process needs low capital investment, low consumable and tooling cost. Since lower magnitudes of pressure are applied in VBO process in compare with autoclave technique, composites with lower quality can be produced with VBO due to higher void content (Tavares et al. 2010b). One possible way to remove the entrapped volatiles from the pre-pregs is the application of faster heating rates for curing (Agius et al. 2013).

In the case of partially impregnated pre-pregs (Cender et al. 2013) or when higher thickness is required, resin film infusion (RFI) technique may be applied (Figure 2-10). In this method, solid or semi-solid resin films are inserted between layers of dry reinforcement. To infuse the resin in between the fibres, heat and pressure are applied. The heat may be supplied from an Autoclave process or inside of an oven. Since RFI can be used for large components, it is cost effective (Bader 2002).

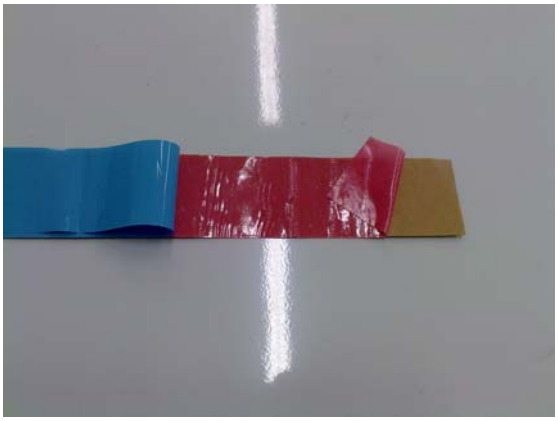

Figure 2-10. Resin film used in RFI process.

Manufacturing of the simple hollow sections can be carried out by pressure bag moulding. In this method, the prepregs are placed between a flexible bag and the mould (Figure 2-11). To make the desirable shape, the bag is pressurised while the whole system is cured in an oven. Pressure bag moulding allows production of pre-pregs with higher consolidation and fibre content (Hollaway 1994).

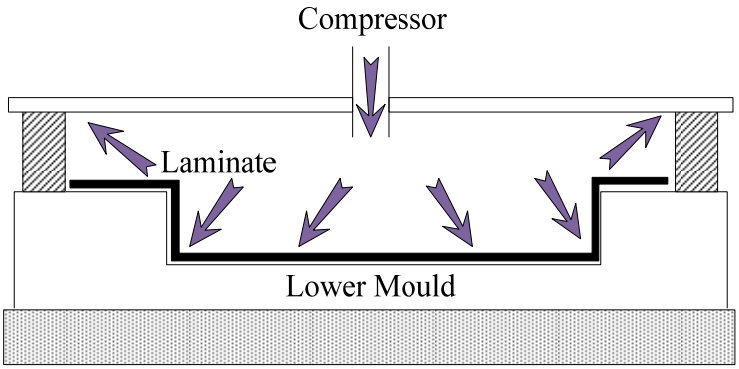

Figure 2-11. Pressure bag moulding.

In press moulding, pre-pregs are placed on the female half of the mould and then using mechanical pressure of the other half; resin distributes and impregnates the fibres (Figure 2-12). Considering the production rate, the curing is carried out under cold or hot environment. High quality and consistent components in terms of dimensions can be produced using this process. In general, the products made by this method have low fibre content with limitation in manufacturing size (Hollaway 1994).

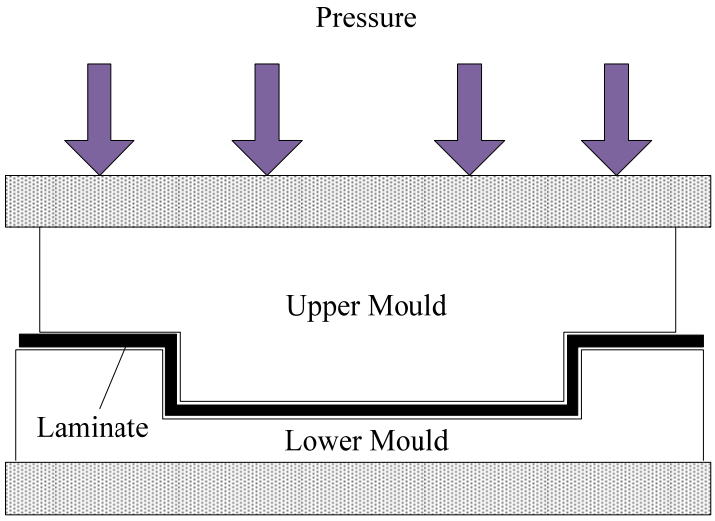

Figure 2-12. Press moulding process.

To mould integrally stiffened structures, thermal expansion moulding is typically used. Pre-pregs are wrapped over blocks of rubber and restrained in a tool. Then, heat is applied to the system which produces high differential thermal expansion between the tool and the block. The resultant high pressure helps to consolidate the pre-pregs. Since the whole process carried out during a single cure cycle, complex shapes can be made with fewer joints or parts.

2.2.5. The Need for the New FRP Processing Techniques

Although the total cost of the wet lay-up method is low, some certain drawbacks led to the development of new manufacturing methods. The production rate is low and it requires intensive labour works for lay up process. Therefore, the quality of the product highly depends on the operator's skill. Since installation and curing of the fibres occurrs under ambient temperature without any control, the resultant thickness and composite uniformity (e.g. misalignment of the fibres, proper resin impregnation, sufficient compaction of fibres) are hard to maintain constant (Boey 1990; Daken et al. 1994; Hollaway 1994).

A high possibility of entrapped air voids inside the composite may result in deterioration and reduction of durability (Karbhari and Zhao 2000). Since the processing technique occurs without any isolation of the resins and volatiles, there are some environmental and safety concerns about wet lay-up system. In addition, the operator is exposed to the chemicals during the entire manufacturing time (Abraham et al. 1998).

Using pultrusion, high fibre content is achievable with consistent longitudinal mechanical properties. Open or closed single or even multicellular sections can be manufactured with high consistency in shape. In addition, different types of thick sections can be made with the pultrusion method. Thick sections offer some superior properties, such as high strength, high stiffness, and high energy absorption. Pultruded profiles show nonlinear material behaviour under multi-directional forces. This characteristic helps the structure to withstand higher stresses and discontinuities.

In terms of the manufacturing cost, pultrusion requires lower facilities, tools and material investments compared with resin transfer moulding or filament winding. This can be obtained through optimisation of the impregnation process, reinforcement selection and curing (Calabrese and Valenza 2003; Silva et al. 2013). This aspect makes pultruded profiles a cost effective option for construction of weight-critical structures, e.g. ship decks and superstructure (Hashim 2009; Nisar and Hashim 2010).

In contrast, there are some disadvantages regarding pultrusion. There are some limitations on the size and length of profiles since they are predefined in manufacturer. Due to the processing method, pultruded profiles are susceptible to generate residual stresses. In terms of cost reduction, the high production rate during the pultrusion process is required. To increase the efficiency of the system, a fast cure rate is utilised using strip heaters attached to the die surface (Kalamkarov et al. 1999).

The final quality of the pultruded profiles are dependent on several variables, such as pulling speed, pulling force, die length, heating die system (Silva et al. 2013), prediction of temperature and curing of the resin within the material (Gorthala et al. 1994). These interdependent variables lay some constraints on the quality control of the pultrusion which are required to be considered during the production (Silva et al. 2013).

The release of chemical vapours from the resin surface and exposure to the chemicals in hand layup or pultruded laminate process are environmental and safety concerns. However in the VARI or HVBO processes, the resin application is under control and set on the fibres using vacuum forces. Therefore, the release of the volatile organic compounds (VOCs) and contact with composite will be minimized in these techniques.

The vacuum assisted resin infusion (VARI) is a closed mould resin infusion process which provides a low cost method for application of FRP for the strengthening of structures in the large components. In addition, the structures with complex geometry can be strengthened by FRP materials using this method (Brouwer et al. 2003; Causse et al. 2012; Correia et al. 2005; Edwards 1998; Hayward and Harris 1990; Teoh and Hsiao 2011). In comparison with other techniques (e.g. hand lay-up, pultrusion and pre-pregs), a composite with better quality is achievable in terms of the mechanical and microstructural properties. This process is repeatable and is able to achieve high fibre-to-resin ratio (Alms et al. 2010; Deka et al. 2009).

Manufacturing methods which are considered in this research are wet lay-up, pultrusion, vacuum assisted resin infusion (VARI) and heated vacuum bag only (HVBO). Among the new FRP fabrication systems, VARI and HVBO are chosen due to their simplicity in moulding and cost effectiveness which may it possible to employ them as an alternative for the methods (wet lay-up and pultrusion) which currently are widely used. In Chapters 3, 4 and 5 the interface behaviour of the FRP-to-concrete bonded joints manufactured with different processing techniques is studied. The performance of these techniques can be compared by evaluation of the local or global response of the strengthened structures. Therefore in the next section, different types of the failure modes in FRP strengthened structures are discussed.

2.3. Failure Modes in FRP Strengthened Structures

Failure in adhesively bonded joints occurs in several ways, namely substrate failure, FRP delamination or failure in bond between two adherends. In this case, debonding may cause

premature failure and therefore can be considered as a destructive factor which leads to the reduction in the maximum load bearing of the strengthened structure (Wu et al. 2006). The failure behaviour depends on the properties of the materials as well as the interface between substrate and the FRP (Gunes et al. 2013).

When a reinforced concrete beam is subjected to the external forces, high tensile and shear forces develop through the beam. These stresses contribute to debonding of the FRP plate from the substrate which is known as the most common failure patterns of the externally bonded (EB) elements. These failure modes are mainly plate end debonding, concrete cover separation, critical diagonal crack debonding, and intermediate crack debonding.

In addition, debonding may occur by FRP delamination, FRP/adhesive separation, cohesion failure (adhesive decohesion), adhesive/substrate separation, and concrete failure. As Figure 2-13 illustrates, failure can be classified into two major types; material decohesion and interface failure (Au and Büyüköztürk 2006; De Lorenzis et al. 2001; Xie and Karbhari 1998). Generally speaking, it is preferred that the failure in flexural elements, e.g. beams, starts from yielding of the steel reinforcement which is followed by concrete crushing. In case of the FRP-strengthened members, since the failure of FRP is more brittle than concrete crushing, FRP rupture should occur after concrete crushing.

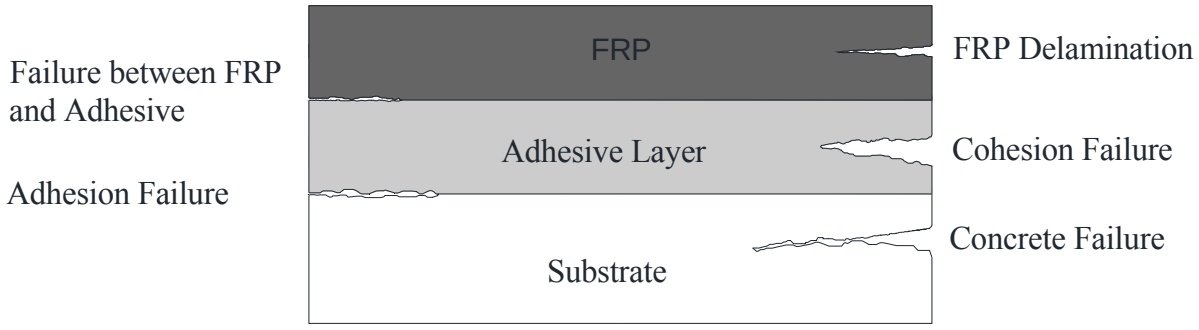

Figure 2-13. debonding modes in EB elements.

2.3.1. Plate End Debonding

When an externally bonded (EB) reinforced concrete beam is loaded by flexural forces, the FRP plate resists against the curvature of the beam which result in the tensile and shear stress developments at the plate end in both concrete and adhesive. These concentrated stresses lead to crack propagation from the plate end inwards. This type of brittle failure in adhesively bonded beams is typically called plate end debonding.

The bending tensile stress, the shear stress, and normal peeling stresses make a contribution to the creation of a bi-axial tensile stress zone in the vicinity of the plate end (Figure 2-14). Concrete is imposed to the peeling stresses as a result of force transferring from the FRP plate to the concrete through the adhesive layer (Pešić and Pilakoutas 2003). The plate end failure is likely to happen in the tension face, compression face and side plated beams.

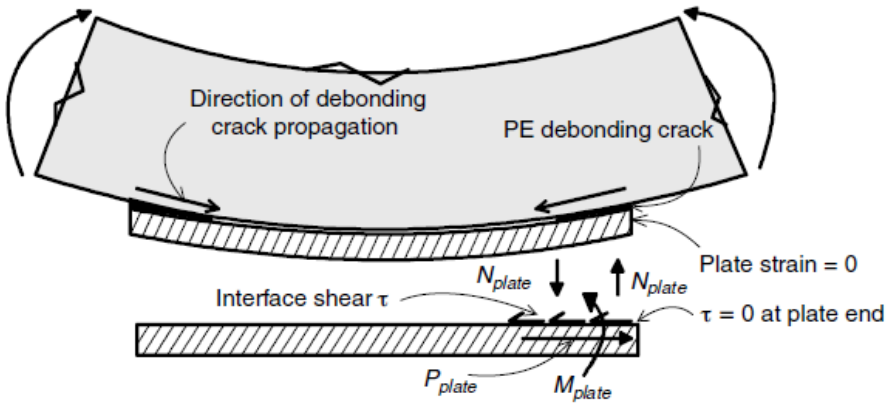

Figure 2-14. Plate end debonding in externally bonded beams (Oehlers 2006).

It is believed that the normal and shear stresses at the end of plates are directly resisted by the direct tensile strength of the concrete. Therefore, in CEB-FIP (2001), the principal tensile stress in concrete at the critical section, σ_1, is limited to the mean concrete strength, $f_{ct,m}$:

$$\sigma_1 = \frac{\sigma_x + \sigma_{n,\max}}{2} + \sqrt{\left(\frac{\sigma_x - \sigma_{n,\max}}{2}\right)^2 + \tau^2_{a,\max}} \qquad 2\text{-}1$$

$\sigma_{n,max}$ and $\tau_{a,max}$ are the maximum normal and shear components at the plate end, respecively.

2.3.2. Concrete Cover Separation

Due to the stress concentration (high interfacial shear and normal stresses) in the vicinity of the plate end, cracks initiate at the end of FRP plate inside the concrete cover and propagate toward the tensile reinforcements (Figure 2-15). After this stage, the crack progress is parallel to the tensile reinforcement which finally leads to the separation of the concrete

cover (Smith and Teng 2002a). Concrete cover separation can be caused by curvature or shear deformations in the tension face plated beams. Since concrete cover separation occurs with plate end or critical diagonal crack debondings, it is confusing to visually distinguish it from other types of failure modes.

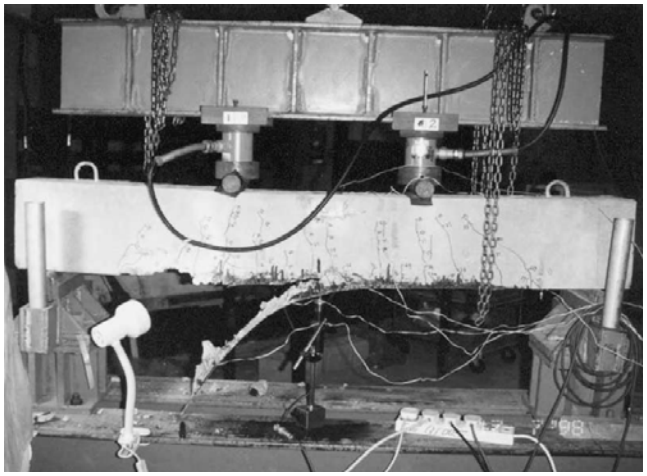

Figure 2-15. Concrete cover separation with plate end debonding (Smith and Teng 2002b).

Based on numerical analysis (Yang et al. 2003), beams with short FRP plate are prone to concrete separation compared with those strengthened with longer plates. In terms of ductility, cover debonding was shown the most brittle among the failure modes in FRP strengthened RC concrete beams (Gunes et al. 2013).

2.3.3. Intermediate Crack Debonding

The bonded plate resists the interface shear and normal stresses transferred from substrate in both shear and flexural strengthened structural members. When FRP traverses a crack in the concrete, stress discontinuity in the vicinity of the crack introduces stress concentration in the FRP. These high stresses lead to debonding along FRP and a thin layer of concrete close to the interface region.

When debonding starts, mainly due to interface shear stresses, intermediate crack (IC) debonding occurs. Debonding initiates at the interception of a plate with an intermediate flexural or intermediate shear/flexural crack and propagates along the interface. In the former, IC debonding is referred as flexural intermediate crack (FIC), and the latter is called shear intermediate crack (SIC) debonding (Figure 2-16) regarding the crack widening procedure (HB 305 2008). By increasing the load, the crack gradually propagates along the bondline

and abates the bonded area until the entire FRP plate separates from the concrete with no further stress transfer.

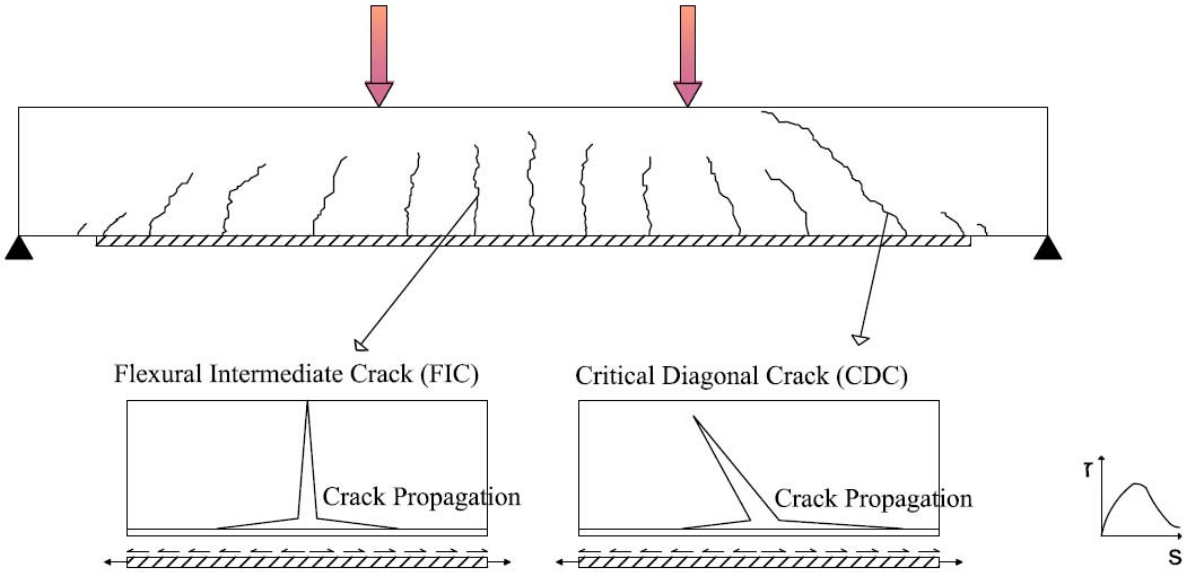

Figure 2-16. Flexural intermediate and critical crack debonding concepts of the externally bonded RC beams.

In reinforced concrete beams strengthened with EB FRP, when the crack is formed in the substrate, the tensile stresses are transferred to the FRP plate (Ombres 2010). If the interfacial stresses reach the strength of the interface, micro-cracks start to form in the vicinity of the concrete substrate and epoxy adhesive (Coronado and Lopez 2006). If the load increases, the micro-cracks propagate and form macro-cracks at one stage (Figure 2-17). Debonding of the interface occurs by propagation of these macro-cracks along the FRP bonded length. Therefore, by the flexural crack development in the beam's soffit, the stress concentration increases at the interface which finally leads to FRP delamination (Carpinteri et al. 2009; Smith and Teng 2001).

The interface behaviour between FRP and concrete in RC beams is mainly characterised in a form of the stress versus deformation relationship which refers to the bond stress-slip law of the interface. The slip is considered as the relative displacement between FRP and the concrete substrate (Bizindavyi and Neale 1999; Nakaba et al. 2001; Täljsten 1996; Wang 2007).

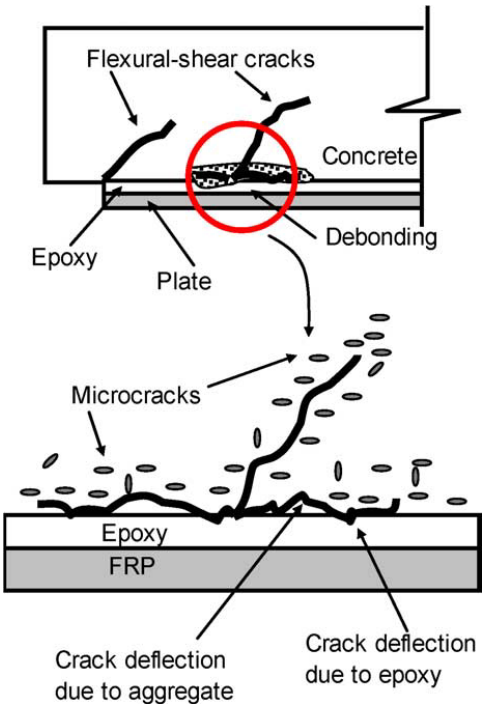

Figure 2-17. Concrete-epoxy interface failure (Coronado and Lopez 2006).

2.3.4. Critical Diagonal Crack Debonding

The debonding initiates from the root of a critical diagonal crack (CDC) (Figure 2-16) which by increasing the load, propagates toward the plate end. It is accompanied by the rigid body displacement of the beam (Figure 2-18) in which the crack propagates rapidly (Oehlers et al. 2003). Therefore, the nature of the CDC debonding is brittle with little warning. The shear deformations in critical diagonal crack widen the CDC and creates axial forces in the plate at the both sides of the crack. These shear deformations are produced as a result of the aggregate interlocks (Oehlers 2006).

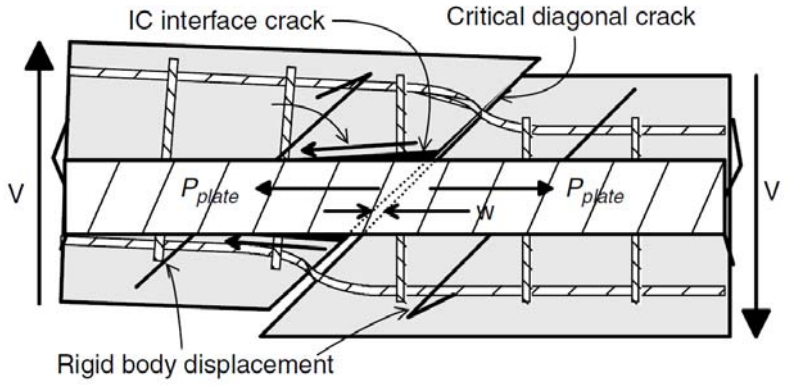

Figure 2-18. Critical diagonal crack propagation (Oehlers 2006).

In case of CDC debonding, FRP plates delay the formation of the CDC in comparison with unplated beams. Cracks may start from the supports and propagate inwards or outwards. Tests have shown that the shear stirrups may not control the debonding mechanism (Ali et al. 2001).

2.4. Different Types of Bond Test

In structures strengthened with fibre reinforced polymer (FRP) materials, interfacial debonding typically governs the critical failure mode. The bond failure may affect the total integrity of the structure considering that the ultimate capacity and desirable ductility of the structure may not be achieved. The possible failure pattern in strengthened flexural or shear members is a complicated phenomenon regarding the interfacial behaviour in externally bonded (EB) joints (Wu et al. 2002).

Extensive experimental (Cao et al. 2007; De Lorenzis et al. 2001; Mazzotti et al. 2008; Nakaba et al. 2001; Nehdi et al. 2003; Taljsten 1997; Ueda et al. 1999; Yang et al. 2007) and theoretical investigations (Brosens and Van Gemert 1998; Dai et al. 2006; Ferracuti et al. 2007) have been carried out and classified in the literature to address the bond behaviour between FRP and concrete substrates.

As crack gradually opens, debonding is accompanied by slip between substrate and FRP. This interfacial behaviour can be addressed by the bond-slip characteristics (shear-slip curves). In order to obtain the interfacial behaviour between the substrate and FRP, different experimental set-ups have been developed. Since the full-scale tests need heavy instrumentation and capital investment, simplified bond tests are proposed to study the interface behaviour in adhesively bonded joints. The commonly used methods which have been reported in literature categorised as; single lap shear (or single face) test, double lap shear (or double face) test, and beam tests.

2.4.1. Single Lap Shear Test

Single lap shear (SLS) test is more commonly used to investigate the intermediate crack debonding in adhesively bonded joints (Yao et al. 2005). A considerable number of studies based on SLS test set-up have been published of which some of them are reported here (Bilotta et al. 2009; Bizindavyi and Neale 1999; Chajes et al. 1996; Dai et al. 2005; Grande et al. 2011; Mazzotti et al. 2008; Pan and Leung 2007; Seracino 2001; Subramaniam et al. 2007; Taljsten 1997; Woo and Lee 2010; Xia and Teng 2005; Yao et al. 2005).

The FRP plates are attached to the top surface of the concrete blocks and placed in the test rig. Then, debonding load is applied to the plate end. The sample is restrained by reaction and positioning frames (Figure 2-19). The positioning frame prevents the block from up-lifting. In this method, the interface is mainly subjected to the shear deformations while the FRP and concrete are under axial deformations.

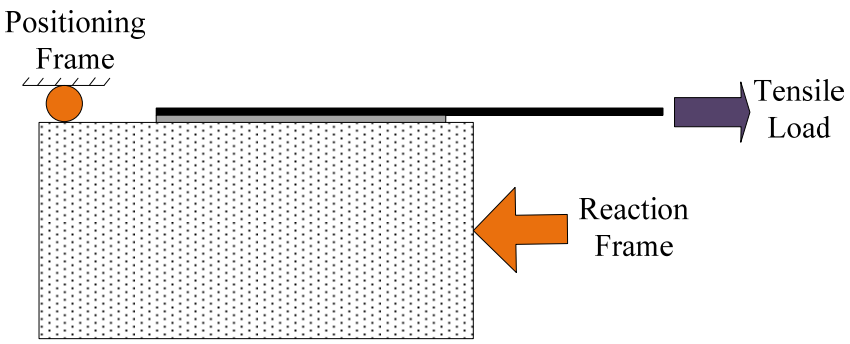

Figure 2-19. Single lap shear test set-up.

Considering the nature of the test, it can be assumed that the shear stress across the interface thickness remains constant. In addition, the FRP and the substrate are subjected to uniformly distributed axial stresses (Cornetti and Carpinteri 2011). The front side of the block is like the crack face in reinforced concrete flexural members (Oehlers 2006). Therefore, the stress state in single lap shear tests is similar to intermediate crack debonding mechanism.

2.4.2. Double Lap Shear Test

To better control the normal stresses in the lap shear joint, double lap shear test set-up is employed. FRP plates are symmetrically applied on both sides of the concrete block. Then, FRP plate ends are subjected to the tensile forces which induce intermediate cracks between the adherents (Figure 2-20). Double lap shear test is usually performed using two identical concrete prisms pre-attached with FRP plates along the centre line of the blocks. One side of the FRP is wrapped by additional sheets to ensure debonding occurs in just one of the blocks. The load may be applied by hydraulic jacks, placed between blocks to push them against each other (Camli and Binici 2007), or by pulling steel bars.

In the double lap shear test, the possibility of the eccentricity of the acting forces has to be kept to a minimum in order to avoid error in the results (Nakaba et al. 2001). Some researches that applied double lap shear test set-up are; Nakaba et al. (2001), Xiao et al.

(2004), Yang et al. (2007), Zhao et al. (2007), Camli and Binici (2007), Foster and Khomwan (2005), Iwashita et al. (2007), Cao et al. (2007), Nehdi et al. (2003).

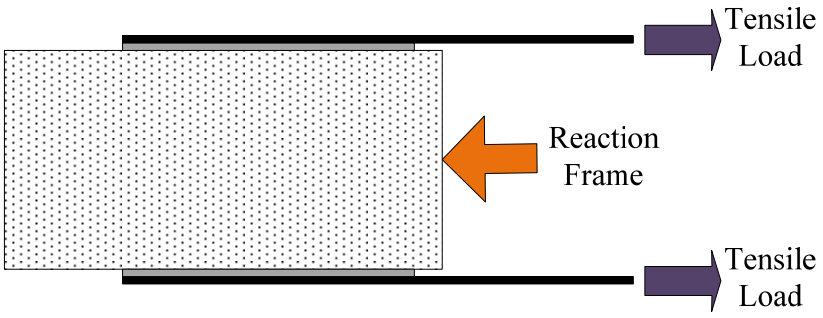

Figure 2-20. Double lap shear test set-up.

2.4.3. Beam Test

The interfacial stress transfer may be resembled with sufficient accuracy by beam tests (Serbescu et al. 2013). Specimens may consist of a concrete beam with a saw cut (notch) in the middle or two concrete blocks joined by a steel hinge on the top (Figure 2-21). When the beam is under the load, the crack grows from the notch to the top joint. Therefore, the crack location is predetermined before the test.

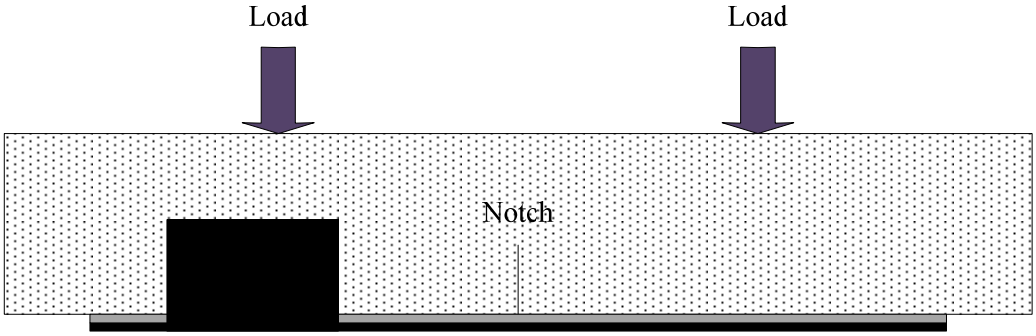

Figure 2-21. Beam test set-up.

The interface is under both shear and flexural stresses at the same time. However, such experiments require heavy test set-ups and higher investment. Some recent studies in which beam test set-up have been used to investigate the bond behaviour are; De Lorenzis et al. (2001), López-González et al. (2012), Guo et al. (2005), Perera et al. (2004), Xiao et al. (2004).

2.5. Parametric Study of the Bond

FRP as a sheet or laminate can be used in shear or flexural strengthening of beams, joints or slabs. In these conditions, FRP contributes to carry a proportion of the load applied to the member. The tensile stresses, produced in the substrate, will be transferred to the FRP through the interfacial region. In order to achieve a desirable stress transferring system, adequate bond between FRP and substrate is necessary. The bond is dependent on several factors such as, surface preparation of substrate, concrete composition, compressive strength of concrete, FRP stiffness, FRP length, bondline thickness and width which their effects should be considered during strengthening procedure.

2.5.1. Concrete Strength

The bond strength in adhesively bonded joints may significantly be dependent on the concrete strength. Considering different concrete compressive strength in the lap shear tests, results showed that the interfacial fracture energy is affected by the concrete strength (Dai et al. 2005). Ueda and Dai (2005) indicated that this effect will be noticeable when concrete compressive strength considerably changes.

Figure 2-22 shows the relation between the concrete strength and the bond capacity for different adhesive thicknesses. It is clear that the maximum debonding force increases with the application of high-strength concrete. In the literature (Chajes et al. 1996; López-González et al. 2012; Savoia et al. 2003), the ultimate debonding load is considered as a proportion of the characteristic compressive strength of concrete ($f'_c{}^{0.56}$, $f'_c{}^{0.9}$, $f'_c{}^{0.5}$, $f'_c{}^{0.19}$ or $f'_c{}^{2/3}$).

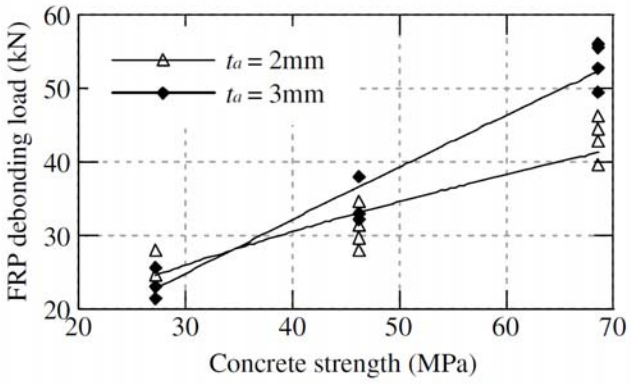

Figure 2-22. Effects of the concrete compressive strength on the interfacial fracture energy of the bond (López-González et al. 2012).

Nakaba et al. (2001) and Chajes et al. (1996) showed that the maximum local bond stress is related to the concrete compressive strength with proportion of $f'_c{}^{0.19}$ and $f'_c{}^{0.5}$. In terms of the fracture, for low-strength concrete specimens, failure occurs inside the concrete while for the high-strength concrete failure is observed in concrete-adhesive interface. It implies that the failure always occur in the weakest part of the joint. In the former, the concrete and in the later the interface are the weakest components, respectively (López-González et al. 2012).

Although in most of the proposed bond-slip relations the bond capacity is directly related to the concrete strength, in some experiments (Camli and Binici 2007; Pan and Leung 2007; Woo and Lee 2010) no clear correlation is found between these two parameters. Considering samples with concrete strength of 35.2 to 61.5 MPa, Pan and Leung (2007) showed that the bond capacity increases with the concrete surface tensile strength (Figure 2-23) while neither change in compressive strength nor splitting tensile strength would lead to the increase in the bond capacity. It is noteworthy to mention that in Pan and Leung (2007), the concrete surface tensile strength is obtained from the pull off tests which may replicate mode I fracture energy. However, the interface behaviour in lap shear tests is mainly governed by mode II fracture energy. The concept of the fracture energy will be discussed in detail in section 2.6.3.

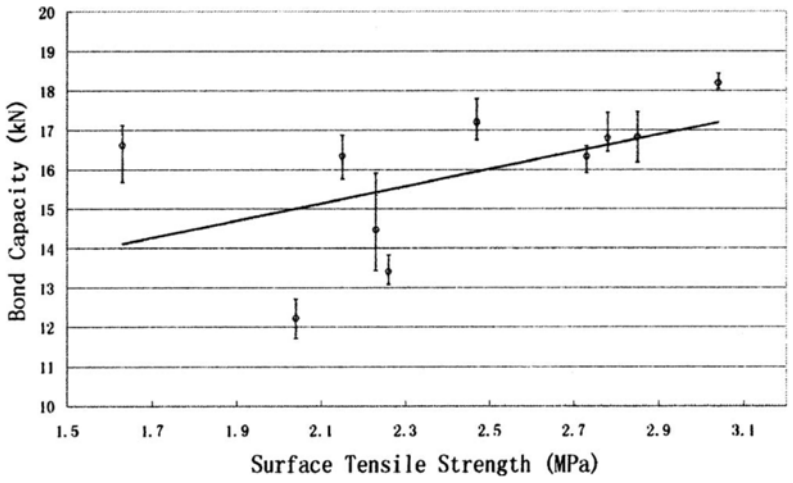

Figure 2-23. Correlation between bond capacity and concrete surface tensile strength (Pan and Leung 2007).

2.5.2. Concrete Composition

Debonding of the samples in the lap shear tests mainly occurs inside the concrete. Furthermore, interlocking along the debonding plane may affect the bond behaviour. The bond capacity is dependent on the residual friction along the attached area of the FRP.

Therefore, the composition of the concrete needs to be considered in the study of interfacial behaviour in adhesively bonded joints.

By application of a digital colour photograph, Pan and Leung (2007) defined the area fraction of the coarse aggregates to the total area of the concrete surface before and after bonding of the FRP. By this method they were able to find out the effects of the aggregate contents in terms of the aggregate interlocking and abrasion on the bond capacity. They showed that a good correlation exists between aggregate content and the bond capacity in FRP bonded joints (Figure 2-24).

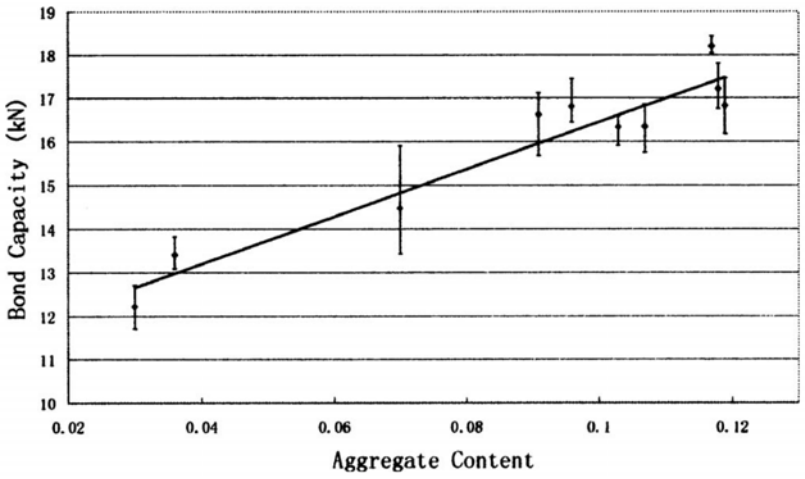

Figure 2-24. Relation between bond capacity and aggregate content (Pan and Leung 2007).

2.5.3. Surface Preparation

It is common knowledge that the presence of moisture, debris or grease may result in reduction in the load carrying capacity of the FRP-bonded joints. Since the failure of the bonded joints mainly occurs in a thin layer of the concrete beneath the FRP, the result of the lap shear tests is highly dependent on the concrete surface treatment (Dai et al. 2006). Therefore, prior to the FRP attachment, the surface of substrate needs to be treated in a way to expose the aggregates and modify the surface condition in terms of the voids and bumps. Using proper surface preparation, it is possible to achieve a reasonable level of the FRP tensile strength during loading in lap shear tests (De Lorenzis et al. 2001).

Controlling the surface preparation is a difficult task, even if a standard procedure of surface treatment is followed. Hence, the final concrete surface condition can still vary.

2.5.4. FRP Bonded Length

The effect of the FRP bond length has been extensively studied. It is acknowledged that the FRP length has significant influence on the failure load in lap shear test (Camli and Binici 2007; Cao et al. 2007; Chen and Teng 2001; De Lorenzis et al. 2001; Mazzotti et al. 2008; Nakaba et al. 2001; Seracino 2001; Taljsten 1997; Woo and Lee 2010; Xiao et al. 2004; Yang et al. 2007; Yao et al. 2005). The ultimate load consecutively increases by application of longer FRP until a specific bond length. This length is usually addressed as the effective bond length, transfer length or critical anchor length (Cao et al. 2007; Taljsten 1997; Yao et al. 2005). Any increase in the length over the effective bond length does not lead to the ultimate load carrying capacity enhancement of the joint.

Experimental results using the electronic speckle pattern interferometry (ESPI) technique (Cao et al. 2007) showed that the area, in which the interfacial stresses transferred, propagates with the increase of the applied load. However, this area remains constant at a certain load level. After this stage, the slip considerably increases while the load does not change.

In general, the stress is transferred from the FRP to the concrete through the bonded region. When the joint is applied to the load, the stresses increase up to a stage after which the interfacial cracks start to propagate from the loaded end toward the free face of the specimens. Nevertheless, still the load keeps increasing till the formation of the macro-crack. During this stage, the stress transfer zone is shifted from the loaded face of the specimen to the free end of the FRP. While the crack grows, specimens experience quite the same value of the maximum load as prior to the formation of macro-cracking. Finally, when the transfer zone reaches the end of the FRP, fracture occurs and load bearing capacity of the joint drops abruptly.

In flexural members, it is recommended to use a development length of approximately three times of the effective bond length (Xiao et al. 2004). In cases when the bond length is relatively short compared to the effective bond length, the stress may not be transferred from FRP to the substrate. In this situation, the failure occurs before the maximum load carrying capacity is achieved. Therefore, it is suggested to consider sufficient FRP bonded length in lap shear test to allow the propagation of the stress transfer zone. In addition, application of longer bond length may contribute to provide further warning time prior to the failure of the system and show more ductile behaviour in the joint (Chen and Teng 2001; Woo and Lee 2010).

2.5.5. FRP Bonded Width

To understand the effects of the FRP bonded width on the interface behaviour, several researches have been implemented (Camli and Binici 2007; De Lorenzis et al. 2001; Mazzotti et al. 2008; Subramaniam et al. 2007; Woo and Lee 2010; Yao et al. 2005). Investigating the effect of FRP width is important since it will contribute to obtain the optimum FRP width in flexural members and also to determine the optimum spacing between FRP plates in shear strengthened members (Subramaniam et al. 2007).

The general response of specimens with different FRP width is quite similar in terms of the load-global slip curve. This trend can be seen in Figure 2-25 for W_{FRP}=25 mm and 38 mm which is reported by Subramaniam et al. (2007). However, wider FRP leads to the increase in the maximum shear stress (Mazzotti et al. 2008).

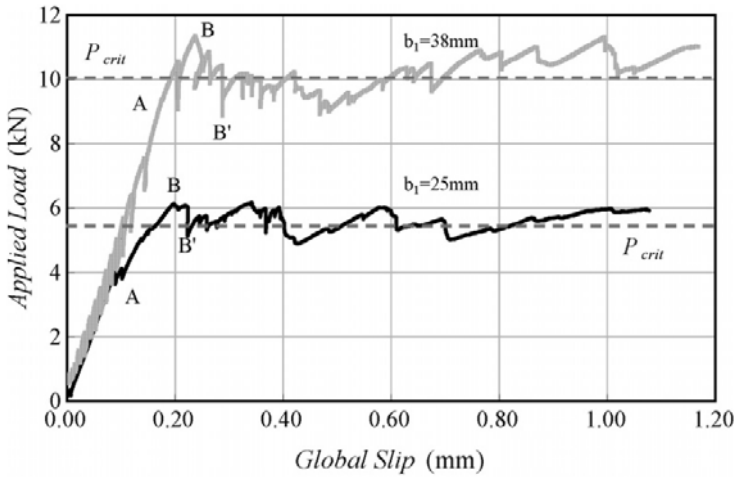

Figure 2-25. Effect of the FRP width on the applied load in lap shear test (Subramaniam et al. 2007).

Subramaniam et al. (2007) indicated that another factor which has to be addressed is FRP-to-concrete width ratio ($w_r = W_{FRP}/W_c$). If the width of the concrete specimens is kept constant, for the samples in which FRP-to-concrete width ratio is small, the load carrying capacity of the joint increases with use of wider FRP. However for large values of w_r, load carrying capacity decreases with wider FRP. In the later case, concrete is not wide enough to allow the propagation of the stress transferring from the FRP into the substrate. Therefore, the level of confinement to the FRP decreases which leads to the failure of the joint in lower loads.

Nevertheless, the average bond strength (Eq. 2-2) may not increase using wider FRP (De Lorenzis et al. 2001; Xia and Teng 2005)

$$\tau_{ave} = \frac{F_{\max}}{W_{frp} L_{frp}} \qquad 2\text{-}2$$

F_{max} is the maximum applied load during the lap shear test while W_{frp} and L_{frp} are FRP width and length, respectively. The effect of the FRP-to-concrete width ratio on the average bond strength is shown in Figure 2-26. Mazzotti et al. (2008) showed that fracture energy is independent from the FRP width.

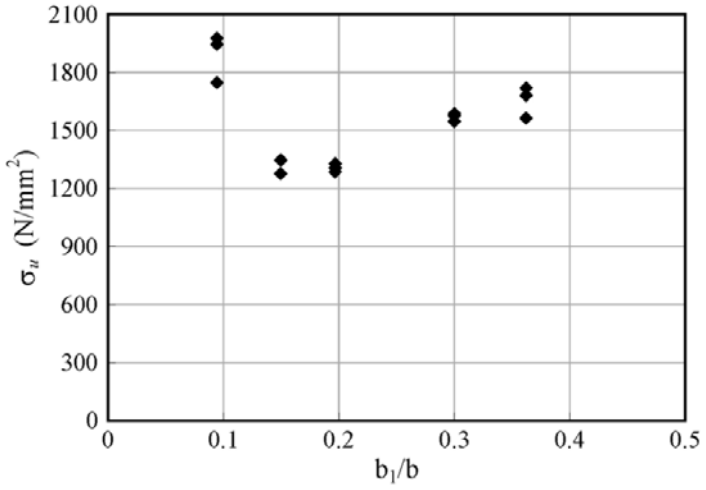

Figure 2-26. Variation of the average bond strength versus FRP-to-concrete width ratio (Subramaniam et al. 2007).

2.5.6. FRP Stiffness

Barnes and Mays (2001) performed double lap shear tests on steel plates externally attached to the concrete blocks and showed that by increasing the plate or adhesive thicknesses, the peak stress level through the interface reduces while the load carrying capacity of the joints increases. In high-strength concrete specimens, when a thin adhesive thickness is used, stress is not able to be distributed along the bond length. In this case, it is advisable to apply thicker adhesive in order to transfer stress to the concrete in more efficient way (López-González et al. 2012).

It was shown that with increase in FRP stiffness, the effective bond length increases (Bizindavyi and Neale 1999; Nakaba et al. 2001). In addition, it was recommended to use

FRP plates with higher Young's modulus with small thickness in order to achieve high stress in externally bonded joints (Chen and Teng 2001). De Lorenzis et al. (2001) showed that with the increase in FRP stiffness, the area under the shear vs slip curve remains the same therefore the local bond ductility decreases. They assumed that the maximum shear stress in the joint is proportional to $(E_{frp}t_{frp})^{0.5}$ and considered the laminate stiffness an influencing parameter in the debonding load. Nakaba et al. (2001) reported that the maximum load carrying capacity of double lap shear joints increases as the FRP stiffness increases.

Regression analysis of the test results (Figure 2-27) performed by Dai et al. (2005) indicates that the fracture energy of the interface is hardly affected by the FRP stiffness with a relation of $(E_{frp}t_{frp})^{0.023}$ in which E_{frp} and t_{frp} are FRP stiffness and thickness, respectively.

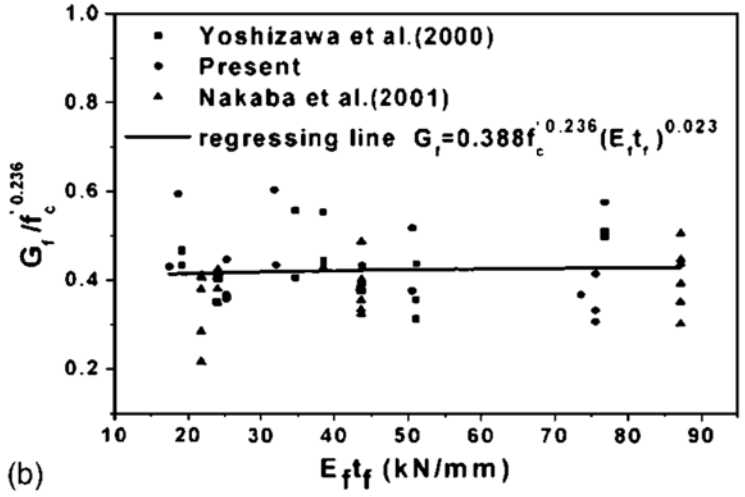

Figure 2-27. Effects of FRP stiffness on the interfacial fracture energy of the bond (Dai et al. 2005).

2.5.7. Adhesive Properties

Test results (Figure 2-28) show that the interfacial fracture energy may be reduced by application of adhesives with higher shear modulus (G_{adh}/t_{adh}). In addition, the maximum bond stress increases with the shear stiffness of the adhesive layer (Dai et al. 2005). Since the available experimental data is limited, the effects of the adhesive properties on the bond need to be investigated more.

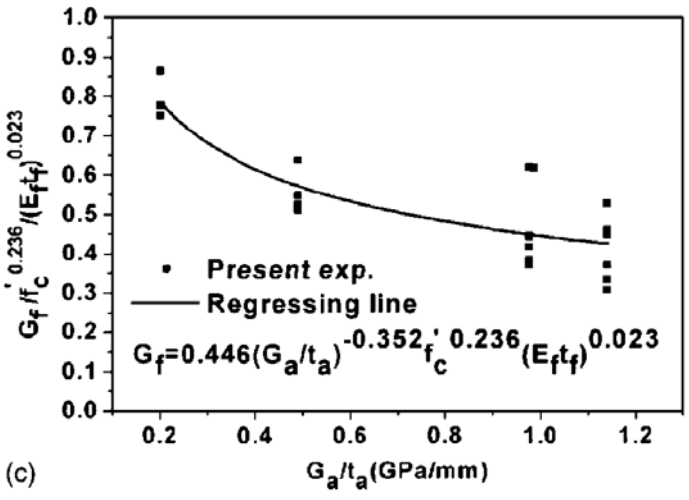

Figure 2-28. Effects of the adhesive properties on the interfacial fracture energy of the bond (Dai et al. 2005).

2.6. Modelling of the Interface

The formulation of the bond between the FRP and the concrete has been the subject of intense research over the last decade. Based on these studies, various mathematical models have been proposed to simulate the interface response under loading. Depending on the methods, the existing analytical models may be classified into three major categories; empirical-based models, elasticity theory-based models or fracture mechanics-based models. Empirical-based models are mainly derived from the regression of the experimental data in the lap shear tests. In the models which are developed by the elasticity theory, the basic governing equations are employed and solved for specific boundary conditions. In other researches, the principles of the fracture mechanics are employed to simulate the bond response.

2.6.1. Empirical-based Models

In empirical-based models, the bond relationships are mainly determined by the regression of the interface parameters based on the experimental results. The advantage of these models is that the formulation is quite simple and straightforward. Despite this simplicity, the outcomes of these models show high variation. This is due to the fact that the bond parameters are derived for specific experimental conditions such as, properties of concrete, FRP or adhesive, loading regime, test set-up, and instrumentation. These conditions may change from one experiment to the other.

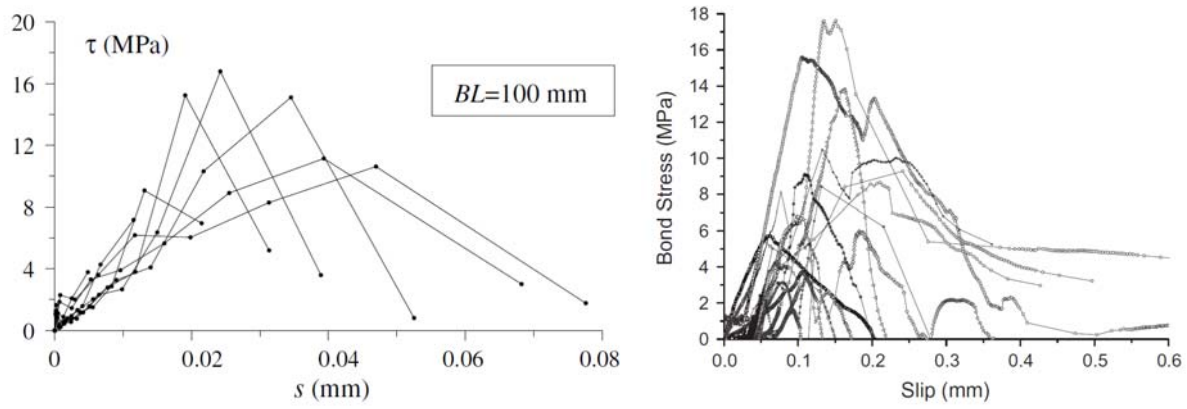

(a) (b)

Figure 2-29. Local bond-slip curves reported in literature (a) Mazzotti et al. (2008) and (b) Liu and Wu (2012).

The interface behaviour, in the majority of the researches, is characterised by the bond strength and more importantly the local shear stress-slip profiles which is called the local interface law. Figure 2-29 illustrates the bond-slip relationships derived from the experiments. The local slip at any location can be derived from the strain values by integration of the strain profile along the bond length to that position while shear stress is obtained from the production of FRP stiffness and the gradient of the axial strain of the FRP.

The local bond-slip law can be defined for different locations of the interface as well as each loading level. However, it was shown that the bond-slip curves experience large variation in terms of the shape and also the fundamental bond parameters such as the maximum shear stress, τ_{max}, local slip at the maximum shear stress, s_0, and ultimate local slip values, s_{ult}, (Abdel Baky et al. 2012; Dai et al. 2005, 2006; Liu and Wu 2012; Ueda and Dai 2005; Zhou et al. 2010). These discrepancies may be due to local composition of the materials (concrete, adhesive or FRP plate), type of instrumentation or the local stress concentrations (bending of the FRP plate due to the thinness of the plate or the roughness of the fractured surface) (Lu et al. 2005a; Yuan et al. 2004). Based on these variations, various local interface laws with different shapes and bond parameters have been proposed.

Figure 2-30 shows some bond-slip models in the literature. Some models have only the descending branch (a-b) while the others consist of ascending and descending branches (c-h). In addition, the distribution of the shear stresses along the bonded length is expressed by linear (a, c-g) or nonlinear (b and h) curves.

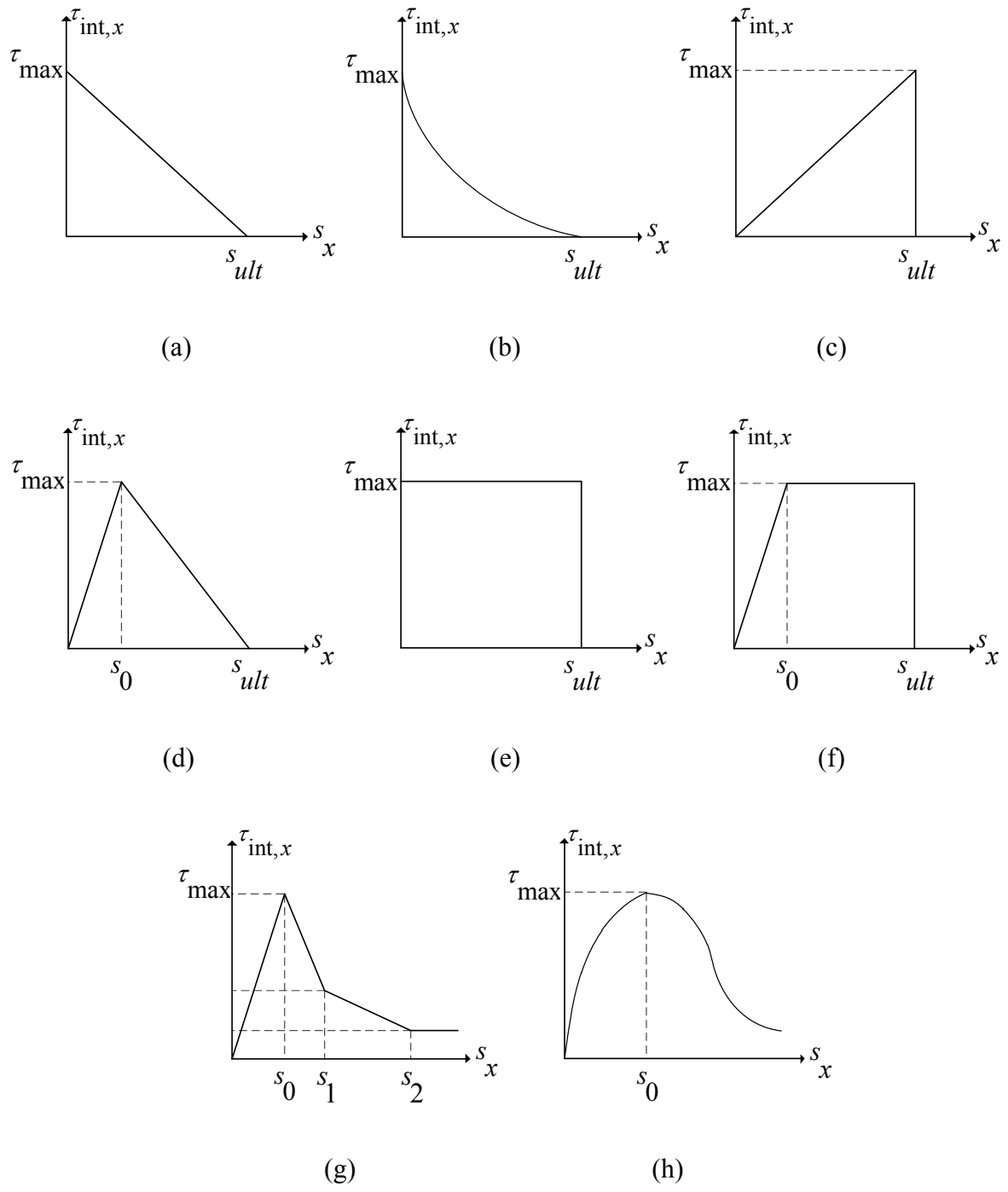

Figure 2-30. The proposed local interface models.

Local Shear Stress profile

Several models consider a direct proportion between the maximum shear stress and the geometry of the samples or properties of the materials. Hiroyuki and Wu (1997) and Tanaka (1996) related the mean value of shear stress ($F_{max}/W_{frp}.L_{frp}$) to the FRP bonded length, L_{frp} (Chen and Teng 2001);

Hiroyuki and Wu model: $\tau_{mean} = 5.88 L_{frp}^{-0.669}$ 2-3

Tanaka model: $\tau_{mean} = 6.13 - \ln L_{frp}$ 2-4

Ueda et al. (1999) assumed that the maximum shear stress, τ_{max}, (in MPa) is about 19% of the FRP stiffness (in GPa) with the maximum value of 7.3 MPa:

$$\tau_{\max} = 0.19 t_{frp} E_{frp} \leq 7.3 MPa \quad 2\text{-}5$$

Nakaba et al. (2001) fitted the bond parameters into Popovic's equation (Popovics 1973) using the least square method

$$\tau_{\text{int},s} = \tau_{\max} \cdot \frac{s}{s_0} \cdot \frac{n}{(n-1) + (s/s_0)^n} \quad 2\text{-}6$$

where n and s_0 are experimentally obtained as 3 and 0.065 mm, respectively, and the maximum shear stress is expressed as a proportion of the concrete compressive strength (for f_c' between 24 and 58 MPa);

$$\tau_{\max} = 3.5 f_c'^{0.19} \quad 2\text{-}7$$

Savoia et al. (2003), Guo et al. (2005) and Ferracuti et al. (2007) also used the same relationship (Eq.2-6), by regression with the experimental results, and proposed s_0 = 0.051, 0.046 and 0.039 mm and n = 2.86, 2.018 and 2.386, respectively. Guo et al. (2005) expressed the maximum shear stress as

$$\tau_{\max} = 0.7512 f_c'^{0.5} \quad 2\text{-}8$$

The shear stress profile (Eq.2-6) is characterised as a function of the concrete compressive strength only. However, recent studies (Abdel Baky et al. 2012; Dai et al. 2006; López-

González et al. 2012) indicate that the bond strength depends not only on the characteristics of the concrete but also the FRP plate and the adhesive.

Woo and Lee (2010) used a three-section bond-slip law with two linear ascending and an exponential descending part

$$\tau_{\text{int},s} = \frac{\beta}{\alpha} \cdot \frac{\tau_{\max}}{s_0} \cdot s_x \qquad \text{for } 0 \le s_x \le \alpha s_0 \qquad \text{2-9}$$

$$\tau_{\text{int},s} = \frac{1}{1-\alpha} \cdot \frac{\tau_{\max}}{s_0} \cdot \left[(1-\beta)s_x + (s_x - \alpha)s_0\right] \qquad \text{for } \alpha s_0 \le s_x \le s_0 \qquad \text{2-10}$$

$$\tau_{\text{int},s} = \tau_{\max} \cdot e^{-\frac{\tau_{\max}}{K} \cdot (s_x - s_0)} \qquad \text{for } s_0 < s_x \qquad \text{2-11}$$

To find the unknown parameters in Eqs. 2-9 to 2-11, Woo and Lee (2010) used an inverse method in conjunction with the finite element analysis. For this, the model was implemented into a two dimensional finite element model using interface elements. By adopting the strain and the failure load values based on the experimental and above equations, unknown parameters are obtained. These parameters vary with the changes in the geometry of the joint. Therefore, Eqs. 2-9 to 2-11 do not provide an explicit solution for the FRP/concrete bonded joints.

Maximum Applied Load

Using the regression of the experimental results, Seracino (2001) proposed the following equation for plates thicker than 1 mm in which the maximum applied load is determined based on the properties of the adhesive, concrete and FRP plate;

$$F_{\max} = 1.71 \times 10^8 \frac{f_c^{'} A_{frp} t_{adh}}{E_c^{1.5}} \cdot \left[E_{frp} / E_{adh}\right]^{0.1} \qquad \text{2-12}$$

The effect of the FRP bonded length is ignored in this equation. Therefore, it can be applied to the joints with bonded length over the effective bond length.

Considering equilibrium and compatibility in the fracture plane of the FRP/concrete joints, Seracino et al. (2007) proposed a J factor (Eq. 2-14) which substitutes the FRP stiffness $(Et)_{frp}$ in Eq. 2-13. Based on this factor, the FRP and also the concrete geometries are taken into account in order to determine the interfacial shear stresses

$$\tau_{\text{int},x} = \frac{1}{E_{frp} t_{frp}} \cdot \frac{d^2 s_x}{dx^2} \qquad 2\text{-}13$$

$$J = L_{per}\left[\frac{1}{E_{frp} A_{frp}} + \frac{1}{E_c A_c}\right] \qquad 2\text{-}14$$

L_{per} is the length of the debonding failure plane which is assumed $L_{per} = W_{frp} + 4$. The maximum applied load obtained by;

$$F_{\max} = \sqrt{\tau_{\max} s_u} \cdot \sqrt{L_{per} E_{frp} A_{frp}} \qquad 2\text{-}15$$

To derive the abovementioned formulae, the bond-slip relation is idealized as a descending linear line with coordinates of $(0,\tau_{max})$ and $(s_u,0)$. Although they substituted FRP stiffness $(EA)_{frp}$ by J factor for determination of the shear stresses, however the concrete axial stiffness $(Et)_c$ is ignored afterwards. Therefore, the only parameter which is considered to derive Eq. 2-15 is $L_{per}/(EA)_{frp}$ and the proposed relation is valid when the fracture occurs inside the concrete.

Up to this stage, the elasticity theory was applied to find the maximum applied load. However, to find the unknown parameters in Eq. 2-15, a linear regression of the experimental results is used. Seracino et al. (2007) assumed that $\tau_{max} \cdot s_u$ is directly related to the concrete compressive strength

$$\tau_{\max} \cdot s_u = C\varphi_f^m f_c'^n \qquad 2\text{-}16$$

in which C, m and n are 0.976, 0.526 and 0.6, respectively. The maximum load carrying capacity of the joint is calculated by

$$F_{\max} = 0.85\varphi_f^{0.25} f_c'^{0.33} \sqrt{L_{per} E_{frp} A_{frp}} \qquad 2\text{-}17$$

Effective Bond Length

Maeda et al (1997) showed that the effective bond length is exponentially related to the FRP stiffness (Chen and Teng 2001)

$$L_{eff} = e^{6.13 - 0.58 \ln E_{frp} t_{frp}} \qquad 2\text{-}18$$

Using experimental results, Bizindavyi and Neale (1999) reported that the transfer length has a bilinear relationship with the relative load level (F/F_{max}), a plateau region (initial transfer length) and an ascending linear branch (transfer length or in this case effective bond length);

$$L_t = L_0 \qquad \text{for } \xi \le \xi_0 \qquad 2\text{-}19$$

$$L_t = L_0 + \left[\frac{\xi - \xi_0}{\xi_{\max} - \xi_0}\right] \cdot (L_{frp} - L_0) \qquad \text{for } \xi_0 \le \xi \le \xi_{\max} \qquad 2\text{-}20$$

The initial transfer length, L_0, is obtained based on two different relations which the first one underestimates (2-21) and the second overestimates (2-22) the actual value;

$$L_0 = \frac{\xi_0 \cdot F_{\max}}{W_{frp} \cdot \tau_{\xi_0}} \qquad 2\text{-}21$$

$$L_0 = \frac{\xi_0 \cdot F_{\max}}{W_{frp} \cdot \tau_{mean}} \qquad 2\text{-}22$$

ξ_0 and $\tau_{\xi 0}$ are the relative load level and the maximum shear stress prior to the initial cracking load while W_{frp} and L_{frp} are width and length of the FRP, respectively.

2.6.2. Elasticity Theory-based models

Taljsten (1997) compared experimental results of the shear stresses in the adhesive layer with the theoretical model derived by Volkersen (2-23). Since Volkersen formula is based on the theory of elasticity, this equation can only predict the elastic response of the joint or in other word at low levels of the load.

$$\tau_{\text{int},x} = \omega F \cdot \frac{\cosh(\omega x)}{\sinh(\omega L)} \qquad \text{2-23}$$

$$\omega^2 = \frac{G_{adh}}{t_{adh}} \cdot \left[\frac{1}{E_{adh} t_{lam}} + \frac{1}{E_c t_c} \right] \qquad \text{2-24}$$

F is the applied load at the loaded end, L is the bonded length, G_{adh} is the shear modulus of the adhesive, E_{adh} and E_c are the modulus of elasticity of the adhesive and concrete, respectively. t_{lam} and t_c are the laminate and concrete thicknesses, respectively.

Based on the shear lag theory, Bizindavyi and Neale (1999) expressed the shear stress along the bond length by a hyperbolic equation. Similar to Taljsten (1997), Eq.2-25 is only valid in the elastic range.

$$\tau_{\text{int},x} = B\cosh(\lambda x) + C\sinh(\lambda x) \qquad \text{2-25}$$

$$B = \tau_m \cdot \frac{\lambda L_{frp}}{\tanh(\lambda L_{frp})} \qquad C = -\lambda L_{frp} \tau_m \qquad \text{2-26}$$

$$\lambda = \left[\frac{G_{adh}}{E_{frp} t_{frp} t_{adh}} \cdot \left(1 + \frac{E_{frp} A_{frp}}{E_c A_c} \right) \right]^{1/2} \qquad \text{2-27}$$

By integration of the shear stress (2-25), the applied load is obtained

$$F_{frp,x} = \frac{\tau_m L_{frp}}{t_{frp} \sinh(\lambda L_{frp})} \cdot \left[\sinh \lambda (x - L_{frp}) \right] \qquad \text{2-28}$$

The analytical results could predict the strain profile along the bond length in elastic range. However by increasing the FRP thickness, theoretical model exhibits stiffer response. Bizindavyi and Neale (1999) concluded that this deviation is due to the ignorance of the peeling stresses in the analysis which dominate the joint behaviour. De Lorenzis et al. (2001) employed a similar method to develop an interface law for FRP/concrete bonded joints. They considered the shear stress as a linear function of the local slip;

$$\tau_{\text{int},x} = K \cdot s_x = K \cdot \frac{F}{\alpha (WEt)_{frp} \sinh \alpha L_{frp}} \cdot \cosh \alpha x \qquad 2\text{-}29$$

$$\alpha = \sqrt{\frac{K}{t_{frp} E_{frp}}} \qquad 2\text{-}30$$

$$K = \frac{G_{adh}}{t_{adh}} \qquad 2\text{-}31$$

For more information, Table 2-1 presents some major bond-slip models which have been developed based on empirical or elasticity theory.

2.6.3. Fracture Mechanics-based Models

If the concrete is subjected to physical loading, micro-cracks start to propagate in the structure. Close to the maximum load, large fractures (macro-cracks) form inside the concrete which finally lead to the failure of the structure. Occurrence of the cracks in the concrete may influence strength, serviceability and durability of the structure. Therefore, it is advisable to investigate the fracture mechanism of the concrete. In this regard, fracture mechanics theory was employed to predict the crack propagation behaviour in the concrete. Since the failure of the FRP/concrete joints under tensile loads is accompanied by fracture of a thin layer of the concrete at the vicinity of the bonded area, fracture mechanics theory may be applied to simulate the interface behaviour.

The improvements in computer programming have been contributed to the increasing interest in the development of models using fracture mechanics theory. Therefore in this section, first the basics of different fracture mechanics approaches such as linear elastic and nonlinear fracture mechanics are briefly described. For more information regarding fracture

mechanics theory author refers to (Bazant and Planas 1997; Mier 2012; Shi 2009).Then, several models which have been developed in literature are presented.

Linear Elastic Fracture Mechanics (LEFM)

Linear elastic fracture mechanics (LEFM) assumes that when a crack occurs in a body, stresses are quite high in the vicinity of a crack which produces an inelastic zone in that area. The disturbance initiated by the inelastic zone would be negligible if the zone is relatively small in comparison to the dimensions of the body (Bazant and Planas 1997).

LEFM is originated from Griffith (1921) energy approach for the brittle fracture of glass. He proposed an energy balance criterion for failure in which the crack propagates only if the available energy is equal to the energy required to extend the crack by a unit surface area (Bazant and Planas 1997). Based on this principle, the rate of differences between internal and external energies corresponding to a crack surface area, A, is equal to $2\gamma_s$;

$$\frac{\delta(U-V)}{\delta A} = 2\gamma_S \qquad 2\text{-}32$$

U and V are the work of the external forces and internal strain energy, respectively. γ is the specific surface energy of the elastic solid and represents the required energy to create a unit area of new surface. Griffith (Yarema 1996) proposed the following equation to determine the breaking load for an elastic plate with a crack length of $2a$ subjected to uniform distributed loads perpendicular to the crack (Figure 2-31)

$$F = \sqrt{\frac{2E\gamma_S}{\pi a}} \qquad 2\text{-}33$$

where E is Young modulus. However, experimental results showed that the forces required to break the plate is much larger than F. In addition, calculating the potential energy of the body is very complicated. To resolve these issues, Irwin proposed the work of plastic deformations at the vicinity of the crack tip related to a unit area of the newly formed surface which is required to be considered as a parameter to the specific surface energy (γ) (Yarema 1996).

Irwin showed that if the characteristic size of the plastic deformations zone is small relative to the crack length, the energy flow into the fracture zone comes from the elastic solid and the stress in elastic bulk of solid is not much different from the elastic solution;

$$\frac{\delta(U-V)}{\delta A} = G \qquad 2\text{-}34$$

G is the energy release rate and determines the energy available for further propagation of the crack by a unit area.

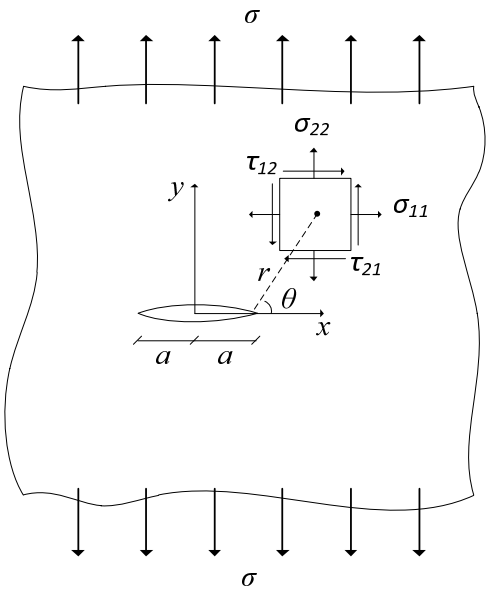

Figure 2-31. An infinite plate with a crack subjected to tensile stresses.

By investigating the distributions of stresses in an elastic plate with crack due to the tensile stresses at the crack tips (Figure 2-31), Irwin (1957)suggested that the principal part of the stress tensor components in the immediate neighbourhood of the crack tip can be expressed in the polar coordinates (r,θ) by

$$\sigma_{ij} = \frac{K}{\sqrt{2\pi r}} f_{ij}(\theta) \qquad 2\text{-}35$$

$f_{ij}(\theta)$ is a function of the polar angle θ, and r is the distance of a given point from the crack tip. The stress fields of different configurations vary corresponding to the stress intensity factor, K. The stress intensity factor depends on the applied load, the size of the crack and the

geometry of the problem (Shi 2009). It can be used in order to determine whether the crack grows or not by comparing this factor to some critical intensity. It also identifies the strength of the crack tip singularity as well as deformation mode. Therefore, it can make a relation between the local material behaviour of the crack and the global response.

Depending on the loading type applied to the crack, surfaces of the crack may displace in various directions (Figure 2-32). Opening mode I occurs when the normal loads applied to the crack plane and cause the displacements of the crack surface perpendicular to the crack plane. Mode II leads to the sliding of the crack surfaces and refers to in-plane shear. The last type is out-of-plane shear in which loads applied to the crack in a way to tear the two crack surfaces apart. Corresponding to each fracture mode, the stress intensity factors can be defined as K_I, K_{II}, and K_{III}, respectively.

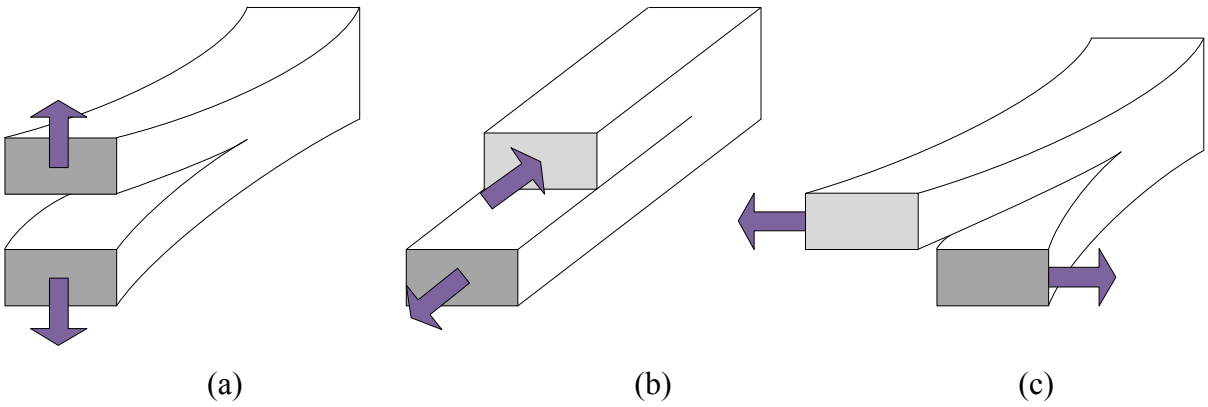

Figure 2-32. Fracture modes; (a) opening mode I, (b) in plane shear mode II, and (c) out-of-plane shear mode III.

Nonlinear Fracture Mechanics (NLFM)

When the fracture process zone (FPZ) is small compared to the body and the fracture occurs at the tip of a sharp crack, LEFM is applicable to the condition which is described in the previous section. However, when the FPZ is large such as in case of concrete or tough ceramics, LEFM is no longer valid and condition can be described by nonlinear fracture mechanics (NLFM).

Two simplified approaches have been proposed to define the FPZ: cohesive crack models (CCM) (or also called fictitious crack model, Dugdale-Barenblatt model, or crack with bridging stresses) and crack band models (CBM). The former considers the FPZ is lumped into the crack line and characterized by a stress-displacement law. It assumes that the volume

of the body remains elastic and the nonlinearity occurs along the crack line. On the other hand, crack band models consider a band width in front of the main crack through which the inelastic deformations in the FPZ are smeared (Bazant and Planas 1997). Crack band models are popular in FE analyses and design practices. This model assumes that infinite numbers of the parallel openings are continuously distributed over the crack band width. In FE analysis when the maximum strength capacity of the material is reached, the material stiffness and strength in the direction normal to the cracks will be reduced.

Proposed Models

Täljsten (1996) used two separate methods, energy criteria of the linear elastic fracture mechanics in conjunction with the simple beam theory and also one-dimensional nonlinear fracture mechanics to estimate the maximum possible load capacity of the joints.

Linear approach:

$$F_{\max} = W_{frp}\sqrt{\frac{2E_{frp}t_{frp}G_F}{1+\alpha}} \qquad 2\text{-}36$$

where

$$\alpha = \frac{E_{frp}t_{frp}}{E_c t_c} \qquad 2\text{-}37$$

Nonlinear approach:

Using nonlinear fracture mechanics and Eqs. 2-23 and 2-24, a general relation is proposed for the maximum normalised applied load considering bond-slip relation with linear ascending branch and sudden drop (Figure 2-30c)

$$\frac{F_{\max}}{\tau_{\text{int},x}W_{frp}(L_{frp}-a)} = \frac{\sqrt{2}}{\omega_1}\tanh(\frac{\omega_1}{\sqrt{2}}) \qquad 2\text{-}38$$

a is crack length and

$$\omega_1^2 = \frac{\tau_{\max}^2 (L_{frp} - a)^2 (1+\alpha)}{E_{frp} t_{frp} G_F} \qquad \text{2-39}$$

For brittle adhesives Eq. 2-38 can be simplified in the form of Eq. 2-36.

Table 2-2 provides a reference for existing models which are developed based on the fracture mechanics theory.

Table 2-1. Empirical and elasticity theory-based models proposed in literature.

Model	Shear Stress Profile		τ_{max}	s_0	F or F_{max}	L_{eff}
	Ascending Branch	Descending Branch				
Nakaba et al. (2001)	$\tau_{\max} \cdot \frac{s}{s_0} \cdot \frac{3}{2+(s/s_0)^3}$		$3.5 f_c^{'0.19}$	0.065	---	---
De Lorenzis et al. (2001)	$K \cdot \frac{F}{\alpha W_{frp} E_{frp} t_{frp} \sinh \alpha L_{frp}} \cdot \cosh \alpha x$		$0.0184(t_{frp} E_{frp})^{1/2}$	---	---	---
Seracino (2001)	---		---	---	$1.71\times10^8 \frac{f_c^{'} A_{frp} t_{adh}}{E_c^{1.5}} \cdot (E_{frp}/E_{adh})^{0.1}$	---
Savoia et al. (2003)	$\tau_{\max} \cdot \frac{s_x}{s_0} \cdot \left[\frac{2.86}{1.86+(s_x/s_0)^{2.86}}\right]$		$3.5 f_c^{'0.19}$	0.051	---	---
Guo et al. (2005)	$\tau_{\max} \cdot \frac{s_x}{s_0} \cdot \left[\frac{2.018}{1.018+(s_x/s_0)^{2.018}}\right]$		$0.7512 f_c^{'0.5}$	0.046	---	---
	$\tau_{\max} \cdot \frac{\overline{k_0}}{\alpha_k} \cdot \left[\frac{1+\alpha_k}{\alpha_k} \cdot \ln(1+\alpha_k \frac{s_x}{s_0}) - \frac{s_x}{s_0}\right]$	$\tau_{\max} \cdot \left[\frac{s_x/s_0}{a+b\,s_x/s_0 + c\,s_x^2/s_0}\right]$				
	$\tau_{\max} \cdot 1.114(\frac{s_x}{s_0})^{0.488}$	$\tau_{\max} \cdot (1.3424 e^{-0.2578\frac{s_x}{s_0}})$				
Foster and Khomwan (2005)	$\tau_{\text{int},x} = 12(\lambda - 2\lambda^2 + \lambda^3) \cdot \frac{\varepsilon_0 t_{frp} E_{frp}}{L_{eff}}$ $s_x = (1-K) \cdot (2 - 2\lambda + 0.6\lambda^2) \cdot (L_{eff} \varepsilon_0 \lambda^3)$		$\frac{16}{9} \cdot \frac{\varepsilon_0 t_{frp} E_{frp}}{L_{eff}}$	$\frac{7}{135}(1-K) \cdot (L_{eff} \varepsilon_0)$	---	Ueda and Dai (2004)

Model	Shear Stress Profile		τ_{max}	s_0	F or F_{max}	L_{eff}
	Ascending Branch	Descending Branch				
Cao et al. (2007)	$\tau_{\max}\cdot\frac{\overline{k_0}}{\alpha_k}\cdot\left[\frac{1+\alpha_k}{\alpha_k}\cdot\ln(1+\alpha_k\frac{s_x}{s_0})-\frac{s_x}{s_0}\right]$	$\tau_j-\overline{k_d}\tau_{\max}\cdot\frac{s_x-s_j}{s_0}$	$1.64f_c'^{0.25}$	0.029	---	---
	$\tau=\tau_{\max}\cdot\left[0.2+1.6\frac{s_x}{s_0}\cdot(1-\frac{s_x}{2s_0})\right]$	$\tau_j=\tau_{\max}\cdot\left[0.2+1.6\frac{s_j}{s_0}\cdot(1-\frac{s_j}{2s_0})\right]$				
Seracino et al. (2007)	---	$\tau_{\max}\cdot(\frac{s_u-s_x}{s_u})$	$(0.802+0.078\varphi_f)f_c'^{0.6}$	$s_u=\frac{0.976\varphi_f^{0.526}}{0.802+0.078\varphi_f}$	$0.85\varphi_f^{0.25}f_c'^{0.33}\sqrt{L_{per}E_{frp}A_{frp}}$	$\frac{\pi}{2\lambda}$ $\lambda^2=\frac{\tau_{\max}L_{per}}{s_u(EA)_{frp}}$
Camli and Binici (2007)	$\frac{F\lambda}{W_{frp}}\cdot\frac{\cosh(\lambda x)}{\sinh(\lambda L)}$ $\lambda^2=\frac{\tau_{\max}}{s_u t_{frp}E_{frp}}$	0	Savoia et al. (2003)	$s_u=f_c'^{\alpha}(\frac{L_{frp}}{L_{eff}})^{\beta}(\frac{W_{frp}}{W_c})^{\gamma}$	$\sqrt{\tau_{\max}s_u}\cdot\sqrt{E_{frp}A_{frp}}\tanh(\frac{\theta L_{frp}}{L_{eff}})$ $\theta=\sqrt{\frac{\tau_{\max}}{s_u\sqrt{f_c'}}}$	---
Zhou et al. (2010)	Infinite joint	$\tau_{\text{int},s}=\frac{E_{frp}t_{frp}}{1+\rho}\cdot\frac{\alpha}{\beta^2}\cdot(1-e^{-\frac{s}{\alpha}})$	$\tau_{\max}=\frac{(Et)_{frp}}{4(1+\rho)}\cdot\frac{\alpha}{\beta^2}$	---	$\frac{\alpha}{\beta}\cdot E_{frp}A_{frp}$	$2\beta\cdot(\frac{1+\delta}{1-\delta})$
	Finite joint	$\tau_{\text{int},x}=\frac{E_{frp}t_{frp}}{1+\rho}\cdot\frac{\alpha}{\beta^2}\cdot\frac{x+\beta}{L_{frp}}\cdot\frac{e^{-\frac{x-x_0}{\beta}}}{(\frac{x}{L_{frp}}+e^{-\frac{x-x_0}{\beta}})^2}$	$\tau_{\max}=\frac{(Et)_{frp}}{4(1+\rho)}\cdot\frac{\alpha}{\beta^2}\cdot(1+\frac{\beta}{x})$	---	$F=\frac{E_{frp}A_{frp}}{1+\rho}\cdot\frac{\alpha}{\beta}\cdot\frac{1}{1+e^{-\frac{L_{frp}-x_0}{\beta}}}$	---
Woo and Lee (2010)	$\tau_{\text{int},x}=\frac{\beta}{\alpha}\cdot\frac{\tau_{\max}}{s_0}\cdot s_x$ $\tau_{\text{int},x}=\frac{1}{1-\alpha}\cdot\frac{\tau_{\max}}{s_0}\cdot[(1-\beta)s_x+(s_x-\alpha)s_0]$	$\tau_{\text{int},x}=\tau_{\max}\cdot e^{-\frac{\tau_{\max}}{K}(s_x-s_0)}$	---	---	---	---

Model	Shear Stress Profile		τ_{max}	s_0	F or F_{max}	L_{eff}
	Ascending Branch	Descending Branch				
Liu and Wu (2012)	5-24 (Zhou et al. 2010) $s_x = \alpha \cdot \ln\left(\frac{A^2-1}{2AB-2}\right)$		---	---	$F = E_{frp} A_{frp} \cdot \frac{\alpha}{\beta} \cdot \sqrt{(1-e^{-\frac{S_l}{\alpha}})^2 - (1-e^{-\frac{S_f}{\alpha}})^2}$	244 mm

Table 2-2. Existing fracture-based models for adhesively bonded joints.

Model	Shear Stress Profile		τ_{max} and s_0	G_f	F_{max}	L_{eff}
	Ascending Branch	Descending Branch				
Täljsten (1996)	$\frac{P_{\max}}{\tau_{\text{int},x} W_{frp}(L_{frp}-a)} = \frac{\sqrt{2}}{\omega_1}\tanh(\frac{\omega_1}{\sqrt{2}})$	---	---	---	$W_{frp}\sqrt{\frac{2E_{frp}t_{frp}G_F}{1+\alpha}}$	---
Neubauer and Rostasy (1997)	---		---	$0.204f_{ct}^{'}$	$0.64k_p W_{frp}\sqrt{E_{frp}t_{frp}f_{ct}^{'}}$ $0.64k_p W_{frp}\sqrt{(Et)_{frp}f_{ct}^{'}}\frac{L_{frp}}{L_{eff}}(2-\frac{L_{frp}}{L_{eff}})$	$\sqrt{\frac{E_{frp}t_{frp}}{2f_{ct}^{'}}}$
Brosens and Van Gemert (1998)	---		$\tau_{\max} = 1.8f_{ct}^{'}$ $s_0 = 2.5\tau_{\max}\left[\frac{t_{adh}}{E_{adh}}+\frac{50}{E_c}\right]$	$\frac{\tau_{\max}s_0}{2}$ $\frac{\tau_{\max}s_u}{2}$	$W_{frp}\sqrt{2E_{frp}t_{frp}G_F}$	$\frac{2P_{\max}}{W_{frp}\tau_{\max}}$
De Lorenzis et al. (2001)	---	---	---	---	---	$\frac{\sqrt{2E_{frp}t_{frp}G_F}}{\tau_{\max}}$ $\tau_{\max} = 0.0184(Et)_{frp}^{0.5}$
Yuan et al. (2001) Bi-linear Model	$\tau_{\text{int},s} = \frac{\tau_{\max}}{s_0}\cdot s_x$ $\tau_{\text{int},x} = \tau_{\max}\cdot\frac{\cosh(\lambda_1 x)}{\sinh(\lambda_1(L_{frp}-a))}$	$\tau_{\text{int},s} = \frac{\tau_{\max}}{s_u-s_0}\cdot(s_u-s_x)$ $\tau_{\text{int},x} = \tau_{\max}\cdot\left[\frac{\lambda_2}{\lambda_1}\tanh(\lambda_1(L_{frp}-a))\sin(\lambda_2(x-L_{frp}+a))-\cos(\lambda_2(x-L_{frp}+a))\right]$			$\frac{\tau_{\max}W_{frp}}{\lambda}$	$a+\frac{1}{2\lambda_1}\cdot\ln\frac{\lambda_1+\lambda_2\tan(\lambda_2 a)}{\lambda_1-\lambda_2\tan(\lambda_2 a)}$
Chen and Teng (2001)	---	---	---	---	$0.427\beta_p\beta_L W_{frp}L_{eff}f_c^{'0.5}$	$\sqrt{\frac{E_{frp}t_{frp}}{f_c^{'0.5}}}$

Model	Shear Stress Profile		τ_{max} and s_0	G_f	F or F_{max}	L_{eff}
	Ascending Branch	Descending Branch				
Dai et al. (2005) and Ueda and Dai (2005)	$\varepsilon_s = A \cdot (1 - e^{-Bs_x})$ $\tau_{\text{int},s} = A^2 B E_{frp} t_{frp} e^{-Bs_x} \cdot (1 - e^{-Bs_x})$		$\tau_{\max} = \frac{1}{2} B G_F$ $s_0 = \frac{0.693}{B}$	$G_F = \frac{1}{2} A^2 E_{frp} t_{frp}$ $G_F = 0.446 \frac{f_c^{0.236} (Et)_{frp}^{0.023}}{(\frac{G_{adh}}{t_{adh}})^{0.352}}$	$F_{\max} = (W_{frp} + 7.4) \cdot (2 E_{frp} t_{frp} G_F)^{0.5}$	$\frac{(2 E_{frp} t_{frp})^{0.5}}{B G_F^{0.5}} \cdot \ln(\frac{1+\alpha}{1-\alpha})$
Lu et al. (2005a)	$\tau_{\text{int},x} = \tau_{\max} \cdot \frac{s_x}{s_0}$	$\tau_{\text{int},x} = \tau_{\max} \cdot \frac{s_u - s_x}{s_u - s_0}$	$\tau_{\max} = 1.5 \beta_W f_{ct}^{'}$ $s_0 = 0.0195 \beta_W f_{ct}^{'}$ $s_u = \frac{2 G_F}{\tau_{\max}}$	$0.308 \beta_W^2 \sqrt{f_{ct}^{'}}$	---	---
Ferracuti et al. (2007)	---	---	---	$\pi \left[\frac{1}{n-1}\right]^{(\frac{n-2}{n})} \cdot \frac{1}{\sin(2\pi/n)}$	---	---
Liu and Wu (2012)	---	---	---	$0.5 E_{frp} t_{frp} (\frac{\alpha}{\beta})^2$	---	---

2.6.4. Finite Element Simulation of FRP/concrete Joints

Several studies have been reported in the literature using different techniques to model the interface behaviour in adhesively bonded joints; (Arduini et al. 1997; Barnes and Mays 2001; Chen et al. 2011; Chen et al. 2007; Coronado and Lopez 2006; Crocombe et al. 2006; Kim and Harries 2011; Lu et al. 2005b; O'Mahoney et al. 2013; Wong and Vecchio 2003; Xu and Wei 2013). Harries and Kim (2012) incorporated the bond-slip property of the fatigue-induced crack within the interface of CFRP-steel beams into a FE model using nonlinear interface elements. Chen et al. (2011) used the smeared-crack approach to simulate concrete cracking with application of the crack band model. They also implemented interfacial elements in the FE analysis to consider the interface between concrete and both internal steel and external FRP.

Using the cohesive elements with the traction-separation constitutive law as the interface, Chen et al. (2007) studied the bond behaviour between two adjacent cracks in which the joint is pulled at both ends. They investigated the effects of different parameters on the interface behaviour such as, FRP bonded length, load ratio and damage factor. Coronado and Lopez (2006) performed a sensitivity analysis of the material constitutive behaviour and modelling considerations on the reinforced concrete (RC) beams strengthened with FRP laminates. By evaluating the results of the numerical analysis, they found that the fracture energy of the concrete-epoxy interface has a great influence on the prediction of the plate-debonding failure.

Lu et al. (2005b) implemented the behaviour of the cracked- and uncracked-concrete into a FE model using elastic-plastic and the smeared crack approaches. A crack band with very fine meshes is considered close to the interface. Based on the crack pattern and the interfacial shear stresses of the FE model, they concluded that debonding starts with shallow inclined cracks within the interface. These shallow cracks (called meso-cantilever columns) may grow with the increase in the applied load which finally lead to the failure of the bond.

Abdel Baky et al. (2012) proposed a nonlinear bond-slip model for FRP/concrete interfaces which considers the variation of the local bond strength along the bonded length (Figure 2-33). FEM result was used to develop the model based on micro plane theory for concrete. The slip in Abdel Baky et al. (2012) model is expressed in terms of the slips in the FRP laminate, adhesive and concrete substrate. Accordingly, the relation between the shear stress of the interface and the aforementioned slips is derived;

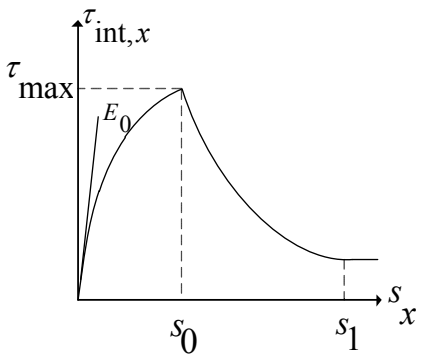

Figure 2-33. Bond-slip model proposed by Abdel Baky et al. (2012)

$$\tau_{\text{int},s} = E_0 + \left[\frac{\tau_{\max} - E_0 s_0}{s_0^3}\right] \cdot s_x^3 \qquad \text{for } s_x \le s_0 \qquad \text{2-40}$$

$$\tau_{\text{int},s} = \tau_{\max} \cdot e^{-\alpha_1 \cdot (\frac{s_x}{s_0} - 1)} \qquad \text{for } s_0 \le s_x \le s_u \qquad \text{2-41}$$

$$\tau_{\text{int},s} = 0.1\tau_{\max} \qquad \text{for } s_x > s_u \qquad \text{2-42}$$

where

$$\frac{1}{E_0} = \frac{t_{lam}}{G_{lam}} + \frac{t_{adh}}{G_{adh}} + \frac{h_{eff}}{G_c} \qquad \text{2-43}$$

$$\frac{1}{\beta} = 1 - \frac{\tau_{\max}}{E_0 s_0} \qquad \text{2-44}$$

$$s_0 = \tau_{\max} \cdot \left[0.35\frac{t_{lam}}{G_{lam}} + 8.5\frac{t_{adh}}{G_{adh}} + 3\frac{h_{eff}}{G_c}\right] \qquad \text{and} \qquad s_u = 4s_0 \qquad \text{2-45}$$

$$\tau_{\max} = \frac{2f_c'}{-\alpha + \sqrt{\alpha^2 + 4}} \qquad \text{2-46}$$

$$\alpha_1 = -\frac{0.9\tau_{\max} s_0}{G_f^p} \quad 2\text{-}47$$

$$G_f^p = \tau_{\max}^2 \cdot \left[\frac{150}{G_c} - 0.405\left(\frac{t_{lam}}{G_{lam}} + \frac{t_{adh}}{4.25G_{adh}}\right)\right] \quad 2\text{-}48$$

Similar to Dai et al. (2005) model, the bond-slip relationship proposed by Abdel Baky et al. (2012) takes into account the properties of different parts of the interface. However, this model is developed based on the finite element results and validated against other models mainly Dai et al. (2005) and Lu et al. (2005a). In addition, the accuracy of the model is compared with the FE results for the joints processed with pultruded laminates and the bond-slip relationship is not validated for the joints manufactured with other types of techniques such as wet lay-up or VARI.

2.7. Summary

Reviewing the literature indicate that the application of wet lay-up or pultrusion technique has been widely used for bonding the FRP materials on the substrate. However, the need for higher quality of the bond necessitates the application of the new manufacturing methods such as vacuum assisted resin infusion, and prepreg processing techniques. Although these techniques have been utilised for production of the aerial or marine elements, their application in structural strengthening has been rarely investigated. Therefore, the bond characteristics between the concrete and the FRPs manufactured by wet lay-up, pultrusion, VARI and HVBO are compared in this research.

Regardless of the manufacturing method, the failure in externally bonded joints is a critical issue in elements of the structures. Failure in the externally bonded joints may occur in different ways, including substrate failure, FRP delamination and failure in bond between FRP and substrate. The most common failure mode in the EB elements is FRP debonding which can cause devastating damages to the whole structure. In terms of the cause of the failure, debonding is considered as plate end debonding, concrete cover separation, critical diagonal crack debonding, or intermediate crack debonding.

In flexural members strengthened with FRP materials, failure is governed by the intermediate crack debonding. Therefore several types of bond tests have been proposed to

investigate the debonding mechanism; single lap shear, double lap shear, and beam tests are some test set-ups which currently are used. Using these testing methods, different parameters have been addressed to investigate their influence on the interfacial behaviour of the joints. The main factors, which are reported in literature, are concrete strength, concrete composition, FRP bonded length, FRP bonded width, FRP stiffness, and adhesive properties.

Despite the large number of studies, still there is a lack of experimental data to gain a comprehensive understanding about the effects of the important factors on the interface behaviour. Therefore, in Chapter 4 the effects of these parameters are considered on the behaviour of the externally bonded joints. The parameters which are considered in this research are concrete surface tensile strength (f'_{cst}), initial unbonded length (IUL), FRP bonded length (L_{frp}), FRP-to-concrete width ratio (w_r), bondline thickness (t_{bl}), surface treatment methods and FRP processing techniques. A modified single lap shear test set-up is implemented to monitor the fracture mechanism of the interface. This set-up monitors the global slip of the FRP relative to the substrate and minimizes errors in order to provide more reliable results.

Several methods have been employed to predict the bond behaviour which are classified into empirical-based models, elasticity theory-based models, fracture mechanics-based models and/or finite element analysis. Empirical-based models are mainly based on the regression of the experimental results. These models provide equations for determination of the load carrying capacity, the effective bond length and also the bond-slip distributions. In the models which are developed by the elasticity theory, the basic governing equations are employed and solved for the specific boundary conditions. Due to the fact that the interface failure of the FRP-bonded joints is accompanied by the fracture of the concrete substrate, fracture mechanics theory can be applied to investigate the bond behaviour.

Although empirical-based models are straightforward and can be developed based on simple methods, the proposed models may lead to largely scattered results. In most cases, models which developed based on the fracture mechanics theory consist of sophisticate parameters which sometimes required to be determined through iterations. In addition, proposed models are mainly developed for the joints with a specific manufacturing technique. According to these facts, a new analytical approach is presented in Chapter 5 which introduces two simplified analytical methods to define the bond-slip law of FRP-concrete interfaces. The advantage of this procedure is that the proposed models are developed only based on the boundary conditions and therefore can be applied to any type of adhesively bonded joints. Subsequently, the bond characteristics obtained from the proposed models are

validated by the experimental results of the modified single lap shear tests which are presented in Chapter 4. In addition, a new relationship is proposed for determination of the fracture energy corresponding to antisymmetric in-plane shear mode.

CHAPTER 3

EXPERIMENTAL PROGRAM

3.1. Introduction

This chapter outlines the experiments which are carried out to investigate the interfacial behaviour between concrete substrate and the FRP composites. Firstly, the methods which are used to perform different experiments are discussed. These experiments consist of concrete compressive strength test, FRP tensile test, pull-off test and modified single lap shear tests.

As it is discussed, the scattered results of the bond-slip relationship reported in literatures may contribute to the test instrumentation and experimental set-ups. A modified single lap shear test set-up is proposed in this section to overcome the problems with the variation of the results in single lap shear tests.

Two processing techniques are mainly reported in the literature for the repair of concrete structures via bond of fibre reinforced polymer (FRP) onto the substrate. These methods are known as pultrusion and wet lay-up systems. However, the test data regarding the interfacial behaviour between concrete and the FRP processed by other manufacturing methods such as heated vacuum bag only and also vacuum assisted resin infusion is very limited. Therefore in the second part of the chapter, the implementation of the several FRP processing techniques such as pultrusion, wet lay-up, heated vacuum bag only (HVBO) and vacuum assisted resin infusion (VARI) is mentioned. This implementation is performed by a standard method for equalisation of the manufacturing techniques. Finally in section 3.4, the properties of the materials used in this research are reported.

3.2. Outline of the Experiments

This section presents a brief description about different experiments which are carried out in this research. All of experiments, except modified single lap shear tests, are performed based on the standards recommended by the American Society for Testing and Materials (ASTM).

Table 3-1. Mix design for concrete prisms.

Ingredients		Kg/m^3	10 Specimens 0.094×(Kg/m^3)
Cement		410	38.54
River Sand		735	69.09
Coarse Aggregate	10 mm Crushed Aggregate	355	33.37
	14 mm Crushed Aggregate	705	66.27
Water		205	19.27

3.2.1. Concrete Casting

Blocks are made from normal concrete with the maximum crushed aggregate size of 14 mm. Details of the mix design is presented in Table 3-1. The maximum aggregate size is defined based on the recommendation proposed by Mazzotti et al. (2008).


(a)


(b)


(c)


(d)

Figure 3-1. Casting of the concrete samples, (a) mixing, (b) placing the concrete inside the wooden moulds, (c) curing under plastic sheets, and (d) curing of the concrete cylinders.

Concrete blocks were cast into wooden moulds with dimensions of 150×150×300 mm (height×width×length). After concrete casting, prisms were cured for 28 days under plastic sheets to avoid cracking on the concrete surface. Figure 3-1 illustrates different stages of the concrete casting and curing process. During concrete pouring, the workability of the concrete was measured by the slump test. For each batch of concrete, nine standard concrete cylinders with dimensions of 100×200 mm (diameter×height) were made in order to determine the compressive strength of the concrete. The properties of the concrete represented in 3.4.1.

3.2.2. Concrete Compression Test

The mean (f'_{cm}) and characteristic (f'_c) compressive strength of the concrete is determined on day twenty eight and day of the modified single lap shear (MSLS) test based on ASTM C39/C39M-09a (2009). The uniaxial compression test was carried out by a universal testing machine (Figure 3-2a) on three standard cylindrical concrete specimens with dimension of 100×200mm. In order to get reliable results, the top and bottom surfaces of the cylinders were cut by a concrete cutting machine prior to the test.

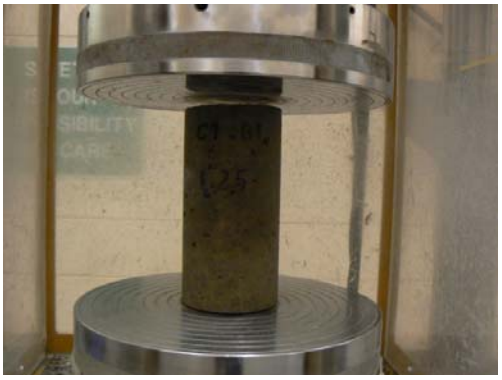
(a)

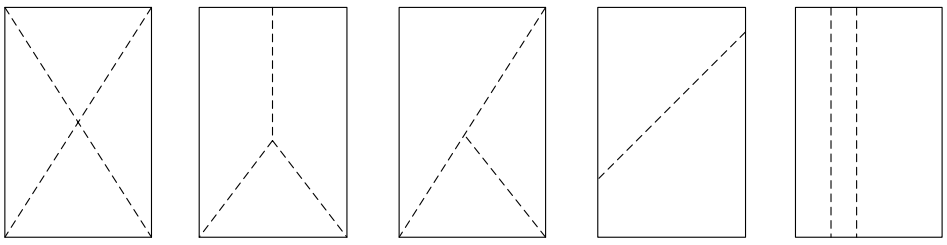

(b)

Figure 3-2. Compressive test on the concrete samples, (a) MTS machine, (b) failure patterns.

Based on ASTM C39/C39M-09a (2009), the load needs to be maintained between the range of 0.25 ±0.05 MPa/s (12-18 MPa/min). In this research, loading rate adopted was as 0.3

MPa/sec. After the test, the compressive strength of concrete is taken as the average maximum applied load divided by the average cross-sectional area and expressed to the nearest 0.1 MPa. Finally, the failure pattern of the cylinders (Figure 3-2b) is recorded.

3.2.3. FRP Tensile Test

The tensile strength and the elastic modulus of the CFRP in the fibre direction are determined based on ASTM D3039/D3039M (2008). According to this standard, at least five samples are to be tested. To make the samples, resin is applied to a release film with dimensions of 600×600×0.076 mm and then the first ply of the dry fibre with a minimum dimension of 300×300 mm is placed on the adhesive. When all of the plies are applied, a release film is placed over the materials for protection. Special care should be paid to remove air bubbles from the material which can be done using a flat edge of a hand tool or a grooved roller. To achieve samples with a flat surface, a rigid and flat plate is placed on the top surface of the release film while the resin is curing. Figure 3-3 shows a schematic view of the coupon samples.

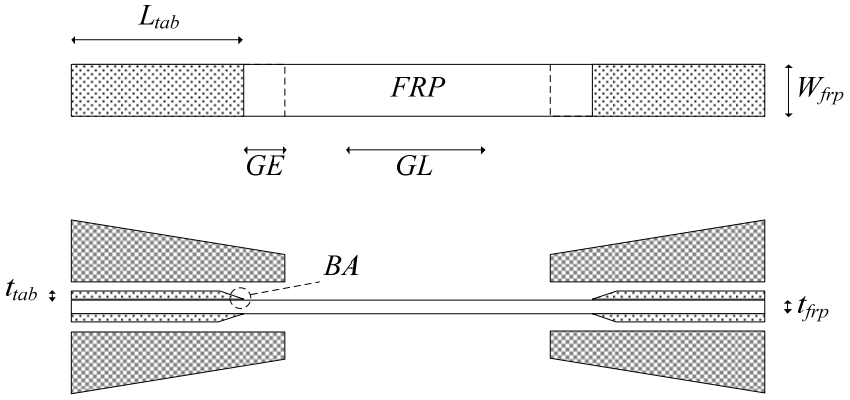

Figure 3-3. Schematic view of the FRP coupon samples.

The thickness and the width of the samples is measured by a micrometre with a flat anvil interface. Cross-sectional area of the samples is measured at three places in the gage section to obtain an average. For testing unidirectional materials, it is highly recommended to use tabs.

Coupon samples were made for different processing techniques considering the curing times recommended by the manufacturers. Then, the FRP sheets/laminates were cut into the desired dimensions with a diamond blade saw machine (Figure 3-4a). The configuration of

the coupon samples based on ASTM D3039/D3039M (2008), EN ISO 527-5 (2009) and also the samples were tested in this research is reported in Table 3-2.

(a)

(b)

Figure 3-4. (a) Cutting the sheets/plates to desired dimensions, (b) performing tensile test.

Table 3-2. Details of the coupon samples in standards and the values adopted in this research.

	ASTM D3039/D3039M (2008)	EN ISO 527-5 (2009)	Current Study
L_{frp}	250	250	250
W_{frp}	15 (±1%)	15 (±0.5)	15
t_{frp}	1.0 (±4%)	1.0 (±0.2)	varied
L_{tab}	56	> 50	50
t_{tab}	1.5 (±1%)	0.5-2	0.5-2
GE(Grip Extension)	10-15	≥ 7	10-15
GL (Gauge Length)	10-50	50 (±1)	10-50
BA (Bevel Angle)	7-10	90	7-10

In order to achieve proper failure mode, aluminium tabs were applied to both ends of the samples. After preparation of the specimens, they were tested with a MTS machine with loading rate of 2 mm/min. An extensometer was employed to measure the strain value of the FRP on gauge length. Therefore, the stress verses strain curves plotted and the tensile strength and modulus of elasticity of the FRPs can be calculated. Results of the tensile tests on the FRP sheets/laminates are reported in section 3.4.2.

3.2.4. Direct Tension (Pull-off) Test

After single lap shear tests, the surface tensile strength of each concrete prism was measured using the test set-up shown in Figure 3-5. The pull off tests were performed based on ASTM C1583-04 (2009). For each sample, three cores with 50 mm in diameter were drilled on the surface of the concrete (Figure 3-5a) and a steel disk was attached to the concrete surface using a high strength epoxy. Then, the disks were pulled off by a Shimadzu Universal Testing Machine (Figure 3-5b) with loading rate of 40 kPa/sec. During the test, the maximum stress was recorded. The correlation between the concrete surface tensile strength and results of the modified single lap shear tests is presented in the next chapter.

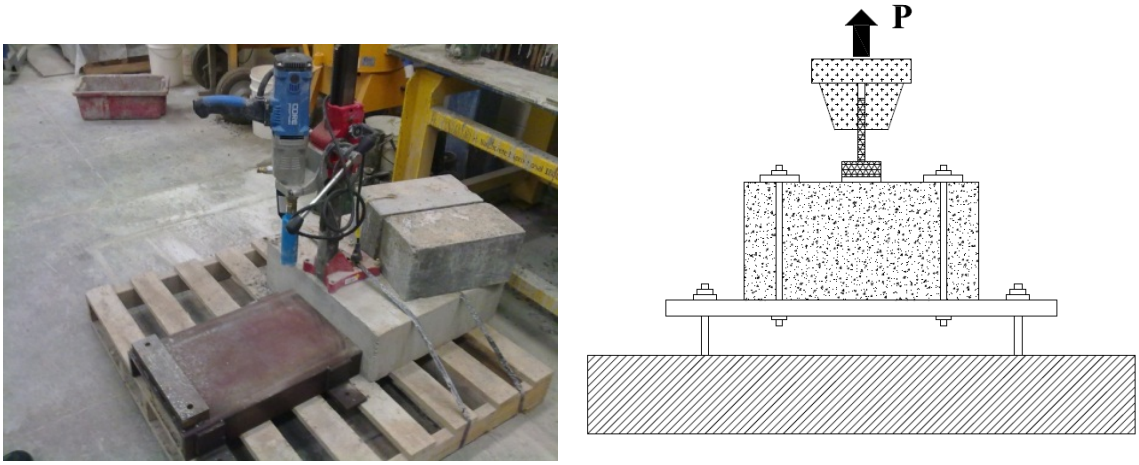

(a) (b)

Figure 3-5. Direct tension test (a) core drilling machine, (b) test set-up

3.2.5. Modified Single Lap Shear Test

As crack gradually opens, debonding is accompanied by slip between substrate and the FRP. This interfacial behaviour can be addressed by the bond-slip characteristics (shear stress-slip curves). Different test set-ups have been implemented to study the interfacial characteristics of adhesively bonded joints such as; single lap shear test, double lap shear test, and beam test (refer to chapter 2).

Among the proposed test set-ups, single lap shear (SLS) test set-up has been successfully adopted by researchers to determine the bond strength. However, the bond-slip responses vary from one experiment to the other (Liu and Wu 2012; Zhou et al. 2010). Therefore, still

no comprehensive formula has been proposed to precisely predict the bond behaviour between FRP and concrete.

The possible reason for these scattered results may attribute to the test set-up. It has been proven that in the lap shear test, the interface is not only under the direct shear. Normal stresses, which are induced by unexpected out of plane movements, play an important role on the local bond strength (Abdel Baky et al. 2012; Dai et al. 2006; Lu et al. 2005b). Therefore, in this research, a modified single lap shear (MSLS) test set-up is employed to monitor the bond which provides more precise results in terms of the interfacial responses and subsequently accurate bond-slip relationships. Using the MSLS test set-ups, the FRP global slip is measured directly relative to the concrete substrate. Therefore, this type of set-up can minimize the effects of out of plane movements (concentrated normal stresses) in lap shear tests.

Test Set-up

According to the fracture mechanism of the FRP-concrete interface, the slip value is quite small and any error in the test set-up can lead to scattered results. One of the main outcomes of single lap shear tests is load verses global slip curves at the loaded end of the FRP. The slip is the relative displacement between the FRP and the concrete substrate which is measured by placing two LVDTs, one at the loaded end and the other at the back of the concrete block (Figure 3-6). Each LVDT is placed on the baseplate and the displacements are captured relative to the baseplate. The global slip is calculated based on the following relationship;

$$S = \delta_1 - \delta_2 \qquad 3\text{-}1$$

where, S is slip at the loaded end and $\delta 1$ and $\delta 2$ are the displacement of the loaded end and the back of the concrete block, respectively.

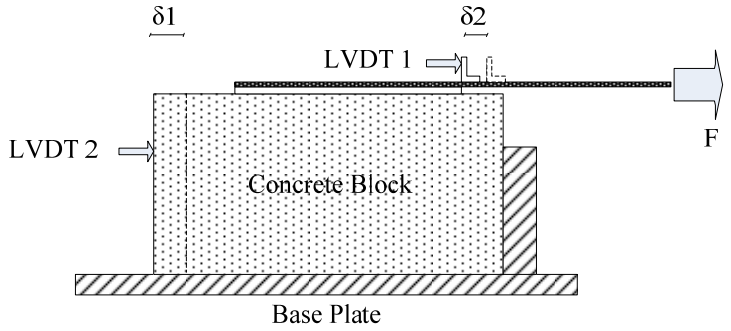

Figure 3-6. Slip between FRP and concrete in the single lap shear test set-ups.

Based on the experimental results, the baseplate experiences small amount of movements during the application of the load to the specimens. Although movements are small but compare to the slip amount at the loaded end (mostly less than 1 mm), they are still significant. In addition, concrete blocks are not perfectly rectangular and may not be tightly held in the frame. Therefore, any out of plane movement of the concrete block can originate errors in the reading of LVDTs.

To avoid these errors, a modified single lap shear test set-up is developed for this research. In the modified test set-up, slip between concrete and the FRP is measured by a LVDT inserted into a frame which mounted on the sides of concrete block. The main advantage of this set-up is that when the concrete block experiences out of plane movements, both concrete and LVDT have the same movements. In addition, the second LVDT is omitted from the calculation of the slips. Therefore, the slip can be monitored directly at the loaded end using just one LVDT with higher precision.

Figure 3-7 represents a schematic view and a picture of the LVDT holder frame set-up employed in the MSLS tests. The base plate is welded to the bottom I girders to minimize the movement of the test rig. However, the LVDT at the back of the concrete was still utilized to monitor the movements of the concrete block. Readings of LVDT at the back of concrete shows that the block displacement is negligible.

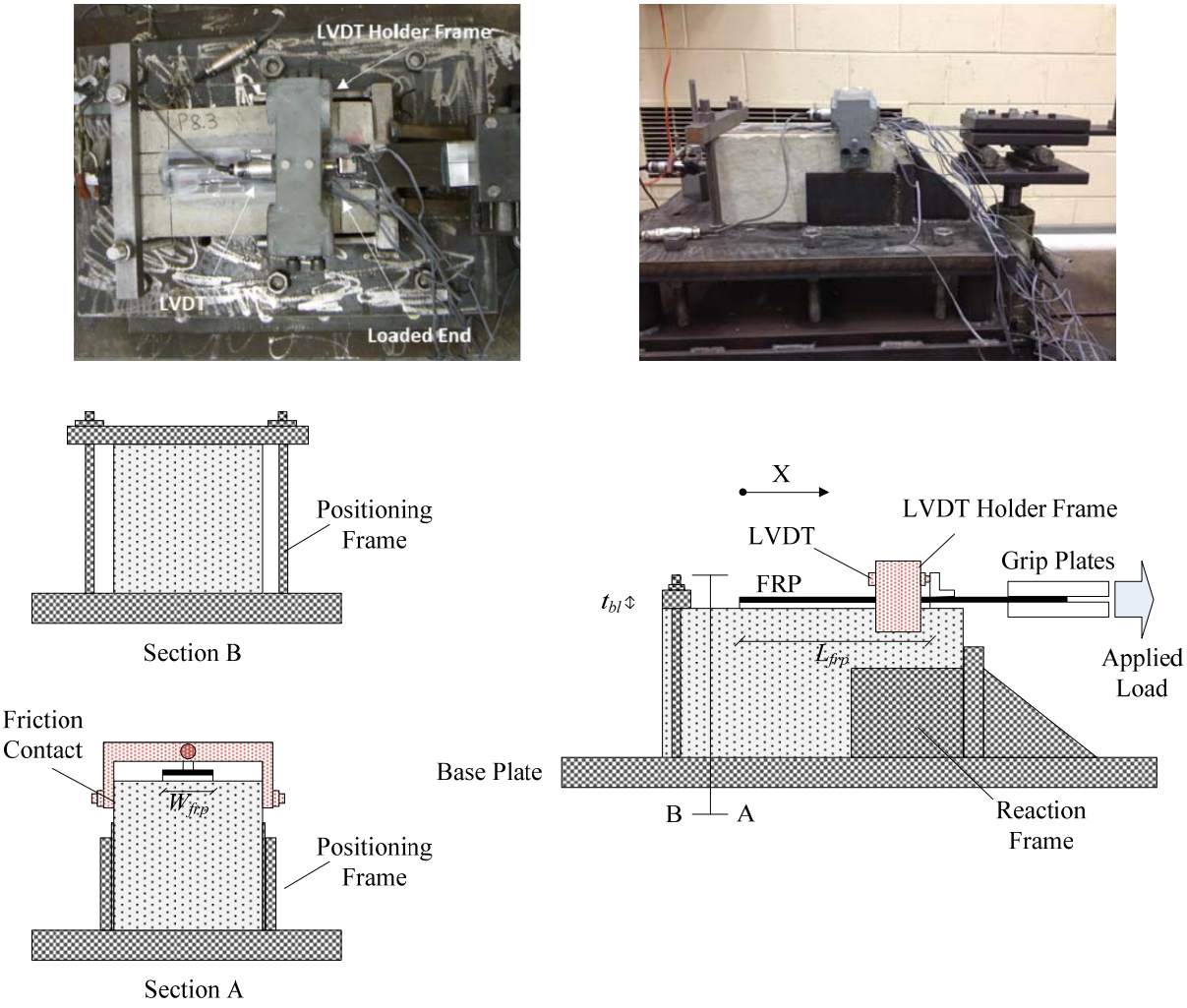

Figure 3-7. Schematic view and pictures of LVDT holder frame.

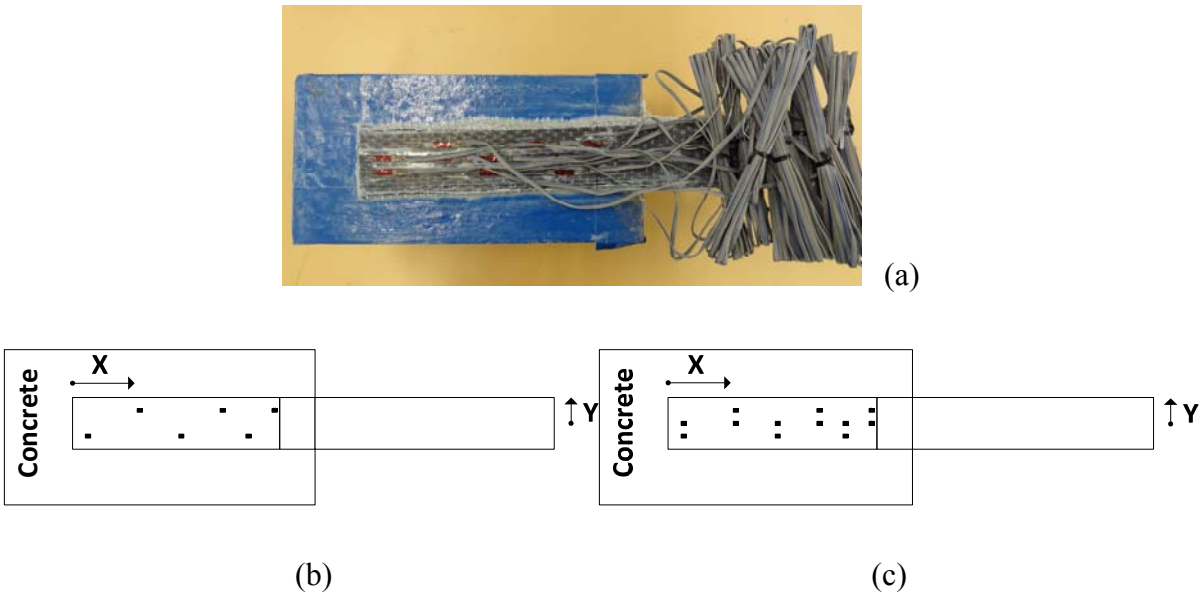

Figure 3-8. Application of the strain gauges on the FRP composites.

Instrumentation

To investigate the interfacial stresses, 10 mm-length strain gauges were attached on the surface of the FRP sheets/plates for the majority of specimens. The gauge factor, gauge resistance and temperature compensation for strain gauges were 2.09±1 %, 119.5±0.5 Ω and $11x10^{6}$/°C, respectively. Figure 3-8 shows the configuration of the strain gauges installed on the FRP sheets.

In majority of the samples, the strain gauges were aligned along the line passing through the top and bottom quarter of the bonded width (Figure 3-8b). However, for further investigation, in samples SF-B-5.3, SF-B-7.3, SF-B-8.3 and W3.3, strain gauges were also attached along the centre line of the bonded width (Figure 3-8c). Strain gauges were installed at shorter distances at the loaded end while the distance was increased toward the free end of the FRP. The first strain gauge was placed at the loaded end and the others were attached at the positions which are reported in Table 3-3. During the test, data from the actuator, LVDTs, and strain gauges were collected by a data logger which was specifically prepared for this research.

Table 3-3. Position of the strain gauges along the bonded length.

	Distance of the strain gauges from the free end (mm)						
Bonded Length (mm)	SG-1	SG-2	SG-3	SG-4	SG-5	SG-6	SG-7
150	145	120	95	55	15		
200	195	170	145	105	65	15	
225	220	195	170	130	90	40	25

Monotonic Loading Regime

Since in most of the cases the maximum slip is less than 2 mm (Cao et al. 2007; Pan and Leung 2007; Yao et al. 2005), the displacement control with a small rate of 0.2 mm/min was chosen for the loading regime in MSLS tests. This increment in displacement allows the capture of data over a small period of time which improves the accuracy of the results. Load was applied to the specimens in two steps, initial loading until about 8 kN which followed by

unloading and then loading until failure. Load was applied with an actuator to the FRP through a grip which was specifically designed for the tests.

3.3. Strengthening Systems

As described in Chapter 2, wet lay-up and pultrusion are commonly used in structural strengthening industry for application of the FRP on the substrate whilst VARI and HVBO attracted less attention. This is the case although these techniques (VARI and HVBO) have been applied in construction of the aerial and marine elements. Therefore in this research, wet lay-up, pultrusion, vacuum assisted resin infusion (VARI) and heated vacuum bag only (HVBO) are considered for manufacturing of the FRP sheets/laminates. VARI and HVBO are chosen based on simplicity in moulding and cost effectiveness. These advantages enable HVBO and VARI to be employed as an alternative for the strengthening of the structures.

Table 3-4. Experimental phases and sub series based on different processing techniques.

	Series	Processing Technique
Phase 1	1	Pultruded-A
	2	
	3	
	4	Pultruded-B
	5	
	6	
Phase 2	1	Wet Lay-up
	2	
Phase 3	Preliminary	HVBO
	1	
Phase 4	1	VARI-B
	2	

Considering four different FRP manufacturing methods, the total experimental program was divided into four phases and each phase consisted of several series (Table 3-4). The interfacial response of the adhesively bonded joints processed with pultrusion technique is studied in the first phase of the experiments. During this phase, the effects of the surface treatment, initial unbonded length, FRP bonded length, FRP bonded width and bondline

thickness on the bond behaviour are examined. *Phase 2* investigates the bond performance in the joints manufactured by the wet lay-up technique considering the surface treatment and bondline thickness. Heated vacuum bag only technique is studied in *Phase 3*. Finally, the effect of the vacuum assisted resin infusion on the bond behaviour between concrete substrate and the FRP is analysed in *Phase 4*. During *Phase 3* and *4*, the effect of the surface preparation and also bondline thickness is investigated through several series of the tests.

The effects of several variables on the interface behaviour have been studied in the experimental program. These variables are; type of the surface treatment, concrete surface tensile strength (f'_{cst}), initial unbonded length (IUL), FRP width (W_{frp}), FRP bonded length (L_{frp}), bondline thickness (t_{bl}) and different FRP processing techniques. It should be mentioned that for each combination of test variables, three repeated specimens are cast in order to achieve reliable results.

Based on the procedures mentioned in Chapter 2, the manufacturing method for the samples in all phases of the tests consists of four similar stages; surface preparation on the concrete blocks, cutting FRP into desirable shapes, cleaning of the adherends from dust and debris, applying adhesive and attaching FRP sheets/laminates on the concrete surface. Details of the samples used in different phases of the experiments are shown in Figure 3-9.

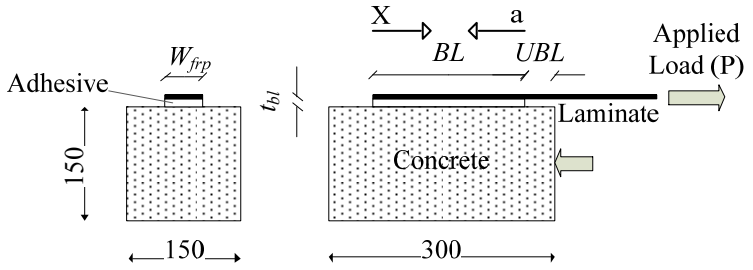

Figure 3-9. Details of the specimens in MSLS tests (dimensions in mm).

Through this research, the concept of bondline is adopted as the overall thickness of the fibres (carbon and glass) and the adhesive (Figure 3-10):

$$t_{bl} = t_{cfib} + t_{gfib} + t_{adh} \qquad 3\text{-}2$$

where t_{cfib}, t_{gfib}, and t_{adh} are carbon fibre, glass fibre and the adhesive thicknesses, respectively.

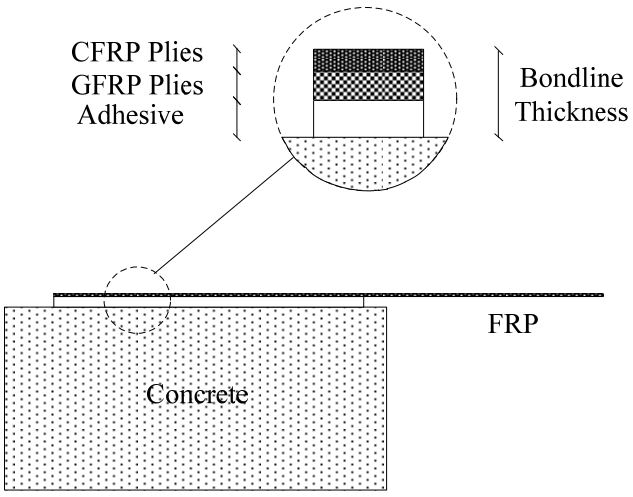

Figure 3-10. Concept of the bondline thickness.

The concrete surface preparation has been found to be an influencing factor on the bondline behaviour. In the series of the experiments various methods were used to address this effect on the interfacial behaviour of the FRP-to-concrete bonded joints processed with different manufacturing techniques. However in all of the samples, the top surface of the concrete blocks was treated prior to FRP attachment in order to remove the mortar beneath the FRP plate until the aggregates exposure.

Table 3-5. Surface treatments adopted in the current research.

Surface Treatment ID	Surface Treatment Method	Specifications
N-SP	No surface prep.	---
SP-1	Diamond grinding wheel plus few rounds of the abrasive belt sanding	Coarse paper No. P36-X
SP-2	Abrasive belt sanding	Coarse paper No. P36-X or P40-X
SP-3	Water blasting	Low pressure- 2000psi
SP-4	Sand blasting	Low aggregate exposure
SP-5	Sand blasting	Medium aggregate exposure
SP-6	Sand blasting	High aggregate exposure

Table 3-5 identifies the surface preparation used through this research. For SP-1, surface preparation carried out majority with diamond grinding cup wheel plus few round of abrasive belt number P36-X. On the contrary, in SP-2 the majority of the preparation was made with

abrasive belt number P36-X. Low pressure (2000psi) water jet blasting was applied in SP-3 while sand blasting method was used for SP-4, SP-5 and SP-6. In SP-6, the surface treatment was carried out in a way to expose the highest amount of the aggregates on the concrete surface. The difference between SP-4 and SP-6 methods is shown in Figure 3-11.

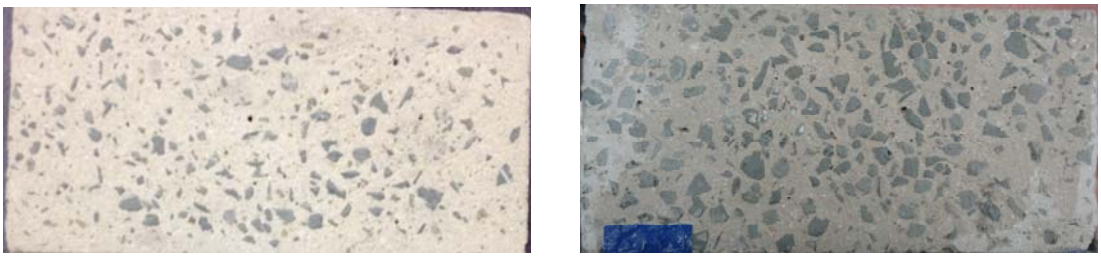

(a) (b)

Figure 3-11. (a) Low aggregate exposure and (b) high aggregate exposure in surface preparation.

3.3.1. Equalisation of the Processing Techniques

One major aspect of the current research is to compare the interfacial behaviour between concrete and the FRP plates fabricated with different manufacturing techniques such as, pultrusion, wet lay-up, HVBO and VARI. However, the fabrication method in these processing techniques is quite different and therefore the final product has various properties. Based on this fact, the characteristics of these processing methods based on a specific criterion are scaled so that comparison can be made. In this research, this is done by equalisation of the processing techniques. According to this concept, the fibre areal weight (mass per area of plate), $(FAW)_{pl}$, is kept constant for all of the processing methods. Fibre areal weight can be calculated from Eq. 3-3;

$$(FAW)_{pl} = \upsilon_{fib} \times \rho_{fib} \times t_{pl} \qquad 3\text{-}3$$

where, υ_{fib}, ρ_{fib}, and t_{pl} are the fibre volume fraction, the density of the reinforcing fibre, and the measured thickness of the plate (or coupon specimen), respectively. Fibre volume fraction can be obtained from the ratio between the modulus of elasticity of the plate, E_{pl}, to the fibre, E_{fib};

$$\upsilon_{fib} = \frac{E_{pl}}{E_{fib}} \qquad 3\text{-}4$$

During the total experimental program, the fibre areal weight of all processing techniques is maintained the same as 1800 gr/m^2. Therefore, the number of plies per plate, n_{ply}, required in each processing technique is determined by

$$(FAW)_{pl} = (FAW)_{ply} \times n_{ply} \qquad 3\text{-}5$$

$(FAW)_{ply}$ is fibre areal weight (mass per area per ply). Finally, the thickness of each ply can be obtained as follows

$$(FAW)_{ply} = \rho_{ply} \times t_{ply} \qquad 3\text{-}6$$

where, t_{ply} and ρ_{ply} are thickness and density of each ply, respectively.

Considering the tensile test results on the FRP coupon samples provided in Appendix A, the required number of reinforcing plies, n_{ply}, in each CFRP plate manufactured by the VARI technique is calculated here. The values obtained from Eqs. 3-3 to 3-6 for other types of the processing techniques are also provided in Table 3-6.

Table 3-6. Equalisation of the processing techniques.

Processing Technique	ρ_{fib} (gr/m^3)×10^6	υ_{fib}	t_{pl} (m)×10^{-3}	t_{ply} (m)×10^{-3}	$(FAW)_{ply}$ (gr/m^2)	$(FAW)_{pl}$ (gr/m^2)	n_{ply}
Pultruded-A	1.80	0.69	1.43	0.33.	1776	593	3
Pultruded-B	1.73	0.72	1.45	0.13	1802	225	8
Wet Lay-up	1.80	0.26	2.03	0.13	1900	238	8
HVBO	1.80	0.64	1.32	0.21	1521	380	4
VARI-A	1.80	0.54	1.83	0.33	1779	593	3
VARI-B	1.80	0.54	1.83	0.33	1779	593	3

$$\rho_{fib} = 1.8 gr/cm^3$$

$$t_{pl} = 0.183 cm$$

$$\upsilon_{fib} = \frac{124691}{230000} = 0.54$$

$$(FAW)_{pl} = 0.54 \times 1.8 \times 0.183 = 0.1779 \, gr/cm^2 = 1779 \, gr/m^2$$

$$n_{ply} = 3$$

$$(FAW)_{ply} = \frac{1779}{3} = 593 \, gr/m^2$$

$$t_{ply} = \frac{593 \times 10^{-6}}{1.8 \times 10^{-3}} = 0.329 mm = 0.0329 cm$$

3.3.2. Pultruded

During the first phase of the experiment, the interfacial behaviour between the concrete and the pultruded FRP laminates is studied. Several parameters affect the bond behaviour, hence in *Phase 1* of the experimental program is divided into six distinguished series. The variables of the tests are; types of the surface treatment, initial unbonded length (IUL), FRP width (W_{frp}), FRP bonded length (L_{frp}) and the bondline thickness (t_{bl}). In the first series of tests, the FRP plates 25 mm in width were attached on three concrete blocks in order to evaluate the effect of changes in FRP to concrete width ratio and also surface preparation on the bond response. The effect of initial unbonded zone length is investigated in the second series of tests considering 0, 25 and 50 mm unbonded lengths for 9 samples. The effective bond length of the FRP system and its effects on the bond behaviour is examined through the third series by performing tests on 10 specimens.

Table 3-7. Detail of the specimens tested in *Phase 1*.

Series	Sample ID	Surface Prep. ID	Initial Unbonded Length, *IUL*, (mm)	FRP Width, W_{frp} (mm)	FRP Bonded Length, L_{frp} (mm)	Bondline Thickness, t_{bl} (mm)
I	TP1	N-SP	25	25	150	4.79
	TP2	N-SP	25	25	150	4.31
	TP3	N-SP	25	25	150	3.65
II	P1.1	SP-2	0	50	150	5.61
	P1.2	SP-2	0	50	150	5.97
	P1.3	SP-1	0	50	150	7.57
	P2.1	SP-2	25	50	150	5.87
	P2.2	SP-1	25	50	150	6.73
	P2.3	SP-2	25	50	150	7.31
	P3.1	SP-2	50	50	150	6.23
	P3.2	SP-2	50	50	150	6.63
	P3.3	SP-2	50	50	150	5.77
III	P4.1	SP-2	25	50	100	3.59
	P4.2	SP-2	25	50	100	4.16
	P4.3	SP-2	25	50	100	4.71
	P4.4	SP-1	25	50	100	4.41
	P5.1	SP-1	25	50	150	4.21
	P5.2	SP-2	25	50	150	4.51
	P5.3	SP-2	25	50	150	4.98
	P5.4	SP-1	25	50	150	4.14
	P6.1	SP-1	25	50	200	4.18
	P6.2	SP-2	25	50	200	4.36
	P6.3	SP-2	25	50	200	5.23
IV	P7.1	SP-2	40	50	200	3.45
	P7.2	SP-2	40	50	200	3.43
	P7.3	SP-2	40	50	200	3.64
	P8.1	SP-2	40	50	200	4.91
	P8.2	SP-2	40	50	200	4.46
	P8.3	SP-2	40	50	200	4.93
	P9.1	SP-2	40	50	200	8.04
	P9.2	SP-2	40	50	200	8.27
	P9.3	SP-2	40	50	200	8.09
V	P10.1	SP-2	40	25	200	4.47
	P10.2	SP-2	40	25	200	4.08
	P10.3	SP-2	40	25	200	4.43
	P11.1	SP-2	40	50	200	4.30
	P11.2	SP-2	40	50	200	4.55
	P11.3	SP-2	40	50	200	4.59
	P12.1	SP-2	40	80	200	4.64
	P12.2	SP-2	40	80	200	4.52
	P12.3	SP-2	40	80	200	4.20

VI	P13.1	SP-6	40	50	200	4.54
	P13.2	SP-6	40	50	200	4.38
	P13.3	SP-6	40	50	200	4.27

During *Series II* and *III*, two different surface preparation methods are applied on the surface of the concrete blocks. In addition, the effect of changes in bondline thickness and FRP-to-concrete width ratio ($w_r=W_{frp}/W_c$) are investigated in *Series IV* and *Series V*, respectively. The FRP width for samples P10.1-3, P11.1-3 and P12.1-3 was 25, 50 and 80 mm, respectively. Table 3-7 provides more information regarding the specimen details which are tested in *Phase 1* of the experiments.

3.3.3. Wet Lay-up (Hand Lay-up)

In *Phase 2* of the experiments, wet lay-up manufacturing method is applied. The main parameters studied during *Series I* and *II* of this phase are the surface preparation method and the bondline thickness (Table 3-8). To remove the top layer of the mortar, the concrete surface is treated prior to the FRP attachment by two different methods; SP-5 and SP-6. For more information about the surface preparation see section 3.3.

To assure the ultimate bond strength is achieved, FRP sheets are attached to the substrate 40 mm away from the concrete loaded face. For all of the samples, the FRP with 50 mm width is used. As it will be discussed in section 4.5, to ensure a complete propagation of intermediate crack along the bond length, FRP plates are located on the concrete samples with the bonded length (L_{frp}) of 200 mm.

Table 3-8. Detail of the specimens tested during *Phase 2*.

Series	Sample ID	Surface Prep. ID	Number of CFRP plies, n_{ply}	Bondline Thickness, t_{bl} (mm)
I	W1.1	SP-6	4	2.31
	W1.2	SP-6	4	3.19
	W1.3	SP-6	4	3.82
	W2.1	SP-6	8	5.59
	W2.2	SP-6	8	4.55
	W2.3	SP-6	8	4.45
II	W3.1	SP-5	8	3.63
	W3.2	SP-5	8	3.48
	W3.3	SP-5	8	3.34

After the surface preparation, the samples were cleaned by air pressure. The surface of the concrete blocks was marked to assure proper application of the FRP sheets. Meanwhile, the CFRP sheets were cut with a scissor into desirable sizes. Following the instructions of the manufacturer, a two-part epoxy was mixed by hand using a spatula and the first layer of the adhesive (gel coat) was applied on the concrete substrate. After the resin is draped with the fibres, rollers are used to impregnate the fibres and brush out the excessive resin and trapped air. The same process can be used for the alternate layers of the Fabrics. Figure 3-12 illustrates the procedure for fabrication of the wet lay-up samples.

3.3.4. Heated Vacuum Bag Only (HVBO)

Heated vacuum bag only (HVBO) method can be applied to bond pre-impregnated (pre-preg) laminates onto the surface of substrates (e.g. concrete or steel members). Figure 3-13 shows a schematic view of the pre-preg laminate application method which is implemented in this research. Similar to the other processing techniques, the surface of the substrate needs to be treated based on the existing condition of the surface and recommended guidelines such as ICRI/ACI (1999) or NCHRP Report 514 (2004). It is recommended that the top layer of concrete (mortar) be removed by sandblasting, water blasting or grinding until the outer surface of the aggregates is exposed.

To achieve the composite material, high temperature is applied onto the laminates to allow the flow of resin between fibres to bond the composite material to the substrate. The curing with temperature depends on the type of the resin (eg. epoxy, polyurethane) but mostly a temperature in the range of 90-100 °C is sufficient for a few hours. Using the elevated temperatures (cure with steam), the curing time for pre-preg laminates can be lowered which leads to reduce job time and therefore cost efficiencies.

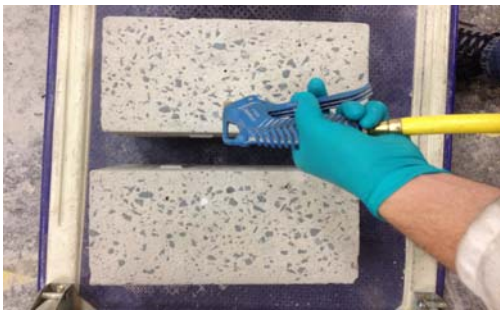
(a)
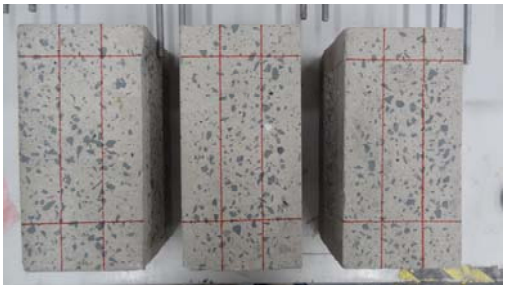
(b)
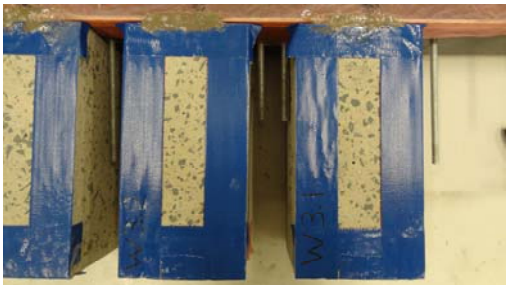
(c)

(d)

(e)

(f)
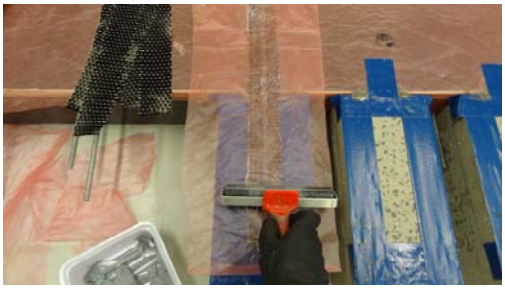
(g)
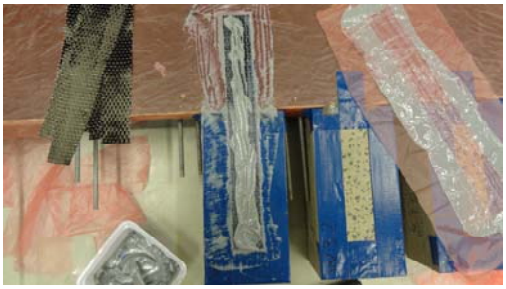
(h)
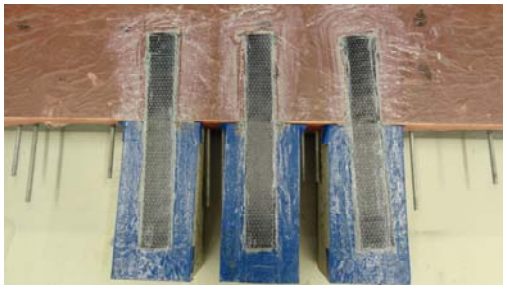
(i)

Figure 3-12. Manufacturing of the FRP in *Phase 2*; (a) surface cleaning, (b & c) marking the surface, (d) cutting the FRP, (e) mixing epoxy, (f) applying first layer of the epoxy, (g) applying fabric and rolling, (h) application of the next layer, and (i) FRP after curing.

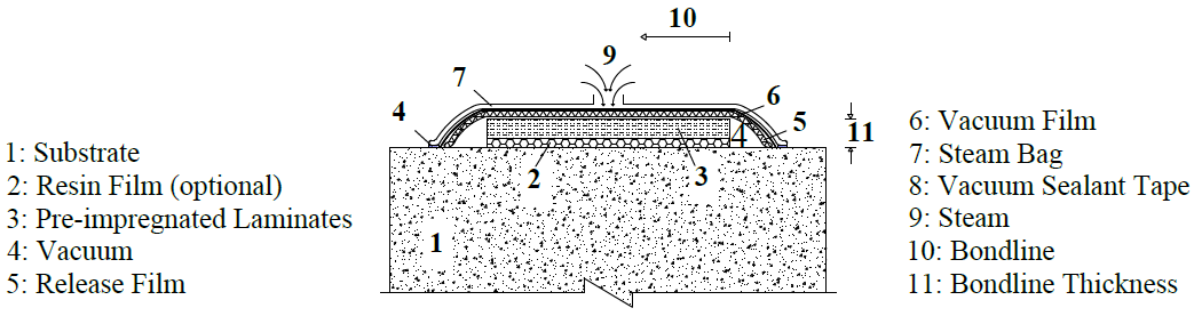

Figure 3-13. A schematic view of heated vacuum bag only technique.

The application of steam with high temperature onto pre-pregs enhances the transitional temperature (T_g) of the resin inside the composite. The fundamental properties of FRP will drastically abate when the ambient temperature exceeds the T_g of the thermosetting resin. This increase in T_g aids the FRP to withstand higher temperatures in hot climate areas and improve the resistance of the composite to the long term thermal degradation. Normally, the transitional temperature of V/H cured pre-pregs is between 100 to 120 °C while for wet lay-up and pultruded FRP application techniques lies between 40 to 50 °C which indicates a more reliable behaviour of composite in strengthening of structures in severe climates compared to the traditional methods.

During the curing process, the entire system is consolidated by vacuum in order to achieve a good bond between composite material and the substrate. Providing even vacuum pressure over the composite, about 8-10 ton/m^2, results in a durable and resistant bond to moisture and chemical attack. Figure 3-14 shows different stages of the HVBO technique which is applied in the current study.

To achieve an accelerated cure, steam is induced in a steam bag on the top of the set-up which also provides a lacuna for producing vacuum. The steam bag is fixed to the substrate using vacuum sealant tapes around the bag. During the process, the temperature and vacuum pressure is precisely monitored to avoid any noticeable changes which can cause a fault inside the composite. It has been shown that elevated temperature can crack the concrete. However, the range of temperature used in the present study has the least effect on the properties of the concrete. The porosity which can affect the compressive strength of the concrete (Odler and Rößler 1985), does not change by elevated temperature for hardened cement pastes and concrete (Zadražil et al. 2004).

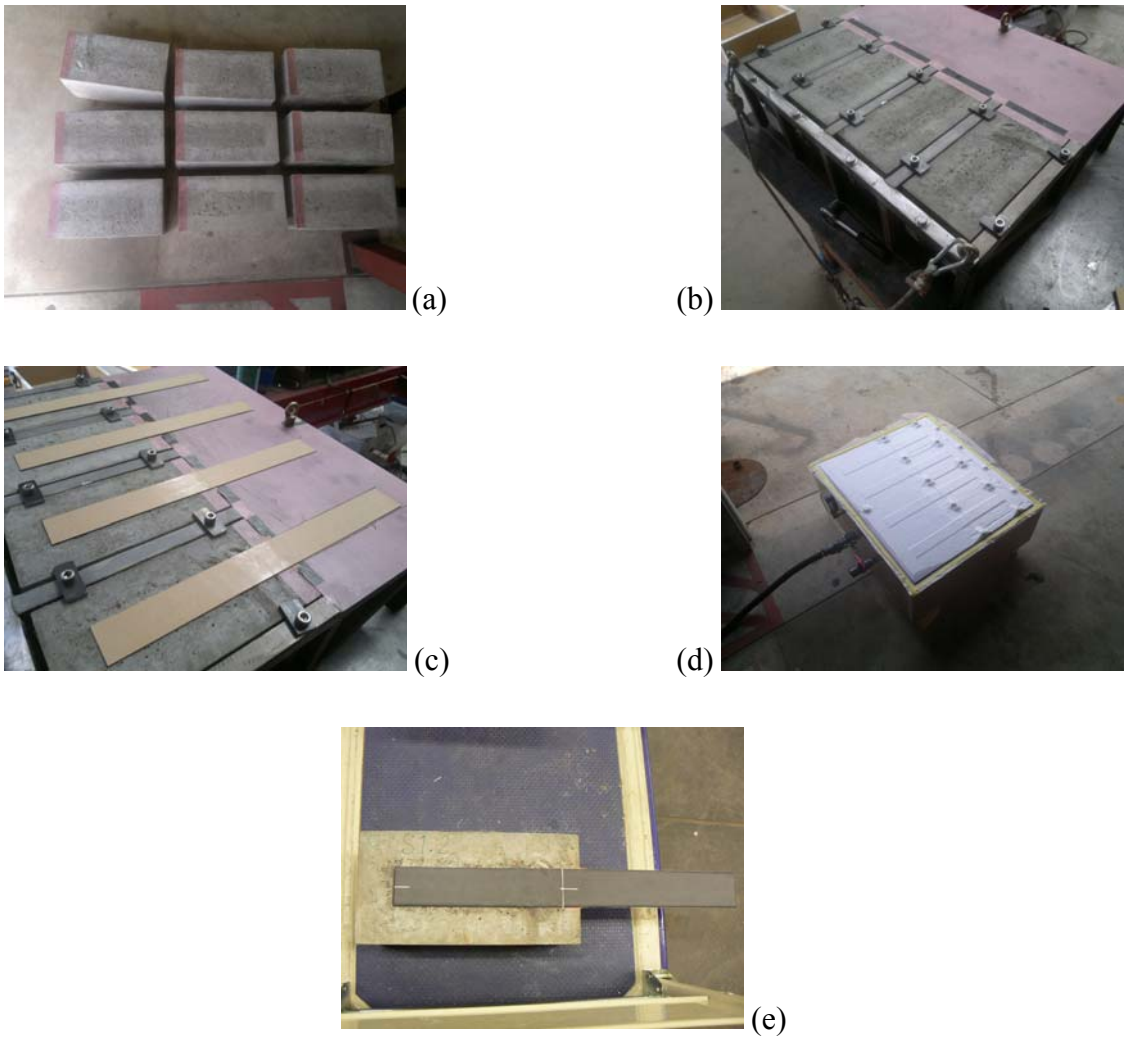

Figure 3-14. Manufacturing of the HVBO samples; (a) surface preparation, (b) positioning samples in vacuum chamber, (c) placing pre-pregs on the samples, (d) applying vacuum, (e) FRP after curing.

The interfacial response of the FRPs processed with heated vacuum bag only technique is investigated during the third phase of the experiments. In this phase, the effect of the bondline thickness on the bond characteristics is studied. The width and the length of the FRP composites are chosen 50 and 225 mm, respectively, with a 25mm initial unbonded length (Table 3-9). FRP with 225 mm in length and 25 mm initial unbonded length are chosen based on the experiments carried out on the samples which are discussed in sections 4.5 and 4.4, respectively. To leave a 25 mm initial unbonded distance, release film is applied between the concrete surface and the adhesive films before applying the pre-preg laminates. To determine the effect of the thickness on the interface behaviour, the film adhesives are inserted into the bondline. The number of film adhesive layers is varied during the experiments and consist of

2, 4 and 8 layers. Since the heat is applied to cure the pre-preg laminates, the pre-impregnated resin melts and covers the whole bonded area.

Table 3-9. Detail of the specimens tested during *Phase 3*.

Series	Sample ID	Surface Prep. ID	Number of Film Adhesive Layers	Bondline Thickness, t_{bl} (mm)
Preliminary	SC1-2R	N-SP	2	
	SC2-4R	N-SP	4	
	SC3-8R	N-SP	8	
I	SC-1.1		2	1.99
	SC-1.2		2	2.16
	SC-1.3		2	2.49
	SC-2.1		4	2.51
	SC-2.2		4	2.77
	SC-2.3		4	2.71
	SC-3.1		8	3.08
	SC-3.2		8	3.42
	SC-3.3		8	3.88

3.3.5. Vacuum Assisted Resin Infusion (VARI)

In this section, the outline of experiments carried out on FRP-to-concrete bonded joints processed by vacuum assisted resin infusion (VARI) technique is described. Therefore, the current research provides an experimental database regarding the interface behaviour between the concrete and the VARI processed FRP plates.

A platform with vacuum chamber is made to keep four concrete specimens at a time tightly in position while the FRP processing with VARI system is carried out (Figure 3-15). The platform also helps to attain better quality of interface in the bonded region. The inside space of the vacuum chamber is isolated from the outside by the vacuum bag and sealant tapes around the chamber. The resin is transferred from the epoxy reservoir to the fibres by four resin hoses. The vacuum provides a force to propagate the epoxy over the carbon fibres. When the epoxy completely saturates the fibres, the valve on the resin hose is shut to maintain the vacuum pressure during the curing time. The samples are kept under the vacuum for almost 24 hours while the epoxy is cured. The process of VARI is described in Chapter 2 in detail.

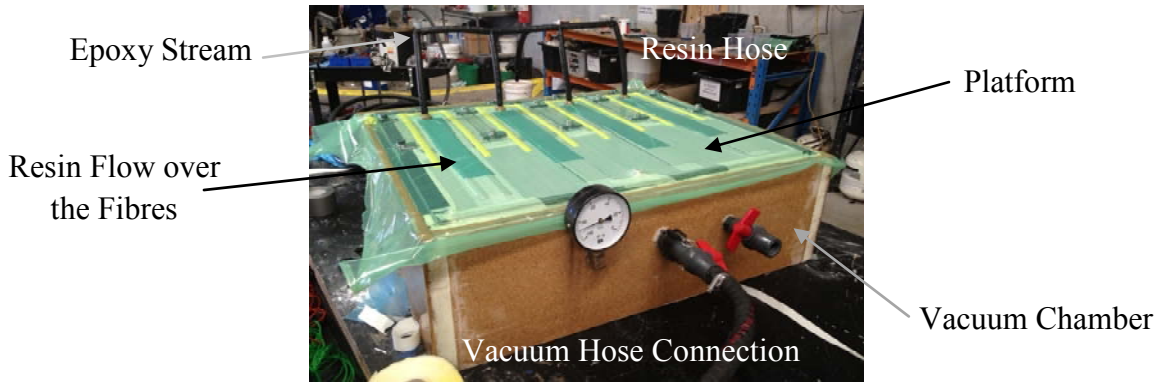

Figure 3-15. Application of VARI on the concrete specimens.

Four different bondline thicknesses, from 2 mm to 7 mm, are tested during the experimental program. The thickness variation is achieved using the VARI technique in which the FRP attachment is under control. To increase the thickness, bi-directional GFRP plates are inserted into the bondline between the substrate and the carbon plates. To minimise the contribution in load carrying capacity, the GFRP plates are placed ±45 degrees relative to the direction of the carbon fibres and the applied load. In addition, the glass fibres are cut to about plus 20 mm from loaded face of the concrete blocks (Figure 3-16). For each bondline thickness, three similar specimens are tested to achieve more reliable results.

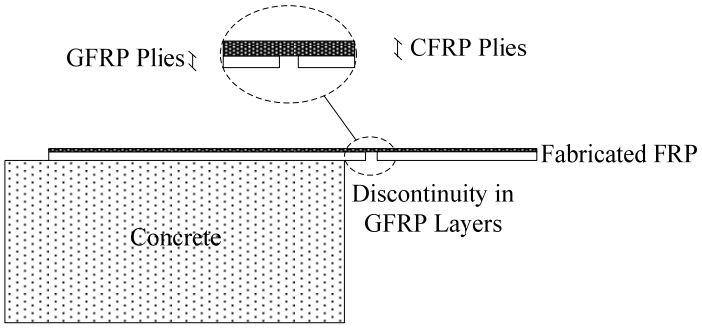

Figure 3-16. Configuration of FRP plies to minimise the contribution of GFRP layers in load carrying capacity.

Three plies of unidirectional carbon fibres (each one with approximate thickness of 0.337 mm) are placed on the top of GFRP fabrics to make the FRP plates. The FRP width adopted for all of the samples is 50 mm. A 25 mm initial unbonded region is considered between the FRP and concrete to avoid concrete crushing in the loaded end of the concrete blocks. This gap is suggested from the results presented in the next chapter (section 4.4). Before bonding the fibres on the concrete, blocks of *Series I* and *II* are treated by low pressure water jet

blasting (SP-3) and sandblasting with low aggregate exposure (SP-4), respectively. Table 3-10 provides detail of the specimens tested in *Phase 4*.

Table 3-10. Detail of the specimens tested in *Phase 4*.

Series	Sample ID	Surface Prep. ID	FRP Bonded Length, L_{frp} (mm)	Number of GFRP Layers	Bondline Thickness, t_{bl} (mm)
I	SF-B-1.1	SP-3	200	0	2.11
	SF-B-1.2	SP-3	200	0	1.91
	SF-B-1.3	SP-3	200	0	2.00
	SF-B-2.1	SP-3	200	1	2.49
	SF-B-2.2	SP-3	200	1	2.74
	SF-B-2.3	SP-3	200	1	2.53
	SF-B-2.4	SP-3	200	1	2.50
	SF-B-3.1	SP-3	200	3	4.06
	SF-B-3.2	SP-3	200	3	4.02
	SF-B-3.3	SP-3	200	3	3.82
	SF-B-4.1	SP-3	200	6	6.28
	SF-B-4.2	SP-3	200	6	6.38
II	SF-B-5.1	SP-4	225	0	2.06
	SF-B-5.2	SP-4	225	0	1.94
	SF-B-5.3	SP-4	225	0	2.05
	SF-B-6.1	SP-4	225	1	2.87
	SF-B-6.2	SP-4	225	1	2.92
	SF-B-6.3	SP-4	225	1	2.96
	SF-B-7.1	SP-4	225	3	4.65
	SF-B-7.2	SP-4	225	3	4.27
	SF-B-7.3	SP-4	225	3	4.78
	SF-B-8.1	SP-4	225	5	6.74
	SF-B-8.2	SP-4	225	5	6.57
	SF-B-8.3	SP-4	225	5	6.64

The main argument in variation of the bondline thickness processed with VARI can be the use of GFRP layers in the interface. Based on Efficiency (Krenchel) Factor in composites (Krenchel 1964), the effect of fibre orientation on stiffness can be determined by the following equation:

$$E_{frp} = \eta_\theta E_f V_f + E_m V_m \qquad 3\text{-}7$$

η_θ is composite efficiency factor (Krenchel) which is 0.25 for the fibres in ±45 degree. E and V are modulus of elasticity and volume fraction, while f and m represent fibre and matrix, respectively. Since elasticity modulus of the matrix is remarkably lower than the fibre, the above equation can be expressed as

$$E_{frp} = \eta_\theta E_f V_f \qquad 3\text{-}8$$

Since GFRP sheets are placed between substrate and CFRP fabrics in order to increase the bondline thickness, modulus of elasticity of the composite can be determined by

$$E_{frp} = \eta_\theta E_{cf} V_{cf} + \eta'_\theta E_{gf} V_{gf} \qquad 3\text{-}9$$

E_{cf} and E_{gf} are elastic modulus of carbon and glass fibres, respectively. Considering that the glass fibres are placed ±45 degree relative to the carbon fibre direction, the contribution of the glass sheets (e.g. for the samples with 6 GFRP layers) in elasticity modulus of the fabricated FRP is

$$0.25\times6/9\times0.3E_{cf} = 0.05 \qquad 3\text{-}10$$

It was assumed that elastic modulus of the glass fibres is $0.3E_{cf}$ (73/230 GPa/GPa). Therefore, the contribution of the glass fibres is totally about 5 per.

3.4. Properties of the Materials

3.4.1. Concrete

In total over 100 concrete blocks were cast to carry out the tests. Following the method mentioned in sections 3.2.1 and 3.2.2, the mean and characteristic compressive strengths and also slump values of the concrete blocks in each phase are presented in Table 3-11. It should be mentioned that $f'_{c,28}$ and $f'_{cm,SLS}$ are the characteristic compressive strength of the concrete at 28 days after casting and the mean compressive strength of the concrete on the day of the modified single lap shear test, respectively.

Table 3-11. Properties of the concrete samples.

	Series	Slump (mm)	$f'_{cm,28}$ (MPa)	$f'^{*}_{cm,SLS}$ (MPa)	$f'_{c,28}$ (MPa)	$f'^{*}_{c,SLS}$ (MPa)
Phase 1	1	57.0	---	48.9	---	---
	2	66.0	---	37.3	---	---
				32.8		
	3	70.0	37.6	27.6	15.6	12.1
	4	33.7	38.0	47.1	25.5	40.4
	5	33.7	38.0	47.1	25.5	40.4
	6	103.5	36.8	40.6	26.9	19.4
Phase 2	1	103.5	36.8	40.6	26.9	19.4
	2	33.7	38.0	39.6	25.5	35.0
Phase 3	Preliminary	55.5	37.8	---	18.2	---
	1	55.5	37.8	48.9	18.2	38.4
		57.0				
Phase 4	1	72.0	36.0	42.4	19.6	31.3
		90.0	48.4	39.0	41.2	31.0
	2	72.0	36.5	46.1	19.6	38.6
		90.0	48.4	52.4	41.2	46.3

*SLS: single lap shear

3.4.2. FRP Sheets/Laminates

Corresponding to each phase of the experiments, different CFRP sheets/laminates were used to fabricate the specimens (Table 3-12). SikaWrap-230 C is a unidirectional woven carbon fibre and can be applied in the wet lay-up system while TORAYCA T700 is a twisted fibre. Density of the fibres for TORAYCA T700S and SikaWrap-230 C is 1.8 g/cm^3, and 1.76 g/cm^3, respectively. In addition, fabric thickness for Kor-CFW600 and SikaWrap-230 C is 0.337 and 0.13 mm, respectively.

SikaCarboDur-S1214 and Kor-CLS 0814 laminates are used as pultrusion systems with the average thickness of 1.44 mm and 1.45 mm, respectively. These laminates may be applied for reinforcing the concrete and timber structures in case of increasing the load requirements, enhancing durability, inadequate design of construction or damaged parts of the structures. Sika Wrap can be applied externally for strengthening of reinforced concrete, masonry and timber elements. This fabric is suitable for retrofitting and confinement works on columns, beams and walls with complex shape.

Table 3-12. Specification of the fibres in FRP systems.

	Processing Technique	Type of Fibre	Tensile Strength, T_{fib} (MPa)*	Tensile Modulus, E_{fib} (GPa)*	Fibre Areal Weight, FAW (g/m^2)*
Phase 1	Pultruded-A	Kor-CLS 0814 (TORAYCA T700S)	4900	230	---
	Pultruded-B	SikaCarboDur-S1214	~ 4300	~ 238	---
Phase 2	Wet Lay-up	SikaWrap-230 C	4300	238	225
Phase 3	HVBO	TORAYCA T700S	4900	230	400
Phase 4	VARI-A	Kor-CFW600 (TORAYCA T700S)	4900	230	610
	VARI-B	Kor-CFW600 (TORAYCA T700S)	4900	230	610

*The values in this table are reported by the manufacturer.

During *Phase 3* and 4, TORAYCA T700S fibres are processed by HVBO and VARI manufacturing methods, respectively. The material properties of the carbon FRP sheets or laminates are presented in Table 3-13. The difference between Table 3-12 and Table 3-13 is that the former provides the properties of the fibres before processing whilst the later represents the properties of the sheets/laminates after processing. The reported values in Table 3-13 are obtained from the standard tensile test carried out on the FRPs which the test process is mentioned in section 3.2.3. In addition, the experimental results of each fabrication method are presented in detailed in Appendix A.

Table 3-13. Properties of the CFRP sheets/laminates used in different processing techniques.

Processing Technique	Tensile Strength, T_{frp} (MPa)	Elastic Modulus, E_{frp} (GPa)	Strain @ Max. Load (%)	Strain @ Break (%)
Pultruded-A	2847	159	1.77	2.15
Pultruded-B	3170	165	1.83	2.06
Wet Lay-up	3972	234	1.63	1.63
HVBO*	1601	134	1.04	---
VARI-A	2529	225	1.35	1.37
VARI-B	2000	225	1.00	1.17

* Values are reported by the manufacturer.

3.4.3. Adhesives

Sikadur-30 and Kor-CPA are used to bond SikaCarboDur-S1214 and Kor-CLS 0814 to the substrate, respectively. Both Sikadur-30 and Kor-CPA are two-component epoxy based adhesives. Part A of the epoxy is the base component while Part B is the hardener which should be mixed at a ratio of 2/1 (Base/Hardener) prior to the application. In case of wet lay-up system, Sika Wrap-230 C is saturated with Sikadur-330 which is a thixotropic epoxy based impregnating resin.

In heated vacuum bag only technique, MTM57 epoxy matrices were used as the film adhesives or impregnating component of the fibre in pre-preg laminates. Their intermediate viscosity and tack make them suitable for proper impregnation of light and medium weight unidirectional and fabric reinforcement. Shear strength of MTM57 is reported by the manufacturer as 34 MPa. MTM57 component prepregs can be used at high temperatures up to 90°C after curing.

Table 3-14. Properties of the adhesives used in different processing techniques.

Processing Technique	Specification of the Adhesive	Elastic Modulus, E_{adh} (MPa)	Tensile Strength, T_{adh} (MPa)	Shear Modulus, G_{adh} (MPa)	Shear Strength, S_{adh} (MPa)	Compressive Strength (MPa)
Pultruded-A	Kor-CPA	12800	---	---	10	90
Pultruded-B	Sikadur-30	11200	24-27*	4308	18**	70-80+
Wet Lay-up	Sikadur-330	4500**	30**	---	---	---
VARI-B	Daron ZW7567	3100	90	---	---	---

* For 7 days curing at +15°C, ** for 7 days curing at +23°C, + for 7 days curing at +10°C, ^ flexural strength and modulus at +22°C

VARI-B sheets consist of a turane resin system. Turane resin systems are a new group of thermosetting resins which during curing combine the chemistry of radical polymerization with polyurethane. Daron turane resin shows excellent mechanical and temperature resistance performance and also high impact and toughness properties. Another advantage of this resin is their curing reaction which can be controlled from very fast to slow reacting systems. They

can be applied in unsaturated polyester and polyurethane fabrics. The properties of the adhesives are presented in Table 3-14. These properties are reported by the resin manufacturer.

3.5. Summary

The outline of experiments was presented in this chapter. First, the process of casting the concrete blocks was described in section 3.2.1. Concrete compression tests and FRP tensile tests were performed on the samples to characterise the properties of the concrete and the FRP materials, respectively. The modified single lap shear test set-up, to monitor the interface behaviour between the FRP and concrete with higher precision, is presented in section 3.2.5. Following the single lap shear tests, the surface tensile strength of concrete prisms were measured based on ASTM C1583-04 (2009) recommendations.

Considering the lack of available test data on the interfacial responses between concrete and FRP materials processed with different manufacturing methods, the application of these techniques is discussed further through this section. The fabrication of the various processing techniques is quite different and hence the equalisation method, to scale the material characteristics of the processing techniques, is presented in section 3.3.1.

The whole experimental program, regarding the FRP processing techniques, was divided into four phases. The effect of different factors on the bond behaviour was investigated for each processing technique through several test series. Finally, the last section of the chapter presents the detail of the material properties which are tested in this research.

Results of the modified single lap shear tests are presented and discussed in the next chapter. The following chapter presents the parametric study on the bond properties considering various parameters such as; concrete surface tensile strength, initial unbonded length, FRP bonded length, FRP-to-concrete width ratio, bondline thickness, surface treatment methods, and FRP processing techniques.

CHAPTER 4

MODIFIED SINGLE LAP SHEAR TEST RESULTS AND DISCUSSION

4.1. Introduction

This chapter presents the experimental results and discussion on the modified single lap shear test outcomes. In addition, the parametric study of the bond is mentioned in this chapter. The parameters which are considered in this research are;

- concrete surface tensile strength (f'_{cst})
- initial unbonded length (IUL)
- FRP bonded length (L_{frp})
- FRP-to-concrete width ratio (w_r)
- bondline thickness (t_{bl})
- surface treatment methods
- FRP processing techniques

Throughout this chapter in order to compare the results of the same response for different samples, the graphs are plotted in a same scale. For more clarity, Appendix B provides unscaled graphs for each sample.

4.2. Bond-slip Relationship

Since bond stress-slip relationship is investigated in this research, the derivation of the bond stress and the local slip is described in this section. The local slip, s_x, at any location from the free end of the FRP, x, is the relative displacement of the FRP to the concrete substrate (Figure 4-1);

$$s_x = u_{frp,x} - u_{c,x} \qquad 4\text{-}1$$

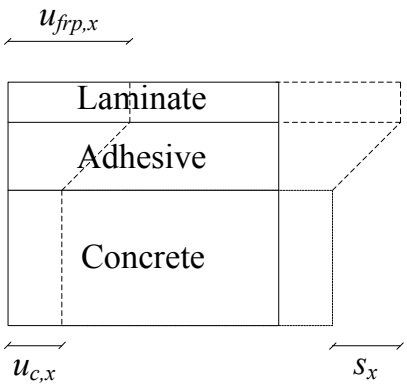

Figure 4-1. Local displacements of the concrete and the FRP.

$$s_x = \int \varepsilon_{frp,x} dx - \int \varepsilon_{c,x} dx \qquad 4\text{-}2$$

$u_{frp,x}$ and $u_{c,x}$ are the displacement of the FRP and concrete at any point, respectively and $\varepsilon_{c,x}$ is the strain in concrete. Strain values of the concrete and the FRP at location of x are indicated by $\varepsilon_{c,x}$ and $\varepsilon_{frp,x}$, respectively. The local slip at any position can be derived from the strain values by integration of the strain profile along the bond length to that position;

$$s_{L-x} = s_L + \int_{L-x}^{L} \varepsilon_{frp,x} dx \qquad 4\text{-}3$$

x is the distance relative to the free end, and s_L is the local slip at the loaded end (Figure 3-9). The interfacial shear stress of the joints, $\tau_{int,x}$, is derived from the following relation;

$$\tau_{\text{int},x} = \frac{d^2 s_x}{dx^2} \cdot t_{frp} E_{frp} = \frac{d\varepsilon_{frp,x}}{dx} \cdot t_{frp} E_{frp} \qquad 4\text{-}4$$

t_{frp}, E_{frp} and $\varepsilon_{frp,x}$ are the FRP thickness, FRP modulus of elasticity and strain of the FRP, respectively. The strain value at the loaded, ε_0, end can be calculated by

$$\varepsilon_0 = \frac{F}{E_{frp} A_{frp}} \qquad 4\text{-}5$$

A_{frp} and E_{frp} are the cross sectional area and the modulus of elasticity of the laminate, respectively. F is the load applied to the sample from the actuator during the test. Therefore, the bond stress versus slip curves which are mentioned in the following sections can be determined based on Eqs. 4-4 and 4-3, respectively.

4.3. Concrete Surface Tensile Strength

To investigate the effect of the concrete surface tensile strength, f'_{cst}, on the interfacial behaviour of the joints, the direct tension test has been carried out on pultruded samples in *Series I* and *II* and also samples processed with heated vacuum bag only technique. Figure 4-2 represents the correlation between the surface tensile strength of the concrete and the maximum applied load, slip values at the maximum load stage and depth of the intermediate crack (IC) debonding in these samples.

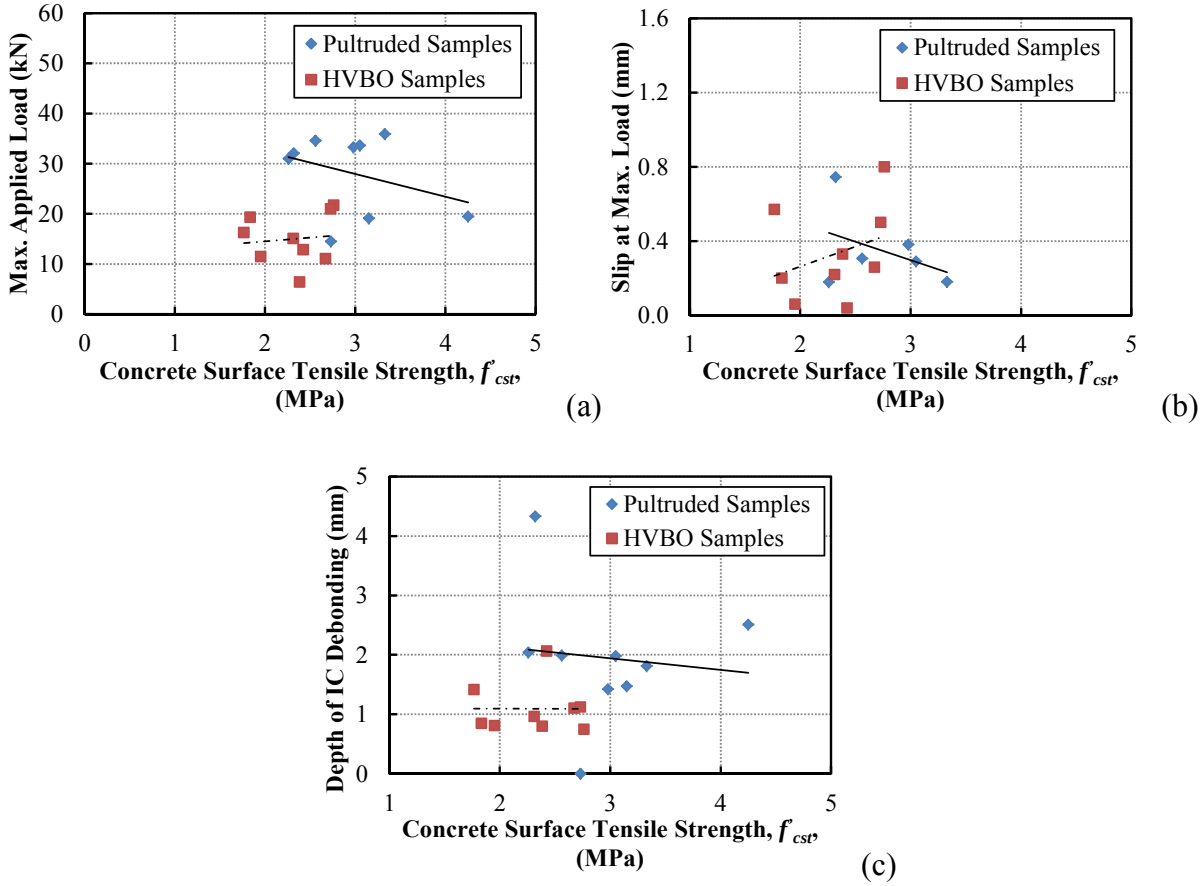

Figure 4-2. Correlation between the concrete surface tensile strength and (a) maximum applied load, (b) slip corresponding to the maximum applied load, and (c) depth of the IC debonding.

The graphs show that the correlation follows a different pattern in pultruded and HVBO specimens. While the load carrying capacity for HVBO specimens slightly increases with higher concrete surface tensile strength, it decreases in case of the pultruded samples. In addition, the same behaviour is observed in terms of the relation between f'_{cst} and the slip at the maximum applied load. However, based on Figure 4-2c, the correlation between f'_{cst} and depth of the IC debonding is poor.

In total, since a large variation was observed from the pull-off tests and a reasonable correlation cannot be achieved between the concrete surface tensile strength and the interface response of the joints (Figure 4-2), no further pull-off tests were carried out on the rest of the specimens in other phases. One possible reason for this disagreement is that the single lap shear test is mainly governed by mode II failure while direct tension test resembles mode I.

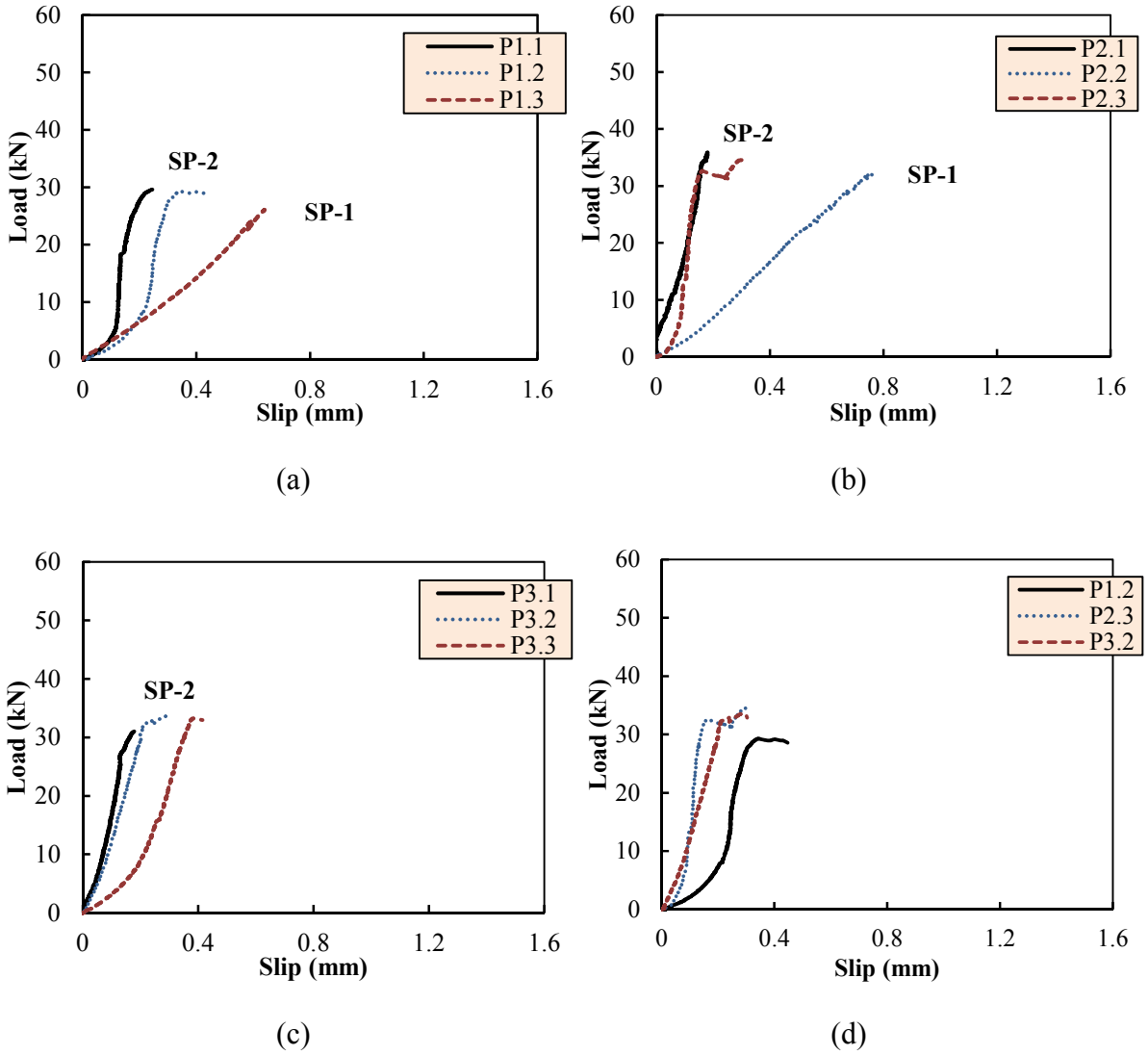

Figure 4-3. Effect of IUL on the load-global slip response of the joints (for unscaled graphs refer to Appendix B).

4.4. Initial Unbonded Length

Generally in order to avoid concrete splitting at the near end face of the concrete blocks (loaded end), an initial un-bonded region between the FRP and the concrete is considered (Mazzotti et al. 2008). However, the effect of the initial unbonded length (IUL) on the bondline behaviour has not been investigated in the literature. Thus, several series of tests were conducted to address the influences of this factor on the bond by monitoring applied load-global slip and local shear stress-slip distributions.

To investigate the effects of the initial unbounded length on the bond behaviour, three unbounded lengths, 0, 25 and 50 mm, were considered. It was achieved by palcing release film between the adhesive and the concrete while the plate was bonded to the substrate.

Figure 4-3 compares the modified single lap shear test results for the samples with 0, 25 and 50 mm initial unbonded lengths. Considering Figure 4-3d, samples with longer initial unbonded length experience higher magnitudes of load. The average maximum load increases from 28.4 kN to 34.2 kN for samples with 0 and 25 mm IUL, respectively. However this increase is not noticeable for samples with 25 and 50 mm unbonded lengths.

Considering load versus strain profiles for the samples (Figure 4-4), the interface crack could not propagate through the bonded region for samples with no initial unbonded length. In the case of the samples with IUL=25 mm and 50 mm, the horizontal section of the load-strain curve indicates that the failure occurred after the formation of the interfacial crack.

For further comparison, the shear stress versus slip relationships of the samples are investigated. The maximum shear stress in samples with no initial unbonded length is recorded as 10.1 MPa while for P2.3 and P3.3 is 17.2 and 15.0 MPa, respectively (Figure 4-5). Therefore, using an appropriate gap in the front side of the concrete block could contribute to the higher shear stresses in the interface. The shear stress-local slip profiles of the samples with initial gap consist of two distinctive parts; ascending and descending branches. However in case of the sample with IUL=0, this profile shows ascending part with no reduction in the shear stress values after the maximum stress. It may attribute to the fact that the interfacial crack could not propagate properly along the bonded region.

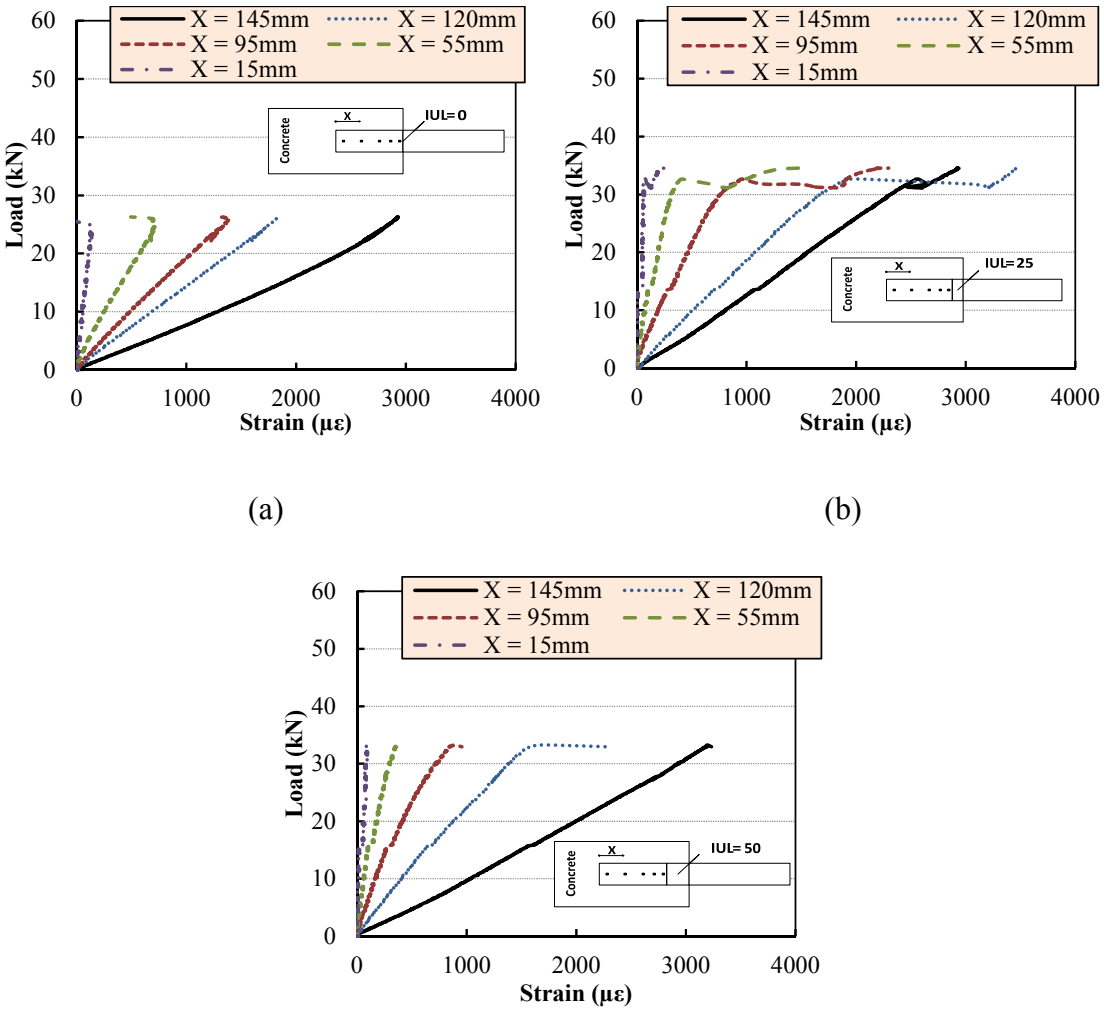

Figure 4-4. Load vs strain profile of the samples with (a) IUL=0 mm, (b) IUL=25 mm, and (c) IUL=50 mm.

For samples with no IUL, like previous researches (Seracino 2001; Yao et al. 2005), a triangular section was split from the front side of the concrete. However, for the rest of the specimens, failure happened inside a thin layer of the concrete under the bonded area. Considering the failure pattern of the samples, it is advisable to leave an unbonded region at the loaded end in order to avoid stress concentration in the front side of the concrete prism and allow FRP to distribute loads through the interface.

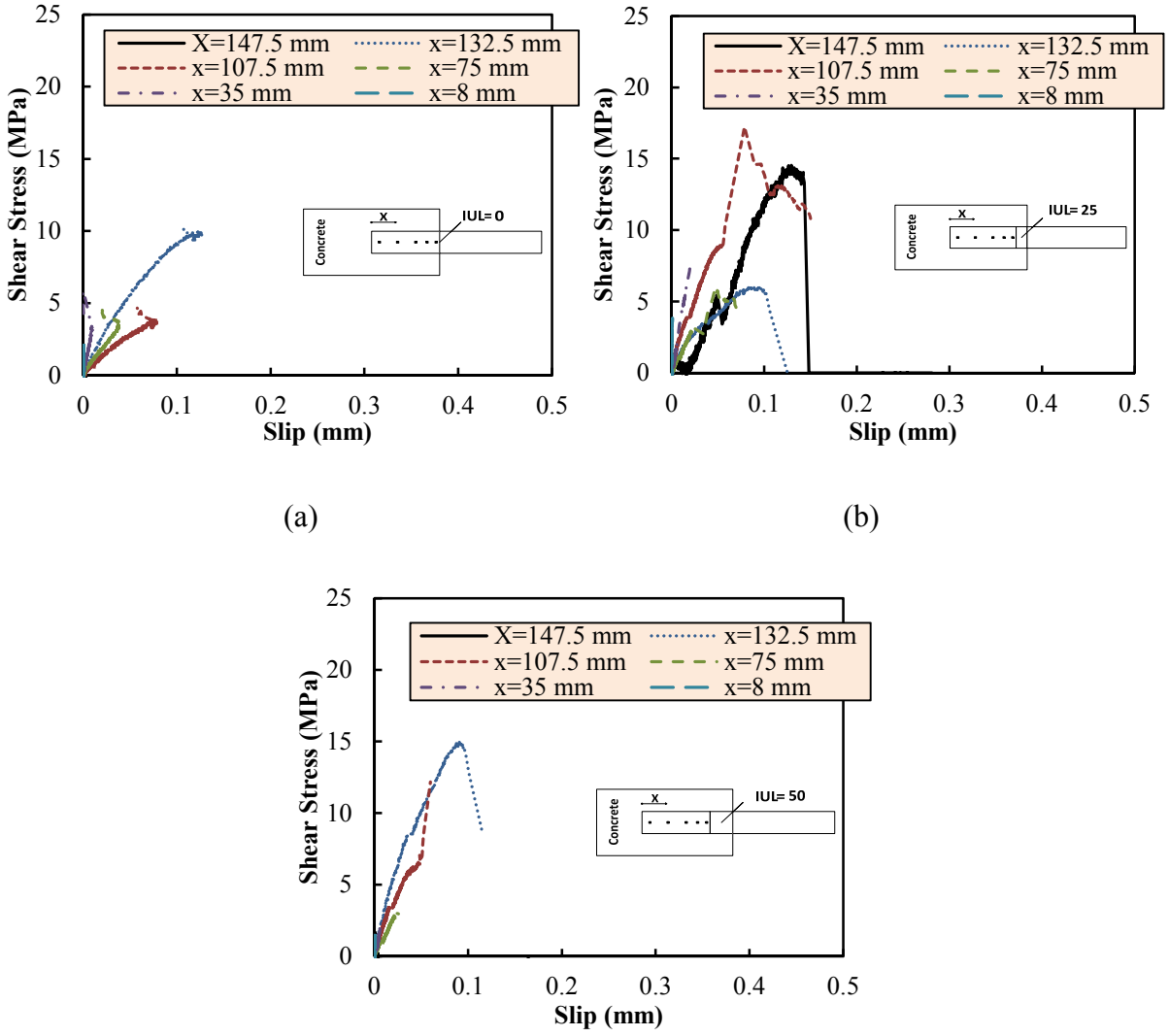

Figure 4-5. Bond stress-local slip data for samples with (a) IUL=0 mm, (b) IUL=25 mm, and (c) IUL=50 mm.

4.5. FRP Bonded Length

When the FRP is subjected to load, after a specific level of applied load, a macro-crack initiates in the interface and starts to propagate toward the free end of the joint. The interface is not able to carry further load and the bond between concrete and the FRP abruptly fails when the crack reaches a certain amount in length, the effective bond length.

The effective bond length is one of the characteristics of the joint and does not change with the FRP bonded length. This concept is on the opposite side of the anchorage length in reinforced concrete (RC) members. In RC structures, the increase in the anchorage length

may lead to load carrying enhancement. However, in members externally bonded with FRP plates, longer FRP does not enhance the load capacity of the joint.

Based on the mechanism mentioned above, an explicit method to determine the effective bond length, L_{eff}, is to alter the FRP bonded length in SLS test. Therefore, in *Series III* of *Phase 1* of experiments, three different lengths (100, 150, and 200 mm) are applied (Table 4-1). During the experiments, samples P6.1 and P6.2 failed and their results are not presented here.

Table 4-1. MSLS results of *Series II* and *III* in *Phase I* of MSLS tests.

Sample ID	Max. Load, F_{max} (kN)	Ultimate Load, F_u (kN)	Failure Mode*
P2.1	35.90	35.90	CD, LFT
P2.2	32.08	32.00	CD, NEF
P2.3	34.55	34.55	CD, TLC
P4.1	22.48	21.73	CD
P4.2	29.43	29.06	CD, NEF
P4.3	29.09	29.09	CD, LFT
P4.4	21.17	21.17	NEF, CD
P5.1	41.75	41.73	NEF, CD
P5.2	33.24	33.13	NEF, CD
P5.3	23.97	4.63	CD
P5.4	31.38	31.38	NEF, CD
P6.1	---	---	---
P6.2	---	---	---
P6.3	31.84	28.13	NEF, CD

*CD: Concrete debonding, LFT: light-fibre-tear failure, NEF: Near end failure

Figure 4-6 illustrates the load versus global slip curves of the tested specimens. In addition, the method of the surface treatment is presented in this figure. For further analysis, the maximum applied load is plotted against the FRP bonded length in Figure 4-7. Based on the interpolation curve, the load remains constant after L_{frp} = 150 mm. Therefore in the case of the pultruded laminates, the effective bond length was assumed about 150 mm.

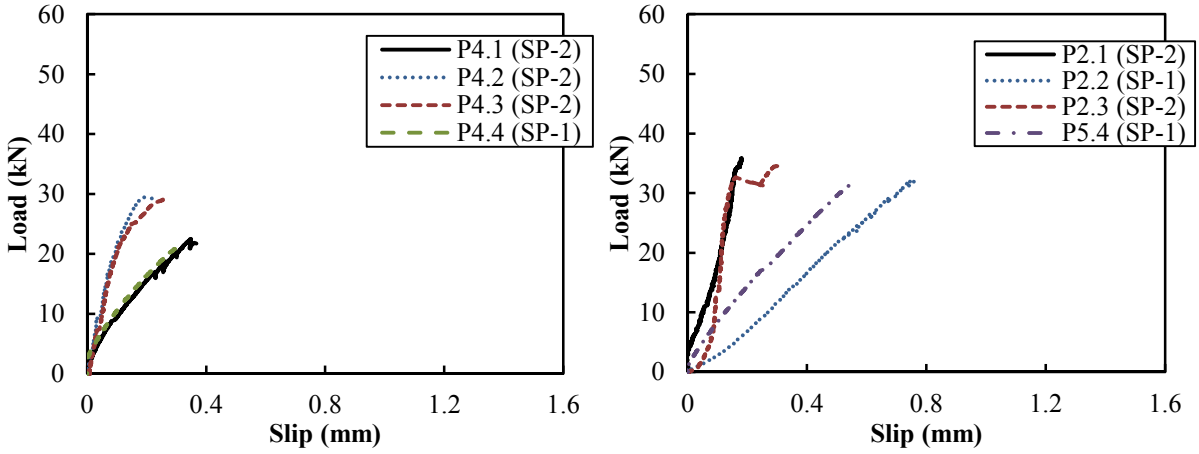

(a) (b)

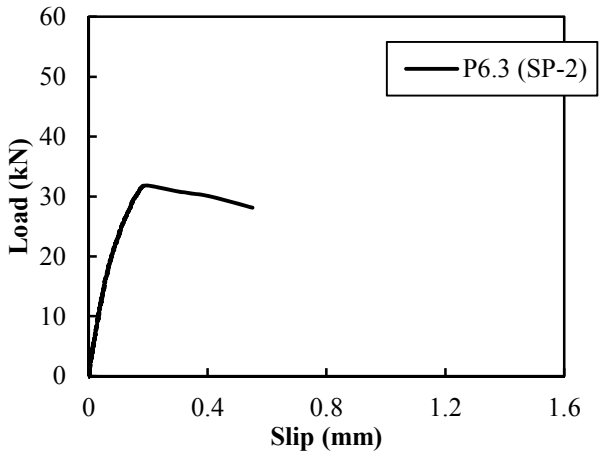

(c)

Figure 4-6. Load vs global slip curves of the joints with bonded length of (a) 100 mm, (b) 150 mm, and (c) 200 mm.

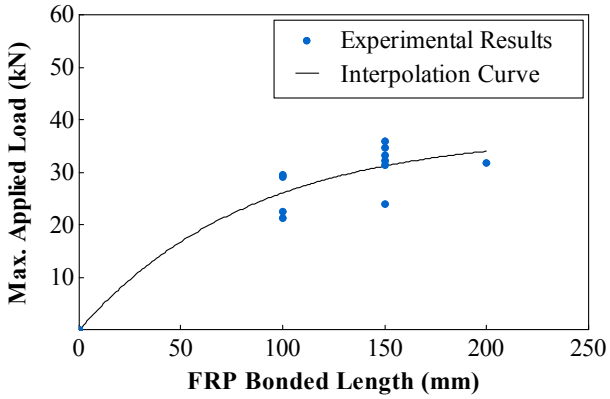

Figure 4-7. Explicit method for determination of the effective bond length.

Investigating the strain distribution profiles along the bonded length indicates that the strain gauges near to the free end of the FRP experience quite minimal strain values even during debonding. After initiation of the macro-crack, the distance from the loaded end to the point where the strain profile reaches zero remains constant up to the failure of the joint. The same behaviour is observed in the previous works (Bizindavyi and Neale 1999; Yao et al. 2005). Therefore in the present study, the effective bond length is defined as the distance between the points corresponding to 99 and 1% of the strain at the loaded end when the strain profile at the loaded face tends to become plateau. This concept is graphically presented in Figure 4-8.

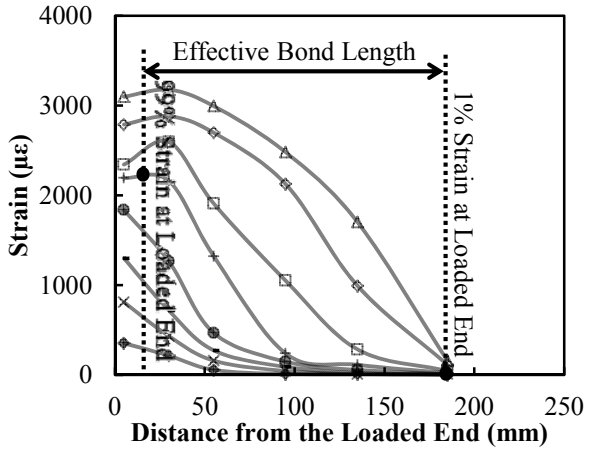

Figure 4-8. Implicit method for determination of the effective bond length.

The peak strain at higher loads is greater than the strain at the loaded end in Figure 4-8. It happens due to the propagation of the macro-crack at final stages of loading. At the loaded end, the FRP laminate/sheet is detached from the substrate and therefore local deformations and stresses can affect the measurements and cause this type of discrepancy.

The effective bond length is determined for different specimens based on the implicit method. In addition, the effective bond length adopted for each manufacturing method is reported in Table 4-2. Results show that EBL for all of the processing techniques is almost the same and around 150 mm. Therefore, the bonded length of the FRP sheets/laminates in different series of the tests is considered at least 150 mm.

Table 4-2. Effective bond length adopted in the present study based on the implicit method.

Manufacturing Method	Sample ID	EBL for Sample (mm)	Adopted EBL (mm)
Pultruded-A	P1.3	137	137
	P2.3	135	
	P3.3	138	
Pultruded-B	P7.3	137	147
	P8.3	161	
	P9.3	164	
	P10.3	152	
	P12.3	121	
	P13.3	144	
Wet Lay-up	W1.3	169	181
	W2.3	188	
	W3.3	186	
VARI-B	SF-B-1.3	119	158
	SF-B-3.3	164	
	SF-B-4.2	159	
	SF-B-5.3	141	
	SF-B-7.3	176	
	SF-B-8.3	189	

As mentioned earlier, the effective bond length is a characteristic of the adhesively bonded joints. Regarding the samples with different bondline thickness, the effective bond length is longer for thicker samples (Table 4-2). In *Series IV* of *Phase 1*, when the thickness changes from 3.5 mm to 4.8 mm, the effective bond length increases while this factor does not change significantly for the samples with 4.77 and 8.13 mm bondline thicknesses. The same response is observed for the VARI system. Considering the effect of the bondline thickness on the maximum applied load, increasing the thickness does not necessarily lead to the load carrying capacity enhancement of the joint. This indicates the existence of an optimum bondline thickness which is presented in detail in section 4.7.

4.6. FRP-to-concrete Width Ratio

The influence of different FRP/concrete width ratio ($w_r = W_{frp}/W_c$) on the interface behaviour is studied in *Series V* of *Phase 1* of experiments.

Table 4-3 presents the results of modified single lap shear tests on the specimens in this series of the tests. In all of the samples, failure occurred within a thin layer of concrete (about 1.2 mm) directly beneath the adhesive (CD). The failure was accompanied with the initiation

of an interfacial crack along the bond length toward the free end of the pultruded laminates. The bondline concept for pultruded samples is considered as the total thickness of CFRP laminate, t_{lam}, and the adhesive, t_{adh}.

Table 4-3. Summary of FRP-concrete bonding tests in *Series V* of *Phase 1*.

Sample ID	Max. Load, F_{max} *(kN)*	Ultimate Load, F_u *(kN)*	Slip at Max. Load, S_{max} *(mm)*	Ultimate Slip, S_u *(mm)*	Failure Mode*
P10.1	17.8	17.3	0.27	0.81	CD, LFT
P10.2	16.0	16.0	0.63	0.63	CD
P10.3	19.4	16.0	0.32	0.72	CD
P11.1	31.1	29.2	0.15	0.49	CD, LFT
P11.2	30.8	29.5	0.40	0.54	CD
P11.3	27.9	24.4	0.14	0.45	CD
P12.1	47.2	44.7	0.11	0.41	CD, LFT
P12.2	52.1	49.6	0.23	0.47	CD, NEF
P12.3	49.2	48.5	0.51	0.53	CD

*CD: Concrete debonding, LFT: light-fibre-tear failure, NEF: Near end failure

Typical load versus slip curves are shown in Figure 4-9 for different width ratio, w_r, (0.167, 0.333 and 0.533). The load-slip relationship for all of the samples with different FRP width is quite similar in shape. The load increases linearly with increase in slip and after a certain stage shows nonlinear behaviour with further increase and the curve then tends to become plateau until failure. Post-nonlinear stage for samples shows the same trend in each series. For samples with 25, 50 and 80 mm FRP width, the average maximum applied load was 17.72, 29.92 and 49.50 kN, respectively.

With increase in w_r (Figure 4-9a), the maximum load increases with the ratio of 1.69 (for 50 to 25 mm FRP width), 1.65 (for 80 to 50 mm FRP width) and 2.79 (for 80 to 25 mm FRP width). This trend attributes to the distribution of shear stresses over a larger area of the bond. The same behaviour has been reported in literature (Subramaniam et al. 2007; Taljsten 1997).

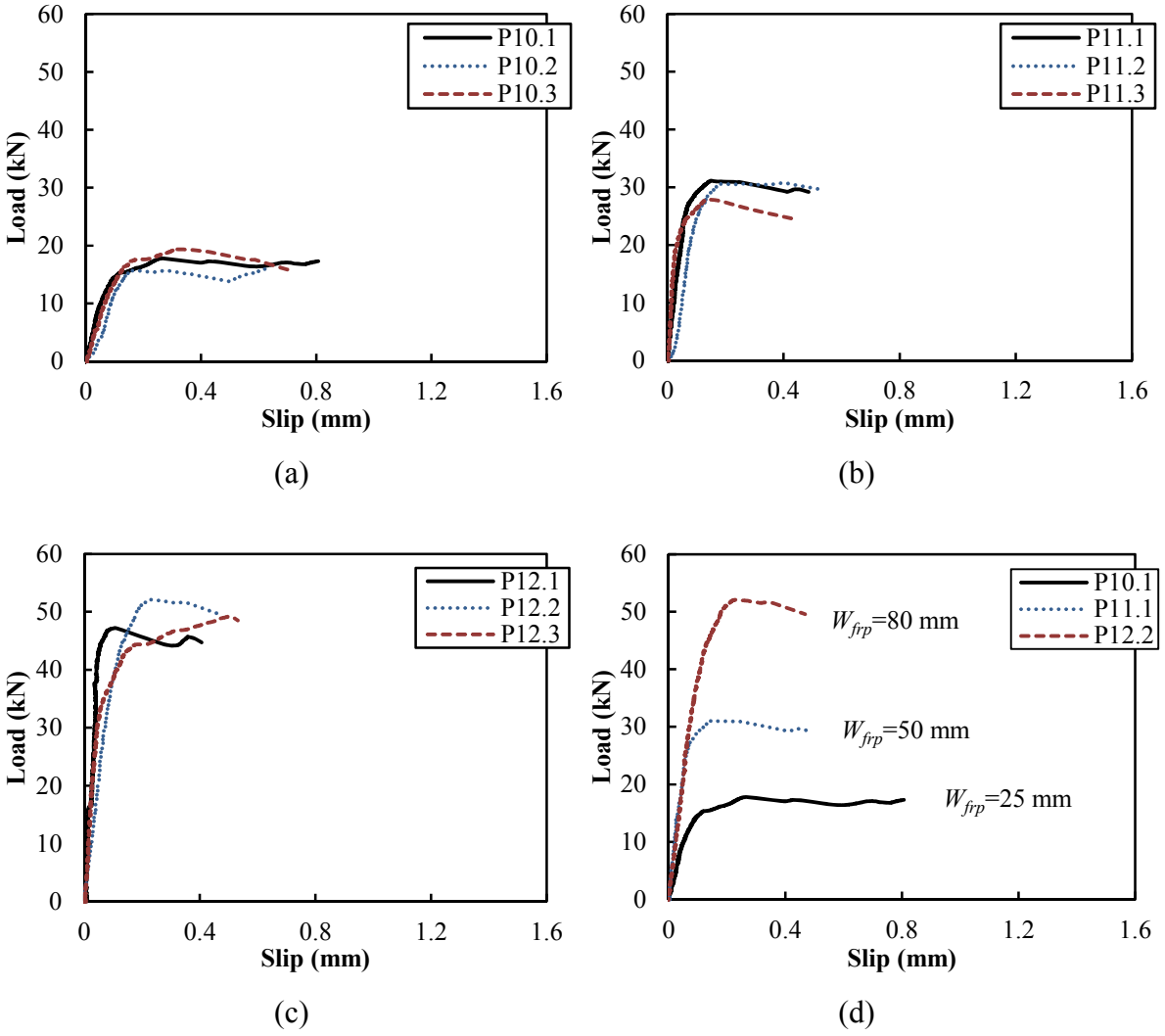

Figure 4-9. Load-slip response of the samples with, (a) W_{frp} =25 mm, (b) W_{frp} = 50 mm, (c) W_{frp} = 80 mm, and (d) comparison.

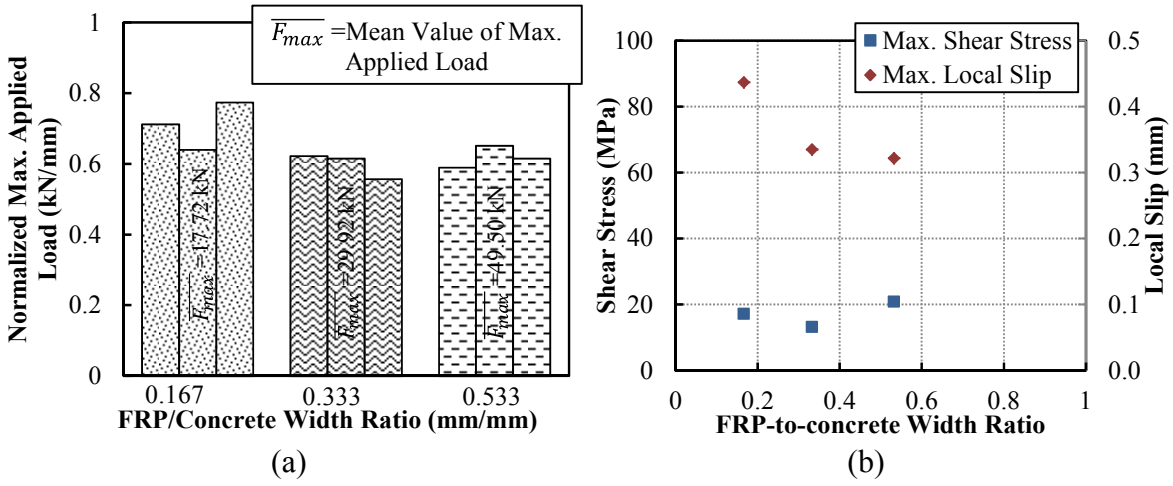

Figure 4-10. Normalized applied load vs FRP-to-concrete width ratio, (b) the effect of the FRP-to-concrete width ratio on the maximum shear stress and the local slip.

Figure 4-10b shows, the maximum shear stress increases for samples with higher FRP-to-concrete width ratio. However, samples with 25 mm FRP width do not follow the trend shown in Figure 4-10b. This provides reason of the discrepancies between experimental and analytical results which is presented in Chapter 5. In addition, the correlation between the FRP width and the normalized maximum applied load is illustrated in Figure 4-10a. In this figure, the maximum load was normalized with respect to the FRP width. According to

Table 4-3 and Figure 4-10b, the maximum local slip decreases for higher FRP to concrete width ratios. It indicates that wider joints show brittle behaviour in comparison with the samples with lower w_r.

Load versus strain values of the interface at different locations along the bondline is presented in Figure 4-11. Load-strain curve at each location consists of three stages: linear, nonlinear (post linear) and plateau (post nonlinear) sections. The load increases sharply with small change in strain values up to 20 kN for sample P10.3 while the post linear stage starts around 5 kN for specimen with W_{frp} = 25 mm (P12.3). Around the macro-crack initiation stage, the load-strain behaviour tends to be plateau and the strains of the interface rapidly increase without noticeable increase in load.

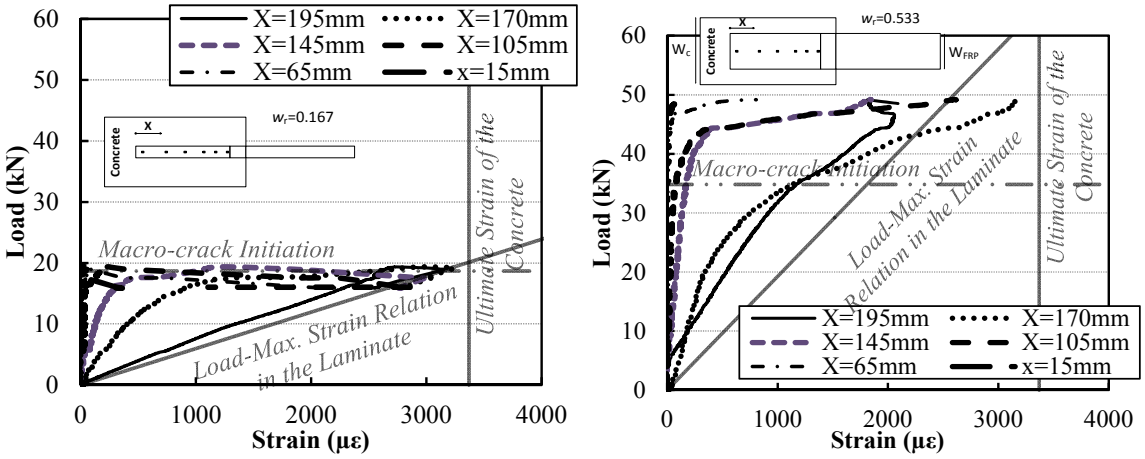

Figure 4-11. Applied load vs strain value along the bondline: (a) P10.3: t_{bl}=4.33, W_{frp}=25 mm, (b) P12.3: t_{bl}=4.45, W_{frp}=80 mm.

Based on Figure 4-11b, sample with t_{bl}=4.45 and W_{frp}=80 mm follows a different behaviour. The strain along the bondline increases even after the initiation of macro-cracks. One possible reason for this distinctive behaviour may be attributed to the width of the FRP. The micro-cracks propagate over the width under the bonded FRP and when the macro-crack spreads through the bond, the crack changes direction instead of growing along straight line.

However, in samples with 25 and 50 mm FRP width, the crack grows along the longitudinal direction of FRP. In sample P12.3, when the macro-crack initiates, the strain values at the distance of 195 and 170 mm away from the free end are the same. After this point the strain in the second strain gauge (x = 170 mm) exceeds the strain of the first gauge.

Since the concrete is a mixture of aggregates and mortar, it is considered as a heterogeneous material. Despite the longitudinal direction of the applied load in *MSLS* tests, cracking occurs between mortar and aggregate in different directions. At a certain level of load, macro-crack starts to initiate and crosses micro-cracks on its way toward the free end of the FRP. Therefore, the energy which is needed to open the cracks depends on whether the macro-crack crosses longitudinal or transverse micro-cracks on its way. If a longitudinal micro-crack is crossed, macro-crack propagates easily with lower energy release. While, a transverse crack is crossed, the macro-crack is bound and more energy is needed to open the crack (Figure 4-12). This can describe the distinctive load-strain response of sample with 80 mm FRP width (Figure 4-11b). For the sample with W_{frp}=80 mm, more space is provided through the FRP width for micro-cracks to propagate. However, for the samples with shorter W_{frp}, the length of micro-cracks is shorter and their number is less (Figure 4-12).

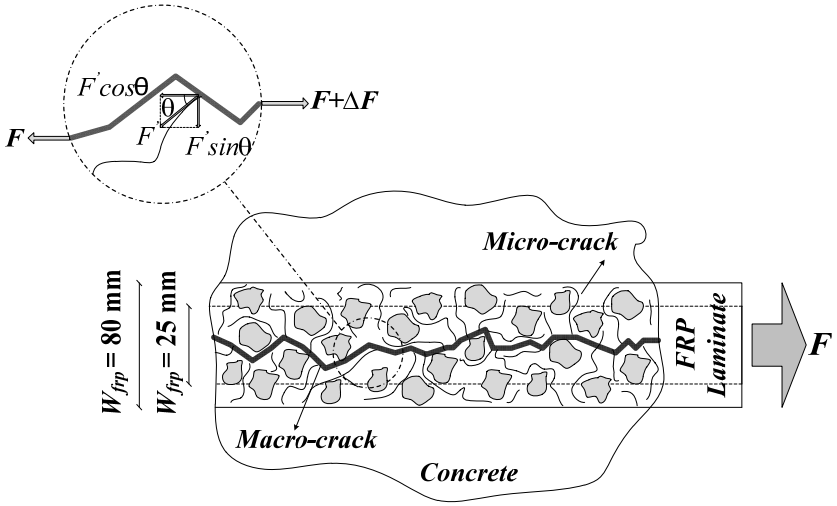

Figure 4-12. Mechanism of interfacial crack propagation.

The effect of FRP-to-concrete width ratio on the global slip at maximum and ultimate load stages is shown in Figure 4-13a. The slip corresponding to the maximum load and ultimate load decreases by higher value of w_r. It indicates that ductility of the joint decreases for wider FRPs. Depth of intermediate crack debonding increases with the use of higher FRP-to-concrete width ratio (Figure 4-13b).

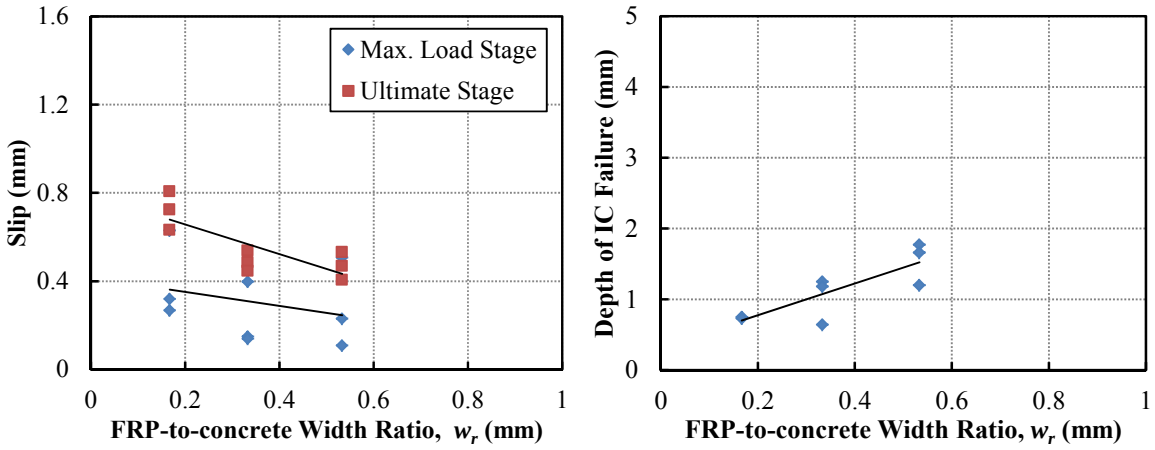

(a) (b)

Figure 4-13. Correlation between FRP-to-concrete width ratio and: (a) the global slip and (b) the depth of IC failure in MSLS tests.

Considering Figure 4-9 and Figure 4-12, the samples show higher initial stiffness for the load-slip curve when the FRP width increases against the concrete width. Micro-cracks have more space to propagate under the wider bondline and when the macro-crack initiates, the possibility to cross micro-cracks on its way is higher. These micro-cracks assist to bind the macro-crack during the loading. Therefore, the bond between wider FRP and concrete substrate is stronger in comparison with the samples with lower w_r.

Based on Figure 4-14, variation in the FRP width does not affect the strain values noticeably at the loaded end at 100%F_{max}. In the bonded joint with W_{frp} = 80 mm, the strain profile shows a large scatter of values near to the loaded end face. It seems that for the samples with higher bonded width, the macro-crack can change direction (refer to the previous section). In addition, in the transverse direction, some parts of the FRP are fully/partially detached while some other parts still bonded to the substrate. Since the strain gauges are placed on the opposite sides of the centre line, one strain gauge can be located on the attached face while the next one is on the fully/partially debonded. Therefore, the readings for two consecutive strain gauges can differ outstandingly.

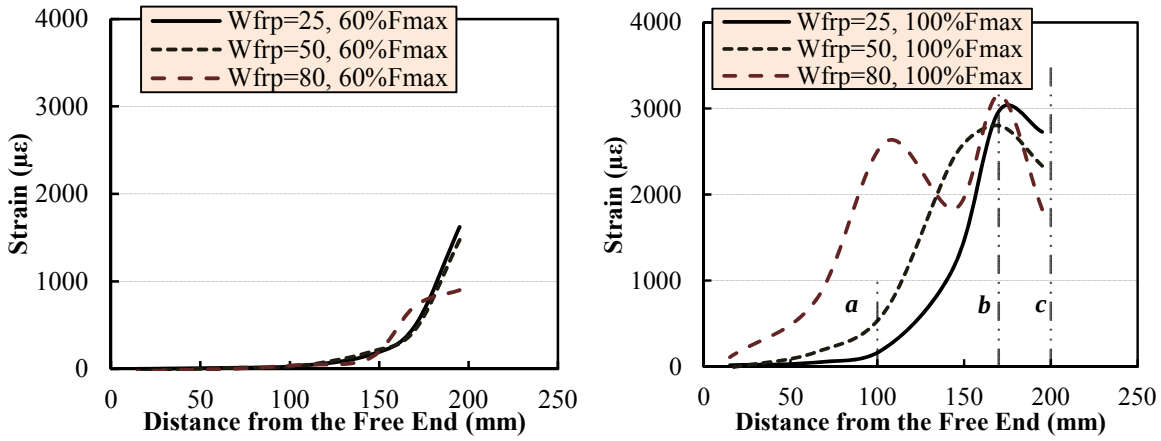

(a) (b)

Figure 4-14. Interfacial strain profile along the bondline at the load levels of (a) 60%F_{max} and (b) 100%F_{max} for different FRP widths.

Figure 4-15 presents the effect of the bonded width on the local slip under 60 and 100% F_{max}. Unlike the strain profile, the local slip follows a smooth increase toward to the loaded end. The effect of the FRP width on the local slip values is small during the initial stages of loading (Figure 4-15a). However close to debonding, with increase in w_r, the local slip increases (Figure 4-15b).

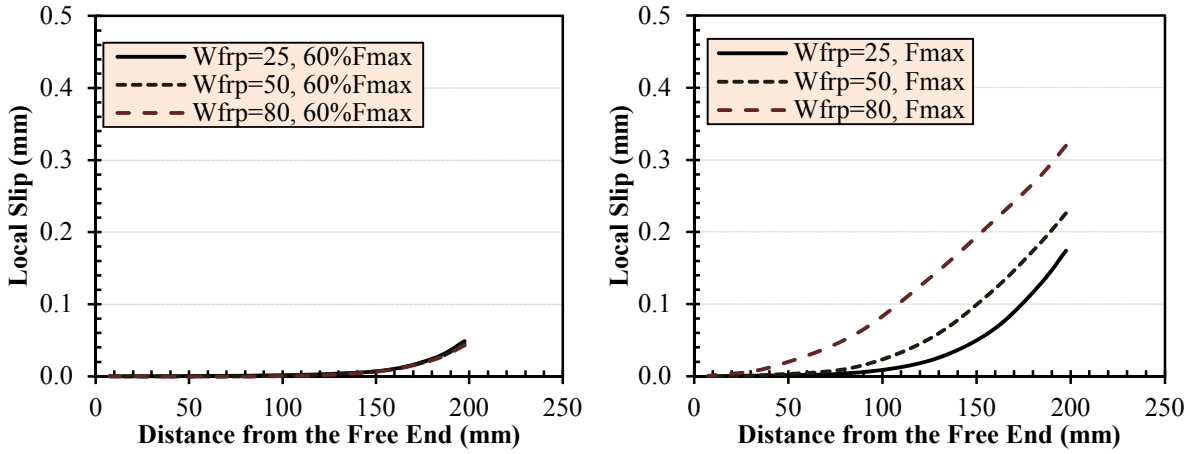

(a) (b)

Figure 4-15. Local slip distribution over the bondline at the load levels of (a) 60%F_{max} and (b) 100%F_{max} for *Series V*.

Local shear stress versus slip is derived based on Eq. 4-4. Figure 4-16 depicts τ-s curves of a point corresponding to 197.5 mm away from loaded end for samples with different FRP width (25, 50 and 80 mm). The maximum shear stress is captured at a location between the

loaded end and the first strain gauge (x = 197.5 mm). The strain at the loaded end was measured based on Eq. 4-5. The shear stress-local slip response depicts more irregular shape at x = 197.5 mm however, toward the free end, the shape and maximum values tend to be consistent.

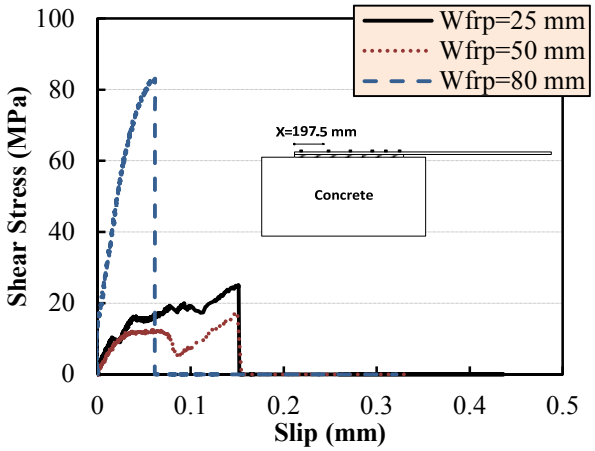

Figure 4-16. Bond stress-slip relationships corresponding to the samples with different FRP widths at the position of x=197.5 mm away from the free end.

4.7. Bondline Thickness

The effect of the bondline thickness on the interface behaviour of the samples processed with different manufacturing techniques is discussed in this section. Failure of the samples are categorised in different modes, named; concrete debonding (CD), near end failure (NEF), light-fibre-tear failure (LFT), and thin-layer cohesive failure (TLC).

Based on concrete debonding (CD) failure mode, which was observed in all of the samples, the fracture occurs inside a thin layer of the substrate under the bonded region. In some cases, a shear crack appeared in the front side of the concrete blocks. This failure mode is called near end failure (NEF) through the research. For some samples very small amount of fibre is peeled off from the laminate which is called light-fibre-tear failure (LFT) based on ASTM Standard D5573-99 (2012). LFT refers to the failure within the FRP adherend, near the surface. In this type of failure a thin layer of the FRP resin matrix is transferred from the adherend and remained on the adhesive. In addition, the thin-layer cohesive failure is named as TLC (ASTM Standard D5573-99 2012).

4.7.1. Pultruded Samples

Table 4-4 summarises the experimental results of the samples with different bondline thicknesses in *Series IV* of *Phase 1*. In this table, the slip when the load reaches its maximum value is presented. The ultimate global slip, S_u, is assumed as the slip after which the load response of the joint drops suddenly. Since the slip is measured by a modified test set-up at the loaded end side, the slip here refers to the global relative displacement of the FRP to the concrete. For all of the samples the most dominant failure pattern was debonding of a thin layer of concrete beneath the bondline which here is called concrete debonding (CD). The bondline concept in the present study is considered as the total thickness of CFRP laminate and the adhesive.

Table 4-4. Summary of FRP-concrete bonding tests in *Series IV* of *Phase 1*.

Sample ID	Max. Load, F_{max} *(kN)*	Ultimate Load, F_u *(kN)*	Slip Corresponding to Max. Load, S_{max} *(mm)*	Ultimate Slip, S_u *(mm)*
P7.1	32.1	32.0	0.69	0.71
P7.2	290	28.9	0.21	0.38
P7.3	30.4	28.5	0.31	0.84
P8.1	30.6	28.1	0.27	0.49
P8.2	31.5	31.4	0.55	0.56
P8.3	34.4	33.5	0.46	0.46
P9.1	34.4	34.4	0.93	0.93
P9.2	---	---	---	---
P9.3	35.5	35.4	0.76	0.76

The load-global slip relationships of the samples with different bondline thicknesses are presented in Figure 4-17. Load-slip response of the samples is quite similar which indicates the reliability of test results using MSLS test set-ups. The load linearly increases corresponding to the increase in the slip during the initial stage of the curves. Subsequently, the load-slip behaviour becomes plateau during which the micro cracks occurs at the FRP-concrete interface and followed by a rapid boost of slip without noticeable changes in load until failure.

In *Series IV* (Figure 4-17d), the samples with the highest bondline thickness (t_{bl} = 8.13 mm) show a softer behaviour compared with other samples with thinner bondline thickness. However, the post-nonlinear response (the plateau) is the same in all of the samples. Since the strain on FRP for all of the three groups of the samples is almost the same and

considering Hooke's law of elasticity in the elastic range, the distinctive response of the P9.1 and P9.3 specimens attributes to the thickness of the bondline. Nevertheless, the initial soft behaviour of the bond is not desirable. In the strengthening of structures, the aim is that the emerging cracks in the substrate are bound by the strengthening elements and to prevent them from further growth.

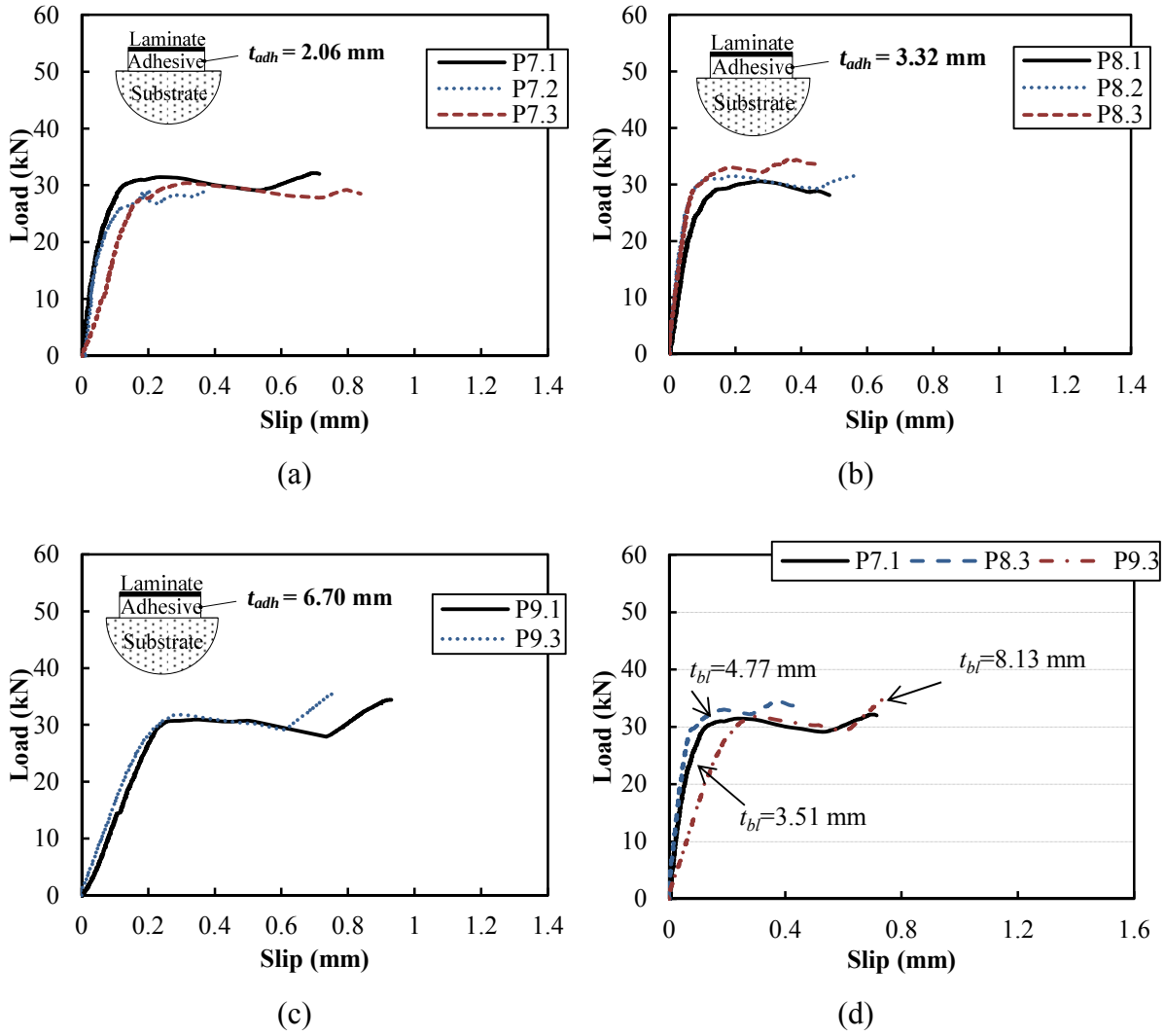

Figure 4-17. Load-global slip response for *Series IV* of experiments.

Load versus strain values of the interface at different locations along the bondline is presented in Figure 4-18 *Series IV*. Similar to the Figure 4-17, load-strain curve at each location consists of three stages: linear, nonlinear (post linear) and plateau (post nonlinear) sections. The load increases sharply with small change in strain values up to 20 kN for all the samples. Following the linear stage, micro-cracks emerge within the interface and the

response becomes nonlinear. After macro-crack initiation, the load-strain curve tends to be plateau with no noticeable change in applied load while the strain increases.

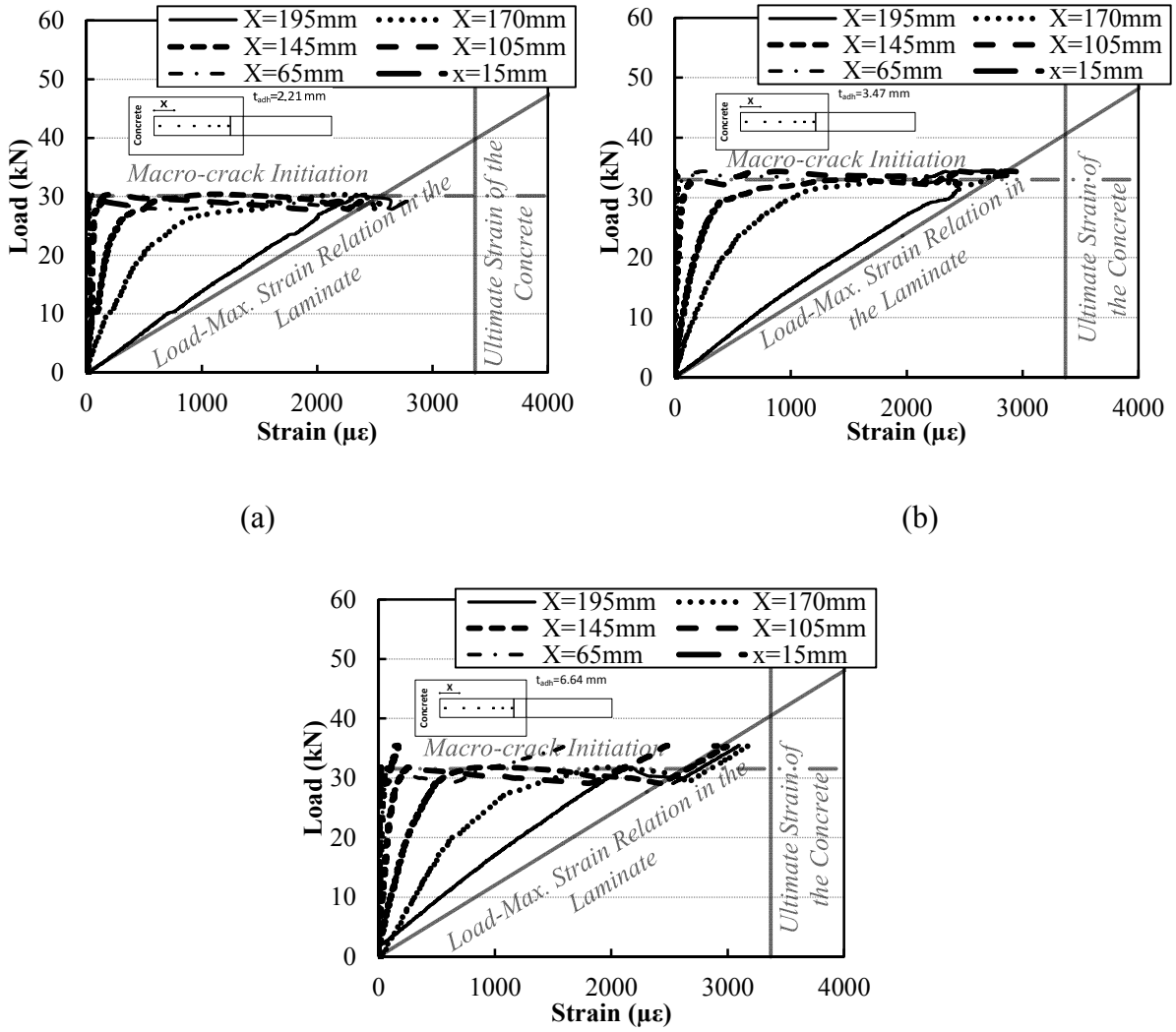

Figure 4-18. Applied load vs strain value along the bondline: (a) P7.3: t_{bl}=3.64 (b) P8.3: t_{bl}=4.77, (c) P9.3: t_{bl}=8.13.

A different pattern has been observed for the first strain gauge at the loaded end in all of the samples. The load versus strain shows a linear behaviour until the formation of macro-crack after which the response follows a plateau. The load-strain response of the interface at 195 mm away from the free end is very close to the maximum strain values in the laminate corresponding to the applied load. The same trend was observed in the previous works (Seracino 2001). It indicates that most of the applied load is carried by the laminate near the

loaded end and is distributed between adherends (laminate and concrete) and adhesive over the bond toward the free end of the FRP.

The strain gauges close to the free end experience a small amount of strain even at the final stages of loading while the FRP is detached from the substrate abruptly. It shows that the FRP length utilised here is sufficiently longer than the effective bond length. As mentioned in the previous section, the effective bond length (EBL) was found between 100 to 160 mm dependent on the bondline thickness. The ultimate strain of the concrete (ε_{cu} = 3370 με) is highlighted in Figure 4-18 for each sample. Though after failure of the joint a thin layer of concrete is attached to the laminate, the interfacial strain in the samples does not exceed the value of ultimate strain of the concrete, ε_{cu} (Figure 4-18). Therefore, the application of concrete behaviour without considering the behaviour of the other elements (adhesive and laminate) in the investigation of the interfacial response, overestimates the bond strength. The load at which the macro-crack initiates through the bondline is shown with long dash dot dot lines in Figure 4-18.

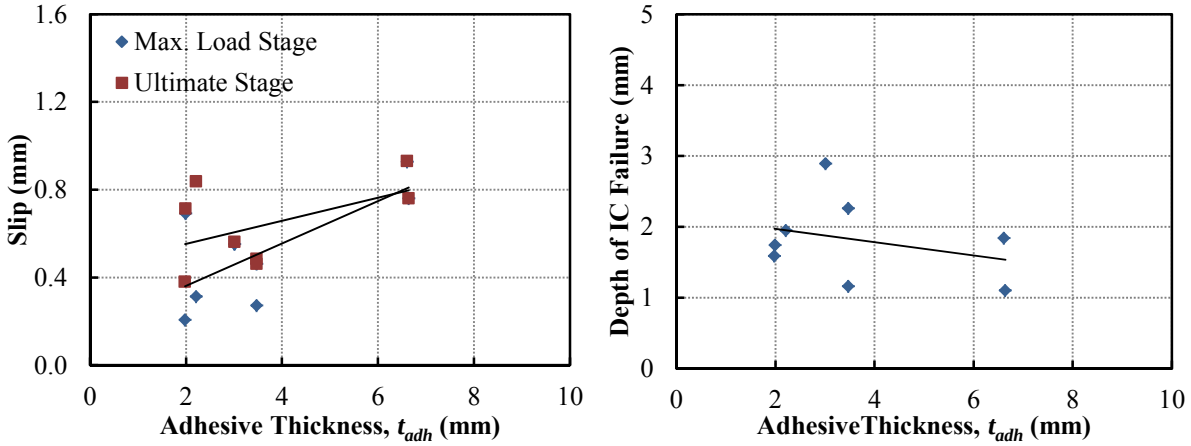

Figure 4-19. The effect of the adhesive thickness on (a) the global slip and (b) the depth of IC failure.

The correlation between adhesive thickness (t_{adh}) and the global slip (S) at the loaded end for both maximum and ultimate load stages is shown in Figure 4-19a. As the adhesive thickness increases, the slip at both maximum and ultimate load stages increases. The average slip values at the maximum load level are 0.40, 0.43 and 0.84 respectively for samples with average adhesive thickness of 2.06, 3.32 and 6.54 mm. It means 6% and 96.8%increase of slip, respectively. Therefore, the higher the bondline thickness, the more ductile the response is in MSLS test. This trend is more noticeable for samples with the greater thickness. The

reason for this type of behaviour can be explained based on the strain profile (Figure 4-21) which is presented in the following and the depth of *IC* failure (Figure 4-19b). According to Figure 4-21, the area under the strain profile for samples with thicker bond is higher, hence the slip is more. Unlike the global slip, the depth of intermediate crack *(IC)* debonding decreases with the adhesive thickness.

In Figure 4-20a, the relationship between the interfacial strength and the bondline thickness obtained from the experiments is shown. The maximum load carrying capacity of the joint increases by application of thicker bondline. However, after a specific thickness, the load capacity does not change noticeably. These results in conjunction with the outcomes of the MSLS tests on pre-pregs and VARI processed samples which are presented in the following section distinctly support the concept of the existence of an optimum bondline thickness for different kinds of FRP processing techniques (pultruded, HVBO and VARI).

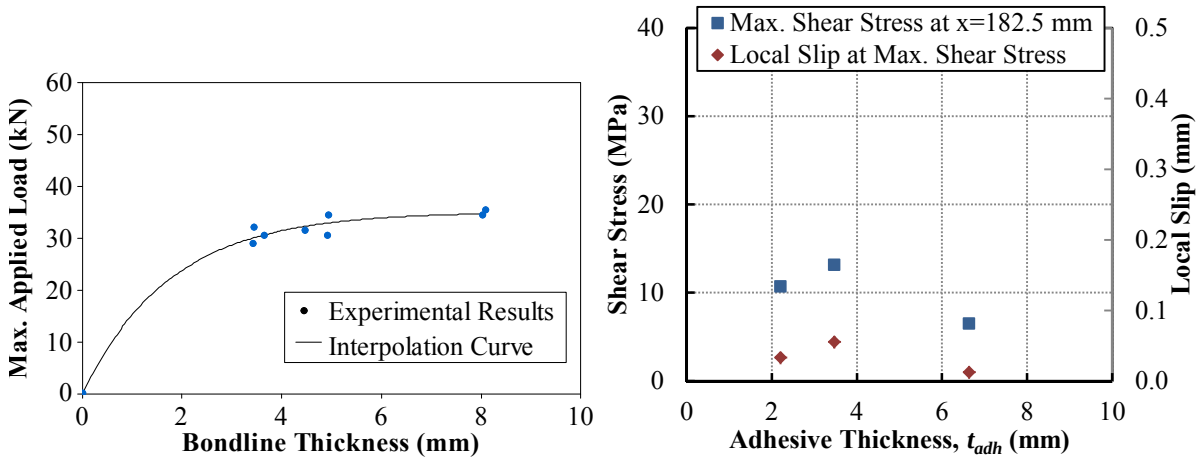

(a) (b)

Figure 4-20. (a) Maximum debonding load vs the bondline thickness, (b) the effect of the adhesive thickness on the shear stress and the local slip.

Further considering the effect of the adhesive thickness on the maximum shear stress, Figure 4-20b indicates that for a bondline thickness greater than almost 5 mm the maximum shear stress decreases. Therefore, the concept of optimum bondline thickness is advisable to be considered in studying the interfacial behaviour of FRP-to-concrete joints. The same factor was recently proposed to study the influence of adhesive thickness on the strength between metals and epoxy in lap shear tests (Grant et al. 2009; Jarry and Shenoi 2006; Kin Loch and Shaw 1981; Taib et al. 2006; Xu and Wei 2012).

The nonlinear regression shows an exponential correlation between the maximum applied load (F_{max}) and bondline thickness (t_{bl}) in MSLS tests. It can be determined based on the experimental results using an asymptotic nonlinear regression model as follows:

$$F_{\max} = \alpha \cdot (1 - e^{-\beta \cdot t_{bl}}) \qquad 4\text{-}6$$

where α and β are constants and in this case obtained as 35 and 0.567, respectively. According to Figure 4-20a and Eq. 4-6, the optimum adhesive thickness for the current pultruded FRP laminates is about 4 mm. Therefore, this thickness was adopted for the samples in *Series V*.

With a thicker bondline, the risk of flaw in the adhesive is higher which would result in stress concentrations. Adhesives are designed to cure in thin layer and application of thick layers can change physical properties of the epoxy after the cure time. From the chemical point of view, thicker bond can lead to more polymerization shrinkage and therefore, internal stresses. In addition, to explain the effects of bondline thickness on the fracture response of the joint, the stress states need to be considered. In a thin layer adhesive, the plane stress governs the response while the plane strain favours thick adhesives. This transition between stress states can result in the optimum bondline thickness in the FRP-to-concrete bonded joints.

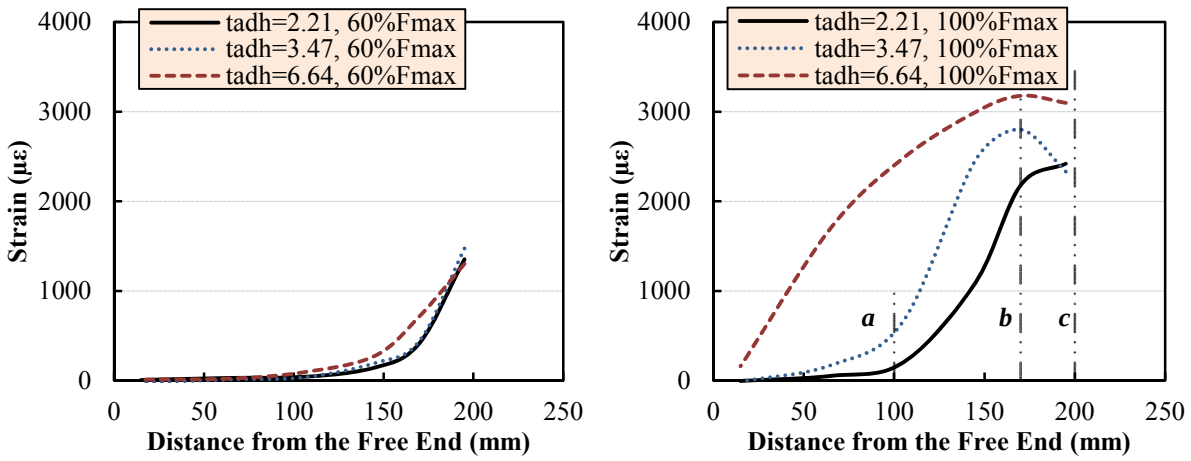

(a) (b)

Figure 4-21. Interfacial strain profile along the bondline at the load levels of (a) 60%F_{max} and (b) 100%F_{max} for different adhesive thicknesses.

The strain profile of the samples with various bondline thicknesses corresponding to different load levels is shown in Figure 4-21. In order to investigate the behaviour of the interface before and after the initiation of macro-crack, the load levels equal to 60% and 100% of F_{max} are chosen, respectively. Samples with different adhesive thicknesses follow the same pattern for strain at the load level of 60%*Fmax*. The strain values are the same for samples P7.3 and P8.3. Sample with t_{adh} = 6.64 (P9.3) mm experiences a slightly higher strain at the distance of x = 100 to 170 mm. However, strain of P9.3 fits to the strain values of the other samples for x greater than 170 mm.

As explained previously, the sample with the thickest bondline shows a softer behaviour in terms of the initial slope in the load-global slip curve (Figure 4-17) and lower depth of IC failure (Figure 4-19b) compared with two other groups with thinner bond. The strain values at the distance of 170 mm away from the free end of FRP for the sample with t_{adh} = 2.21 and 6.64 mm are 418.81 and 719.05 με while the local slip values at this point are 0.0169 and 0.0268 mm (Figure 4-22), respectively. This means 72% and 59% differences in local strain and slip respectively. Since the local slip was not available at the position of strain gauges (e.g. x = 170 mm), it was obtained from interpolation of the local slip values at points of x = 157.5 and 182.5 mm.

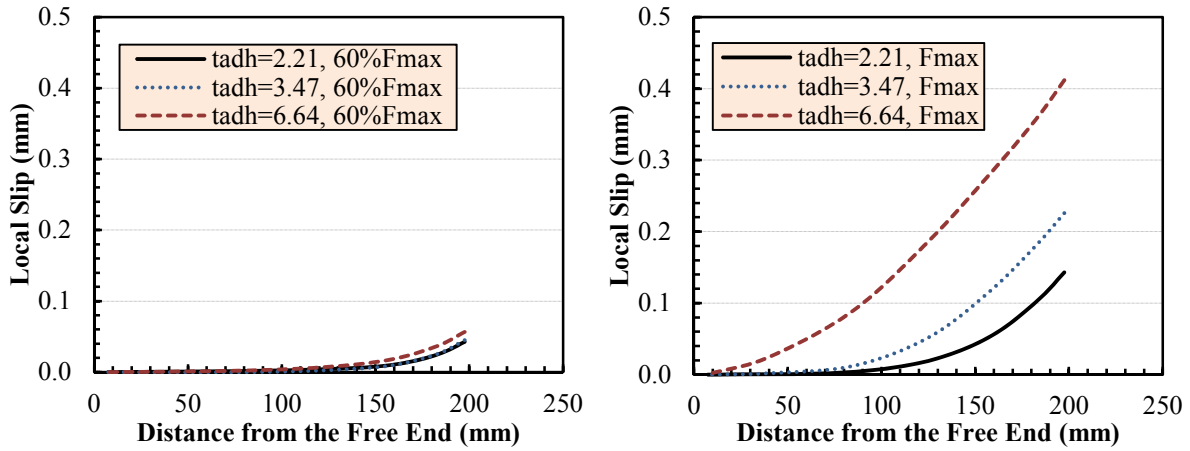

Figure 4-22. Local slip distribution over the bondline at the load levels of (a) 60%F_{max} and (b) 100%F_{max} for samples in *Series IV*.

When the applied load increases, the strain profile tends to become plateau and keep this response till the maximum applied load is reached. Apparently, the sample with the thickest bond shows the highest values of strain (Figure 4-21b). The strain values at the level of F_{max}

at x =170 mm are 2180.04 and 3178.19 µs for samples with t_{adh} = 2.21 and 6.64 mm and local slips are 0.0772 and 0.3186 mm, respectively. The increase in strain and slip are 46% and 312% compared to samples with thinner and thickest bond.

The strain profile of the samples along the bonded length consists of three sections with the same trend. The boundaries of these sections are defined by the sudden change in the slope (lines a, b and c in Figure 4-21b). However, this is not valid for the samples with the highest thickness which can imply the transition state from plane stress to the plane strain explained previously. Prior to the line *a*, the strain increases with a gentle slope while at the point *a* changes to a steep slope until the point *b*. From point *b* to the end of the profile, the slope again changes. Unlike the strain profile, the local slip follows a smooth increase toward to the loaded end. The effect of the bondline thickness on the local slip values is small during the initial stages of loading (Figure 4-22a). However close to debonding, with increase in the adhesive thickness, the local slip increases (Figure 4-22b).

Considering Figure 4-23, the maximum shear stress does not increase after a certain amount of the bond thickness. The sample P8.3 (optimum bondline thickness) shows higher maximum shear stresses in comparison with the sample with the highest bond thickness (P9.3). In addition, the slip corresponding to the maximum shear stress is quite similar for the samples.

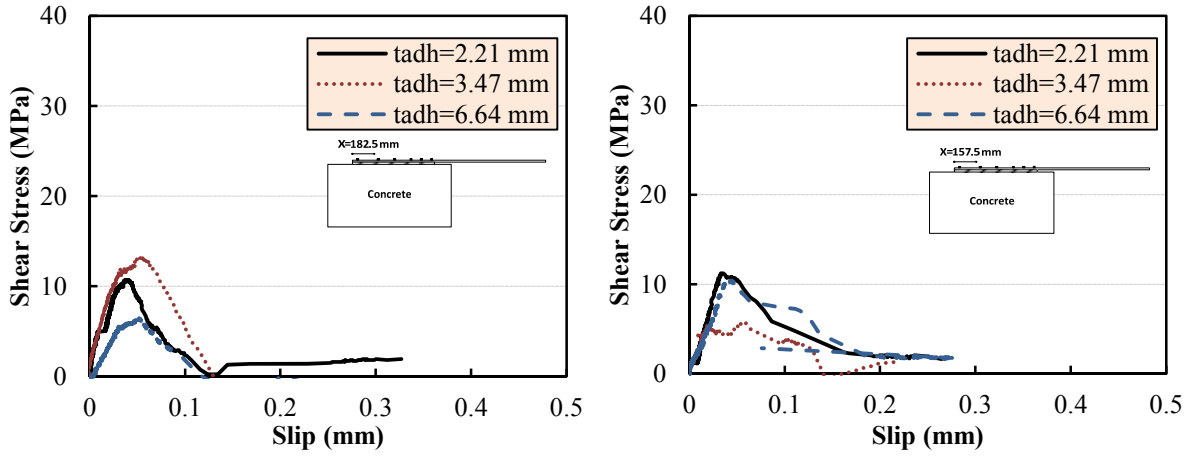

(a) (b)

Figure 4-23. Bond stress-slip relationships corresponding to different bondline thicknesses at the position of (a) x=182.5 mm and (b) x=157.5 mm away from the free end.

4.7.2. Wet Lay-up Samples

Wet lay-up samples with two different bondline thicknesses were tested using 4 and 8 layers of CFRP plies. MSLS test results are presented in Table 4-5. In addition, Figure 4-24a illustrates the load versus global slip at the loaded end for all of the samples. Although the load-slip pattern is the same for samples with 4 and 8 CFRP layers, the maximum applied load is almost doubled for the samples with 8 layers of CFRP. However, the global slip of the samples corresponding to the maximum and ultimate load stages decreases with the increase in CFRP layers (Figure 4-24b). It distinctly indicates that with more number of CFRP plies, the joint tends to be more brittle while the load carrying capacity increases.

Table 4-5. Modified single lap shear test results of wet lay-up samples.

Sample ID	Max. Load, F_{max} *(kN)*	Ultimate Load, F_u *(kN)*	Slip Corresponding to Max. Load, S_{max} *(mm)*	Ultimate Slip, S_u *(mm)*
W1.1	22.7	20.7	0.44	1.14
W1.2	26.0	23.3	0.55	0.99
W1.3	23.4	23.3	1.07	1.07
W2.1	35.7	33.4	0.52	0.78
W2.2	40.0	38.8	0.53	0.63
W2.3	34.1	30.4	0.31	0.52

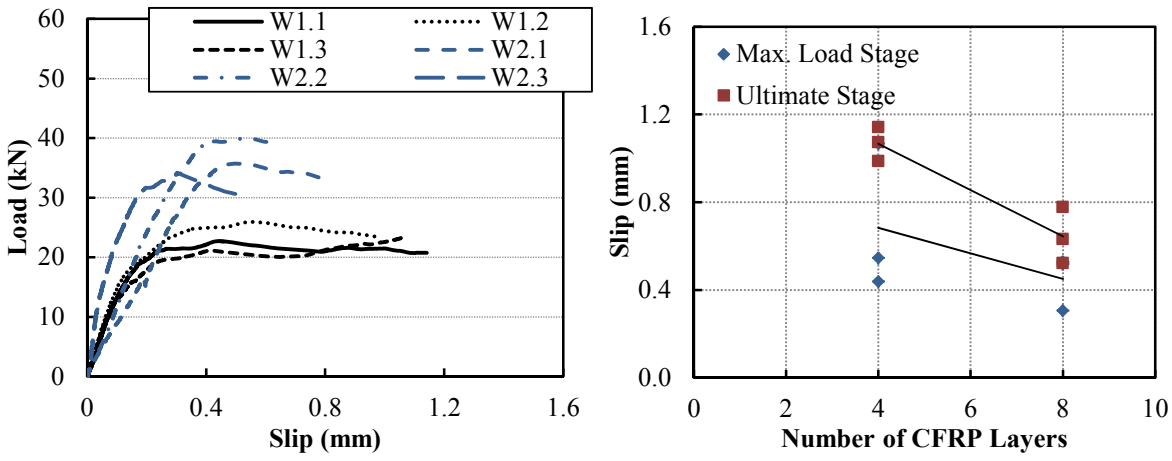

(a) (b)

Figure 4-24. (a) Load-global slip response and (b) normalized maximum applied load vs CFRP layers for wet lay-up samples.

For further investigation, the strain profile, local bond-slip relationship and also distribution of the local slip of the joints are studied. Wet lay-up samples experience high strain values during loading (Figure 4-25). The maximum strain values occur at the loaded end. Before the maximum load is reached, the strain decreases with a rapid gradient close to the loaded end (x between 170 and 200 mm) while the reduction rate is slower after x = 170mm. During the final stages of loading, a macro-crack propagates along the bonded length which ultimately leads to the failure of the joint.

Based on the strain profiles, it is clear that the effective bond length for samples with more CFRP layers is longer which is discussed in detail in section 4.5. This indicates that the effective bond length may be dependent to the bondline thickness of the joint.

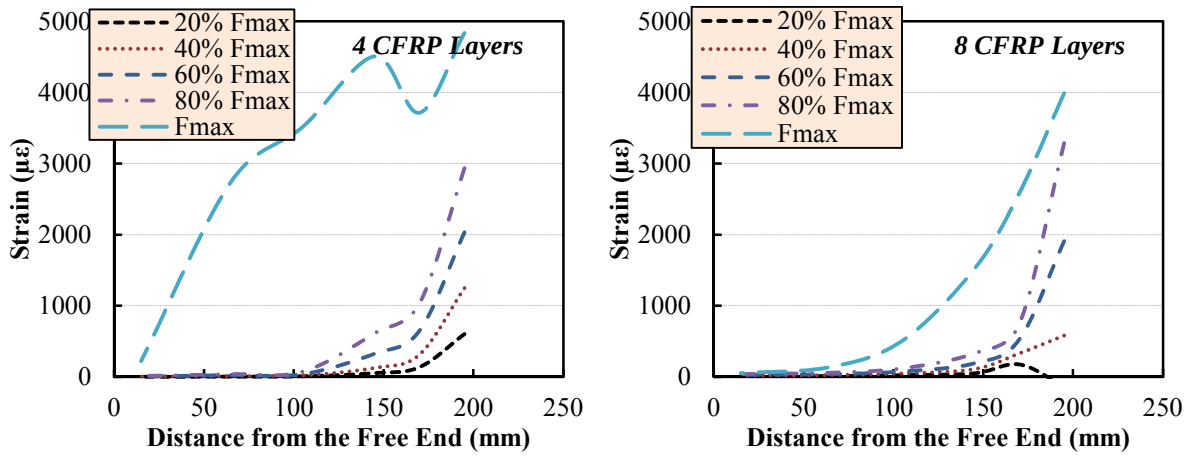

(a) (b)

Figure 4-25. Strain profile of the wet lay-up samples along the FRP bonded length.

Figure 4-26a and b illustrates the local bond-slip relationship for the samples with 4 and 8 layers of CFRP, respectively. Maximum shear stress of the interface in sample W2.3 with 8 layers of CFRP is 26.5 MPa while this is 9.8 MPa in W1.3. It indicates that the fracture energy in the samples with more CFRP plies is higher. The local slip profile along the bonded length is more stable in comparison to the shear stress-slip profile (Figure 4-26c and d). The slip has the maximum value at the loaded end and gradually decreases toward the free end of the FRP. In addition, the profile shape is almost similar for both samples at different loading levels. Prior to the maximum applied load, the sections between x = 0 and 85 mm do not experience any local slip.

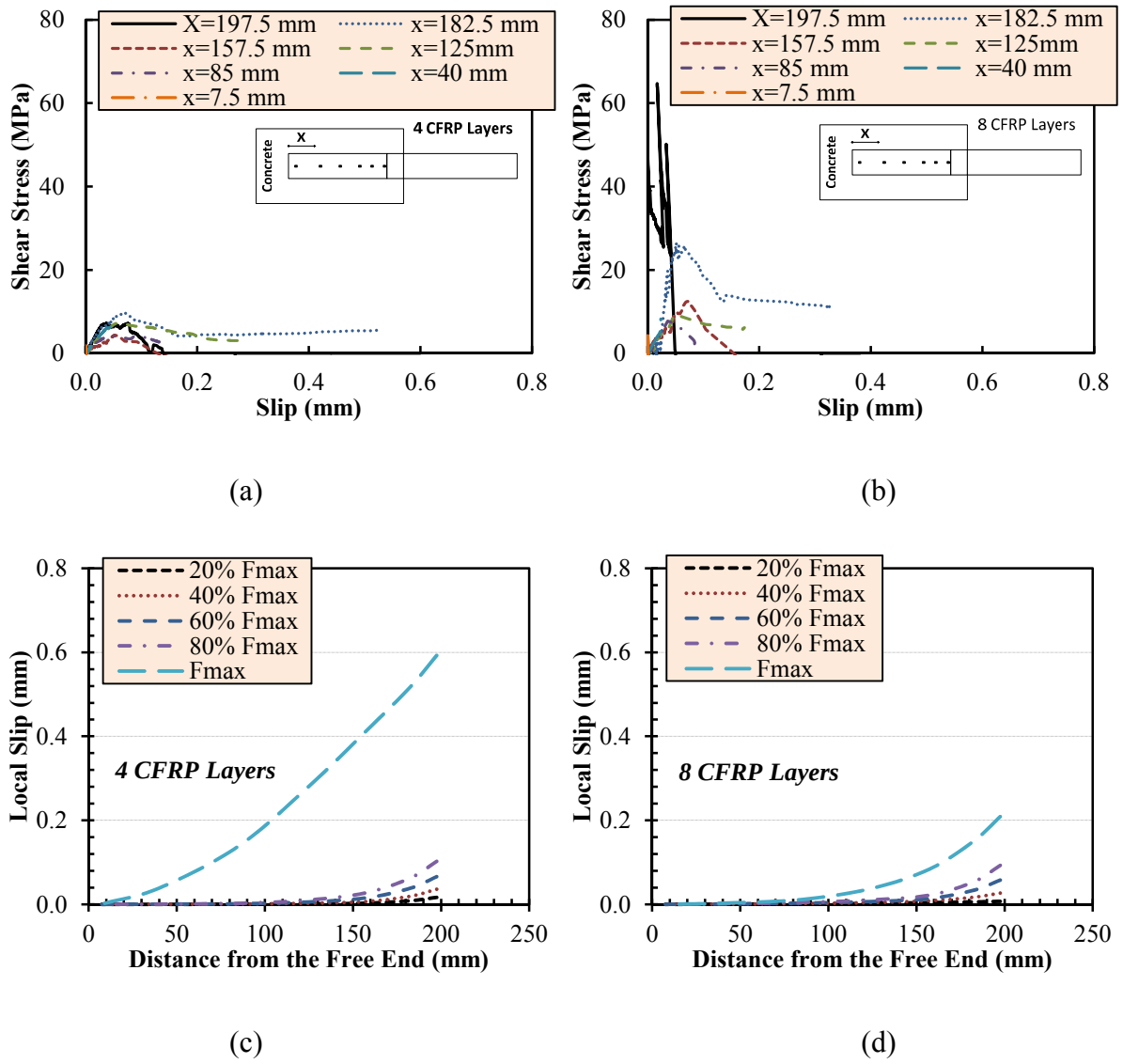

Figure 4-26. (a and b) Bond-local slip relationship and (c and d) local slip distribution of the wet lay-up samples.

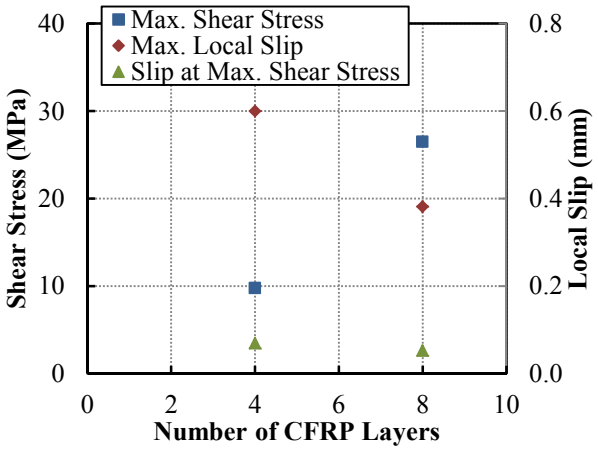

Figure 4-27. Effect of variation in number of CFRP layers on shear stress and local slip.

The effect of the number of CFRP layers on the maximum shear stress, the maximum local slip and also the local slip corresponding to the maximum shear stress is plotted in Figure 4-27. Despite the increase of the maximum shear stress values by increase in CFRP layers, the local slip decreases with use of more carbon layers. A similar response was observed regarding the load-global slip relationship. Therefore, it can be concluded that when the strength criteria governs the design for the strengthening of reinforced concrete structures, increase in the bondline thickness may lead to higher load carrying capacity. However in case of ductility, higher thicknesses lead to more brittle adhesively bonded joints using wet lay-up manufacturing techniques.

Table 4-6. MSLS test results of HVBO samples.

Sample ID	Max. Load, F_{max} (kN)	Ultimate Load, F_u (kN)	Failure Mode
SC1-2R	11.6	10.3	CD
SC2-4R	15.3	14.8	CD
SC-1.1	11.0	10.7	CD
SC-1.2	16.3	14.7	CD, NEF
SC-1.3	6.4	4.8	CD
SC-2.1	21.7	21.6	CD, NEF
SC-2.2	12.8	9.8	CD, NEF
SC-2.3	15.1	14.9	CD
SC-3.1	20.9	17.8	CD
SC-3.2	19.3	18.4	CD, NEF
SC-3.3	11.5	11.5	CD, NEF

4.7.3. HVBO Samples

The results of the single lap shear tests for the specimens processed with the heated vacuum bag only (HVBO) technique are reported in Table 4-6. Since the maximum load of SC-1.3 is much lower than the samples with the same configuration, in the analysis, result of this specimen is ignored.

The typical relationship between the load versus slip for HVBO pre-impregnated samples is presented in Figure 4-28a. The initial stiffness of the load-slip curve is similar for samples consisting of 4 and 8 layers of the film adhesive while samples with 2 film adhesive layers show a distinctive behaviour. The load carrying capacity of the joint increases with the application of higher bondline thicknesses. However, considering the mean value of the maximum applied load for the samples of group SC-2 and SC-1, it can be seen that the

maximum load of the samples with 4 layers of the film adhesives is almost the same as the samples with 8 layers of the film adhesives. In addition, if a comparison is made between the slip of the samples at the level of the maximum and the ultimate applied load, the laminates with 4 layers of resin film show higher slip values than SC-3 group (Figure 4-28b). These facts imply that, like pultruded samples, by increasing the bond thickness a higher load may not be achieved and there is an optimum thickness through which the bond characteristics are constant. It can be attributed to this phenomenon that by increasing the bondline thickness, the thin plate theory concept no longer governs the interfacial stress distribution. Nonlinear analysis of the results (Figure 4-28c) show that Eq. 4-6 is applicable to the HVBO samples with α and β equal to 17.25 and 0.743, respectively.

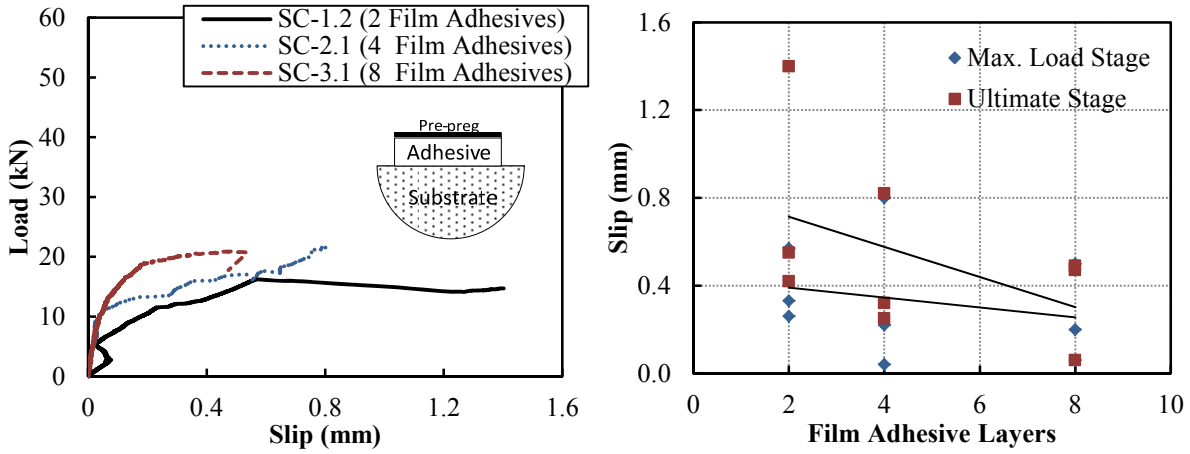

(a) (b)

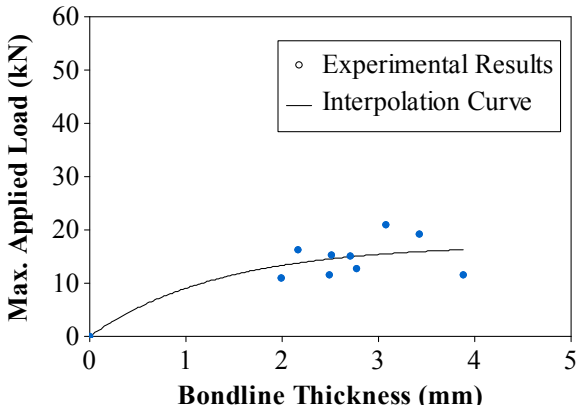

(c)

Figure 4-28. (a) Load vs global slip profile, (b) correlation between the film adhesive layer and slip, and (c) correlation between the bondline thickness and the maximum applied load for the samples processed with HVBO.

Figure 4-29 shows the failure pattern of the samples with different bondline thicknesses. Failure occurred due to the detachment of a thin layer of the concrete (almost 1 mm) under the bonded region. The profiles of the pre-preg laminates after the experiments showed that the film adhesive could penetrate the voids on the surface of the concrete during the cure time. The melted resin film was penetrated well into the voids on the surface of the concrete and contributed to the formation of a sufficient bond between FRP and concrete.

(a) (b) (c)

Figure 4-29. Failure mode of the samples processed with HVBO (a) SC-13, (b) SC-2.3, and (c) SC-3.3.

4.7.4. VARI Samples

For the vacuum assisted resin infused (VARI) samples, GFRP plates were inserted into the bondline to increase the thickness without any contribution in the load carrying mechanism. Figure 4-30 shows the relation between the load and the global slip of the bonded joints with different bondline thicknesses. The bondline thickness consists of the total thickness of the fibres (glass and carbon) and the adhesive;

$$t_{bl} = t_{cfib} + t_{gfib} + t_{adh} \qquad 4\text{-}7$$

where t_{cfib}, t_{gfib}, and t_{adh} are carbon fibre, glass fibre and the adhesive thicknesses, respectively. The bondline thickness, t_{bl}, which is shown in Figure 4-30, is the average value of the bondline thickness of three identical samples in each group. The global slip is the relative displacement of the FRP plate to the substrate at the loaded end. The slip was

monitored by the modified single lap shear test set-up. According to this figure, the load-slip behaviour for the samples follows a similar pattern. During the tests, sample SF-B-2.3 failed prior to reaching the ultimate load carrying capacity in the SLS test and is not presented here.

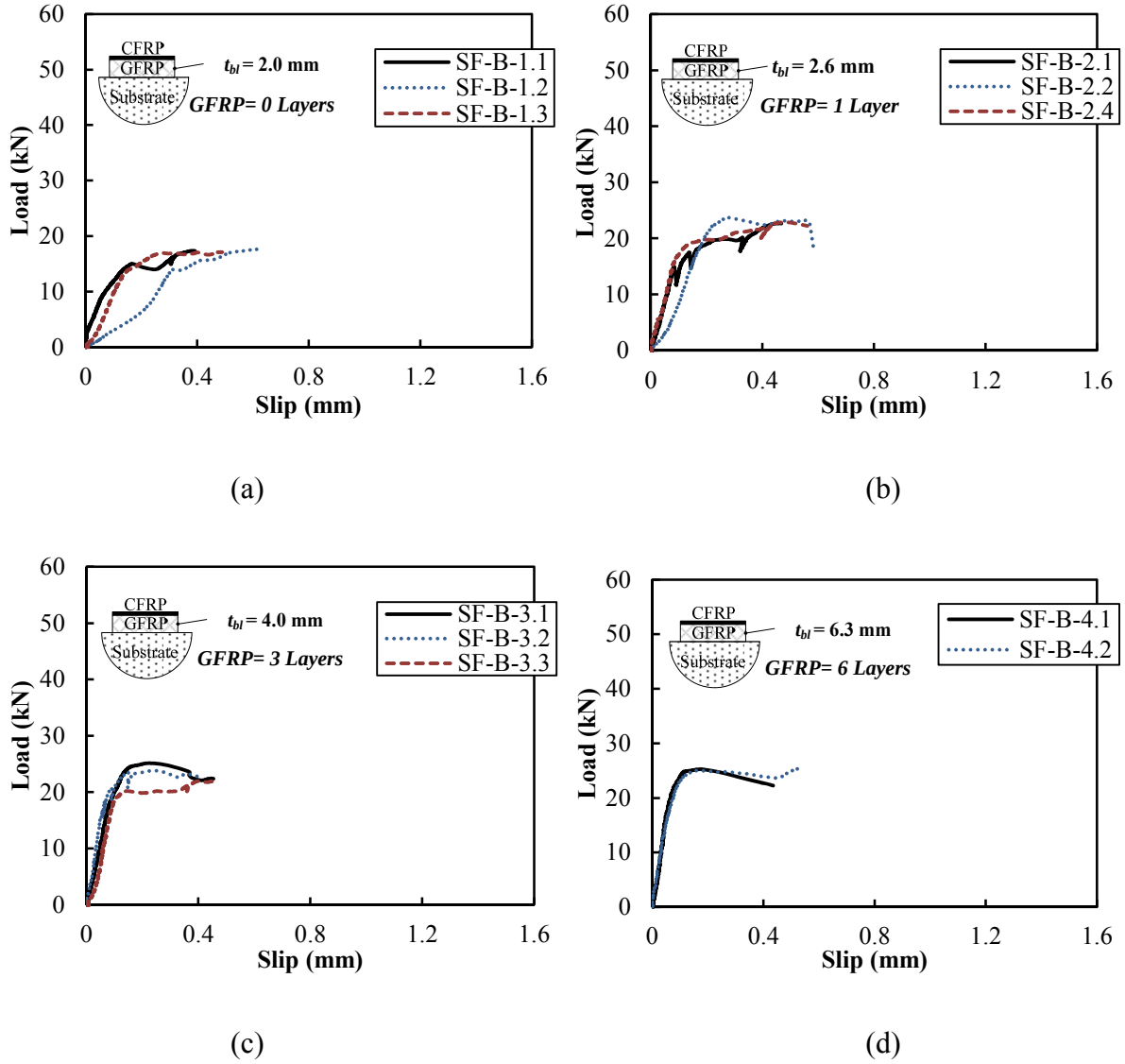

Figure 4-30. Load vs slip curve for the samples with (a) 0 GFRP layers, (b) 1 GFRP layer, (c) 3 GFRP layers, and (d) 6 GFRP layers.

Samples with 0 and 1 GFRP layers, SF-B-1.2 (Figure 4-30a) and SF-B-2.2 (Figure 4-30b) show different pattern in terms of the initial stiffness. This response is different for SF-B-3 and SF-B-4 groups (Figure 4-30c and d). As the bondline thickness increases in SF-B-3 and SF-B-4 groups, the specimens show the same initial stiffness. Nevertheless after the maximum load, the behaviour turns out to be quite similar for all of the samples. As it will be

discussed in section 4.8, the surface preparation has great influence on the load-slip curve pattern in the SLS tests.

The surface preparation may lead to a different initial stiffness in the load-slip curves while the maximum load seems to be unaffected. Therefore, the distinctive response of SF-B-1.2 and SF-B-2.2, during the initial loading, may attribute to the surface preparation effect. In samples of SF-B-3 and 4 groups, thicker bondline is applied and the effect of the concrete surface is negligible. In addition considering Figure 4-31, the depth of the cohesive failure is more for specimens with thicker bondline. Therefore, when the bondline thickness decreases (i.e. in SF-B-1 and 2 groups), the effect of the concrete surface condition on the interfacial behaviour increases.

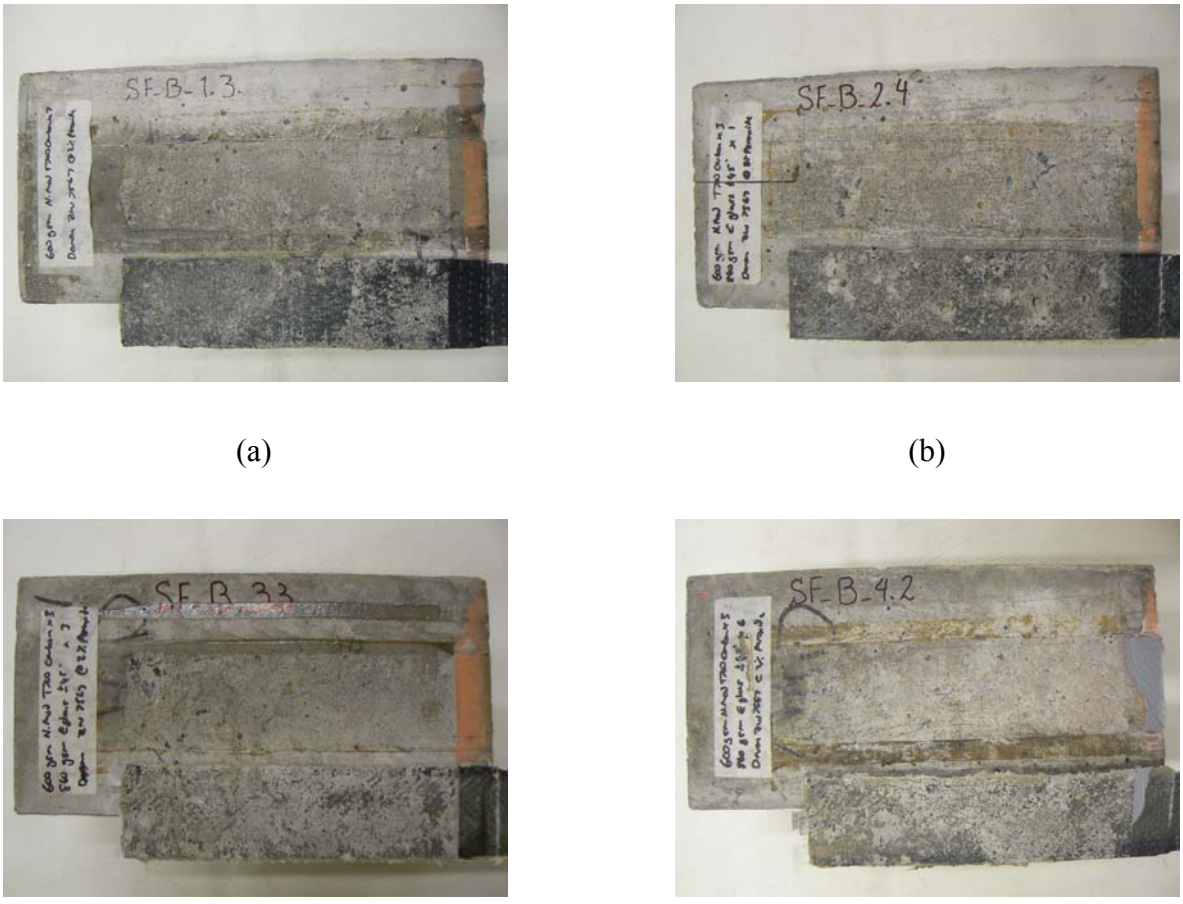

(a) (b)

(c) (d)

Figure 4-31. Fractured interface of the specimens with, (a) 0 GFRP layers, (b) 1 GFRP layer, (c) 3 GFRP layers and (d) 6 GFRP layers.

Similar to the pultruded samples, the total load-slip response of the bonded joints can be categorized into three different stages. During the first stage, increase in the load is

accompanied with a small increase in the global slip. Load-slip curves show almost linear behaviour with the maximum slip of 0.07 to 0.1 mm. After this phase, since micro-cracking occurs in the interface between concrete and the FRP, the response becomes nonlinear until the propagation of the macro-crack. The slip corresponding to the maximum applied load is between 0.2 to 0.5 mm. The nonlinearity of the bond continues until the macro-crack occurs in the interface and the slip increases rapidly while the load carrying capacity remains constant. The ultimate slip varies between 0.4 to 0.6 mm for samples with different thicknesses. Finally when the macro-crack propagates at a certain length, debonding occurs in the interface with an explosive sound. The maximum global slip at the loaded end, S_{max}, is less than 0.6 mm (Table 4-7). This small amount of value could properly be captured using the modified single lap shear test set-ups.

Table 4-7. Modified single lap shear test results of VARI samples.

Specimen ID	Max. Load, $(F_{max})_{exp.}$, *(kN)*	Ultimate Load, F_u, *(kN)*	Slip Corresponding to Max. Load, S_{max}, *(mm)*	Ultimate Slip, S_u, *(mm)*
SF-B-1.1	17.4	17.3	0.38	0.39
SF-B-1.2	17.7	17.6	0.60	0.61
SF-B-1.3	17.1	17.1	0.49	0.49
SF-B-2.1	22.7	22.6	0.45	0.47
SF-B-2.2	23.7	18.3	0.27	0.58
SF-B-2.4	22.8	22.2	0.48	0.56
SF-B-3.1	25.1	22.4	0.22	0.45
SF-B-3.2	23.8	22.6	0.24	0.41
SF-B-3.3	21.9	21.9	0.40	0.46
SF-B-4.1	25.3	22.2	0.17	0.44
SF-B-4.2	25.4	25.3	0.53	0.53

A comparison was made between the load-slip curves of the samples with different bondline thicknesses (Figure 4-32). Samples with no and one glass fibre (i.e. samples in group SF-B-1 and SF-B-2) show a soft behaviour during the initial steps of the loading. Since one of the major purposes in the strengthening of the concrete members is binding the emerged cracks on the substrate and preventing them from further growth, the higher the initial stiffness of the strengthening method, the better. Therefore, the samples with no and one GFRP layer cannot sufficiently lock the cracks during the loading while the other samples with 3 and 6 layers of GFRP have higher initial stiffness.

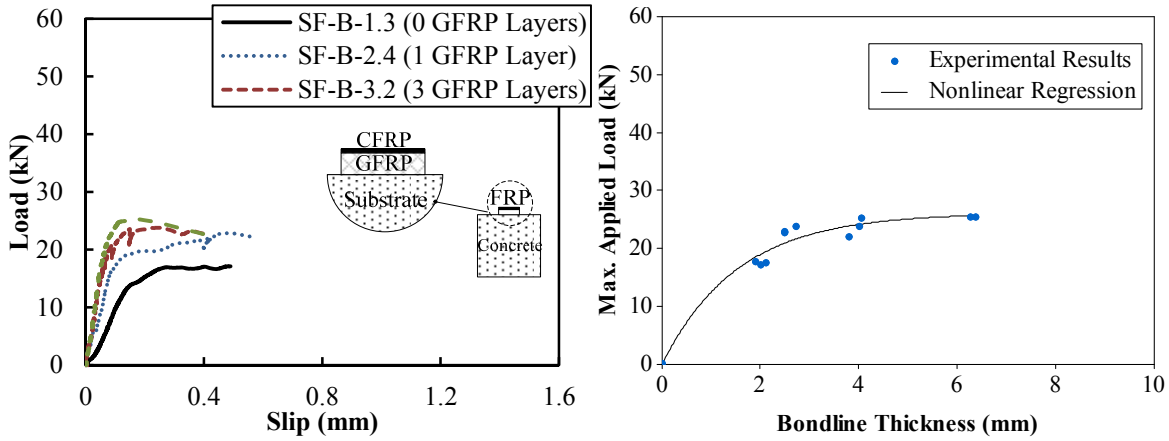

Figure 4-32. (a) Load vs slip curves, and (b) correlation between the maximum applied load and the bondline thickness for VARI samples.

Figure 4-32 shows the correlation between the average bondline thickness and the maximum applied load for the samples processed with vacuum assisted resin infusion. The curve was fitted to the results of MSLS tests by a nonlinear regression analysis. By increasing the bondline thickness, the maximum applied load increases from 17 kN for t_{bl}=2.00 mm up to 24 kN for t_{bl}=2.57 mm (Table 4-7). After this thickness, the load tends to remain constant and any increase in the thickness does not change the maximum load carrying capacity (i.e. samples with 3 or 6 layers of glass fibres). It indicates that the increase in the bondline thickness may not continuously lead to the load carrying capacity enhancement. Similar behaviour was observed for the pultruded and HVBO processed specimens.

In the existing empirical and fracture mechanics models, thicker bondline leads to higher load carrying capacity of the adhesively bonded joints. However, based on the results of the MSLS tests on the pultruded samples and specimens processed by heated vacuum bag only and also the results of this section, there exists an optimum bondline thickness beyond which no increase in the load carrying capacity can be achieved. This concept is necessary to be considered in the design of the members externally bonded with FRP materials. Therefore, the current formulae for determination of the maximum load need to be verified in order to consider the effect of thickness on the bond behaviour.

The optimum bondline thickness for the samples processed by VARI technique is about 5 mm. The correlation between the maximum applied load and the bondline thickness for VARI samples may be expressed by Eq. 4-6. For VARI system, α and β are obtained 26.01 and 0.646, respectively.

Results indicate that using thicker bondline leads to the reduction in the global slip (Figure 4-33a) and slightly increase the depth of intermediate crack (*IC*) debonding (Figure 4-33b). When the bondline thickness increases, deeper surfaces of the concrete under the FRP get involved in the interfacial stress transferring. The depth of IC debonding, attached to the FRP plates after the tests, increases for samples with 0 to 6 GFRP plates. Consequently, the slip at the maximum load stage decreases which leads to more brittle response of the joints. Contrary, for pultruded samples, thicker bondline leads to higher slip and lower depth of IC debonding. Therefore for design purposes, when a ductile behaviour is expected from the FRP-strengthened system, thinner bondline may be more appropriate for VARI technique while thicker bondline can be used for pultruded plates.

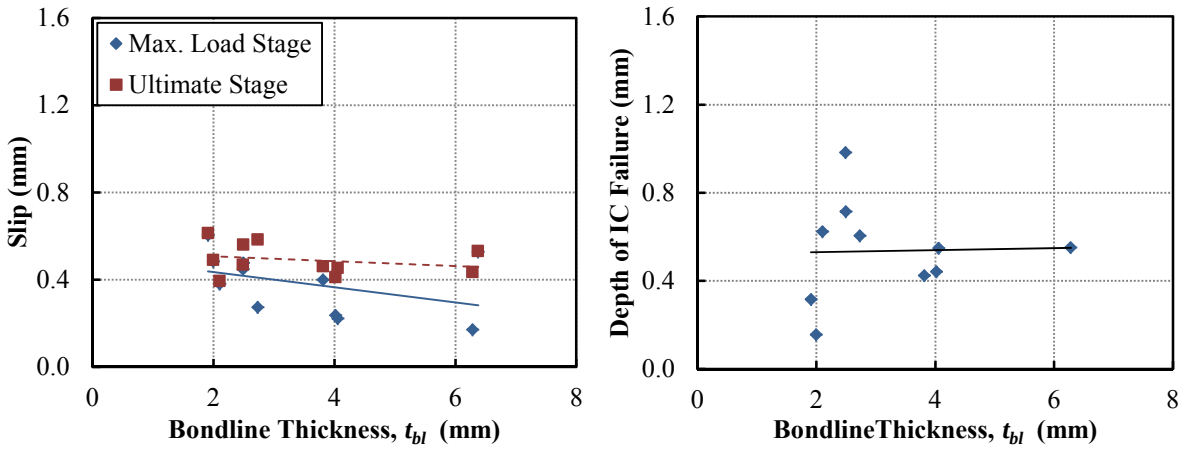

Figure 4-33. Correlation between slip and depth of IC failure with the bondline thickness for VARI processed samples.

The shear stress-local slip (τ-s) profile of the samples with different bondline thicknesses is presented in Figure 4-34. According to Figure 4-34a, the loaded end experiences high variation in the shear-local slip profile. Therefore in the analysis, shear stress-local slip curves of the inner sections, x=182.5 and 157.5 mm in which the τ-s profiles are smoother, used rather than the loaded end. Based on Figure 4-34b to d, samples with 3 GFRP layers show higher maximum shear stresses.

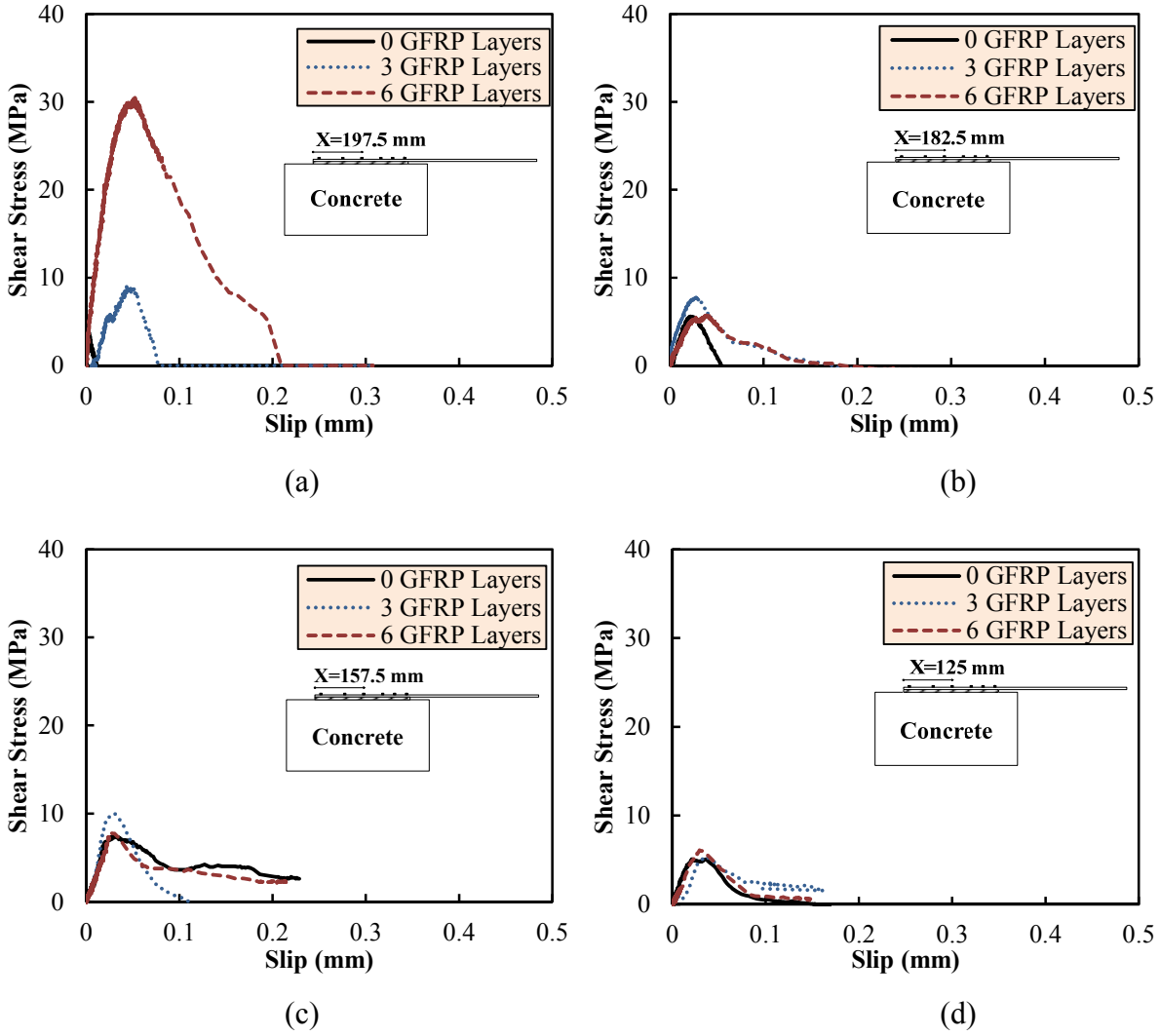

Figure 4-34. Interfacial shear stress-local slip profiles for the samples at different locations; x= (a) 197.5 mm, (b) 182.5 mm, (c) 157.5 mm, and (d) 125 mm.

The maximum shear stress of the samples decreases towards the free end of the FRP plate. Samples with different bondline thicknesses show the same trend in terms of the shear stress-slip curves closer to the FRP free end (Figure 4-34c and d). Local slip of the sections very close to the free end (x= 40 and 7.5 mm), which are not presented here, is negligible. The shear stress has the maximum value at the loaded end while decreases towards the end of the effective bond length (L_{eff}). It indicates that the effective bond length is less than 200 mm in the samples processed with VARI technique which in this research is adopted as 158 mm (section 4.5).

The changes of the maximum shear stress corresponding to the bondline thickness for different positions along the bonded length are shown in Figure 4-35. For t_{bl}=6.38 mm, the maximum load at the loaded end was obtained almost 30 MPa while for the other locations,

the maximum value is 7.8 MPa. Since the variance is high, this maximum shear stress is ignored and the modified graph is shown in Figure 4-35b. Except for x=125mm, the maximum shear stress increases for the bondline thickness up to 3.82 mm and then it drops for t_{bl}=6.38 mm. This maximum shear stress response for different bondline thicknesses can support the concept of the optimum bondline thickness.

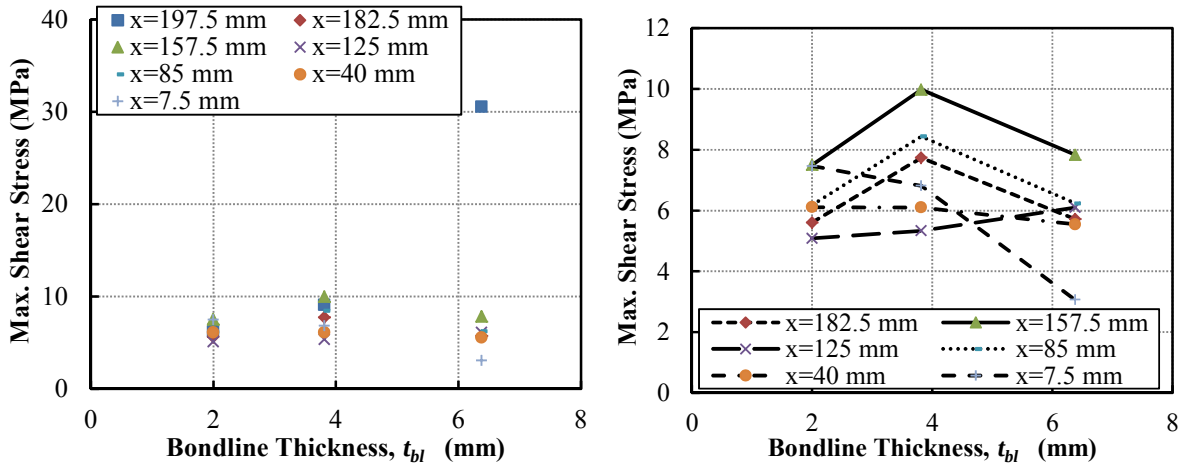

Figure 4-35. Maximum shear stress along the FRP plate considering different bondline thicknesses.

4.8. Surface Preparation Method

To achieve sufficient bond between the FRP and concrete, substrate surface is required to be treated by proper methods. In most of the cases, it is advisable to remove the top layer of mortar from the surface of the concrete in order to directly bond the FRP to the aggregates. This may contribute to transfer the interfacial stresses further into the substrate which will help the joint to carry higher amount of loads.

Although application of several procedures have been reported in the literature (Bizindavyi and Neale 1999; Cao et al. 2007; Chajes et al. 1996; Iwashita et al. 2007; López-González et al. 2012; Mazzotti et al. 2008; Pan and Leung 2007; Taljsten 1997; Ueda and Dai 2005; Ueda et al. 1999), there exists no comprehensive study on the effect of this factor on the interfacial behaviour of the adhesively bonded joints. Therefore, in this research different surface preparation techniques are used to provide further experimental data regarding this factor. The surface treatment methods which are used here are reported in Chapter 3 (Table 3-5).

Figure 4-3 and Figure 4-6 show the effect of grinding (SP-1) and abrasive belt sanding (SP-2) on the load-slip response of the samples with different initial unbonded length and also different FRP bonded length, respectively. According to these figures, the surface preparation with diamond grinding cup wheel greatly affected the slip deformation of the joints while the maximum applied load slightly decreases for the samples treated by the abrasive belt sanding method. The ultimate slip is noticeably higher in the samples with SP-1 compared with those with SP-2.

Changes in the surface preparation lead to different load-slip trends during MSLS test. The initial stiffness of the load slip curve is softer with grinding as opposed to abrasive belt sanding method. The samples prepared by SP-1 have linear behaviour until failure while the others experience slip hardening after their maximum load was reached. This could be explained by this fact that the grinding is a severe method compared to the abrasive belt sanding. With grinding of the substrate, the possibility of the debonding between the aggregates and mortar of the concrete is higher. Therefore, it is more likely that micro-cracks appear inside the substrate while the surface preparation is undergoing. Due to the brittle response and lower initial stiffness of the samples prepared with SP-1, it may be advisable to use abrasive belt sanding as surface treatment method prior to the FRP attachment instead of grinding.

During *Series I* and *II* of *Phase 4* of experiments, water blasting (SP-3) and sandblasting with low aggregate exposure (SP-4) are used as the surface treatments for the VARI processed specimens, respectively. The samples treated with SP-4 show higher values of the maximum applied load during the MSLS tests (Figure 4-36a). This difference is more noticeable when the bondline thickness increases. The same behaviour is observed for the samples when the slip corresponding to the maximum applied load and the ultimate load are compared in Figure 4-36b and c, respectively. Apparently, the global slip both at the maximum load and ultimate load stages is higher in samples prepared with SP-4. Since the exposure of the aggregates in both of the procedures is similar (low aggregate exposure), it can be claimed that the interfacial behaviour of the joint is more appropriate when the samples are treated by sandblasting rather than the water basting method.

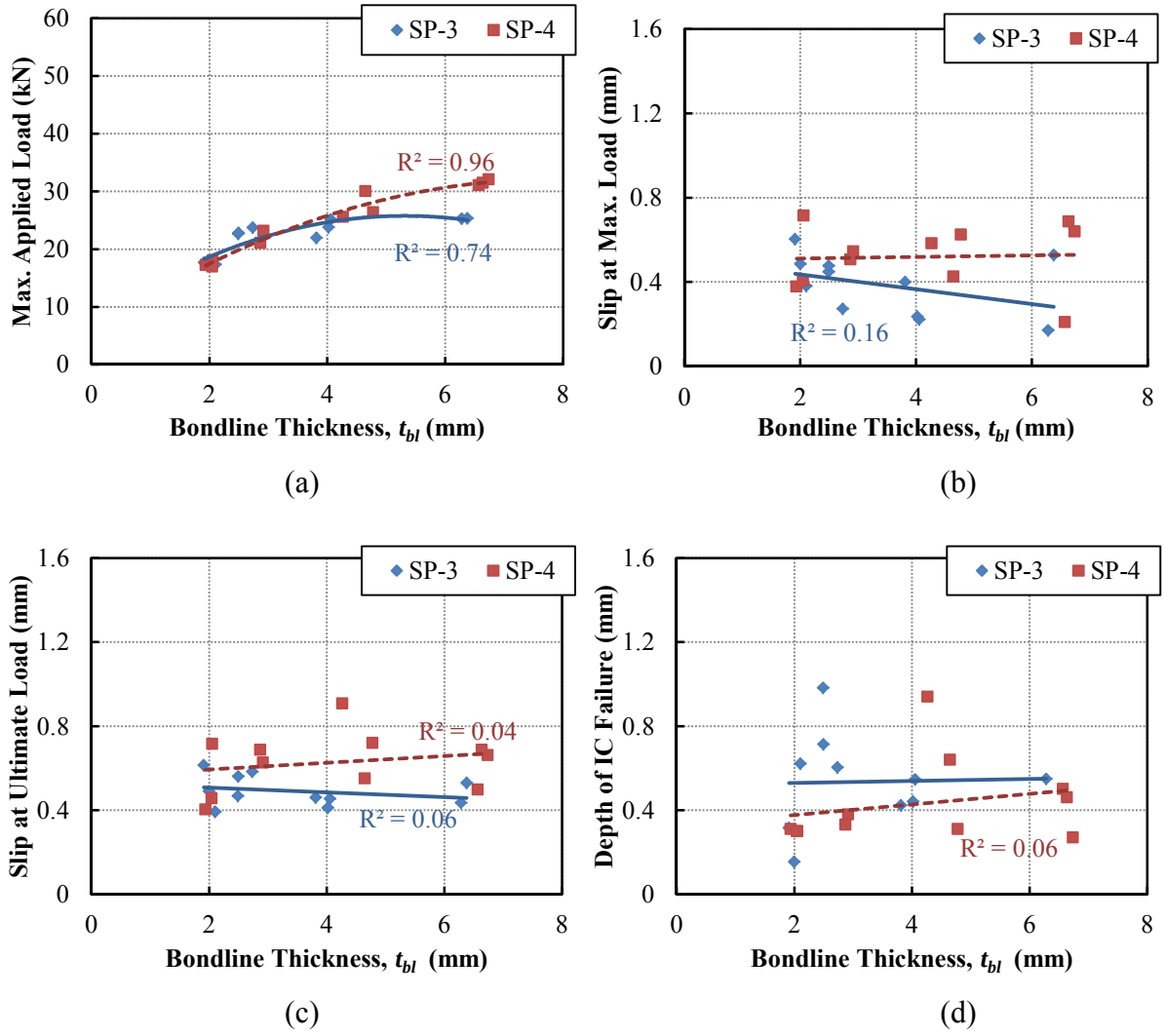

Figure 4-36. Interface behaviour of the specimens treated with water blasting (SP-3) and sandblasting with low aggregate exposure (SP-4).

To study the effect of the abrasive belt sanding and sandblasting methods on the interface behaviour, the maximum applied load, global slip at the maximum applied load and also the maximum shear stress of the joints are shown in Figure 4-37. The maximum applied load of the specimens with SP-6 is higher than those prepared with SP-2. The same trend is observed for the slip corresponding to the maximum applied load (Figure 4-37b) and also the maximum shear stress profile along the bonded length (Figure 4-37c).

The interface mostly experiences higher shear stresses in the samples prepared with sandblasting compared with abrasive belt sanding method. It is noteworthy to mention that this difference is mainly due to the fact that with abrasive belt sanding, low to medium exposure of the aggregates may be attained and high exposure of the aggregates can be particularly troublesome with this method. However with SP-6, high aggregate exposure is

easily achievable. According to the results, sandblasting is applied to most of the samples in this research as an appropriate method of the surface preparation.

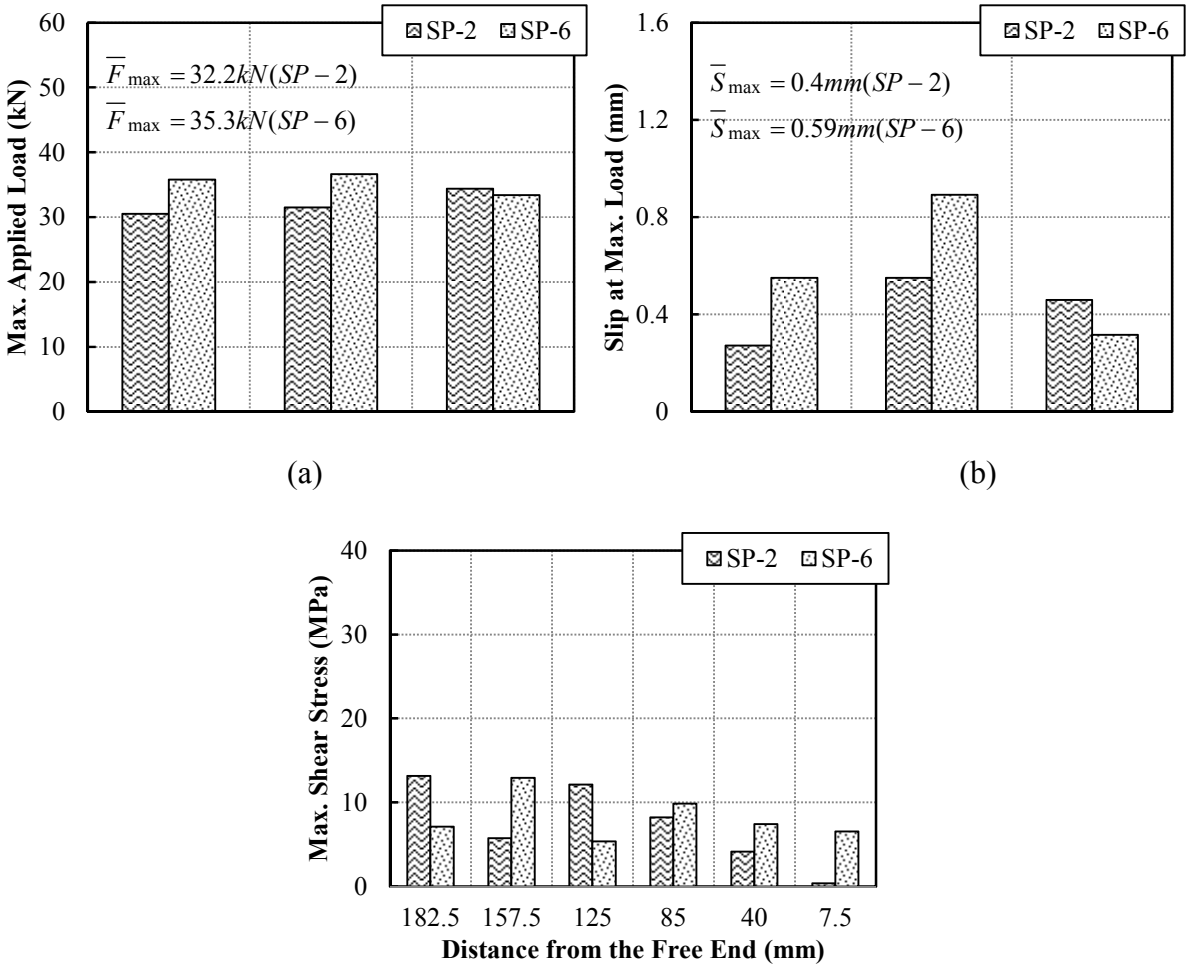

Figure 4-37. The effect of different sanding methods on the interfacial behaviour.

Finally, the effect of aggregate exposure is investigated through *Phase 2* of the experiments. Figure 4-38 presents the parametric studies on the wet lay-up joints treated by sandblasting with medium and high aggregate exposure. As long as higher aggregates are exposed through the surface preparation stage, higher maximum applied loads are achievable (Figure 4-38a). This can be explained by the fact that the bond between the FRP and the aggregates is stronger than the bond between the FRP and the mortar.

For the samples with medium aggregate exposure, more percentage of the bonded area is adhered to the mortar. Therefore, the bond is weaker in these samples compared with those prepared with SP-6. Maximum shear stress profile along the FRP bonded length also supports

this concept (Figure 4-38c). As it was explained before, the aggregates can transfer shear stresses into the substrate in more efficient ways rather than the mortar. Therefore, this phenomenon leads to higher shear stresses in the samples with SP-6 (sand blasting with high aggregate exposure).

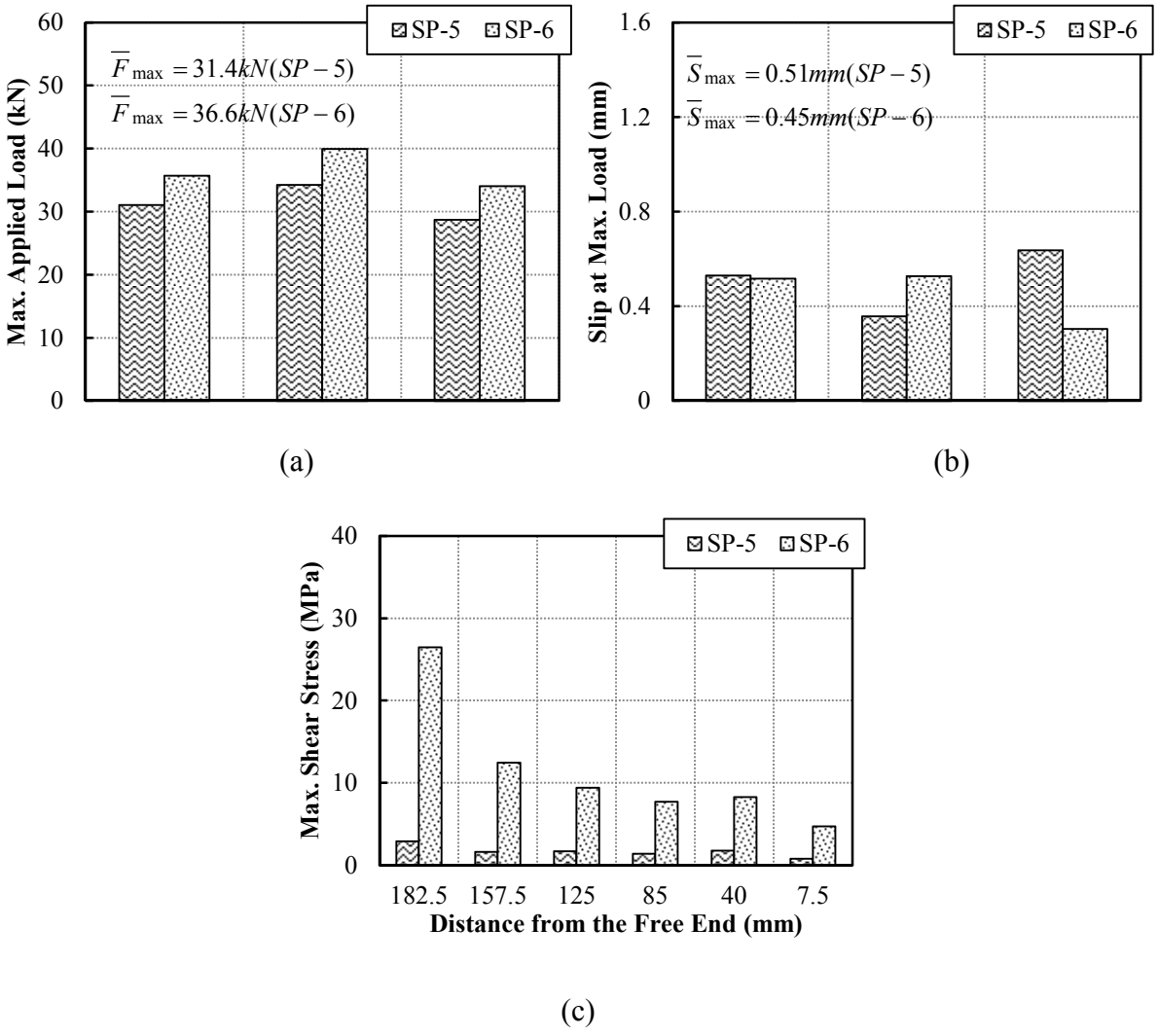

Figure 4-38. The effect of the aggregate exposure ratio in surface preparation method on the interface behaviour.

4.9. FRP Processing Technique

Various researches have been carried out to investigate the bond behaviour between concrete and the FRP fabricated by commonly used processing techniques such as, wet lay-up or pultruded systems (Bizindavyi and Neale 1999; Cao et al. 2007; Iwashita et al. 2007; Yao et al. 2005). These studies mainly address the effect of different parameters on the bond

performance through the experimental, analytical or numerical approaches. Nevertheless, the influence of FRP application on the substrate with various processing techniques has received less consideration in the interface study.

The available experimental data about the bond characteristics between concrete and the FRP using heated vacuum bag only (HVBO) and vacuum assisted resin infusion (VARI) techniques is very limited. Although the use of HVBO and VARI system is common in marine and aerospace industries, very little attention has been paid to the application of these systems in the strengthening of the structures by FRP materials. Therefore, the interfacial behaviour between concrete and FRP plates which processed by heated vacuum bag only and also vacuum assisted resin infusion techniques is investigated in this section. Single lap shear tests are performed on several adhesively bonded joints using a modified test set-up, proposed and successfully tested in section 3.2.5.

In order to compare the interfacial behaviour of the samples processed with different manufacturing methods, a generalized method, equalisation of the processing techniques, is used. This process, which is developed in the current research, is discussed in detail in chapter 3. Based on this method, the fibre areal weight (mass per area per plate) of the FRP plates is kept constant for all of the processing techniques. In all of the samples, geometry of the concrete and also FRP bonded length and width are the same.

Load carrying capacity of the samples is shown in Figure 4-39. Load vs slip curves follow the same trend, an initial sharp and steep increase in load corresponding to the small amount of the slip until the formation of the micro-cracks. At this point response tends to be nonlinear. By development of the macro-crack in the interface, the curve becomes plateau. This trend is dominant until the entire failure of the joint. Therefore the interface behaviour of the samples fabricated with HVBO and VARI techniques is similar to the commonly used processing methods in terms of the load-slip profiles.

Although the shape of the load-slip curves is the same for all of the manufacturing techniques, some variations are observed regarding other interfacial characteristics of the joints. By studying the maximum applied load recorded from the MSLS tests, it reveals that HVBO samples have outstandingly the lowest amount of load in comparison to other techniques (Figure 4-39a). This peculiar response may be attributed to the lower FRP stiffness in HVBO samples (Figure 4-39c). Since a specific amount of heat and resin film is recommended by the manufacturer, the number of the pre-preg laminates did not increase for further tests.

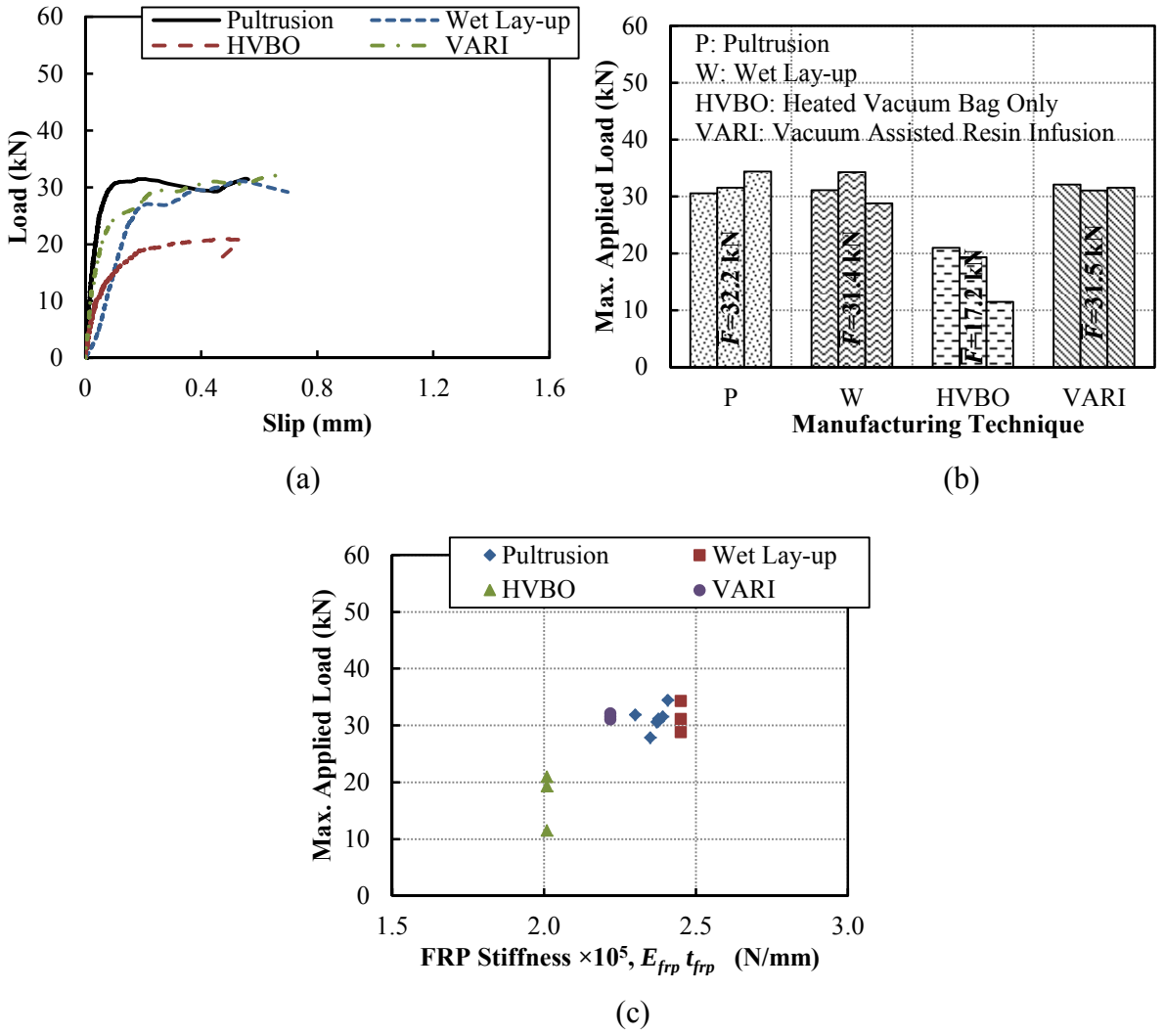

Figure 4-39. Load carrying capacity of the joints processed with different manufacturing techniques.

The increase in CFRP layers requires higher temperature for curing of the resin while such heat may contribute to damages to the substrate. The application of the heat for curing of the pre-preg laminates may weaken the concrete substrate. It may cause the formation of the micro-cracks on the top layers of the substrate where the concrete is exposed to the heat. Whereas, vacuum assisted resin infused samples represent the similar behaviour compared to pultrusion and wet lay-up samples.

The average maximum applied loads for pultruded, wet lay-up and VARI samples are 32.2, 31.4 and 31.5 kN while the average global slips corresponding to the maximum applied loads (Figure 4-40a) are 0.43, 0.51 and 0.51 mm, respectively. This indicates that the interface behaviour of the samples processed with pultrusion, wet lay-up and VARI techniques is quite similar in terms of the global load-slip response.

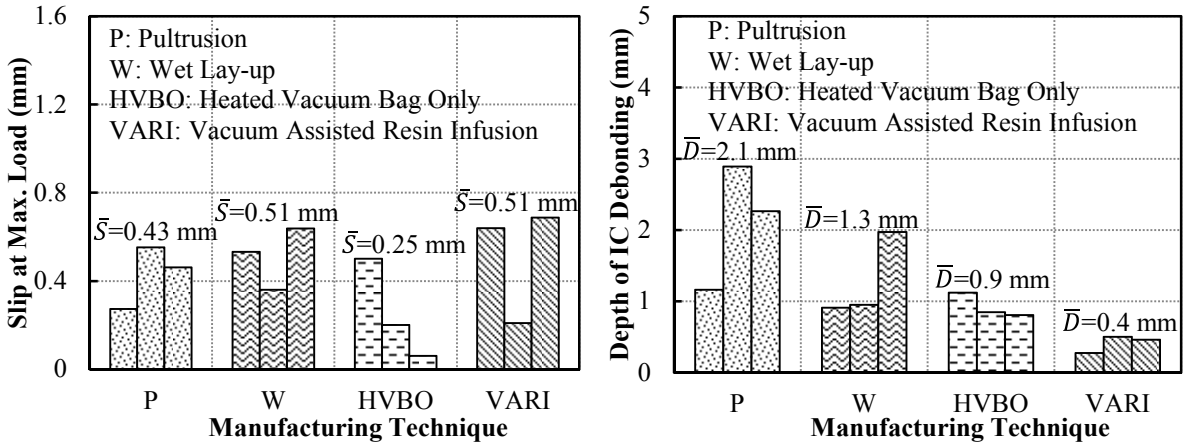

(a) (b)

Figure 4-40. Comparing (a) slip at maximum applied load and (b) depth of intermediate crack debonding for various manufacturing techniques.

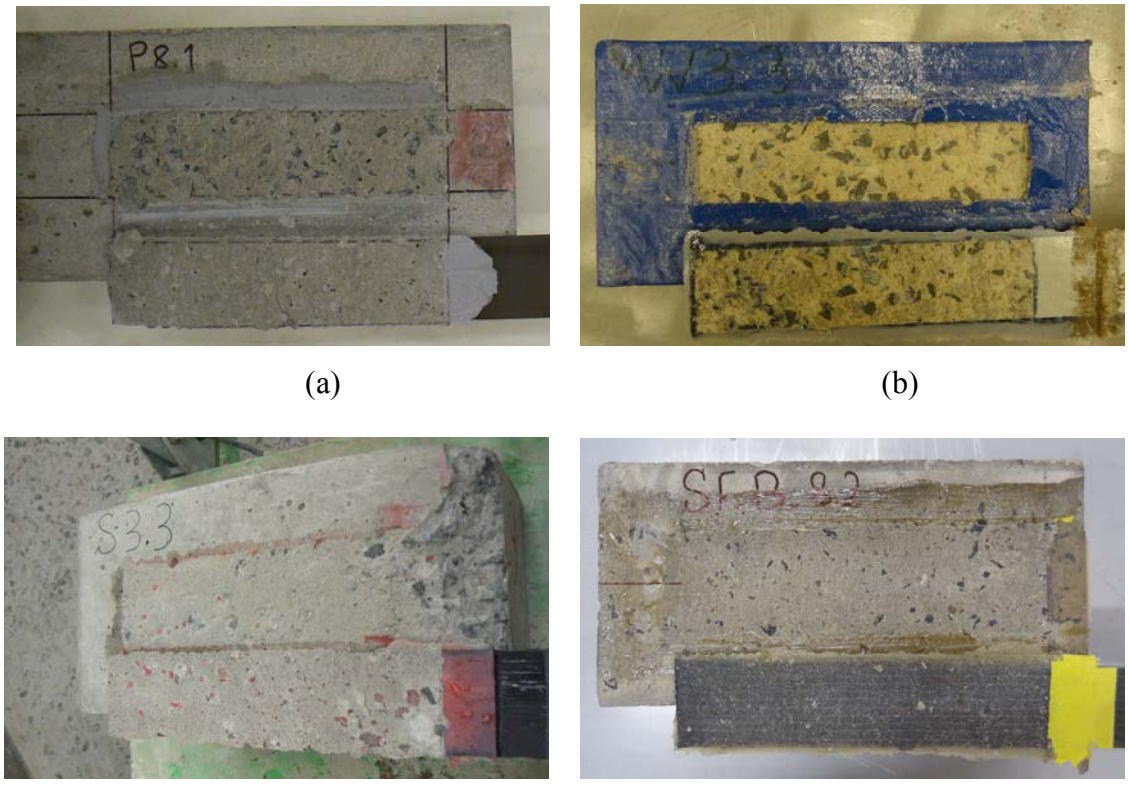

(a) (b)

(c) (d)

Figure 4-41. Fractured interface of (a) pultrusion, (b) wet lay-up, (c) HVBO and (d) VARI specimens.

After the tests, it was observed that in all of the samples, debonding occurred in a thin layer of the concrete close to the interface which is called cohesive failure. The thickness of the fractured layer is shown in Figure 4-40b. Cohesive failure mainly occurs due to the lower

shear and tensile strength of the concrete in comparison with the resin. The same type of debonding was observed for the samples processed with different techniques (Figure 4-41). It indicates that for the samples which were prepared by heated vacuum bag only and vacuum assisted resin infusion methods, the quality of the bond between fibres and resin/adhesive and also between FRP and concrete is satisfactory. Therefore, samples processed by HVBO and VARI techniques can significantly show the same pattern in terms of debonding failure mode as the commonly used processing methods, such as pultruded or wet lay-up technique. Some protruding parts of the adhesive film on pre-preg laminates were observed after the tests which may indicate that the film adhesive could penetrate the voids on the surface of the concrete substrate during the curing time.

Figure 4-42 illustrates the strain profile of the interface along the bonded length corresponding to the loading levels of 60% and 100% of the maximum applied load. During the experiment, wet lay-up samples experience lower strains. Before initiation of macro-crack (60% F_{max}), strain profiles of the samples follow a similar trend. However when the load increases (e.g. 100% F_{max}), strain profiles tend to change.

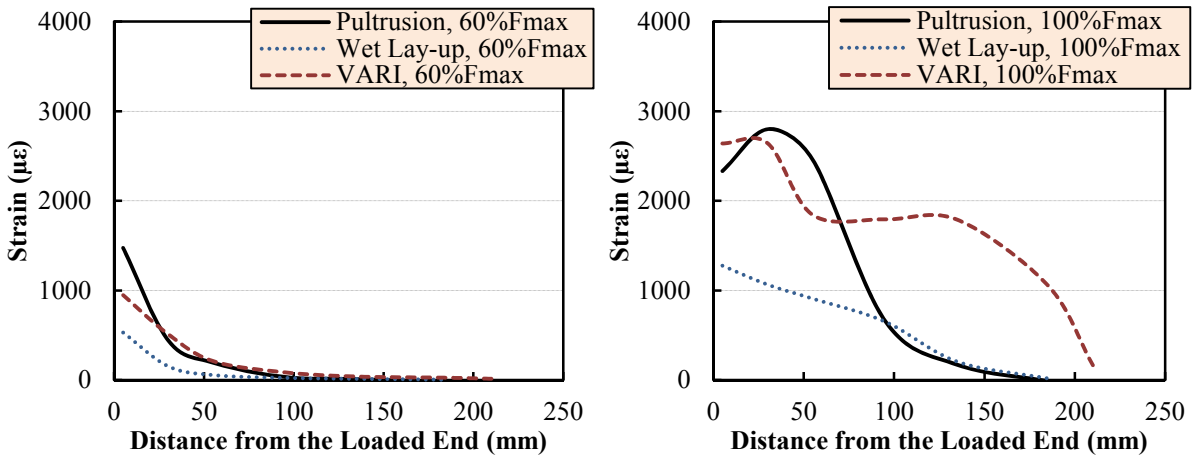

(a) (b)

Figure 4-42. Strain profile of the joints s at (a) 60% F_{max} and (b) F_{max}.

Further investigation on the strain profile indicates that the proportion of the FRP bonded length which transfers the shear load is longer for wet lay-up samples. As it was mentioned in section 4.5, the effective bond lengths for pultruded, wet lay-up and VARI processed specimens are 147, 181 and 158 mm, respectively (Table 4-2). Therefore, in strengthening of the reinforced concrete structures with wet lay-up sheets, longer anchorage length is required to achieve the maximum basic debonding resistance.

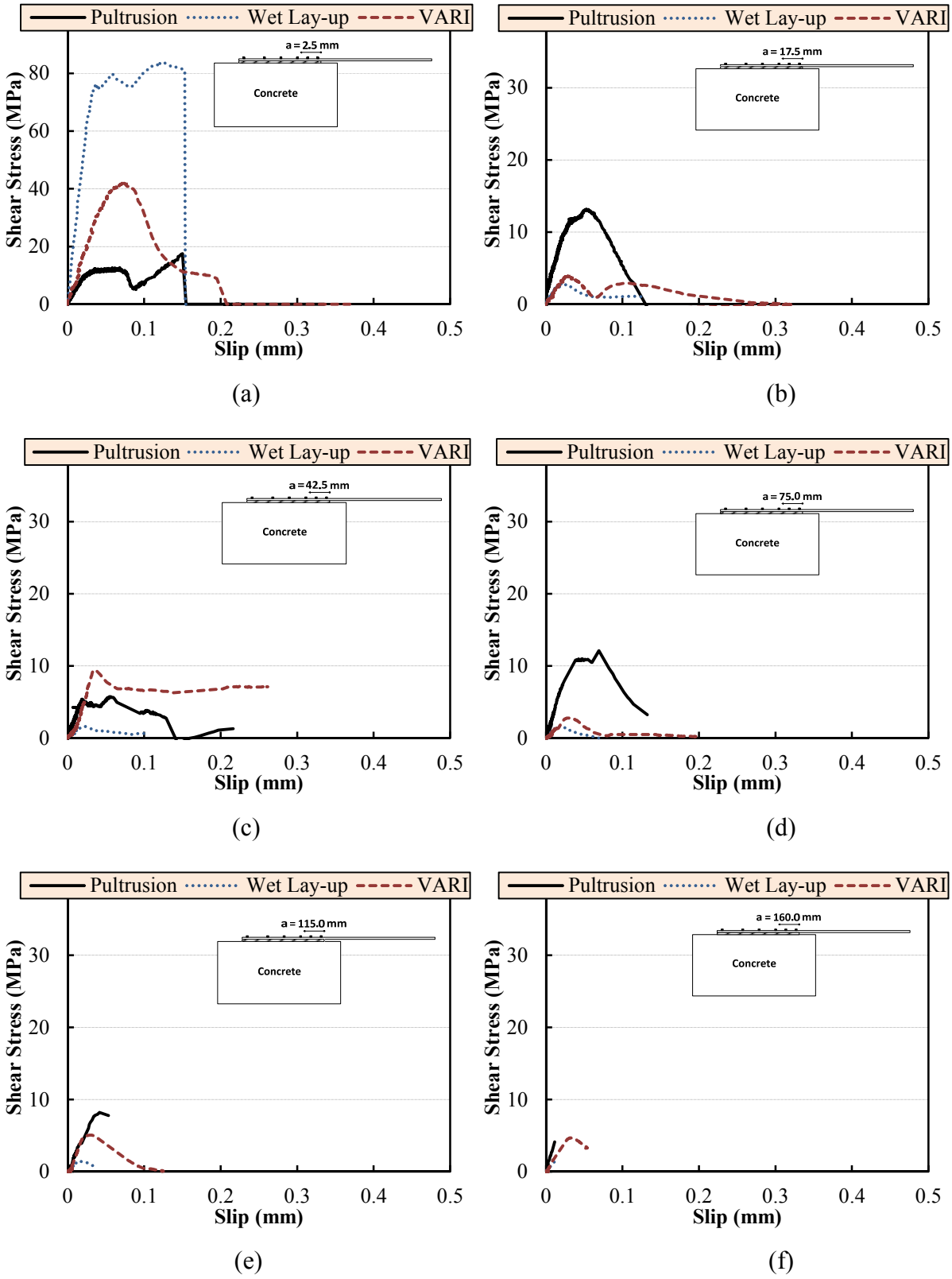

Figure 4-43. Bond-local slip relationship of the joints at different position considering the processing techniques.

For further investigation, shear stress against local slip curves are plotted in Figure 4-43. The local interface law in this figure corresponds to different positions on the bonded length of the FRP. Parameter *a* in this figure is the distance from the loaded end of the FRP which is defined in Figure 3-9. Stress concentration occurs in a zone close to the loaded end face of the FRP processed with wet lay-up and VARI techniques. However with shifting into the inside region of the bonded length (a=17.5 mm), the shear stress turns out to be more stable. Except at the loaded end, the wet lay-up specimen experiences lower shear stresses along the FRP bonded length. In addition, it has the lowest amount of the local slip while VARI samples show more ductile behaviour in comparison with the other two methods (wet lay-up and pultrusion).

The shear stresses corresponding to 60%F_{max} in wet lay-up and VARI samples drops from almost 60 and 40 MPa, respectively, at a = 2.5 mm with a sharp slope to less than 10 MPa at a = 17.5 mm (Figure 4-44a) while for pultrusion sample it does not change dramatically. After this position, samples show the same response. When the maximum load is reached, wet lay-up sample undergoes high gradient of the shear stress at the loaded end zone (Figure 4-44b). After a = 17.5 mm, the shear stress remains almost constant up to the free end of the FRP. This also indicates that the effective bond length where the shear stresses transferred to the substrate in wet lay-up samples is longer than other samples.

In VARI sample, some sections of the plate have zero or negative shear stress values (negative values are not shown here). Zero stress is a sign of FRP debonding from the concrete substrate. On the other hand, the pultruded sample carries the shear stress through the entire length except the zone close to the loaded end. The absolute maximum shear stress value of the samples at each point is shown in Figure 4-44c. It is clear that the interface in pultruded samples undergoes higher maximum shear stresses through the bonded length while wet lay-up specimens show the lowest amounts.

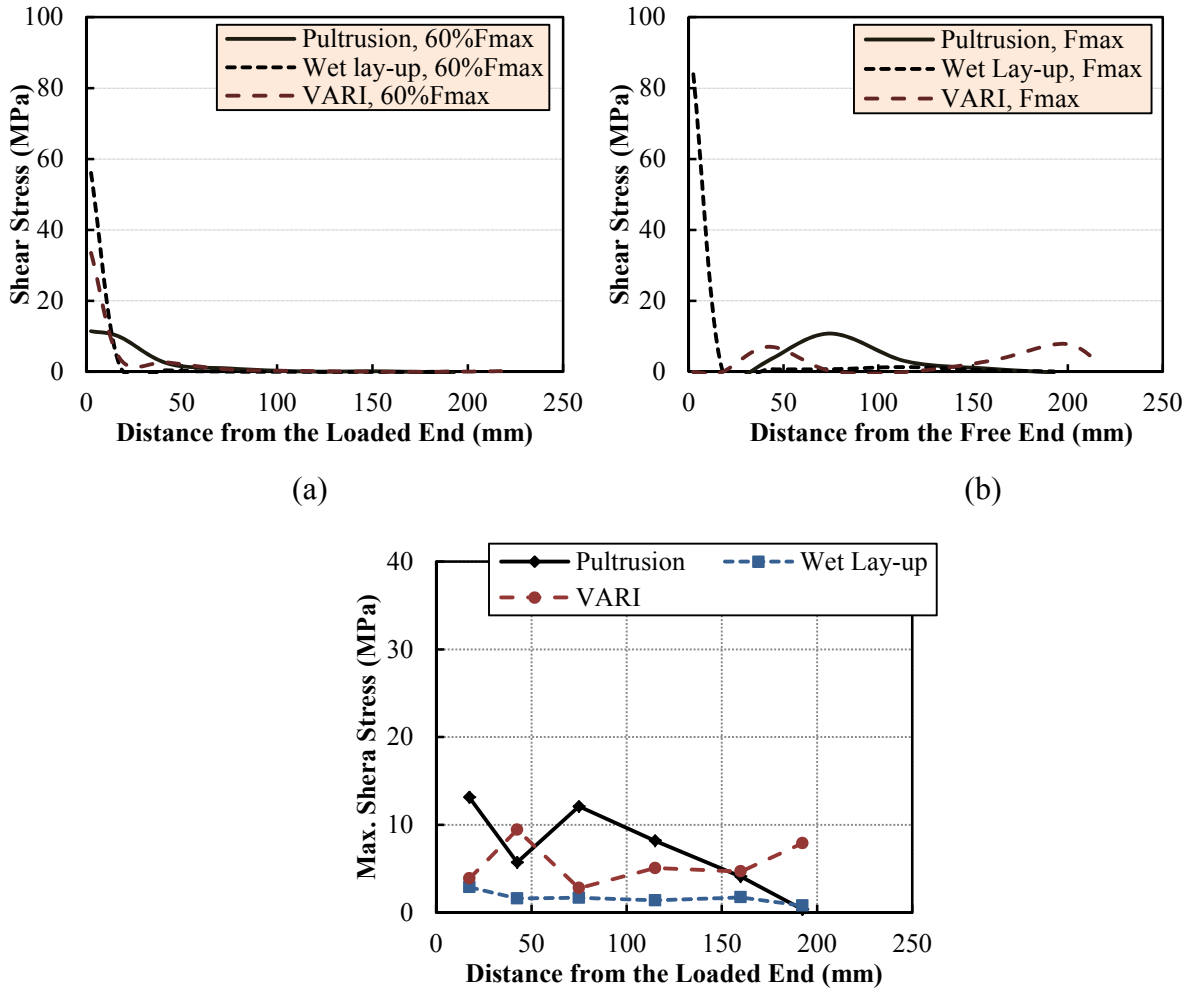

Figure 4-44. Shear stress distribution of the joints processed with various processing techniques at (a) 60% F_{max}, (b) F_{max} and (c) maximum shear stress value.

The local slip profile of the specimens fabricated with different processing techniques (pultrusion, wet lay-up and VARI) follows the same pattern prior to the formation of the macro-crack (Figure 4-45a, b and c). Throughout the loading, the loaded end of the FRP plates experiences the maximum values of the local slip. Up to stage 80%F_{max}, the maximum local slip is almost the same for pultruded and VARI samples, s = 0.07 mm (Figure 4-45d). After this stage of loading, although the local slip profile remains the same for all of the samples (Figure 4-45e) however the maximum value varies from one to other method. The maximum local slip values are plotted in Figure 4-45f. Wet lay-up and VARI samples show the lowest and highest local slip, respectively.

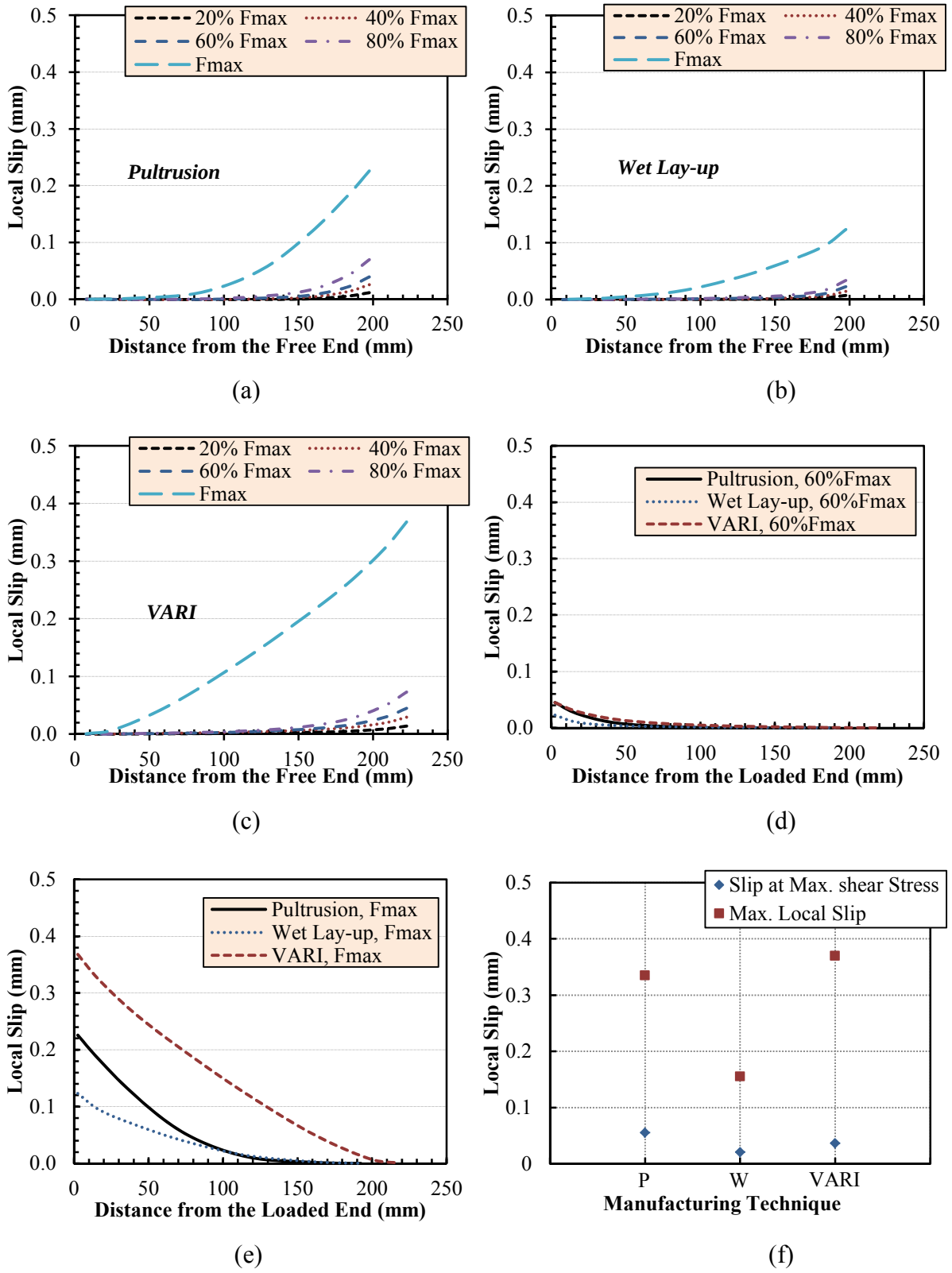

Figure 4-45. Local slip variation along the FRP bonded length for different processing techniques.

4.10. Summary

Results from the modified single lap shear tests have been presented in this chapter. The effect of different parameters on the interfacial behaviour of the adhesively bonded joints was investigated through several series of experiments. Parameters considered are the concrete surface tensile strength, initial unbonded length, FRP bonded length, FRP-to-concrete width ratio, bondline thickness, and surface preparation method. The effect of these factors on the interface behaviour of the adhesively bonded joints processed with different manufacturing techniques such as pultrusion, wet lay-up, heated vacuum bag only (HVBO) and vacuum assisted resin infusion (VARI) are studied. The results showed that the modified single lap shear test set-up employed in this research is able to successfully capture the bond characteristics of the specimens with high precision.

Direct pull-off test were performed on the specimens in order to find the effect of the concrete surface tensile strength and the bond characteristics. According to the variation of the results, it was shown that there is no direct correlation between these two parameters. It may be explained by the failure modes which govern two tests. Failure in modified single lap shear tests is mainly due to mode II of fracture while mode I is dominant in direct pull-off tests.

Results showed that it is required that a reasonable initial unbonded length (IUL) is considered at the front side of the concrete blocks in order to avoid splitting of the concrete at this section. Near end failure of the blocks occurs when the stress concentration happens. In all of the samples with no IUL, failure was accompanied by splitting of the front side of the concrete. However, as long as a sufficient IUL is considered, the maximum value of the load is reached before failure and the fracture occurred inside a thin layer of the concrete under the bonded area.

Previous studies show that there exists a length beyond which no increase in load carrying capacity is observed even if longer bonded length is applied. This specific length is addressed as effective bond length (EBL) or anchorage length. Although research has been carried out on this factor, no investigation has been attempted to characterize this parameter for specimens processed with different FRP processing techniques. In section 4.5, this parameter is determined based on an implicit method for pultruded, wet lay-up and vacuum assisted resin infusion samples. Among these manufacturing methods, wet lay-up has the longer effective bond length which is adopted as 181 mm in this research. However, other

processing techniques show shorter EBL (around 150 mm). In addition, it was shown that the EBL increases for the samples with thicker bondline.

The effect of the FRP-to-width ratio is studied in section 4.6. The load-global slip of the samples with different FRP width follows the same pattern. The load increases with small increase in slip until the micro-cracks occur. After this stage, the joint response becomes nonlinear. In the post-nonlinear stage of the response, the formation of macro-crack, is accompanied by a plateau until the failure of the joint. The maximum applied load and shear stresses increase for the samples with wider FRP. However, the local slip of the joints decreases for higher FRP to concrete width ratios. The local slip profile of the samples with different FRP width is quite similar during the initial stages of the loading while with increase in load, samples with wider FRP experience higher values of the local slip.

One major parameter in the interface behaviour of the FRP to concrete bonded joints is the bondline thickness. In this research the effects of the bondline thickness is studied for samples processed with pultrusion, wet lay-up, HVBO, and also VARI techniques. The outcomes of the MSLS tests on pultrusion, pre-pregs and VARI processed samples support this concept that there exists an optimum bondline thickness for different kinds of FRP processing techniques beyond which the bond characteristics of the joints do not improve.

Results indicate that although the maximum load carrying capacity of the joint increases by application of thicker bondline, after a specific thickness, load capacity does not change noticeably for thicker FRPs. This optimum bondline thickness is defined based on a nonlinear regression analysis and characterized by an exponential equation for different processing techniques. In addition, the local and global response of the joints were investigated through strain profiles, local bond-slip curves, and also shear stress and local slip profiles along the bonded length of FRP.

In the next part of the chapter, the effect of different surface treatments on the interfacial behaviour of the joints was studied. Surface preparation attributes to the transmission of the interfacial stresses into the substrate. Therefore, proper surface treatment may assist the bonded joints to withstand higher amount of the loads. The surface preparation methods which were employed in this research are diamond grinding, abrasive belt sanding, water blasting, and sandblasting considering different level of aggregate exposure.

It was shown that the initial stiffness of the load-slip curves in the samples treated with diamond grinding is noticeably lower than the abrasive belt sanding. As well as the initial slope, the load-slip response is mainly linear until failure in grinded samples. These distinctive responses may be attributed to the loss of the bond between mortar and aggregates

in the concrete substrate. Therefore, it is recommended that abrasive belt sanding is applied as the surface treatment instead of grinding. By comparing water blasting and sandblasting, it was shown that samples prepared with sandblasting carry higher loads during MSLS tests especially when the bondline thickness increases. In addition, the effect of sandblasting and the abrasive belt sanding is compared. The maximum applied load, slip at the maximum applied load and also the maximum shear stresses along the bonded length of the samples treated by sandblasting show higher values. These outcomes in conjunction with the fact that sandblasting is a more convenient surface treatment method suggest that it is advisable to employ sandblasting for removing the top mortar layer on the concrete substrate.

Based on the experiments carried out on the specimens manufactured with different processing techniques, it is determined that advanced processing techniques such as heated vacuum bag only and vacuum assisted resin infusion are able to accomplish a satisfactory interface behaviour in comparison with the more commonly used methods such as wet lay-up and pultrusion.

The bond between the FRP and concrete using VARI method is investigated in detail considering different parameters of the interface, load-global slip curve, type of failure, strain profile, bond-slip law, and shear stress and local slip profiles. These responses indicate that the VARI method can successfully be applied in strengthening of the reinforced concrete structures with the same and in some cases higher quality of the bond compared to more conventionally methods. As it was discussed, heat is one major part of HVBO technique, however few researches are available about the effect of the heat on the properties of the adherends (FRP and concrete) and adhesive. Therefore, further investigation is required to achieve a comprehensive understanding about the interface behaviour of the joints fabricated by HVBO technique.

CHAPTER 5

PROPOSED ANALYTICAL AND FE MODELS FOR INTERFACIAL BOND

5.1. Introduction

Several methods such as indirect analytical methods and finite element analysis have been employed to reduce the inconsistency in the bond-slip relationships obtained from the experimental results. However, the previous models determine the interfacial behaviour in terms of the factors which are not available in the literature or empirically verified. Therefore they cannot be extended to different types of FRP processing techniques.

To overcome these problems, in this chapter a new method is presented by which the local and global strain profiles of FRP-to-concrete bonded joints can be estimated with high precision. The non-linear and continuously differentiable strain function can be solved based on two types of boundary conditions to determine the bond stress for each point along the interface. Based on the boundary conditions, strain fixity condition and slip fixity condition, two sets of local bond-slip laws, *Method A* and *Method B*, are respectively obtained. *Method A* employs the effective bond length whilst *Method B* is developed based on the FRP length. Therefore when the effective bond length is unknown, *Method B* can be used as a more generic method.

The proposed nonlinear models have two distinct advantages: development of the bond-slip law based on boundary conditions of the joint and also the characterisation of the bond properties based on the applied load and FRP material properties. Therefore, with these methods a more stable and accurate bond-slip relationship is achievable which can be applied to any type of the FRP processing technique. A new relationship is proposed for determination of the fracture energy corresponding to antisymmetric in-plane shear mode II. In addition, the modelling procedure of the MSLS tests by Abaqus finite element analysis software (Abaqus/Standard) is presented in the next part of the chapter.

5.2. Previous Models

Previous work has shown that the strain profile over the bond length, $\varepsilon_{frp,x}$, can be fitted into different functions, such as exponential or quadratic equations (Bizindavyi and Neale 1999; Dai et al. 2005; Foster and Khomwan 2005) in order to obtain more reliable bond-slip law.

5.2.1. Foster and Khomwan Model

Considering the boundary condition of the joints, Foster and Khomwan (2005) showed that the strain profile is defined by the 4th order polynomial (Figure 5-1)

$$\varepsilon_{frp,x} = \left[6\lambda^2 - 8\lambda^3 + 3\lambda^4\right] \cdot \varepsilon_0 \qquad \lambda = \frac{x}{L_{eff}} \qquad 5\text{-}1$$

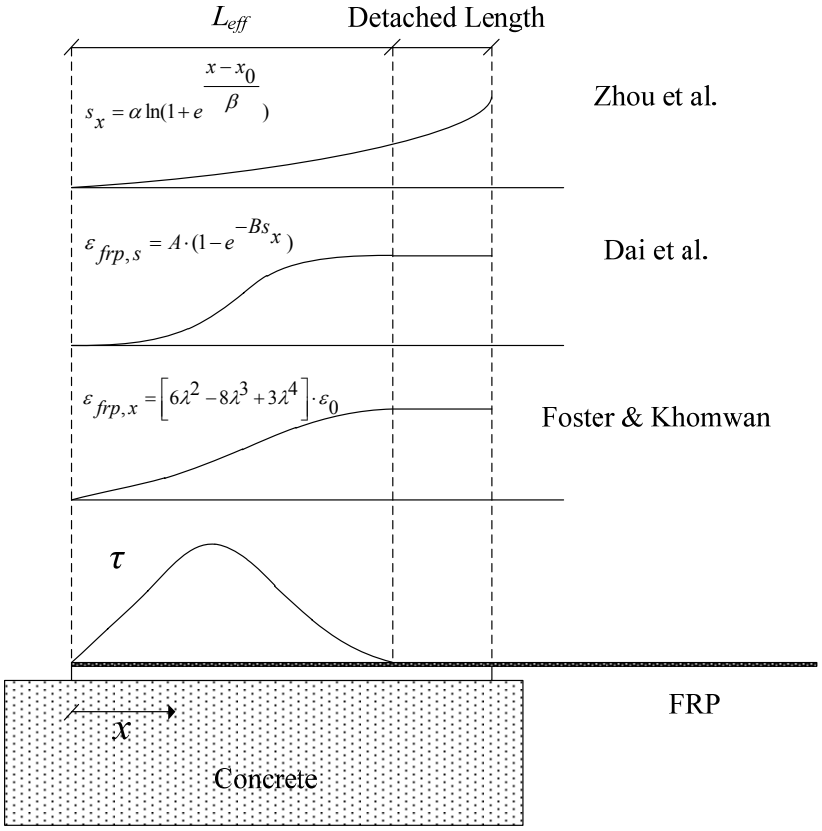

Figure 5-1. Proposed strain/slip profiles by Foster and Khomwan (2005), Dai et al. (2005), and Zhou et al. (2010).

Using Eq. 2-13, the interface shear stress is obtained by

$$\tau_{\text{int},x} = 12(\lambda - 2\lambda^2 + \lambda^3) \cdot \frac{\varepsilon_0 t_{frp} E_{frp}}{L_{eff}} \quad 5\text{-}2$$

where the maximum shear stress value is

$$\tau_{\max} = \frac{16\varepsilon_0 t_{frp} E_{frp}}{9L_{eff}} \quad 5\text{-}3$$

Since they developed their model for double lap shear test set-ups, the strain value at the loaded end is calculated by

$$\varepsilon_0 = \frac{F}{2(WEt)_{frp}} \quad 5\text{-}4$$

The slip profile is obtained by subtracting the displacement of the FRP from the concrete;

$$s_x = (1-K) \cdot (2 - 2\lambda + 0.6\lambda^2) \cdot (L_{eff}\varepsilon_0\lambda^3) \quad 5\text{-}5$$

$$K = 2\frac{(WEt)_{frp}}{A_e E_c} \quad 5\text{-}6$$

where A_g is the equivalent area of the cross section

$$A_e = A_g + (n-1)A_{st} \quad 5\text{-}7$$

Considering that the maximum slip occurs at λ=1/3

$$s_{\max} = \frac{7}{135}(1-K) \cdot (L_{eff}\varepsilon_0) \quad 5\text{-}8$$

They used the effective bond length, L_{eff}, which is adopted by Ueda and Dai (2004)

$$L_{eff} = 38.1 \frac{(Et)_{frp}^{0.38}}{(G/t)_{adh}^{0.657} f_c'^{0.118}} \quad 5\text{-}9$$

Their results showed that the strain and the bond-slip profiles can be predicted well with Eqs. 5-1, 5-2 and 5-5, respectively.

5.2.2. Dai et al Model

Dai et al. (2005) showed that an exponential function governs the relationship between the strain of FRP sheets and the slip at the loaded end (Figure 5-1)

$$\varepsilon_{frp,s} = A \cdot (1 - e^{-Bs_x}) \quad 5\text{-}10$$

and the shear stress

$$\tau_{\text{int},s} = A^2 B E_{frp} t_{frp} e^{-Bs_x} \cdot (1 - e^{-Bs_x}) \quad 5\text{-}11$$

Considering the area under the shear-slip diagram as the fracture energy

$$G_F = \frac{1}{2} A^2 E_{frp} t_{frp} \quad 5\text{-}12$$

and the maximum shear stress and corresponding slip are expressed by

$$s_0 = \frac{0.693}{B} \quad 5\text{-}13$$

$$\tau_{\max} = \frac{1}{2} B G_F \quad 5\text{-}14$$

For the maximum applied load, Dai et al. (2005) derived the same equation as Eq. 2-36 proposed by Täljsten (1996) with α = 1. In the above equations, A and B are parameters which are determined by regression of the experimental data. For design purposes the experimental data is not available and it is hard to find parameters A and B. Therefore, Dai et al. (2005) suggested the following relations which developed based on the regression of the experimental data

$$G_F = 0.446 \frac{f_c^{0.236} (Et)_{frp}^{0.023}}{(G/t)_{adh}^{0.352}} \quad \text{5-15}$$

$$B = 6.846 (E_{frp} t_{frp})^{0.108} \left(\frac{G_{adh}}{t_{adh}}\right)^{0.833} \quad \text{5-16}$$

and therefore based on the experimental results, Eq. 5-11 may be simplified to (Ueda and Dai 2005)

$$\tau_{\text{int},s} = 10.7 f_c'^{0.236} (e^{-10.4 s_x} - e^{-20.8 s_x}) \quad \text{5-17}$$

Based on the shear stress profiles along the bonded length, Ueda and Dai (2005) suggested the following expression for the effective bond length

$$L_{eff} = \frac{(2E_{frp} t_{frp})^{0.5}}{B G_F^{0.5}} \cdot \ln\left[\frac{1+\alpha}{1-\alpha}\right] \quad \text{5-18}$$

$$F_{\max} = (W_{frp} + 7.4) \cdot \sqrt{2E_{frp} t_{frp} G_F} \quad \text{5-19}$$

α can be taken as 0.96 for design purposes. The advantage of Dai et al.'s model (2005) compared with other relationships is that the properties and geometries of different elements of the joint (FRP, adhesive and concrete) are involved in determination of the bond behaviour. In addition, the bond-slip relationship can be derived by the magnitude of loads and slip at the loaded end which are available in most of the literature. The drawback of Dai

et al. (2005) model is that it is applicable to the joints with very stiff adhesive layer. By studying the effect of adhesive shear stiffness on the maximum shear stress, Dai et al. (2005) model leads to higher maximum shear stresses when the shear stiffness of the adhesive increases. However, it is shown that increasing the shear stiffness of the adhesive contributes to transfer more shear stresses to the substrate and more rapid fracture (Abdel Baky et al. 2012). In addition, some parameters such as G_F, B or A, are derived based on the regression of the experimental results.

5.2.3. Zhou et al. Model

Unlike Dai et al. (2005) which developed the interface law by assuming a typical strain profile Eq. 5-10, Zhou et al. (2010) considered a logarithmic relation for the local slip along the bonded FRP (Figure 5-1);

$$s_x = \alpha \ln(1 + e^{\frac{x - x_0}{\beta}}) \qquad 5\text{-}20$$

Based on the FRP bonded length, they divided the joints into infinite and finite joints. Joints over 300 mm in length were considered infinite. Considering the equilibrium and deformation compatibility conditions of the joint, an asymptotic equation can be derived for the strain profile for joints with infinite and finite bond lengths:

For joints with infinite bond length

$$\varepsilon_{frp,x} = \frac{1}{1+\rho} \cdot \frac{\alpha}{\beta} \cdot \frac{1}{1 + e^{-(x - x_0)/\beta}} \qquad 5\text{-}21$$

$$\varepsilon_{frp,s} = \frac{1}{1+\rho} \cdot \frac{\alpha}{\beta} \cdot (1 - e^{-\frac{s}{\alpha}}) \qquad 5\text{-}22$$

Eq. 5-22 is identical to Dai et al. (2005) formula. The shear stress along the bonded length is defined by

$$\tau_{\text{int},x} = \frac{E_{frp} t_{frp}}{1+\rho} \cdot \frac{\alpha}{\beta^2} \cdot \frac{e^{-(x-x_0)/\beta}}{(1+e^{-(x-x_0)/\beta})^2} \quad \text{5-23}$$

In addition, the local interface law is expressed by

$$\tau_{\text{int},s} = \frac{E_{frp} t_{frp}}{1+\rho} \cdot \frac{\alpha}{\beta^2} \cdot e^{-\frac{s}{\alpha}} \cdot (1-e^{-\frac{s}{\alpha}}) \quad \text{5-24}$$

$$\rho = \frac{E_{frp} t_{frp} W_{frp}}{E_c t_c W_c} \quad \text{5-25}$$

For joints with finite bond length

$$\varepsilon_{frp,x} = \frac{1}{1+\rho} \cdot \frac{\alpha}{\beta} \cdot \frac{x/L_{frp}}{x/L_{frp} + e^{-(x-x_0)/\beta}} \quad \text{5-26}$$

$$s_x = s_0 + \cdot \frac{\alpha}{\beta} \cdot \int_0^x \frac{t/L_{frp}}{t/L_{frp} + e^{-(t-x_0)/\beta}} dt \quad \text{5-27}$$

$$\tau_{\text{int},x} = \frac{E_{frp} t_{frp}}{1+\rho} \cdot \frac{\alpha}{\beta^2} \cdot \frac{x+\beta}{L_{frp}} \cdot \frac{e^{-(x-x_0)/\beta}}{(x/L_{frp} + e^{-(x-x_0)/\beta})^2} \quad \text{5-28}$$

$$s_x = s_0 + \cdot \frac{\alpha}{\beta} \cdot \int_0^x \frac{t/L_{frp}}{t/L_{frp} + e^{-(t-x_0)/\beta}} dt \quad \text{5-29}$$

α, β, and x_0 in the above equations (Eq. 5-21 to Eq. 5-29) are determined by the regression of the experimental results. Zhou et al. (2010) showed that when the bonded length of the FRP is infinite (in this case more than 300 mm) the maximum load carrying capacity is different

from the case in which shorter bonded length (finite length) is used. Regarding the bonded length Zhou et al. (2010) proposed the following relations

For an infinite bond length:

$$F_{\max} = \frac{\alpha}{\beta} \cdot E_{frp} A_{frp} \qquad 5\text{-}30$$

For a finite bond length:

$$F = \frac{E_{frp} A_{frp}}{1+\rho} \cdot \frac{\alpha}{\beta} \cdot \frac{1}{1+e^{-(L_{frp}-x_0)/\beta}} \qquad 5\text{-}31$$

as previously mentioned, parameters α, β, and x_0 are determined by the regression of the experimental data.

5.3. Development of the New Interfacial Bond Models

Despite the above mentioned models, the strain profiles of the samples tested in this research (Figure 4-8, Figure 4-14, Figure 4-21, Figure 4-25 and Figure 4-42) indicate that the strain distributes along the bonded length with a third degree polynomial function (Eq. 5-32) for different processing techniques.

Figure 5-2 shows the fitted third degree polynomial function (analytical curve) to the experimental observations for strain distribution corresponding to maximum load and 60% of the maximum load levels for samples processed with different manufacturing techniques. A good correlation exists between the experimental data and the polynomial function for both initial and ultimate stages of loading;

$$\varepsilon_{frp,x} = \frac{ds_x}{dx} = Ax^3 + Bx^2 + Cx + D \qquad 5\text{-}32$$

s_x is the slip between the FRP and concrete as a function of position. x is the coordinate along the bond length (Figure 3-9) where $x = 0$ corresponds to the free end and $x = L$ represents the loaded end of the laminate. A, B, C and D are constant values which are defined as followed.

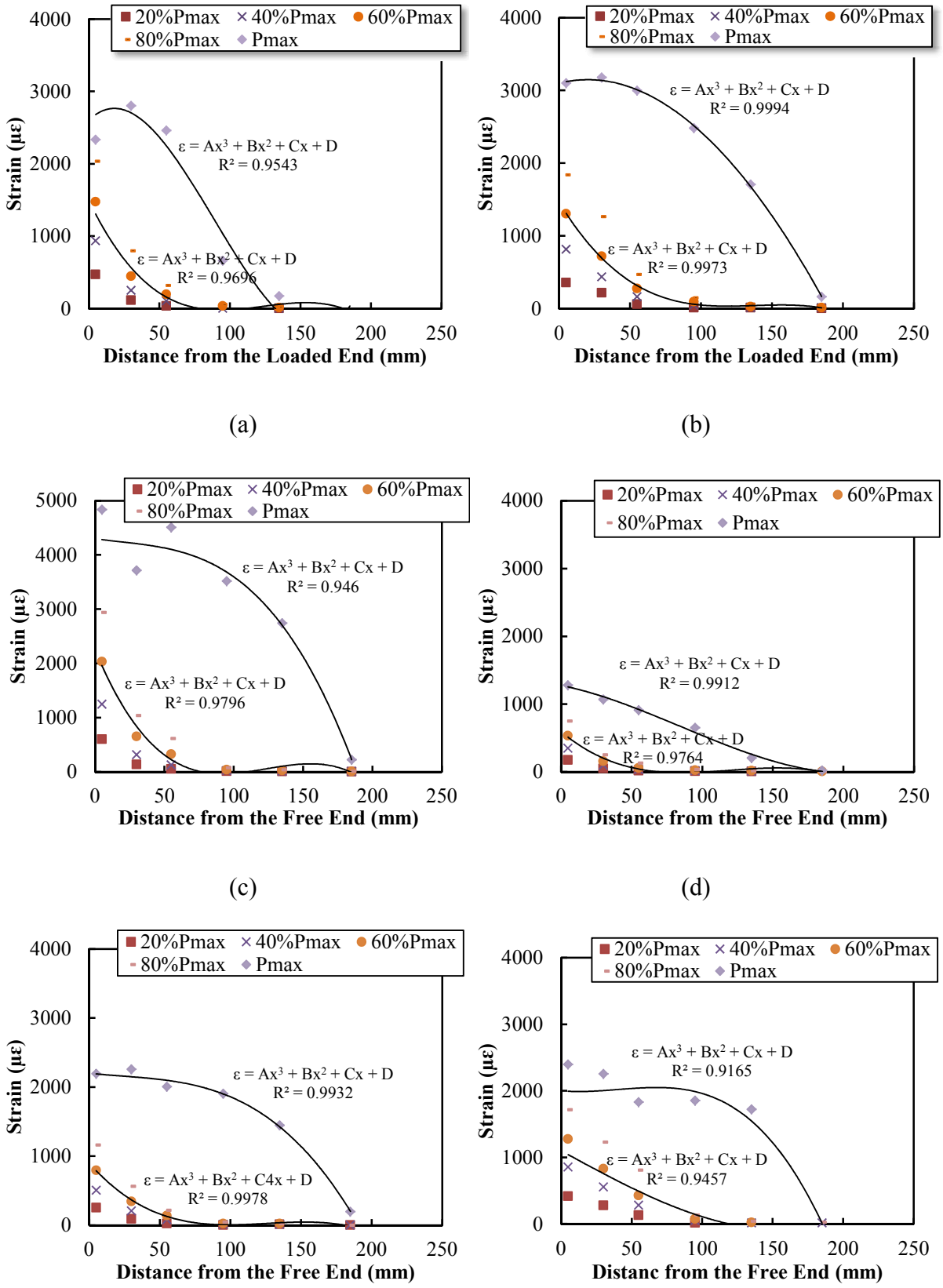

Figure 5-2. Strain distribution along the bonded length and interpolation curves of the samples: (a) P8.3, (b) P9.3, (c) W1.3, (d) W3.3, (e) SF-B-4.2, and (f) SF-B-7.3.

The strain profile of the samples along the bonded length consists of different stages. During the initial stage, the slip between the FRP and the concrete substrate linearly increases by the applied load. Then, micro-cracks start to propagate through the interface until the formation of the macro-crack. By formation of the macro-crack, the load carrying capacity of the joint does not increase and the length of bond through which the interfacial shear stresses are transferred to the substrate can be defined as the effective bond length (L_{eff}).

Along the bonded region, the FRP strain on the detached parts of the laminate remains constant. When the effective bond length is reached, any increase in load leads to a rapid shifting of the unbonded region to the end of the FRP. Based on these conditions, two sets of local bond-slip laws (*Method A-strain fixity condition* and *Method B-slip fixity condition*) are proposed and introduced in the next sections.

5.3.1. Method A-Strain Fixity Condition

Strain Profile

Based on the strain values at the free end of the FRP and $x=L_{eff}$, the boundary conditions for the interface can be expressed as (Figure 5-3):

$$\varepsilon_{frp,x} = 0 \qquad \text{when} \quad x = 0 \qquad \text{5-33}$$

$$\frac{d\varepsilon_{frp,x}}{dx} = 0 \qquad \text{when} \quad x = 0 \qquad \text{5-34}$$

$$\varepsilon_{frp,x} = \varepsilon_0 \qquad \text{when} \quad x = L_{eff} \qquad \text{5-35}$$

$$\frac{d\varepsilon_{frp,x}}{dx} = 0 \qquad \text{when} \quad x = L_{eff} \qquad \text{5-36}$$

ε_0 and L_{eff} are the strain at the loaded end and the effective bond length, respectively. Assuming the FRP laminate has a linear elastic behaviour, ε_0 is calculated from the values of the applied force, F, as follows:

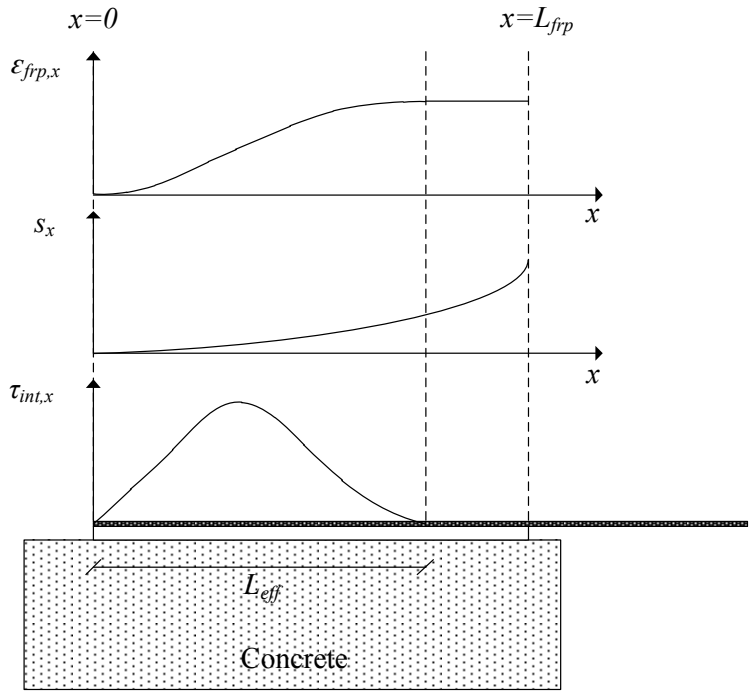

Figure 5-3. Strain, slip and shear stress profiles based on the proposed models.

$$\varepsilon_0 = \frac{F}{E_{frp} A_{frp}} \tag{5-37}$$

where E_{frp} and A_{frp} in pultruded system are modulus of elasticity and the cross section of the laminate ($W_{lam} \times t_{lam}$), respectively. Solving Eq. 5-32 for boundary conditions 5-33 and 5-34 gives:

$$C = D = 0 \tag{5-38}$$

Considering boundary conditions 5-35 and 5-36:

$$BL_{eff}^2 + AL_{eff}^3 = \varepsilon_0 \tag{5-39}$$

$$2BL_{eff} + 3AL_{eff}^2 = 0 \tag{5-40}$$

Solving Eqs. 5-39 and 5-40 simultaneously leads to:

$$A = -\frac{2\varepsilon_0}{L_{eff}^3} \qquad 5\text{-}41$$

$$B = \frac{3\varepsilon_0}{L_{eff}^2} \qquad 5\text{-}42$$

then, Eq. 5-32 becomes

$$\varepsilon_{frp,x} = -\frac{2\varepsilon_0}{L_{eff}^3}x^3 + \frac{3\varepsilon_0}{L_{eff}^2}x^2 \qquad 5\text{-}43$$

by substituting Eq. 5-37 into Eq. 5-43:

$$\varepsilon_{frp,x} = \frac{F}{E_{frp}A_{frp}L_{eff}^2}\cdot(3 - \frac{2}{L_{eff}}x)x^2 \qquad 5\text{-}44$$

Therefore, the strain distribution along the bond length can be determined by the following equations:

$$\varepsilon_{frp,x} = \frac{ds_x}{x} = -\frac{2\varepsilon_0}{L_{eff}^3}x^3 + \frac{3\varepsilon_0}{L_{eff}^2}x^2 \qquad for \quad 0 < x < L_{eff} \qquad 5\text{-}45$$

$$\varepsilon_{frp,x} = \varepsilon_0 = \frac{F}{E_{frp}A_{frp}} \qquad for \quad L_{eff} < x < L \qquad 5\text{-}46$$

Equations 5-45 and 5-46 are valid for the joints longer than the effective bond length where a perfect bond is taken into account at the free end. The capability of the proposed equations in determination of the interface strain profile is shown in section 5.4.1.

Shear Stress

The interfacial stress along the bond length, $\tau_{int,x}$, can be obtained from the following differential equation (Figure 5-3):

$$\tau_{\text{int},x} = \frac{1}{\Omega} \cdot \frac{d^2 s_x}{dx^2} = \frac{1}{\Omega} \cdot \frac{d\varepsilon_{frp,x}}{dx} \qquad 5\text{-}47$$

$$\Omega = \frac{1}{E_{frp} t_{frp}} + \frac{W_{frp}}{E_c t_c W_c} \qquad 5\text{-}48$$

W_{frp} represents the width of the FRP. Differentiating Eq. 5-45 and substituting into Eq. 5-47 gives

$$\tau_{\text{int},x} = \frac{9 t_{frp} E_{frp} \varepsilon_0}{L_{eff}^2} \cdot \left[x - \frac{1}{L_{eff}} x^2 \right] \qquad 5\text{-}49$$

Considering Eqs. 5-37 and 5-49, the following relation gives the interfacial bond stress of each point along the bond length:

$$\tau_{\text{int},x} = \frac{9F}{W_{frp} L_{eff}^2} \cdot \left[x(1 - \frac{x}{L_{eff}}) \right] \qquad 5\text{-}50$$

Therefore, the bond stress along the bond length can be obtained directly from the applied load in SLS test regardless of the strain measurements on the FRP. Equation 5-50 indicates that the bond stress is independent from the bondline thickness and is only related to the applied load, FRP width and the location. In addition, the maximum shear stress can be obtained by

$$\tau_{\max} = \frac{9F_{\max}}{4W_{frp} L_{eff}} \qquad 5\text{-}51$$

Slip Profile

As it was explained in Chapter 2, generally, the behaviour of FRP/concrete joints is represented in terms of bond-slip relationship. In this section, two different relations are proposed for slip profile based on the shear stress distribution (Eq. 5-50) presented in the previous section. Figure 5-4 shows the equilibrium of the applied forces and compatibility of

deformations in a finite element of the joint. According to this figure, the slip is expressed as the relative displacement between the FRP and concrete.

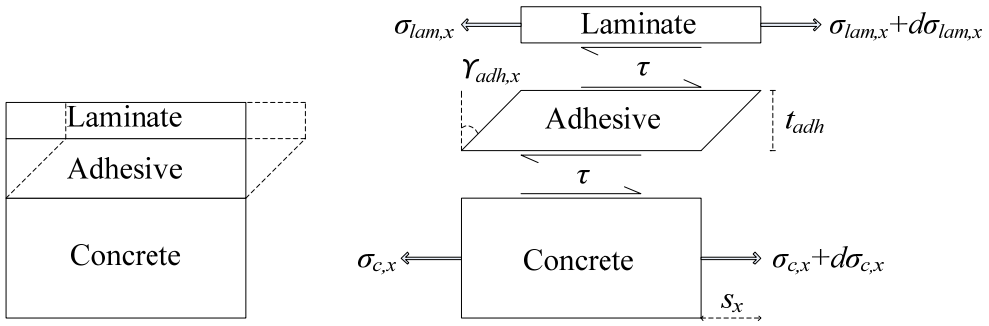

Figure 5-4. Deformation and free body diagram of an infinitesimal element of the joint.

At each point, the slip can be determined by differences between the integration of strain for FRP laminate and concrete. Since the axial stiffness of concrete is large, the slip in concrete can be neglected. In addition, assuming adherends do not experience any relative displacement at the free end of the joint, the following equation can be inferred for slip (s_x):

$$s_x = u_{frp,x} - u_{c,x} \tag{5-52}$$

$$u_{frp,x} = \int \varepsilon_{frp,x} dx \tag{5-53}$$

$$u_{c,x} = \int \varepsilon_{c,x} dx \tag{5-54}$$

$u_{frp,x}$, $u_{c,x}$ and ε_c are the displacement of FRP, the displacement of the concrete and the strain in the concrete block, respectively.

For $0 \le x \le L_{eff}$:

Considering Eqs. 5-45 and 5-53

$$u_{frp,x} = \frac{\varepsilon_0}{L_{eff}^2} x^3 - \frac{\varepsilon_0}{2L_{eff}^3} x^4 \tag{5-55}$$

$$u_{c,x} = \frac{W_{frp}}{A_c E_c} \cdot \int_0^x \int \tau_{\text{int},x} dx^2 \tag{5-56}$$

A_c and E_c are the cross sectional area and modulus of elasticity of the concrete, respectively. Substituting Eq. 5-50 in 5-56 and take double integration from the free end till effective bond length:

$$u_{c,x} = \frac{3F}{2A_cE_cL_{eff}^2} \cdot x^3 \left[1 - \frac{x}{2L_{eff}}\right] \quad \text{5-57}$$

For $L_{eff} < x \leq L$:

$$u_{frp,x} = \int_0^{L_{eff}} \left(-\frac{2\varepsilon_0}{L_{eff}^3}x^3 + \frac{3\varepsilon_0}{L_{eff}^2}x^2\right)dx + \int_{L_{eff}}^{x} \varepsilon_0 dx \quad \text{5-58}$$

$$u_{frp,x} = \frac{\varepsilon_0}{2} \cdot (2x - L_{eff}) \quad \text{5-59}$$

$$u_{c,x} = \frac{W_{frp}}{A_cE_c} \cdot \int \int_0^{L_{eff}} \tau_{\text{int},x} dx^2 = \frac{3FL_{eff}}{4A_cE_c} \quad \text{5-60}$$

Therefore, considering Eqs. 5-55 to 5-57 and Eqs. 5-59 to 5-60, the governing equation for slip between the FRP and concrete can be written:

For $0 \leq x \leq L_{eff}$:

$$s_x = \left[\frac{\varepsilon_0}{L_{eff}^2} - \frac{3F}{2A_cE_cL_{eff}^2}\right] \cdot x^3 + \left[\frac{3F}{4A_cE_cL_{eff}^3} - \frac{\varepsilon_0}{2L_{eff}^3}\right] \cdot x^4 \quad \text{5-61}$$

For $L_{eff} < x \leq L$:

$$s_x = \varepsilon_0 x - \left[\frac{\varepsilon_0 L_{eff}}{2} + \frac{3FL_{eff}}{4A_cE_c}\right] \quad \text{5-62}$$

Since the cross sectional area and the modulus of elasticity of the concrete is large, the slip in the concrete can be neglected and equations 5-61 and 5-62 can be rewritten as;

$$s_x = \frac{\varepsilon_0}{L_{eff}^2} x^3 - \frac{\varepsilon_0}{2L_{eff}^3} x^4 \quad \text{5-63}$$

$$s_x = \varepsilon_0 x - \frac{\varepsilon_0 L_{eff}}{2} \quad \text{5-64}$$

The strain profile can also be obtained based on the shear stress distribution and the properties of the adhesive. Experimental results of the MSLS samples presented in Chapter 4 in conjunction with outcomes of other references (Camli and Binici 2007; Cao et al. 2007; Ferracuti et al. 2007; Liu and Wu 2012; Subramaniam et al. 2007; Yuan et al. 2004; Zhou et al. 2010) indicate that the displacement of the concrete is negligible and if the elongation of the FRP is ignored (in most cases up to 1.7%) (Abdel Baky et al. 2012), therefore the interface slip (Figure 5-4) can be expressed by

$$s_x = \int t_{adh} \frac{d\gamma_x}{dx} dx \quad \text{5-65}$$

where

$$\gamma_x = \frac{\tau_{\text{int},x}}{G_{adh}} \quad \text{5-66}$$

γ_x and G_{adh} are the shear strain and shear modulus of the adhesive. Derivation from Eq. 5-66 leads to

$$\frac{d\gamma_x}{dx} = \frac{1}{G_{adh}} \cdot \frac{d\tau_{\text{int},x}}{dx} \quad \text{5-67}$$

By substituting Eq. 5-67 into 5-65, local slip takes the form of

$$s_x = \left(\frac{t}{G}\right)_{adh} \cdot \tau_{\text{int},x} \quad \text{5-68}$$

Using the proposed equation for determination of the shear stress along the bondline (Eq. 5-50) in the above relation gives

$$s_x = \frac{t_{adh}}{G_{adh}} \cdot \frac{9F}{W_{frp} L_{eff}^2} \cdot x \left[1 - \frac{x}{L_{eff}} \right] \qquad 5\text{-}69$$

The advantage of the above equation (Eq. 5-69) in comparison with Eqs. 5-63 and 5-64 is that the properties of the adhesive are considered in prediction of the slip values.

Fracture Energy

When the crack forms inside the concrete, the FPZ at the crack tip elongates extensively and the inelastic zone may not be lumped into a small zone (Figure 5-5). Therefore, NLFM is required to investigate the development of the fracture zone. Hillerborg et al. (1976) considered a tension-softening FPZ with a length of l_p along a fictitious crack at the tip of a pre-existing crack (a_0). The closure tractions act on the FPZ in a way that the closure stresses have the maximum values (f'_{ct}) at the end of micro-cracking area and gradually reduce to zero in the vicinity of the open crack where the crack opening displacement (COD) is equal to W_c (Figure 5-5c). The modulus of elasticity of the fracture process zone is lower than the modulus of the undamaged material ($E^* < E$). Therefore, the fracture of the concrete elements cannot be expressed only by one of the stress intensity factors (K) or the energy release rate (G).

In order to model the fracture mechanism, both of the fracture process zone and the tension-softening law are required. When the FPZ extends to its full length, the crack opening displacement (COD) of the fictitious crack reaches the critical value of W_c (Figure 5-5c) and the tensile stress reduces to zero and an open crack appears. In this condition, the relation between the cohesive stress and crack opening displacement for the FPZ can be stated as a tension-softening curve such as Figure 5-6a. The area under tension-softening curve is the fracture energy and can be defined as

$$G_F = \int_0^{w_c} \sigma dw \qquad 5\text{-}70$$

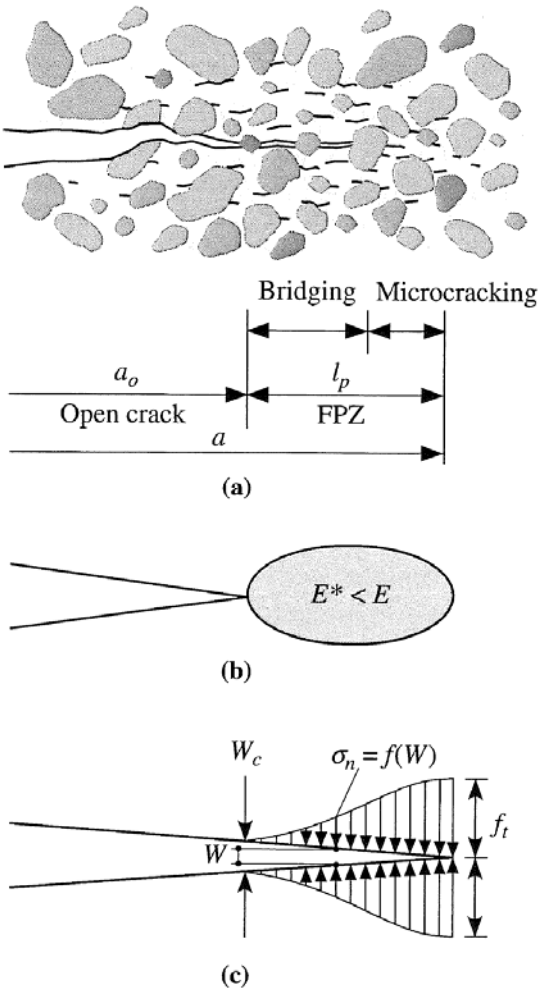

Figure 5-5. (a) Cracking in concrete, (b) reduction of elasticity modulus of FPZ, and (c) tension-softening in concrete (Shi 2009).

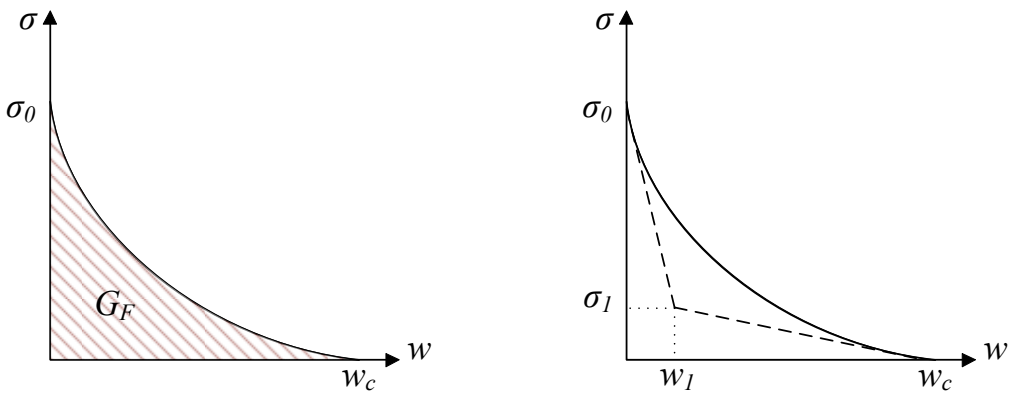

(a) (b)

Figure 5-6. (a) Relation between tensile stress and the COD along the FPZ and (b) normalized tension-softening law.

Except the fracture energy, the shape of the tension-softening relation of the concrete is another important parameter which is required to be defined. In most cases, this relation is idealized in a bilinear form (Figure 5-6b). The first section depicts a rapid loss of the strength, σ, while the section with lower slope is accompanied by increase in crack opening displacement, w.

When the bonded length is sufficiently greater than the effective bond length, the maximum transferable load in the single lap shear test can be predicted by Eq. 2-36. G_F is the interfacial fracture energy (antisymmetric in-plane shear mode). By substitution of Eq. 2-36 into Eq. 5-37,

$$\varepsilon_{0(\max)} = \frac{W_{frp}\sqrt{\frac{2(Et)_{frp}G_F}{1+\alpha}}}{W_{frp}(Et)_{frp}} \qquad 5\text{-}71$$

$$\varepsilon_{0(\max)} = \sqrt{\frac{2G_F}{(Et)_{frp}(1+\alpha)}} \qquad 5\text{-}72$$

Then, the following relationship can be proposed for G_F;

$$G_F = \frac{1}{2}(1+\alpha)\cdot(Et)_{frp}\cdot\varepsilon_{0(\max)}^2 \qquad 5\text{-}73$$

Since the axial stiffness of concrete is much higher than the FRP, it can be assumed that α is equal to zero, therefore:

$$G_F = \frac{1}{2}(Et)_{frp}\varepsilon_{0(\max)}^2 \qquad 5\text{-}74$$

Based on Eq. 5-74, the interfacial fracture energy can be determined by the FRP stiffness and the strain value at loaded end. Considering an exponential equation between the strain profile and slip at the loaded end, Dai et al. (2005) proposed the same relation for G_F except $\varepsilon_{0(max)}$ is replaced by a parameter, A, (Eq. 5-12). The same approach was adopted by Liu and Wu (2012) in which $\varepsilon_{0(max)}$ is replaced by α^2/β^2. A and α^2/β^2 are required to be determined by regression of the experimental results.

The fracture energy may also be determined based on the maximum shear stress which is obtained by Eq. 5-51. Considering Eqs. 5-37 and 5-51, the maximum shear stress can be estimated by

$$\tau_{\max} = \frac{9}{4} \cdot \frac{(Et)_{frp}}{L_{eff}} \cdot \varepsilon_{0(\max)} \qquad 5\text{-}75$$

By solving Eq. 5-75 for $\varepsilon_{0(max)}$ and substituting into Eq. 5-74

$$G_F = \frac{1}{2}(Et)_{frp} \cdot \left[\frac{4}{9} \frac{L_{eff}}{E_{frp} t_{frp}} \cdot \tau_{\max} \right]^2 \qquad 5\text{-}76$$

Therefore, the fracture energy can be calculated by

$$G_F = \frac{8L_{eff}^2}{81(Et)_{frp}} \cdot \tau_{\max}^2 \qquad 5\text{-}77$$

Eq. 5-74 determines the fracture energy based on the strain value at the loaded end corresponding to the maximum applied load while it is defined based on the maximum shear stress in Eq. 5-77. The accuracy of Eqs. 5-74 and 5-77 in prediction of the fracture energy is compared in section 5.4. The effective bond length (L_{eff}) for determination of the local interface law is obtained from Table 4-2 of Chapter 4.

5.3.2. Method B-Slip Fixity Condition

To obtain interfacial parameters using *Method A*, the effective bond length has to be known. In a more generic model (*Method B*), the bond-slip law can be developed based on the FRP length which is available in most of the tests. In addition, the slip of the loaded end is captured during the single lap shear tests in majority of the experiments. Therefore, it is advisable to determine the interface behaviour based on the global slip. This approach is used in *Method B* to obtain the local strain profile, shear stress and slip profiles. The advantage of this method is that the bond-slip law is expressed based on the properties of both adherents (adhesive) and adherends (FRP plate/laminate).

Strain Profile

Unknown parameters (*A*, *B*, *C* and *D*) of Eq. 5-32 can be found based on the following boundary conditions;

$$\varepsilon_{frp,x} = 0 \qquad \text{at} \qquad x = 0 \qquad \text{5-78}$$

$$s_x = 0 \qquad \text{at} \qquad x = 0 \qquad \text{5-79}$$

$$\varepsilon_{frp,x} = \varepsilon_0 \qquad \text{at} \qquad x = L \qquad \text{5-80}$$

$$s_x = s_l \qquad \text{at} \qquad x = L \qquad \text{5-81}$$

s_l is the global slip at the loaded end which is captured during the MSLS tests. Strain at the free end is zero which by substitution into Eq. 5-32 leads to $D = 0$.

Shear stress, $\tau_{int,x}$, may be expressed by the product of the FRP stiffness and the strain gradient over the bonded length

$$\tau_{\text{int},x} = \frac{d\varepsilon_{frp,x}}{dx} \cdot t_{frp} E_{frp} = \varepsilon'_{frp,x} E_{frp} t_{frp} \qquad \text{5-82}$$

Using Eqs. 5-82 and 5-68, the slip profile along the bonded joint is defined by

$$s_x = \frac{t_{adh}}{G_{adh}} \cdot (Et)_{frp} \cdot \varepsilon'_{frp,x} \qquad \text{5-83}$$

Eq. 5-83 can be simplified by considering an interface property factor, λ, which represents the properties of both the FRP and the adhesive layer

$$s_x = \lambda \cdot \varepsilon'_{frp,x} \qquad \text{5-84}$$

$$\lambda = \left(\frac{t}{G}\right)_{adh} \cdot (Et)_{frp} \qquad 5\text{-}85$$

By derivation of Eq. 5-32

$$\varepsilon'_{frp,x} = 3Ax^2 + 2Bx + C \qquad 5\text{-}86$$

$$s_x = \lambda \cdot (3Ax^2 + 2Bx + C) \qquad 5\text{-}87$$

and using boundary condition at the free end (Eq. 5-79)

$$C = 0 \qquad 5\text{-}88$$

To determine the other two unknown parameters in Eq. 5-87, boundary conditions Eq. 5-80 and 5-81 may be employed

$$\varepsilon_0 = AL^3 + BL^2 \qquad 5\text{-}89$$

$$s_l = \lambda \cdot (3AL^2 + 2BL) \qquad 5\text{-}90$$

Solving Eqs. 5-89 and 5-90 simultaneously ends to the following relation for strain profile along the bonded length;

$$\varepsilon_{frp,x} = Ax^3 + Bx^2 \qquad 5\text{-}91$$

$$A = \frac{1}{\lambda L^3} \cdot (s_l \cdot L - 2\varepsilon_0 \lambda) \qquad 5\text{-}92$$

and

$$B = \frac{1}{\lambda \cdot L^2} \cdot (3\lambda\varepsilon_0 - s_l L) \qquad 5\text{-}93$$

where λ is obtained from Eq. 5-85.

Shear Stress

The same procedure as *Method A* (Eq. 5-47) can be applied to obtain the shear stress profile of the joints. By substituting the derivative of Eq. 5-91 into Eq. 5-47;

$$\frac{d\varepsilon_{frp,x}}{dx} = \varepsilon'_{frp,x} = 3Ax^2 + 2Bx \qquad 5\text{-}94$$

$$\tau_{\text{int},x} = (Et)_{frp} \cdot (3Ax^2 + 2Bx) \qquad 5\text{-}95$$

Therefore, the maximum shear stress can be found by

$$\tau_{\max} = -\frac{B^2}{3A} \cdot (Et)_{frp} \qquad 5\text{-}96$$

Slip Profile

Ignoring the concrete displacement, Eq. 5-52 leads to the following expression for the calculation of the local slip along the bonded joint;

$$s_x = \int (Ax^3 + Bx^2)dx \qquad 5\text{-}97$$

$$s_x = \frac{1}{4}Ax^4 + \frac{1}{3}Bx^3 \qquad 5\text{-}98$$

where *A* and *B* are determined based on Eqs. 5-92 and 5-93.

Considering the above equations (Eqs. 5-91, 5-96 and 5-98), the advantage of *Method B* in comparison to *Method A* is that the governing equations of the interface (strain profile, shear stress, and slip profile) are determined based on the properties of both the adhesives and the FRP plate/laminate.

5.4. Validation of the Proposed Models against Different Processing Techniques

This part of the chapter evaluates the ability of the proposed models to predict the interface behaviour. It presents a comparison between the analytical results based on the methods proposed in section 5.3 and the test data obtained from MSLS tests reported in Chapter 4. The validation is carried out by evaluation of different characteristics of the joints, such as the maximum load carrying capacity, the strain, shear stress and slip profiles and also the fracture energy of the interface and the effective parameters.

5.4.1. Method A-Strain Fixity Condition

The maximum strain at the loaded end, ε_0, can be predicted based on the applied load and the FRP axial rigidity. Figure 5-7 compares the strain values which are calculated based on Eq. 5-37 with those recorded during MSLS tests. The values are presented for different types of processing techniques (pultrusion, wet lay-up and VARI). This figure indicates that Eq. 5-37 agrees well with the test data for the adhesively bonded joints manufactured with various methods. The overall average value of the observed to the predicted maximum strain ratio is 1.06 with standard deviation (S.D.) of 0.26 and coefficient of variation (C.O.V.) of 24 percent.

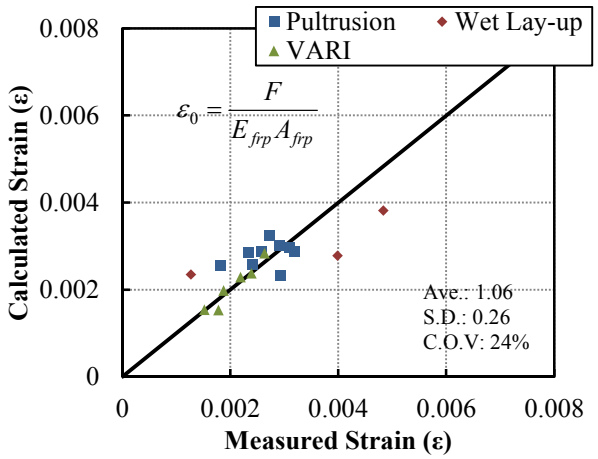

Figure 5-7. Comparison between experimental and predicted maximum strain value, ε_0, at the loaded end.

Figure 5-8 and Figure 5-9 compare the experimental results of the strain profile against the predicted strain values obtained from the proposed analytical method. Figure 5-8 and Figure 5-9 represent the FRP strain at the level of loading as the interfacial crack starts to

propagate over the bond length and the strains corresponding to the ultimate applied load, respectively.

The analytical results obtained from Eqs. 5-45 and 5-46 are in good agreement with experimental observations. Although some deviation exists between the experimental and analytical results, the strain profile is predicted well for both initial and ultimate stages of loading. This variation is due to the effects of external parameters such as, local stresses at the loaded end of the FRP (Yao et al. 2005). Furthermore, the proposed model can significantly follow interfacial debonding along the bond length.

Due to local stresses and deformations, the strain captured by two consecutive strain gauges (one on the detached part of the FRP and the other on the bonded region) after macro-crack development can differ (e.g. sample SF-B-3.3). Therefore, the strain values can reach higher values at inside regions of the bonded area rather than the loaded end. Based on this fact, the analytical approach provides more stable results compared with the strain gauges readings."

The prediction of the proposed model is compared with Dai et al.'s model (2005) and (2006) for samples in Figure 5-10. Figure 5-10 shows that, both the present and Dai et al.'s model (Dai et al. 2005, 2006), are in good agreement with experimental observations.

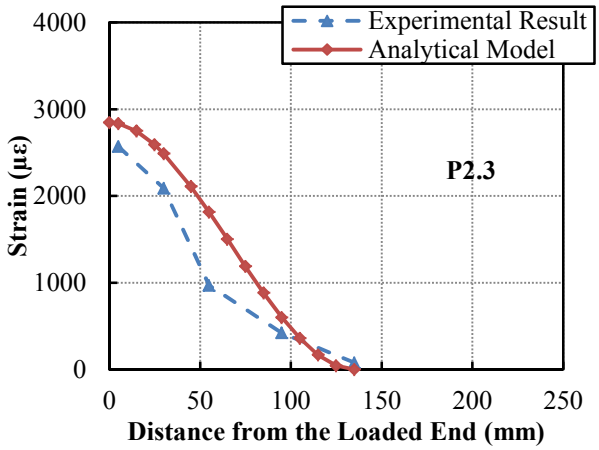
Experimental Result
Analytical Model
P2.3
Strain (με)
Distance from the Loaded End (mm)
0
1000
2000
3000
4000
0
50
100
150
200
250

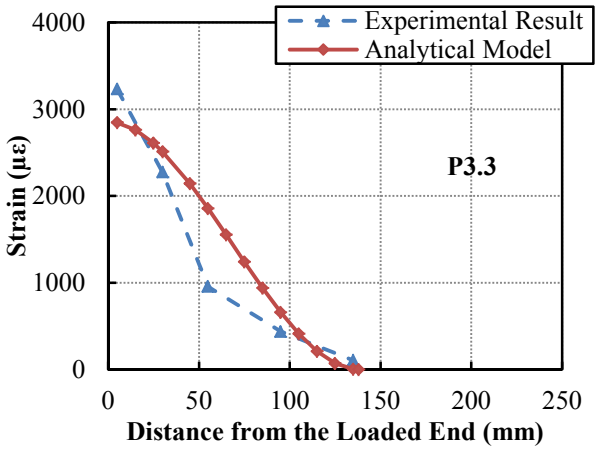
Experimental Result
Analytical Model
P3.3
Strain (με)
Distance from the Loaded End (mm)
0
1000
2000
3000
4000
0
50
100
150
200
250

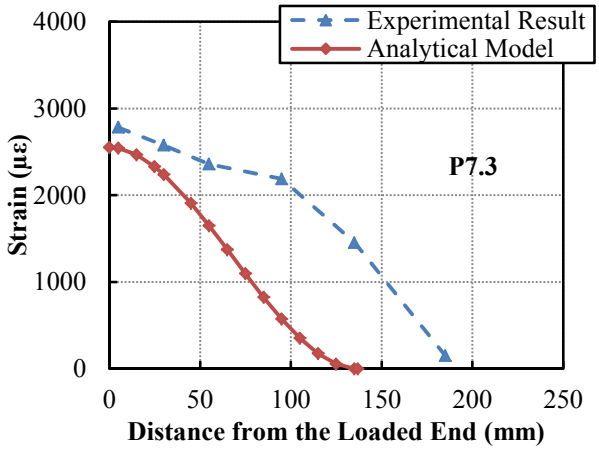
Experimental Result
Analytical Model
P7.3
Strain (με)
Distance from the Loaded End (mm)
0
1000
2000
3000
4000
0
50
100
150
200
250

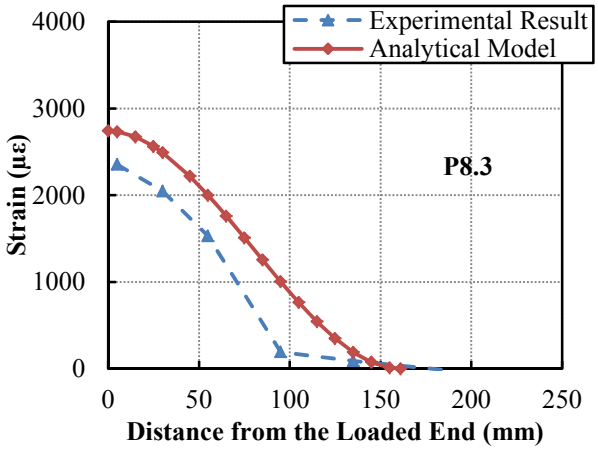
Experimental Result
Analytical Model
P8.3
Strain (με)
Distance from the Loaded End (mm)
0
1000
2000
3000
4000
0
50
100
150
200
250

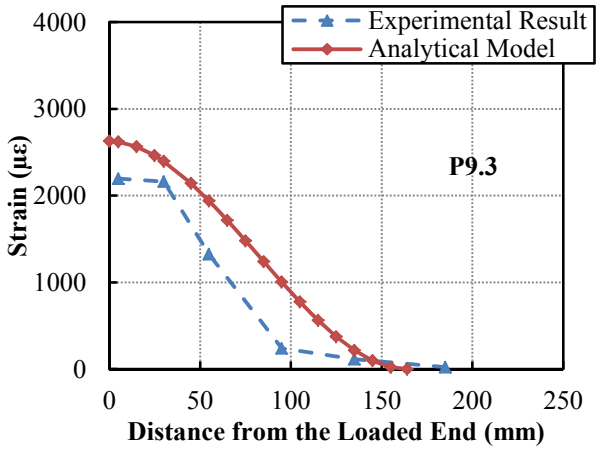
Experimental Result
Analytical Model
P9.3
Strain (με)
Distance from the Loaded End (mm)
0
1000
2000
3000
4000
0
50
100
150
200
250

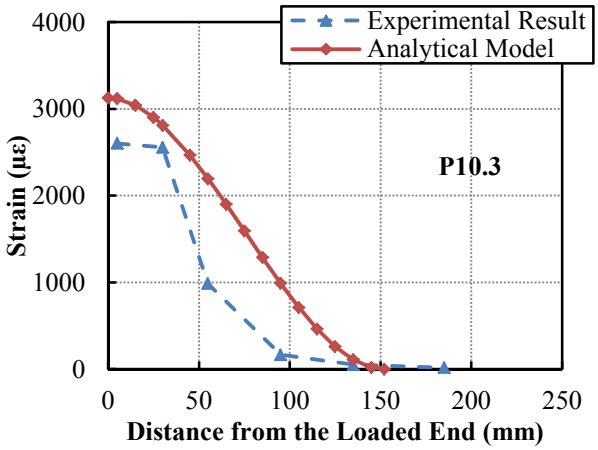
Experimental Result
Analytical Model
P10.3
Strain (με)
Distance from the Loaded End (mm)
0
1000
2000
3000
4000
0
50
100
150
200
250

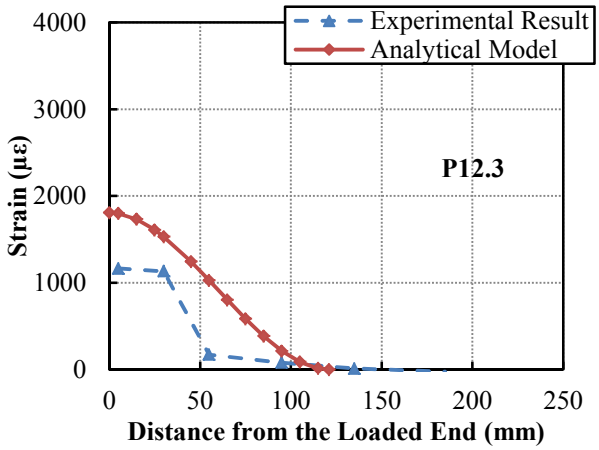
Experimental Result
Analytical Model
P12.3
Strain (με)
Distance from the Loaded End (mm)
0
1000
2000
3000
4000
0
50
100
150
200
250

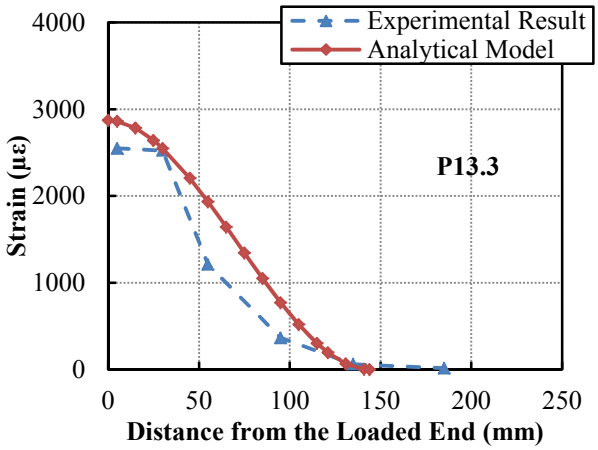
Experimental Result
Analytical Model
P13.3
Strain (με)
Distance from the Loaded End (mm)
0
1000
2000
3000
4000
0
50
100
150
200
250

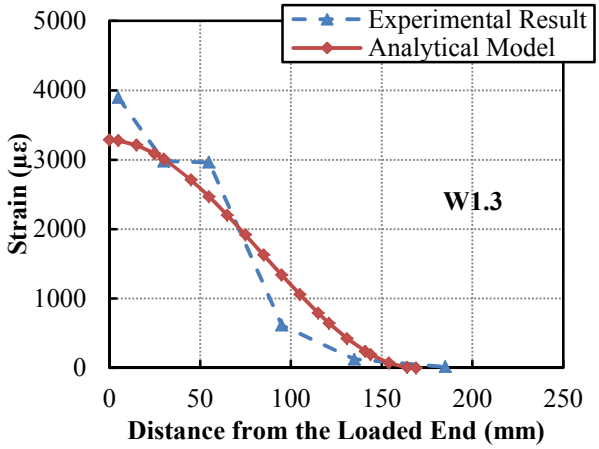
Experimental Result
Analytical Model
W1.3
Strain (με)
Distance from the Loaded End (mm)
0
1000
2000
3000
4000
5000
0
50
100
150
200
250

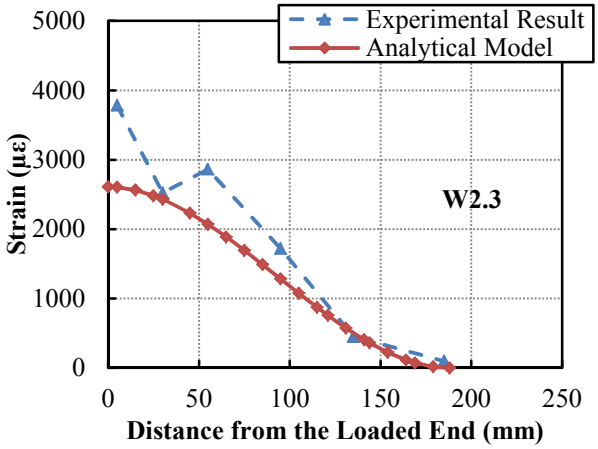
Experimental Result
Analytical Model
W2.3
Strain (με)
Distance from the Loaded End (mm)
0
1000
2000
3000
4000
5000
0
50
100
150
200
250

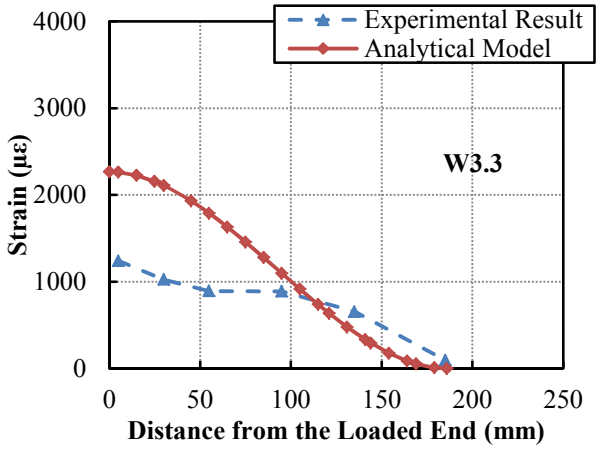
Experimental Result
Analytical Model
W3.3
Strain (με)
Distance from the Loaded End (mm)
0
1000
2000
3000
4000
0
50
100
150
200
250

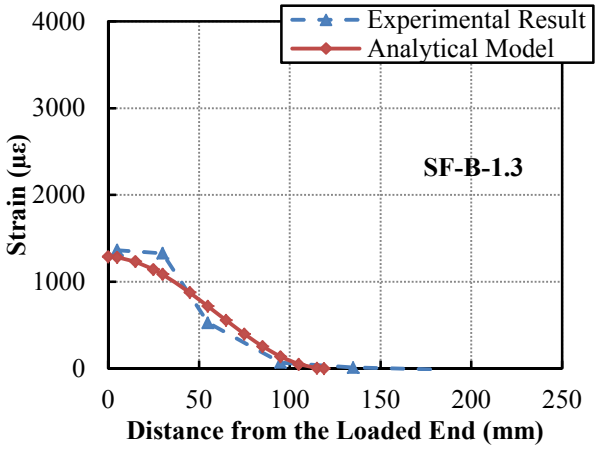
Experimental Result
Analytical Model
SF-B-1.3
Strain (με)
Distance from the Loaded End (mm)
0
1000
2000
3000
4000
0
50
100
150
200
250

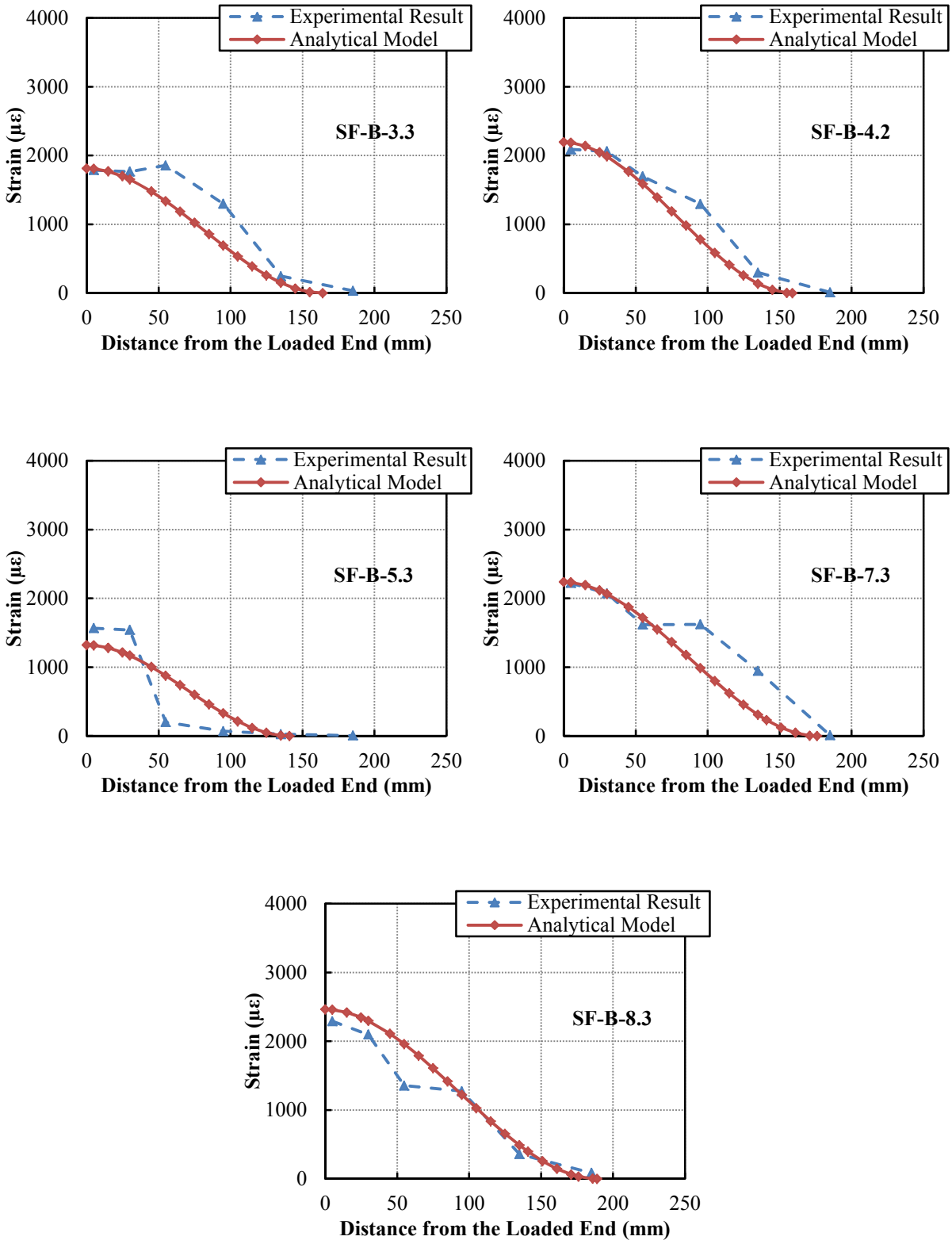

Figure 5-8. Analytical prediction of the strain distribution corresponding to the initiation of the interfacial crack (*Method A*).

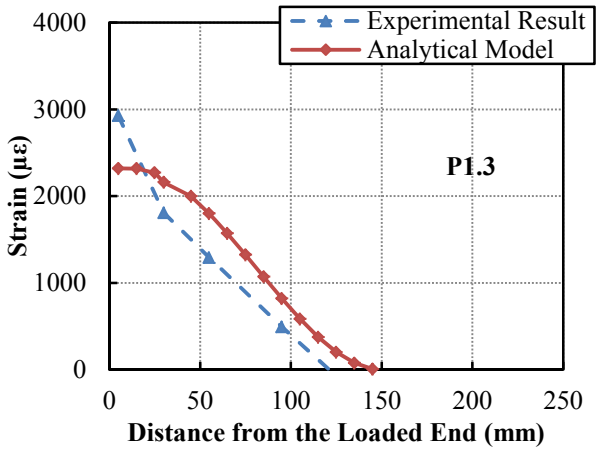
Experimental Result
Analytical Model
P1.3
Strain (με)
Distance from the Loaded End (mm)
0
1000
2000
3000
4000
0
50
100
150
200
250

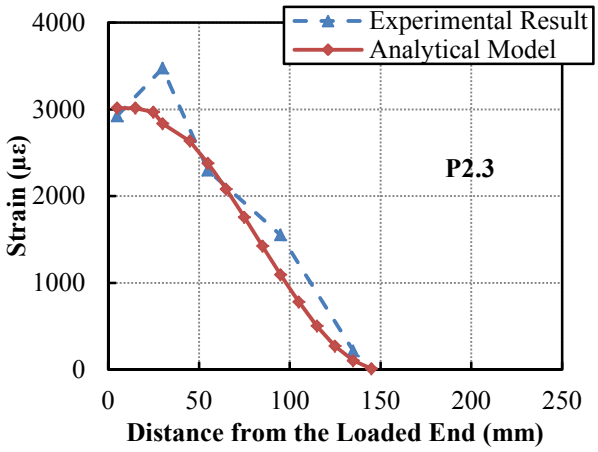
Experimental Result
Analytical Model
P2.3
Strain (με)
Distance from the Loaded End (mm)
0
1000
2000
3000
4000
0
50
100
150
200
250

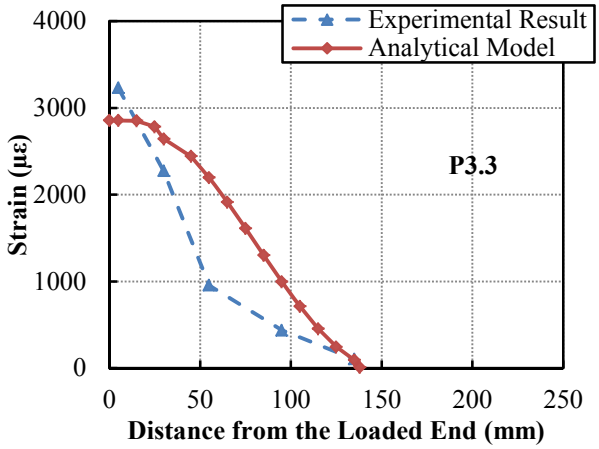
Experimental Result
Analytical Model
P3.3
Strain (με)
Distance from the Loaded End (mm)
0
1000
2000
3000
4000
0
50
100
150
200
250

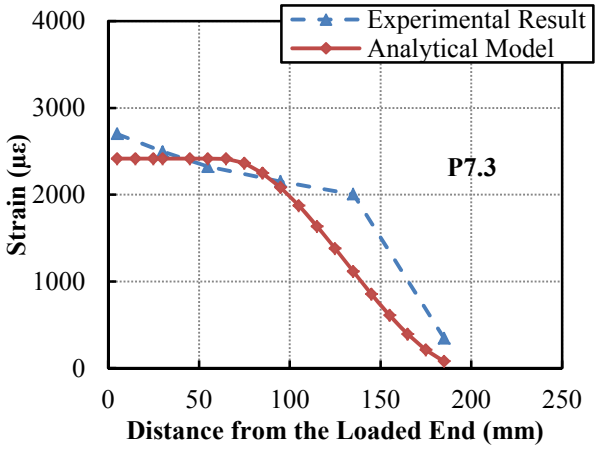
Experimental Result
Analytical Model
P7.3
Strain (με)
Distance from the Loaded End (mm)
0
1000
2000
3000
4000
0
50
100
150
200
250

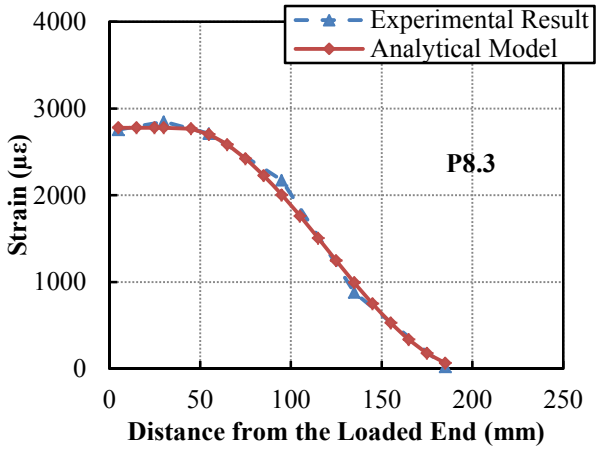
Experimental Result
Analytical Model
P8.3
Strain (με)
Distance from the Loaded End (mm)
0
1000
2000
3000
4000
0
50
100
150
200
250

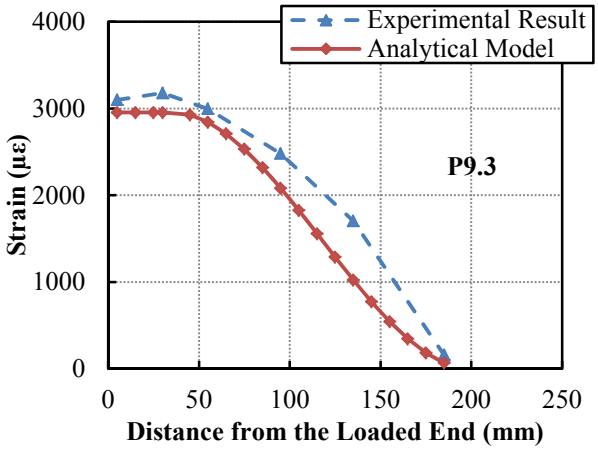
Experimental Result
Analytical Model
P9.3
Strain (με)
Distance from the Loaded End (mm)
0
1000
2000
3000
4000
0
50
100
150
200
250

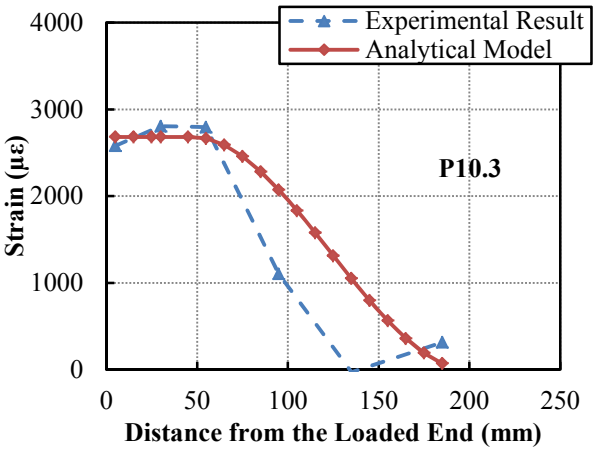
Experimental Result
Analytical Model
P10.3
Strain (με)
Distance from the Loaded End (mm)

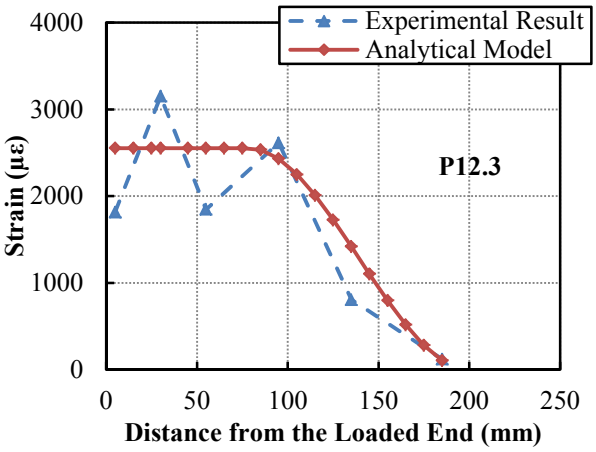
Experimental Result
Analytical Model
P12.3
Strain (με)
Distance from the Loaded End (mm)

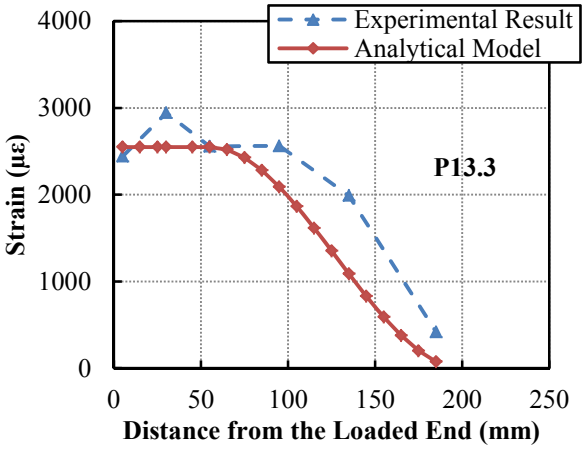
Experimental Result
Analytical Model
P13.3
Strain (με)
Distance from the Loaded End (mm)

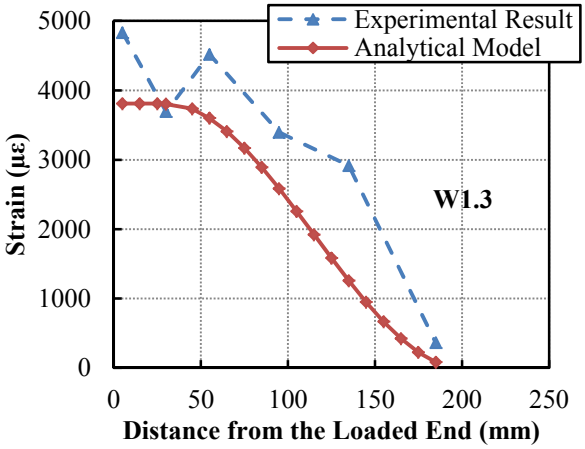
Experimental Result
Analytical Model
W1.3
Strain (με)
Distance from the Loaded End (mm)

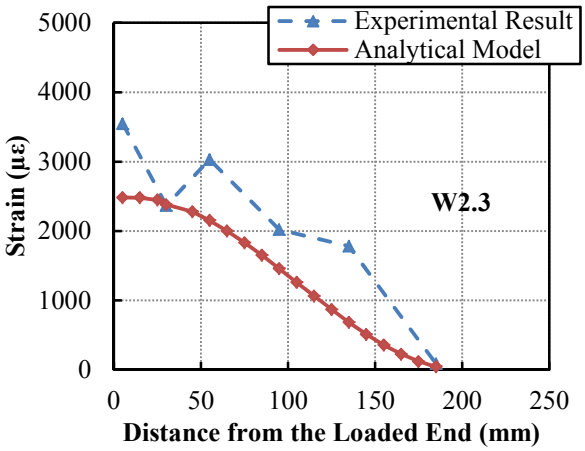
Experimental Result
Analytical Model
W2.3
Strain (με)
Distance from the Loaded End (mm)

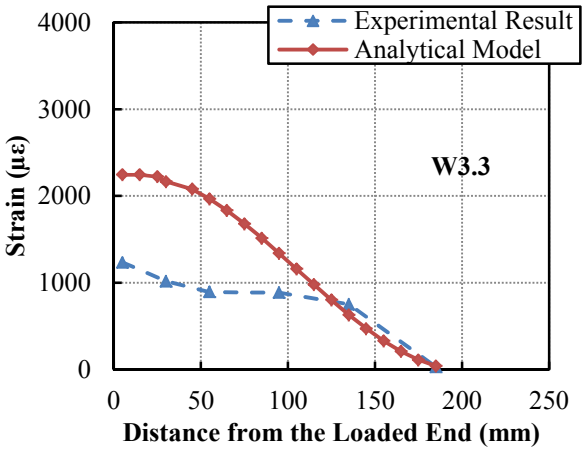
Experimental Result
Analytical Model
W3.3
Strain (με)
Distance from the Loaded End (mm)

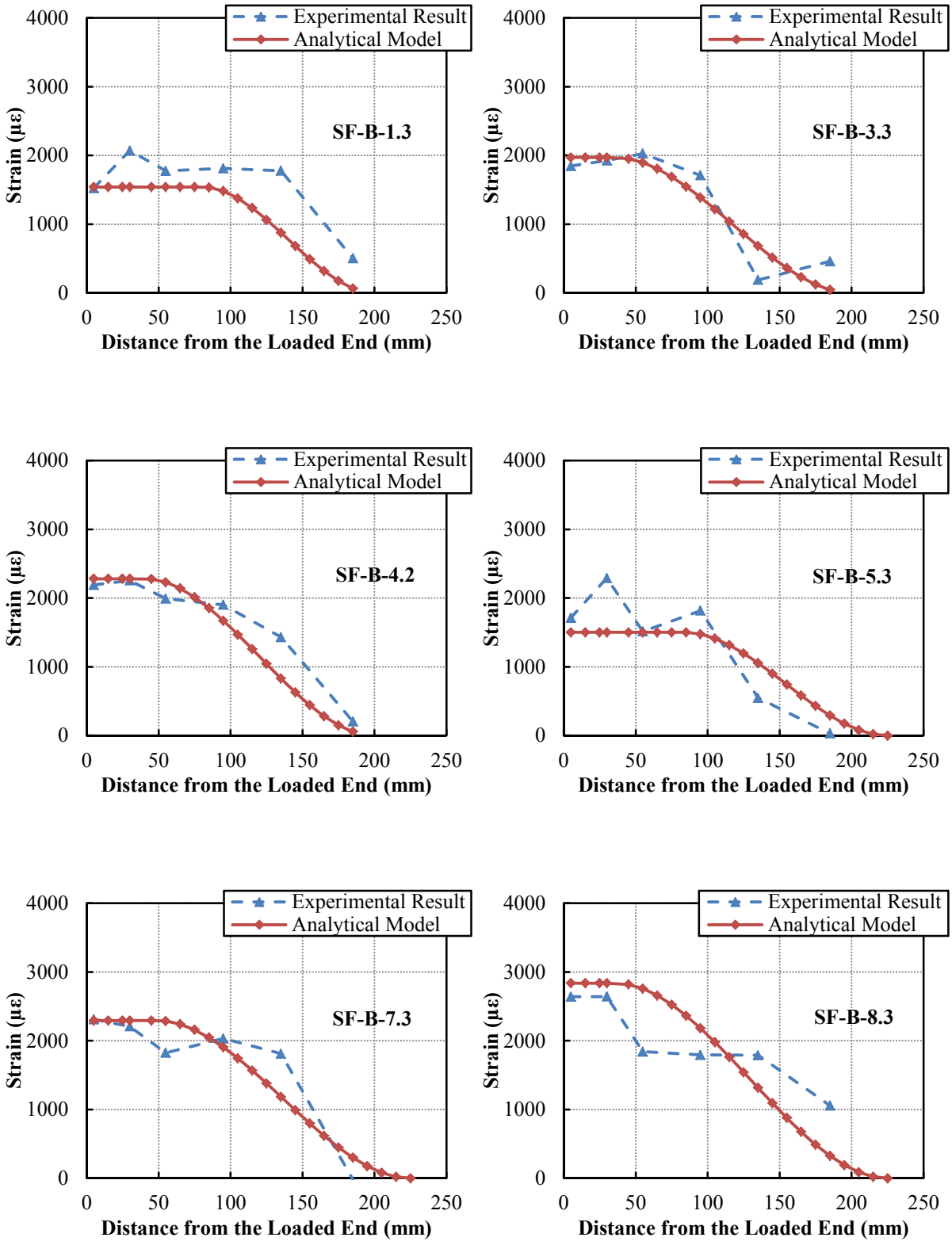

Figure 5-9. Analytical prediction of the strain distribution corresponding to the ultimate applied load (*Method A*).

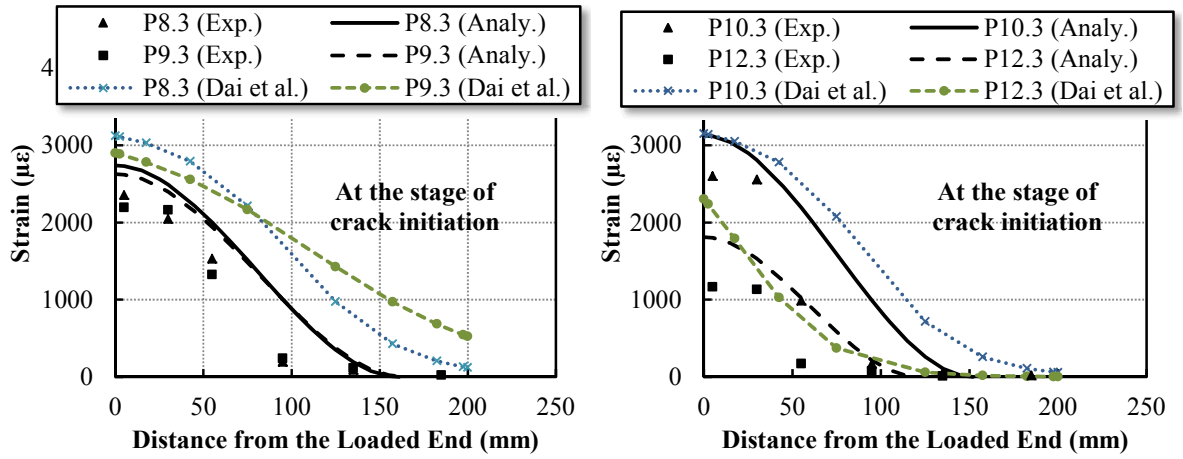

Figure 5-10. Comparison between Dai et al's (2006) and the present models.

Comparison between the experimental and analytical bond stress distribution of samples is presented in Figure 5-11. The shear stresses correspond to the level of crack initiation and the ultimate load. For the experimental results, the strain at the loaded end was calculated based on equation 5-37. The proposed analytical approach can estimate the bond stress and its distribution over the FRP constantly and smoothly. The crack starts at the loaded end and propagates toward the free end during different stages of loading and finally leads to FRP debonding.

In the models suggested in the literature, a constant shear stress is assumed along the bonded region after the initiation of macro-crack. However, experimentally-observed distributions of the shear stress of the joints at different loading levels reveal that the magnitude of τ_{max} changes along the bondline. The predicted shear stress profile of the specimens in Figure 5-11 shows that the model which is proposed in this research is able to successfully capture the variation of the stress profile along the FRP. This can be due to the fact that the effective parameters (e.g. FRP properties, applied load, and effective bond length) are considered in *Method A* for determination of the shear stress profile.

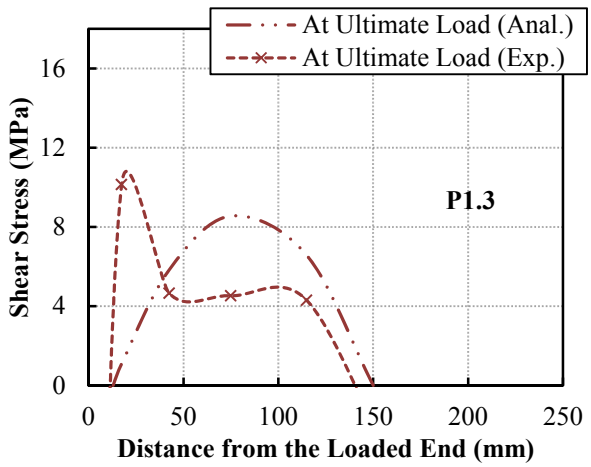
At Ultimate Load (Anal.)
At Ultimate Load (Exp.)
P1.3
Shear Stress (MPa)
Distance from the Loaded End (mm)
0
4
8
12
16
0
50
100
150
200
250

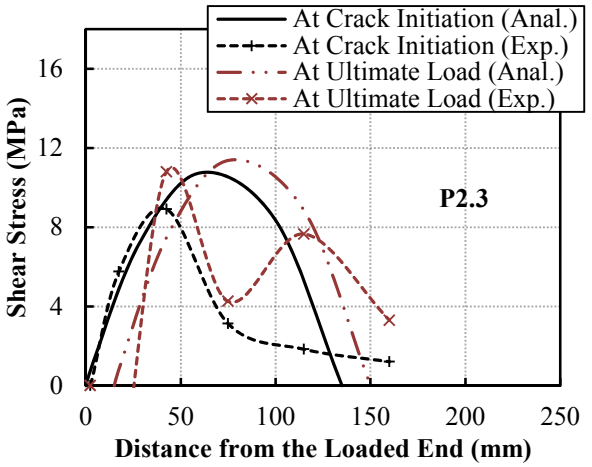
At Crack Initiation (Anal.)
At Crack Initiation (Exp.)
At Ultimate Load (Anal.)
At Ultimate Load (Exp.)
P2.3
Shear Stress (MPa)
Distance from the Loaded End (mm)
0
4
8
12
16
0
50
100
150
200
250

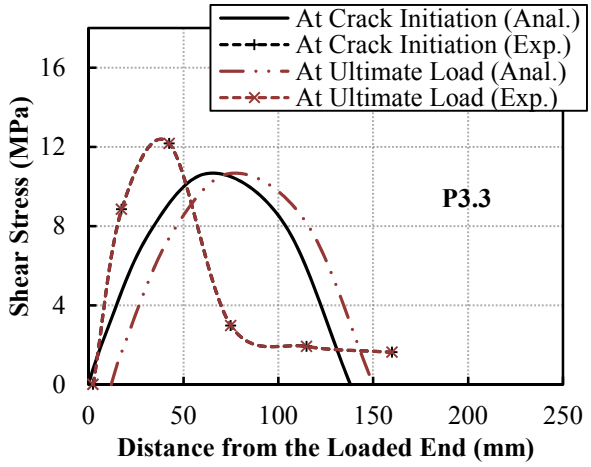
At Crack Initiation (Anal.)
At Crack Initiation (Exp.)
At Ultimate Load (Anal.)
At Ultimate Load (Exp.)
P3.3
Shear Stress (MPa)
Distance from the Loaded End (mm)
0
4
8
12
16
0
50
100
150
200
250

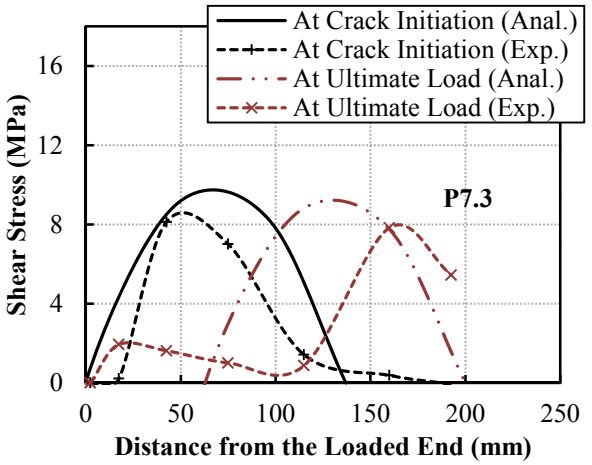
At Crack Initiation (Anal.)
At Crack Initiation (Exp.)
At Ultimate Load (Anal.)
At Ultimate Load (Exp.)
P7.3
Shear Stress (MPa)
Distance from the Loaded End (mm)
0
4
8
12
16
0
50
100
150
200
250

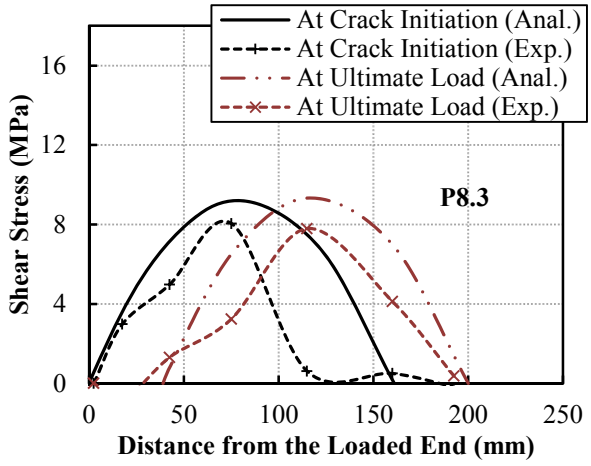
At Crack Initiation (Anal.)
At Crack Initiation (Exp.)
At Ultimate Load (Anal.)
At Ultimate Load (Exp.)
P8.3
Shear Stress (MPa)
Distance from the Loaded End (mm)
0
4
8
12
16
0
50
100
150
200
250

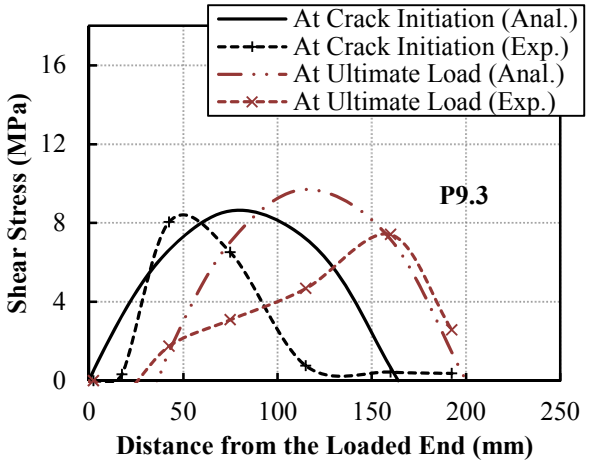
At Crack Initiation (Anal.)
At Crack Initiation (Exp.)
At Ultimate Load (Anal.)
At Ultimate Load (Exp.)
P9.3
Shear Stress (MPa)
Distance from the Loaded End (mm)
0
4
8
12
16
0
50
100
150
200
250

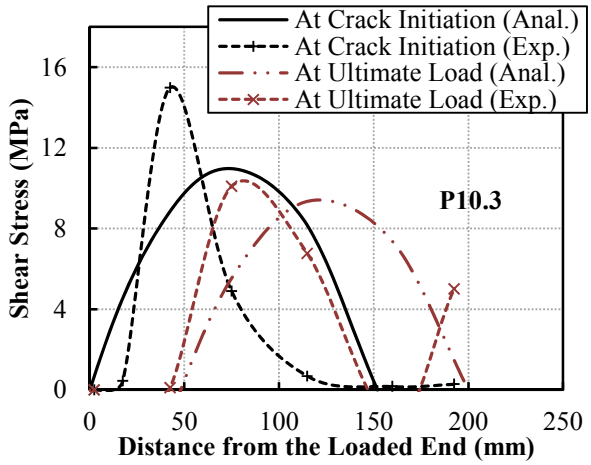
At Crack Initiation (Anal.)
At Crack Initiation (Exp.)
At Ultimate Load (Anal.)
At Ultimate Load (Exp.)
P10.3
Shear Stress (MPa)
Distance from the Loaded End (mm)

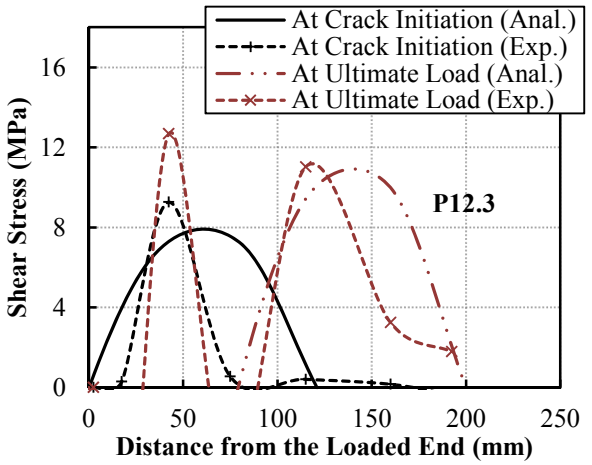
At Crack Initiation (Anal.)
At Crack Initiation (Exp.)
At Ultimate Load (Anal.)
At Ultimate Load (Exp.)
P12.3
Shear Stress (MPa)
Distance from the Loaded End (mm)

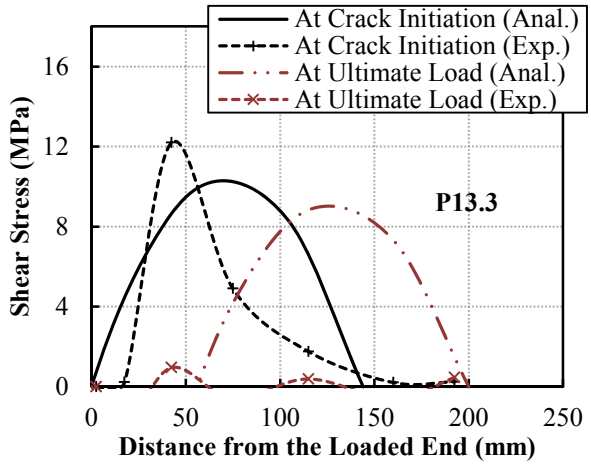
At Crack Initiation (Anal.)
At Crack Initiation (Exp.)
At Ultimate Load (Anal.)
At Ultimate Load (Exp.)
P13.3
Shear Stress (MPa)
Distance from the Loaded End (mm)

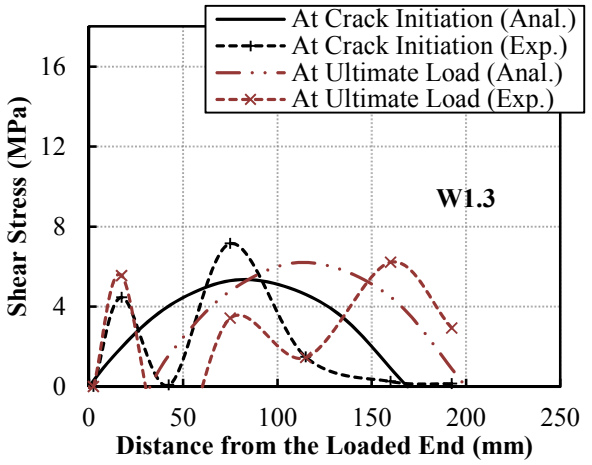
At Crack Initiation (Anal.)
At Crack Initiation (Exp.)
At Ultimate Load (Anal.)
At Ultimate Load (Exp.)
W1.3
Shear Stress (MPa)
Distance from the Loaded End (mm)

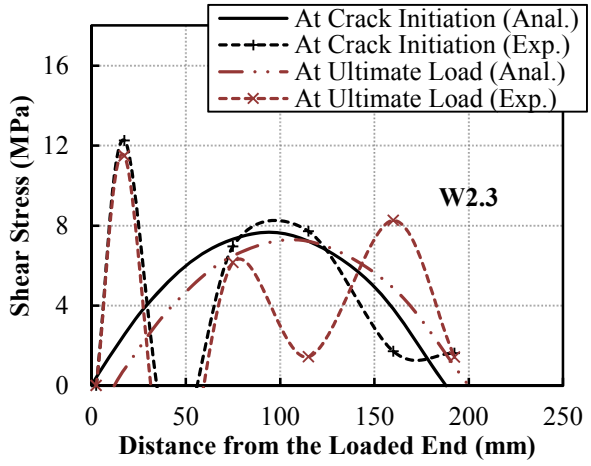
At Crack Initiation (Anal.)
At Crack Initiation (Exp.)
At Ultimate Load (Anal.)
At Ultimate Load (Exp.)
W2.3
Shear Stress (MPa)
Distance from the Loaded End (mm)

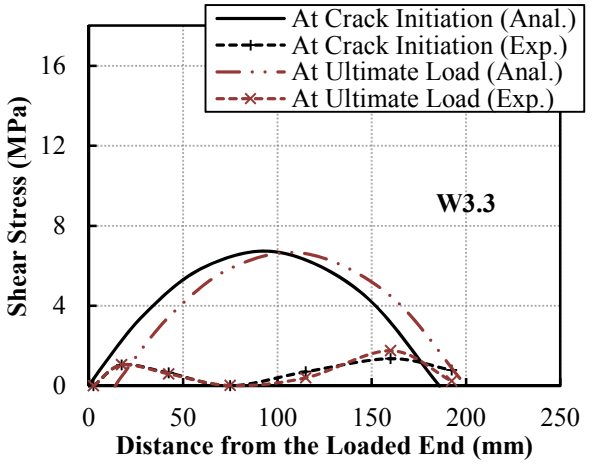
At Crack Initiation (Anal.)
At Crack Initiation (Exp.)
At Ultimate Load (Anal.)
At Ultimate Load (Exp.)
W3.3
Shear Stress (MPa)
Distance from the Loaded End (mm)

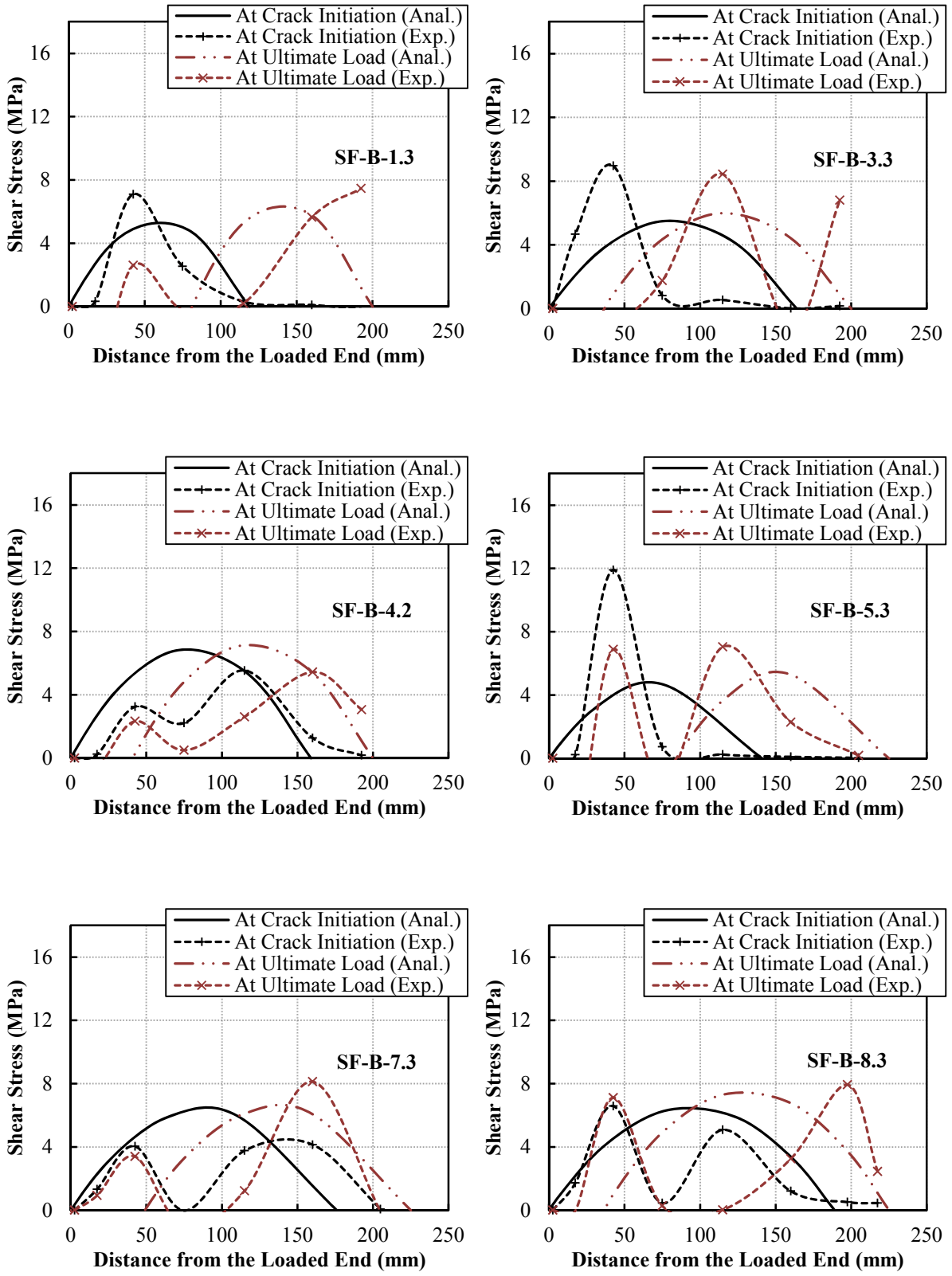

Figure 5-11. Experimental and analytical (*Method A*) distribution of the bond stress for the samples processed with different manufacturing techniques.

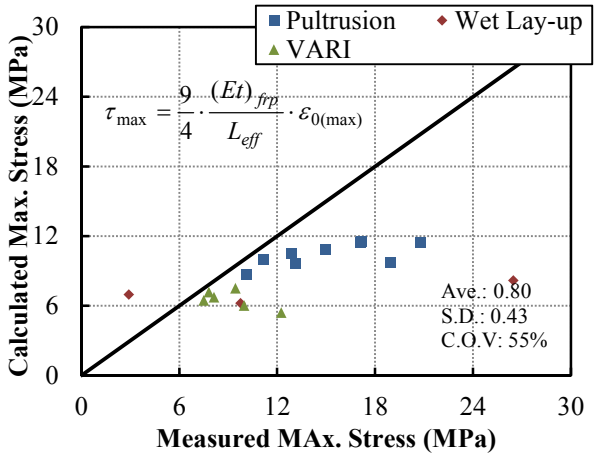

Figure 5-12. Calculated (*Method A*) vs measured maximum shear stresses.

Some variations in terms of maximum bond shear and stress distribution are observed. It can be explained by discontinuity of the bond and more importantly the heterogeneous nature of the concrete. As it was described in section 4.6, the readings for two consecutive strain gauges can differ outstandingly if one strain gauge is installed over an aggregate and the other placed on the mortar. It may cause stress concentration and discrepancies in experimental results and finally differences between analytical result and test data. However, the proposed model successfully estimates the shear stress values considering the crack growth along the bonded area. In addition, the overall value of the maximum shear stress in the bonded joints calculated based on Eq. 5-75 shows a good agreement with the experimental results (Figure 5-12). The proposed model slightly underestimates τ_{max} (total average of 0.8).

To compare the results of the proposed model with the previously developed models, Yuan et al. (2001) and Dai et al. [38], the stress distribution of the samples at crack initiation is shown in Figure 5-13. For more information regarding the formulation of the shear stress based on Yuan et al.'s and Dai et al.'s model, author refer to Yuan et al. (2001) and Dai et al. (2005). Figure 5-13 indicates that the present model is able to predict the shear stresses along the bonded length with reasonable accuracy.

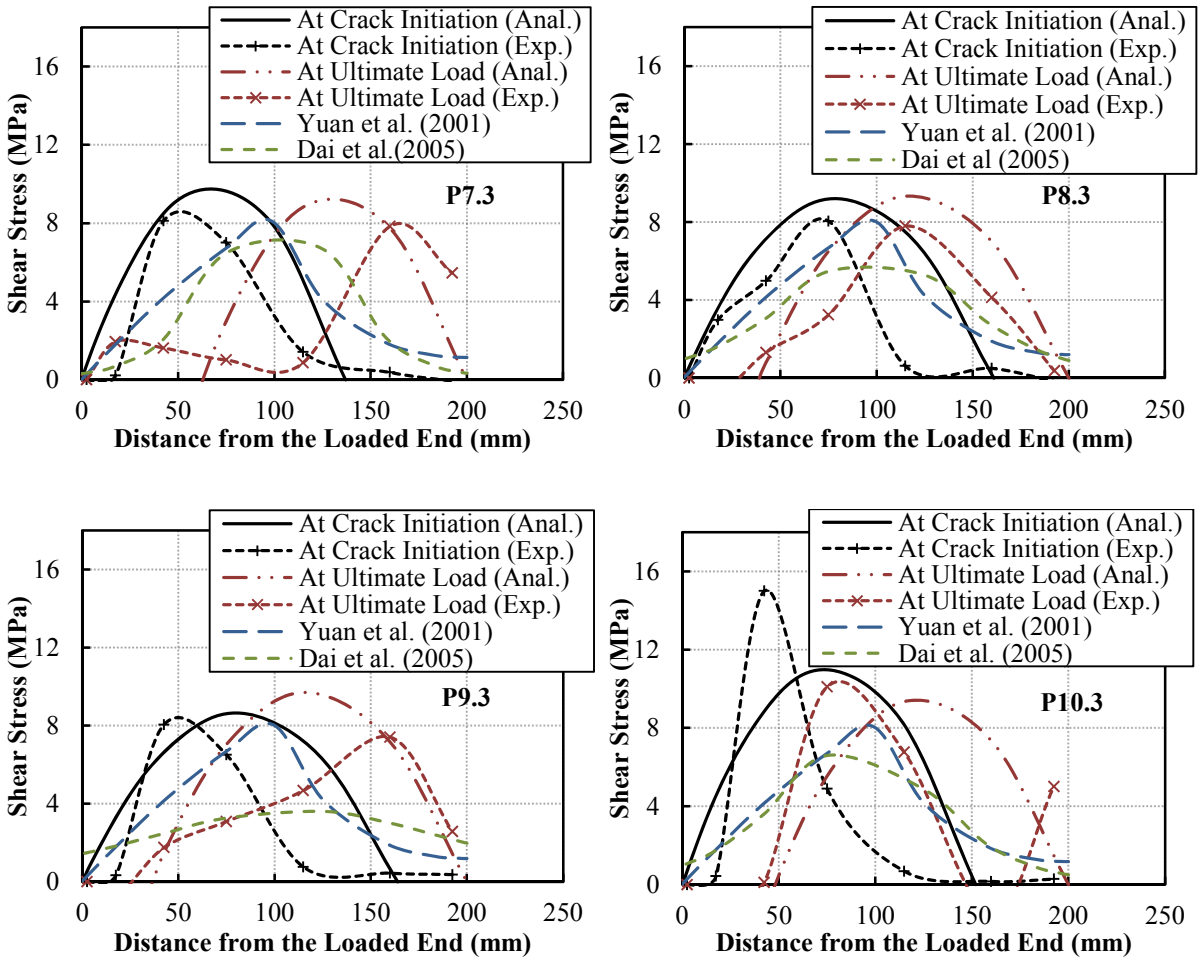

Figure 5-13. A comparison between the present model and other proposed models.

For further investigation, the experimentally obtained bond slip profile is compared with the analytical ones based on Eqs. 5-63 and 5-64. The slip gradually reduces toward the free end of the joint with a polynomial function of degree four. Figure 5-14 reveals that the slip distributions predicted by the analytical derivation agrees well with the results measured experimentally. This close agreement is valid throughout the total loading levels, the linear (prior to crack initiation) up to the nonlinear stages and finally ultimate load.

As it was mentioned previously in section 4.4, sample P1.3 (with no initial unbonded length, IUL=0.0) reached its maximum load carrying capacity prior to the complete propagation of the interfacial crack along the bonded region (Figure 4-4). Therefore, the analytically-obtained slip profile of the specimen is just compared with the corresponding experimental one at the ultimate load level in Figure 5-14. Based on this figure, the proposed relationships are also valid for the short joints in which the interface crack is not able to propagate completely through the bonded length prior to the failure.

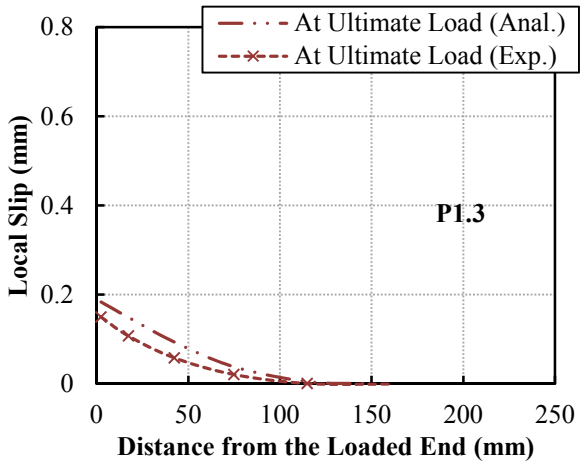
At Ultimate Load (Anal.)
At Ultimate Load (Exp.)
P1.3
Local Slip (mm)
Distance from the Loaded End (mm)
0
0.2
0.4
0.6
0.8
0
50
100
150
200
250

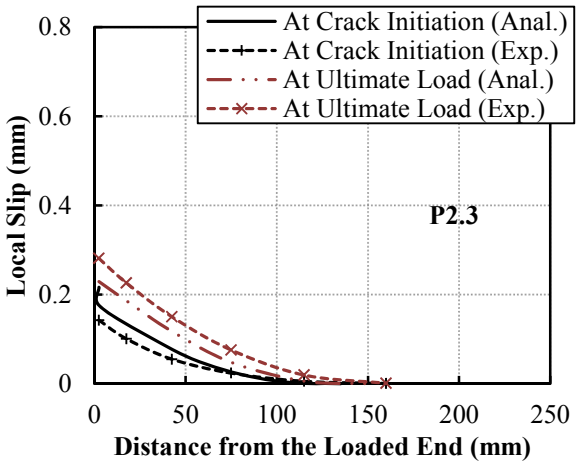
At Crack Initiation (Anal.)
At Crack Initiation (Exp.)
At Ultimate Load (Anal.)
At Ultimate Load (Exp.)
P2.3
Local Slip (mm)
Distance from the Loaded End (mm)
0
0.2
0.4
0.6
0.8
0
50
100
150
200
250

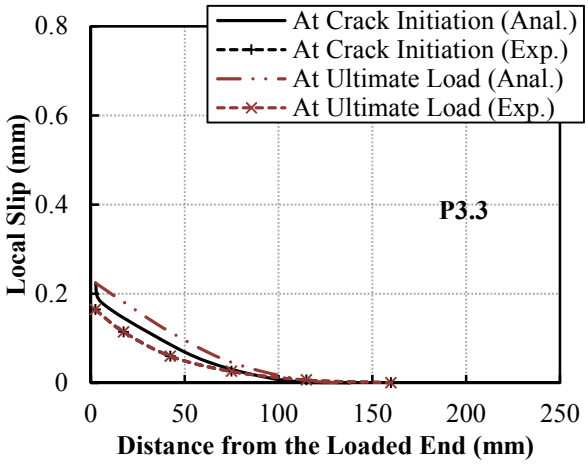
At Crack Initiation (Anal.)
At Crack Initiation (Exp.)
At Ultimate Load (Anal.)
At Ultimate Load (Exp.)
P3.3
Local Slip (mm)
Distance from the Loaded End (mm)
0
0.2
0.4
0.6
0.8
0
50
100
150
200
250

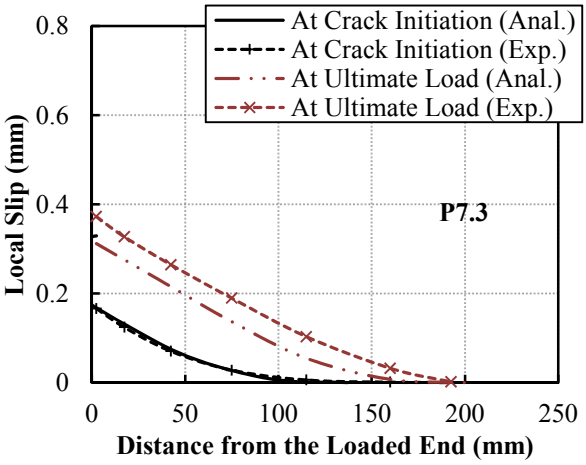
At Crack Initiation (Anal.)
At Crack Initiation (Exp.)
At Ultimate Load (Anal.)
At Ultimate Load (Exp.)
P7.3
Local Slip (mm)
Distance from the Loaded End (mm)
0
0.2
0.4
0.6
0.8
0
50
100
150
200
250

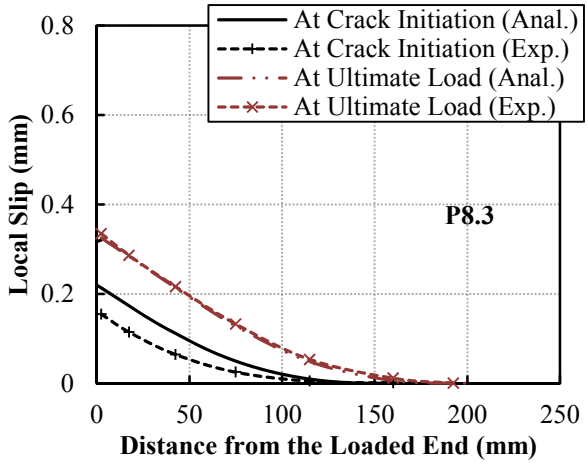
At Crack Initiation (Anal.)
At Crack Initiation (Exp.)
At Ultimate Load (Anal.)
At Ultimate Load (Exp.)
P8.3
Local Slip (mm)
Distance from the Loaded End (mm)
0
0.2
0.4
0.6
0.8
0
50
100
150
200
250

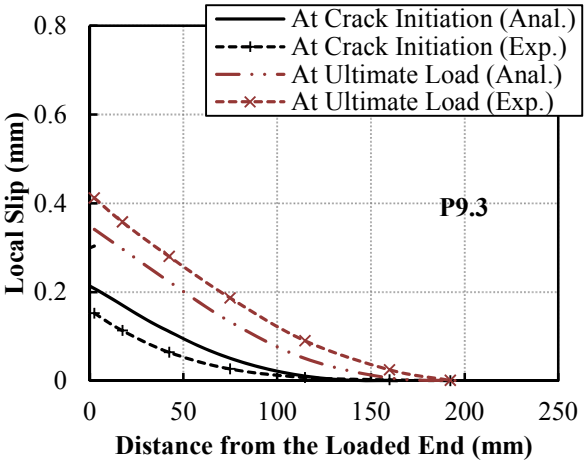
At Crack Initiation (Anal.)
At Crack Initiation (Exp.)
At Ultimate Load (Anal.)
At Ultimate Load (Exp.)
P9.3
Local Slip (mm)
Distance from the Loaded End (mm)
0
0.2
0.4
0.6
0.8
0
50
100
150
200
250

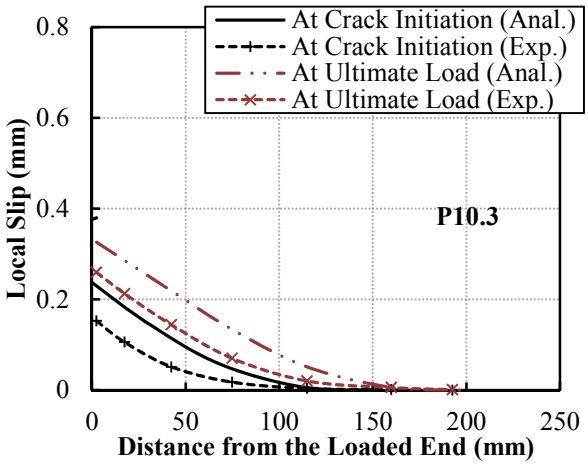
At Crack Initiation (Anal.)
At Crack Initiation (Exp.)
At Ultimate Load (Anal.)
At Ultimate Load (Exp.)
P10.3
Local Slip (mm)
Distance from the Loaded End (mm)
0
0.2
0.4
0.6
0.8
0
50
100
150
200
250

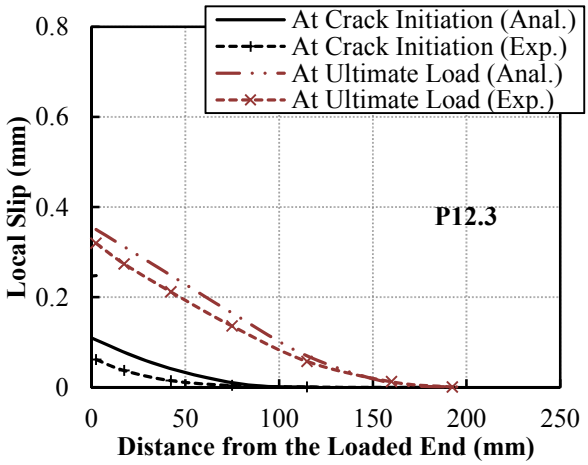
At Crack Initiation (Anal.)
At Crack Initiation (Exp.)
At Ultimate Load (Anal.)
At Ultimate Load (Exp.)
P12.3
Local Slip (mm)
Distance from the Loaded End (mm)
0
0.2
0.4
0.6
0.8
0
50
100
150
200
250

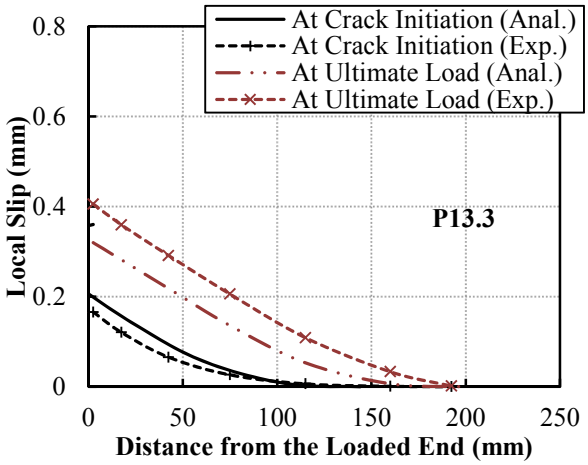
At Crack Initiation (Anal.)
At Crack Initiation (Exp.)
At Ultimate Load (Anal.)
At Ultimate Load (Exp.)
P13.3
Local Slip (mm)
Distance from the Loaded End (mm)
0
0.2
0.4
0.6
0.8
0
50
100
150
200
250

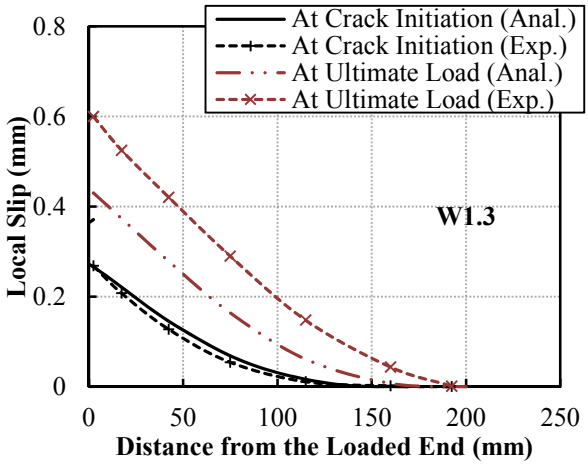
At Crack Initiation (Anal.)
At Crack Initiation (Exp.)
At Ultimate Load (Anal.)
At Ultimate Load (Exp.)
W1.3
Local Slip (mm)
Distance from the Loaded End (mm)
0
0.2
0.4
0.6
0.8
0
50
100
150
200
250

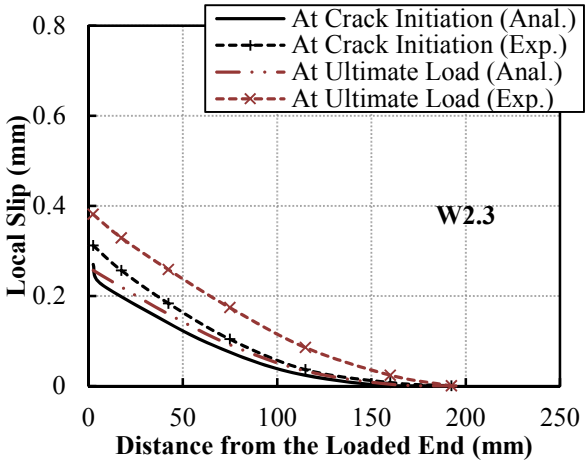
At Crack Initiation (Anal.)
At Crack Initiation (Exp.)
At Ultimate Load (Anal.)
At Ultimate Load (Exp.)
W2.3
Local Slip (mm)
Distance from the Loaded End (mm)
0
0.2
0.4
0.6
0.8
0
50
100
150
200
250

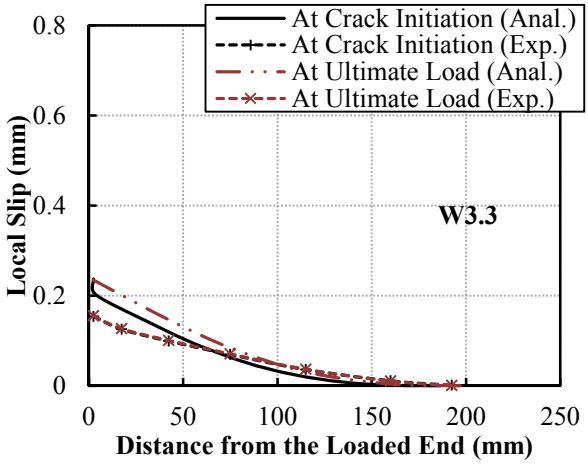
At Crack Initiation (Anal.)
At Crack Initiation (Exp.)
At Ultimate Load (Anal.)
At Ultimate Load (Exp.)
W3.3
Local Slip (mm)
Distance from the Loaded End (mm)
0
0.2
0.4
0.6
0.8
0
50
100
150
200
250

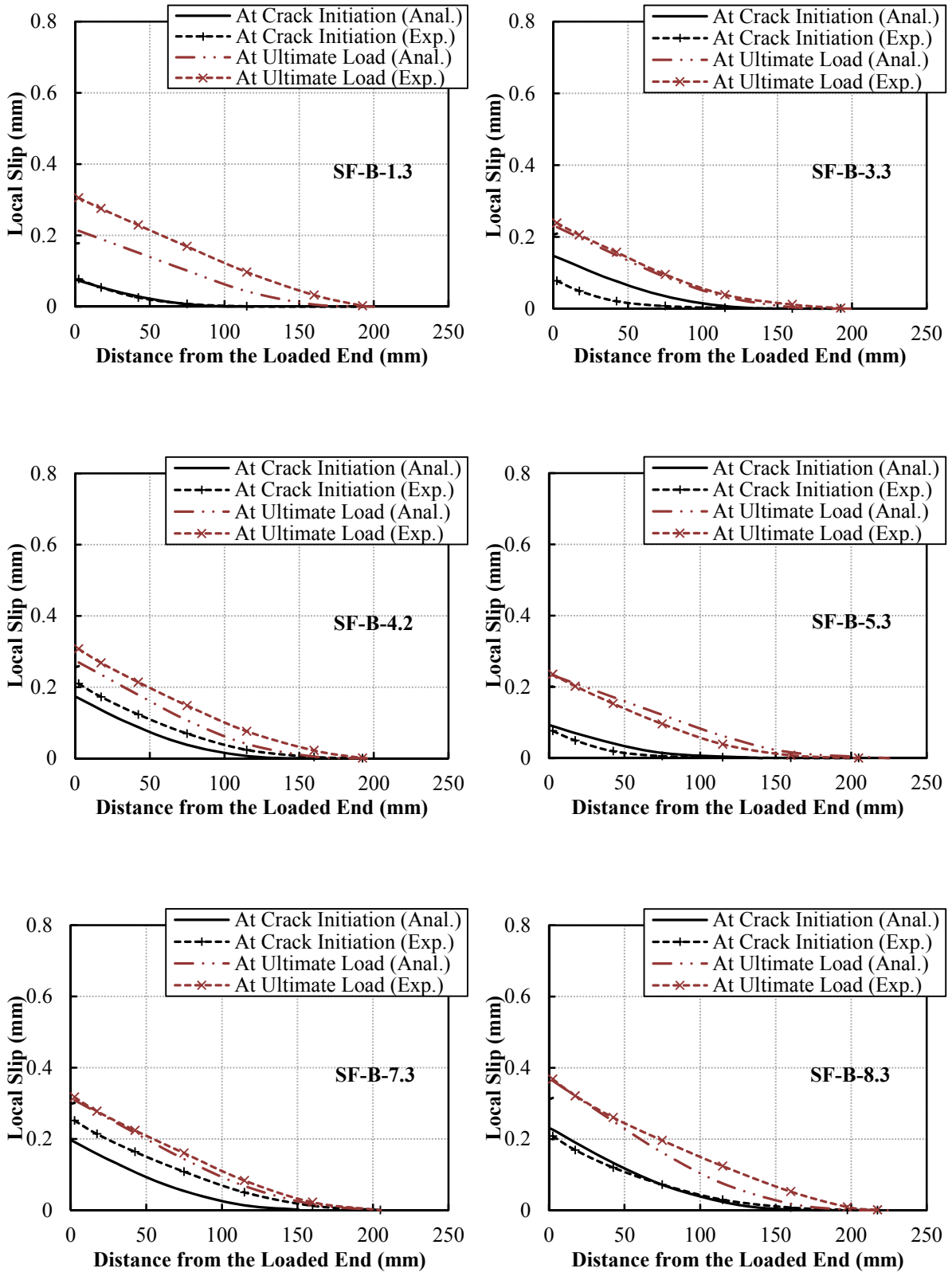

Figure 5-14. Comparison between the local slip values obtained from the experiments and the proposed model (*Method A*) for different processing techniques.

Prediction of the maximum applied load using Eq. 5-71shows good agreement with the test data for different processing techniques (Figure 5-15). The overall average value of the analytical-to-experimental ratio is 0.89. The abbreviations of S.D. and C.O.V. in Figure 5-15 are the standard deviation and coefficient of variation, respectively. In the case of the samples with FRP-to-concrete width ratio (w_r) of 0.533, the predicted maximum applied loads are 23 percent of the actual values Eq. 5-71 predicts. It indicates that Eq. 5-71underestimates the maximum applied load value for the joints with w_r over 0.333, although the effect of the FRP width is considered in this equation. The same response was observed by Camli and Binici (2007).

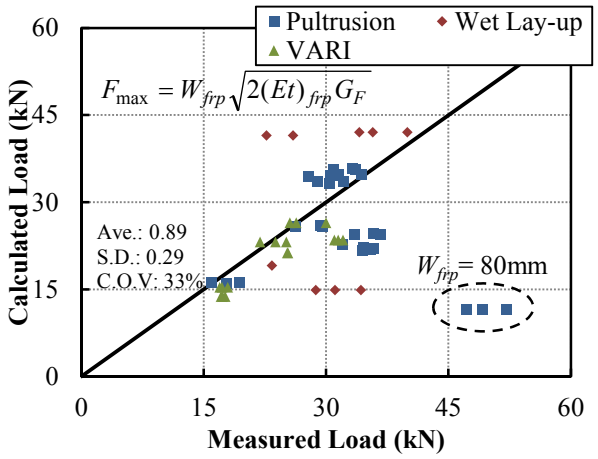

Figure 5-15. Measured vs calculated (*Method A*) maximum applied loads.

Figure 5-16 illustrates the comparison between the interfacial fracture energy obtained based on the area under shear stress-slip curves of the samples and the fracture energy calculated by Eqs. 5-74 or 5-77. The comparison is made for the test data at the first and also the second strain gauges. The maximum strain at the loaded end and the maximum shear stress in these equations are determined based on Eq. 5-37 and Eq. 5-75, respectively.

According to Figure 5-16, the fracture energy of the interface can be adequately estimated by Eqs. 5-74 and 5-77. However, the analytical results show closer agreement with the experimental results at the second strain gauges. It may be due to the stress intensity at the loaded end of the bond. Mode II fracture energy calculated based on Eq. 5-77 is plotted against bondline stiffness, depth of IC debonding and FRP width (Figure 5-17). The interfacial fracture energy increases for thicker bondlines (Figure 5-17a). This trend is almost consistent for the samples processed with different manufacturing methods.

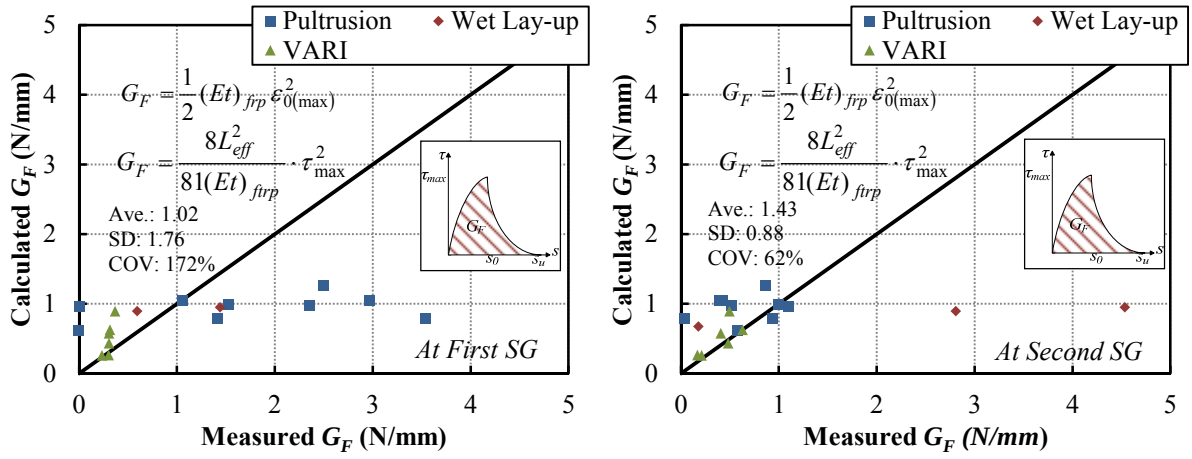

(a) (b)

Figure 5-16. Comparison between experimental and analytical interfacial fracture energy based on Eqs. 5-74 and 5-77 at (a) first strain gauge, and (b) second strain gauge.

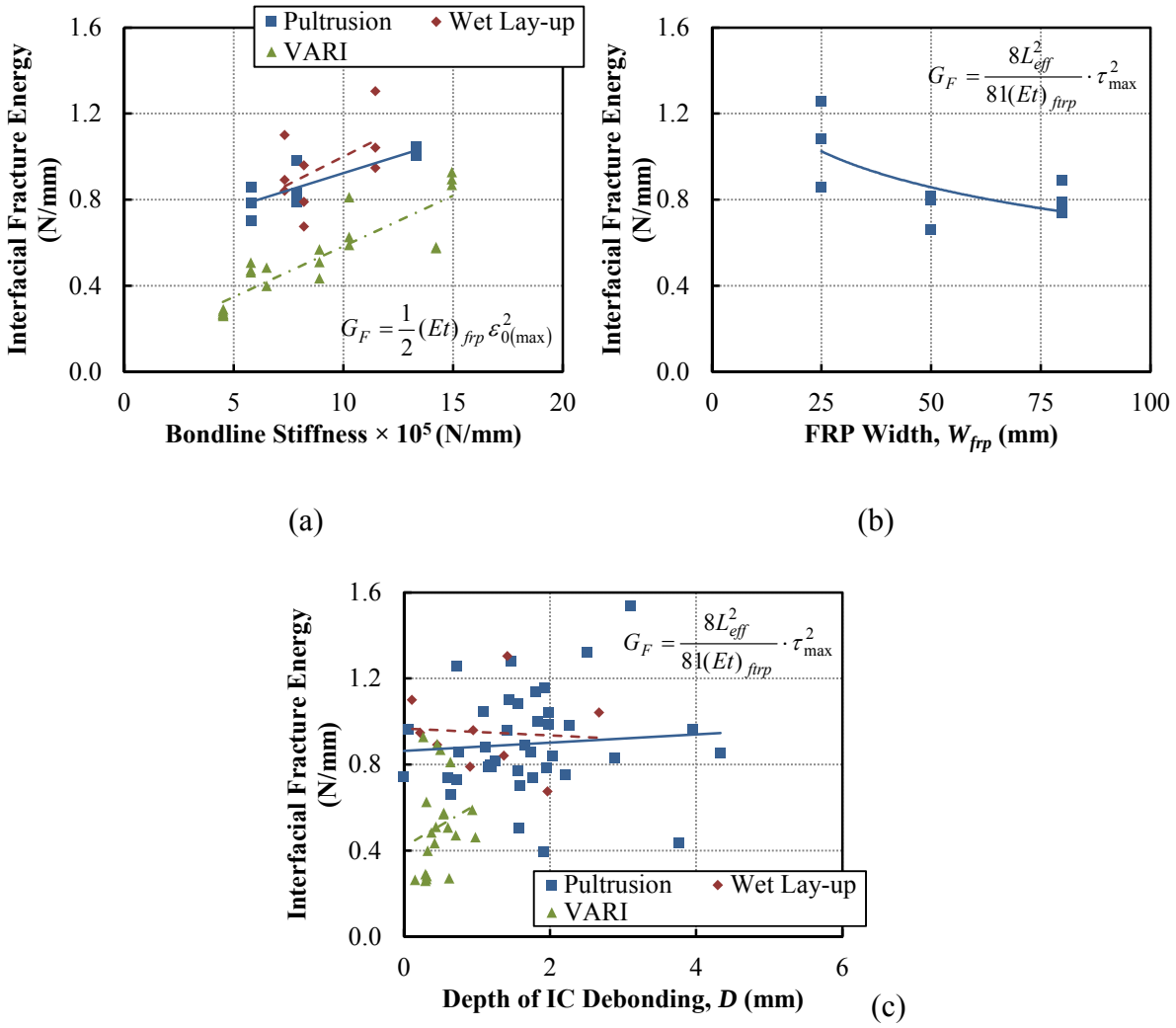

(a) (b) (c)

Figure 5-17. Effect of different parameters on the interfacial fracture energy.

Although the results for different FRP width are slightly scattered, thicker bond and narrower FRP can improve the interfacial fracture energy in adhesively bonded joints. However considering Figure 5-17c, there is not a clear correlation between the depth of intermediate crack debonding, D, and the fracture energy. Since D factor is directly related to the properties of the concrete substrate therefore, other parameters of the joints (properties of FRP and adhesive layer) rather than just the concrete are required to determine the fracture energy of the interface.

Figure 5-18 shows the correlation between the interfacial fracture energy, G_F, and the maximum shear stress, τ_{max}, which are calculated based on Eqs. 5-74 and 5-75, respectively. In this Figure, C.O.D. is the coefficient of determination. Two different relations can be proposed for determination of the maximum shear stress;

Logarithmic:

$$\tau_{\max} = 1.63\ln(G_F) + 9.19 \qquad 5\text{-}99$$

Powered:

$$\tau_{\max} = 11.88 G_F^{1.192} \qquad 5\text{-}100$$

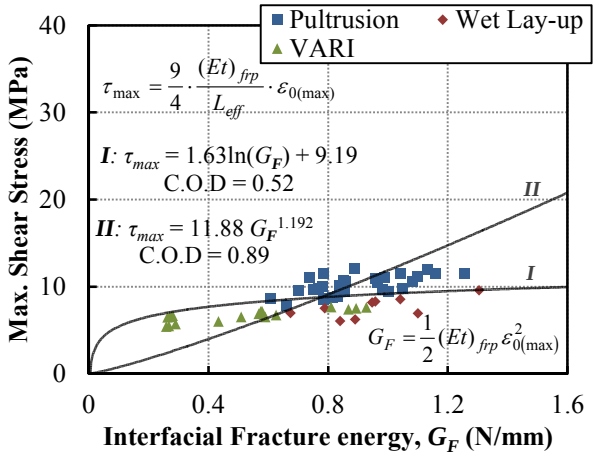

Figure 5-18. Correlation between G_F and the maximum shear stress (based on proposed analytical equations).

Although the coefficient of determination of Eq. 5-100 is higher than the counterpart however, the logarithmic form estimates the shape of the increase in a more efficient way.

Data indicates that the maximum shear stress does not increase constantly with the higher fracture energy. It should be mentioned that these relations are obtained by regression of 55 joints considering different manufacturing techniques. Therefore, Eqs. 5-99 and 5-100 are applicable to the FRP-to-concrete bonded joints using different processing methods (pultrusion, wet lay-up, and VARI).

5.4.2. Method B-Slip Fixity Condition

Strain distribution of the samples at the level of crack initiation and ultimate load calculated based on *Method B* (Eq. 5-91) are compared with experimental results in Figure 5-19 and Figure 5-20, respectively. In addition, the shear stress and slip profiles along the bonded length are shown in Figure 5-21 and Figure 5-22, respectively. These figures demonstrate that *Method B* is able to simulate the interface behaviour of the joints processed with different manufacturing methods with sufficient accuracy.

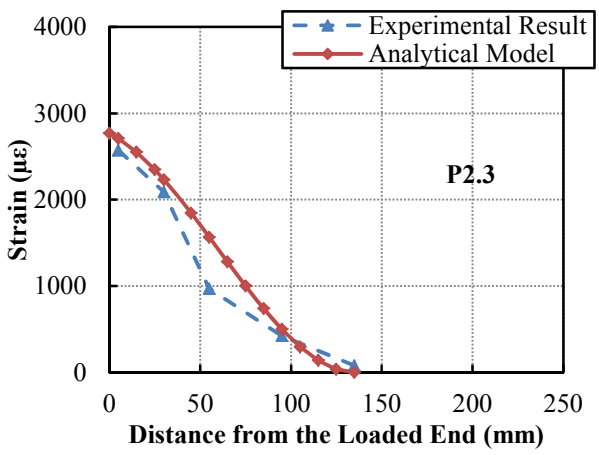
Experimental Result
Analytical Model
P2.3
Strain (με)
Distance from the Loaded End (mm)
0
1000
2000
3000
4000
0
50
100
150
200
250

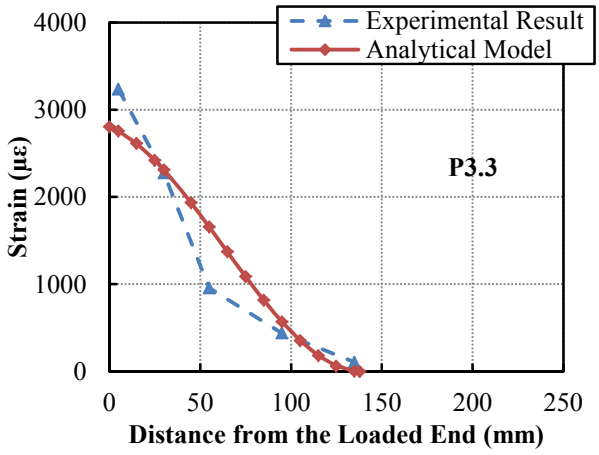
Experimental Result
Analytical Model
P3.3
Strain (με)
Distance from the Loaded End (mm)
0
1000
2000
3000
4000
0
50
100
150
200
250

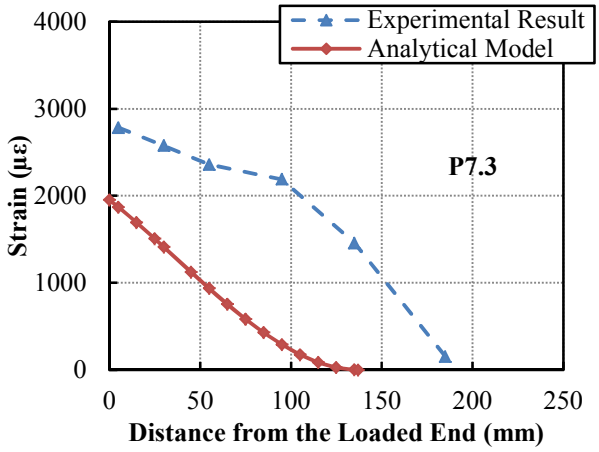
Experimental Result
Analytical Model
P7.3
Strain (με)
Distance from the Loaded End (mm)
0
1000
2000
3000
4000
0
50
100
150
200
250

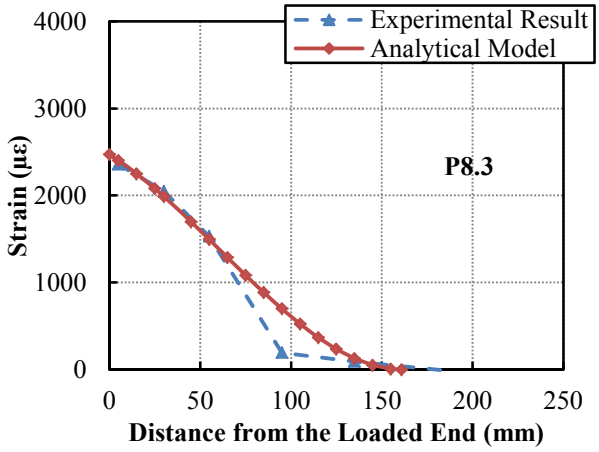
Experimental Result
Analytical Model
P8.3
Strain (με)
Distance from the Loaded End (mm)
0
1000
2000
3000
4000
0
50
100
150
200
250

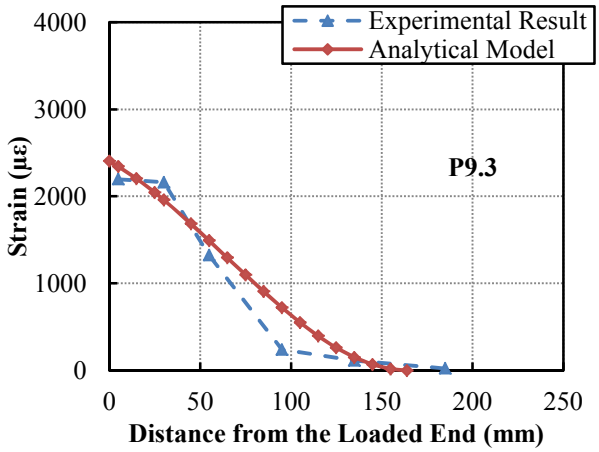
Experimental Result
Analytical Model
P9.3
Strain (με)
Distance from the Loaded End (mm)
0
1000
2000
3000
4000
0
50
100
150
200
250

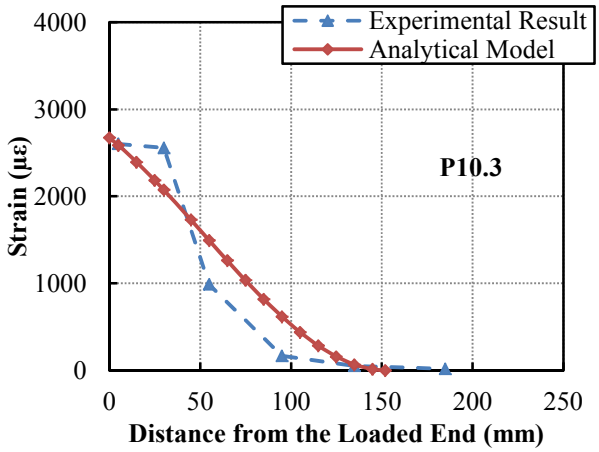
Experimental Result
Analytical Model
P10.3
Strain (με)
Distance from the Loaded End (mm)
0
1000
2000
3000
4000
0
50
100
150
200
250

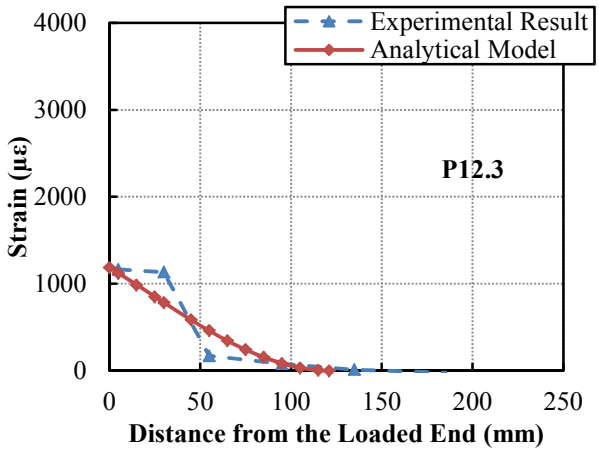
Experimental Result
Analytical Model
P12.3
Strain (με)
Distance from the Loaded End (mm)

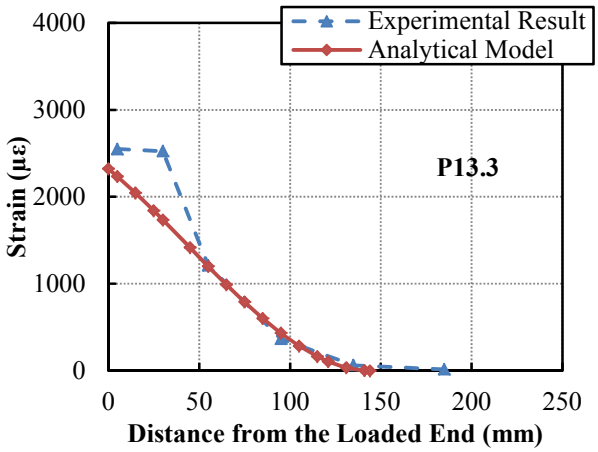
Experimental Result
Analytical Model
P13.3
Strain (με)
Distance from the Loaded End (mm)

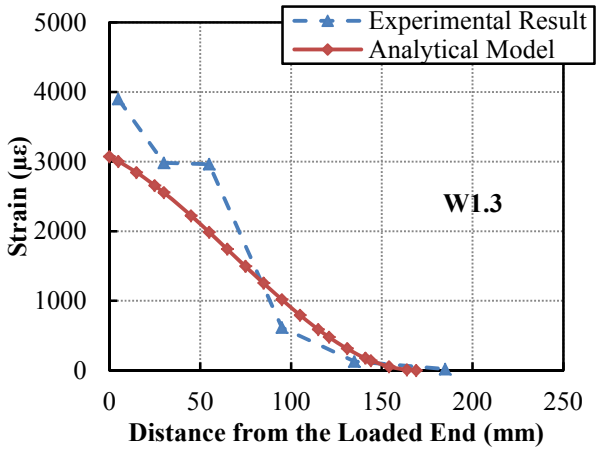
Experimental Result
Analytical Model
W1.3
Strain (με)
Distance from the Loaded End (mm)

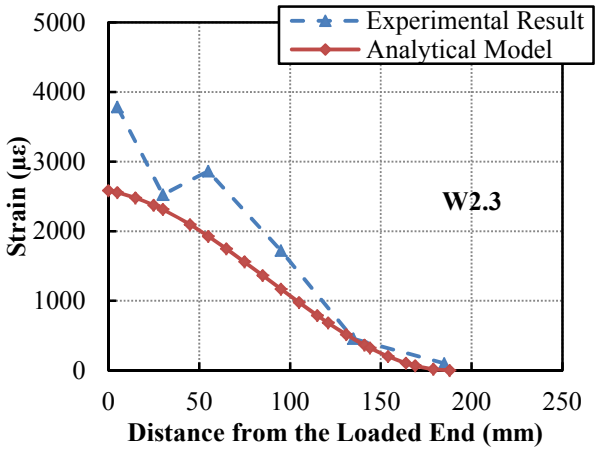
Experimental Result
Analytical Model
W2.3
Strain (με)
Distance from the Loaded End (mm)

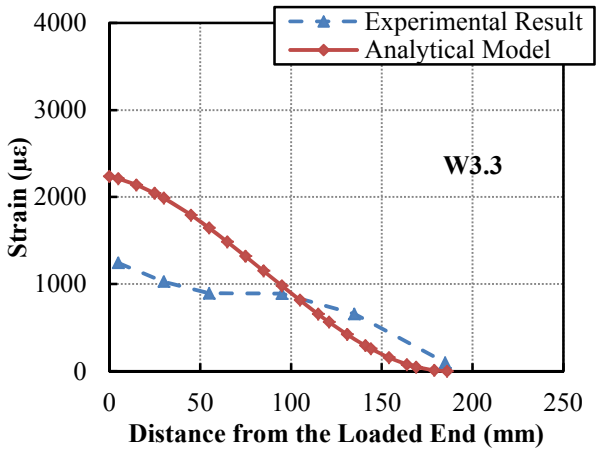
Experimental Result
Analytical Model
W3.3
Strain (με)
Distance from the Loaded End (mm)

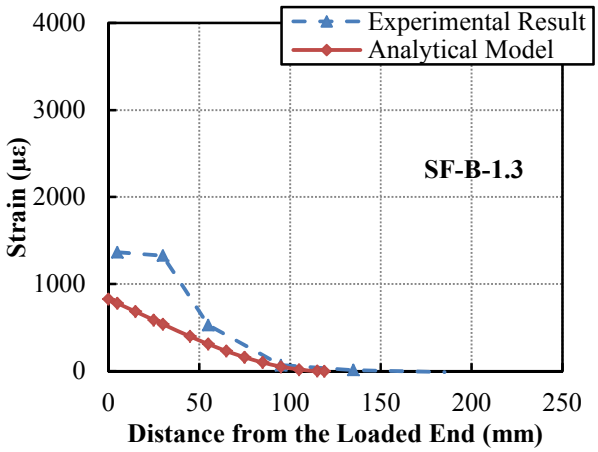
Experimental Result
Analytical Model
SF-B-1.3
Strain (με)
Distance from the Loaded End (mm)

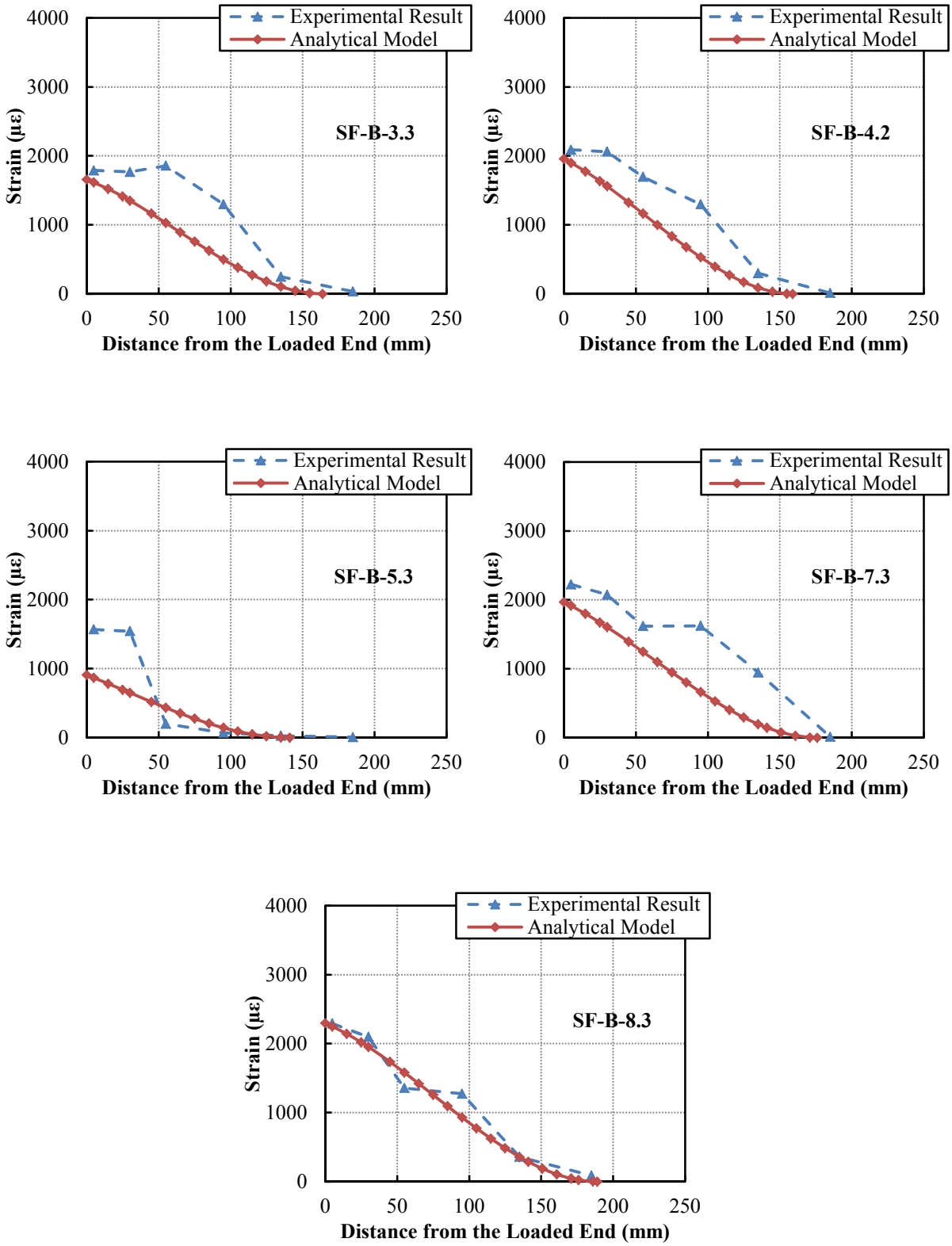

Figure 5-19. Analytical prediction of the strain distribution corresponding to the initiation of interfacial crack (*Method B*).

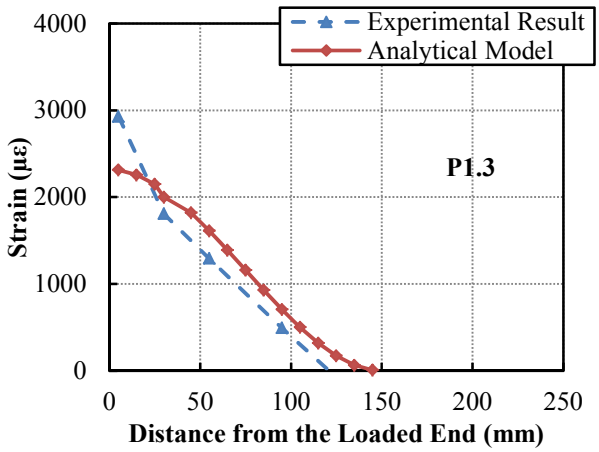
Experimental Result
Analytical Model
P1.3
Strain (με)
Distance from the Loaded End (mm)
0
1000
2000
3000
4000
0
50
100
150
200
250

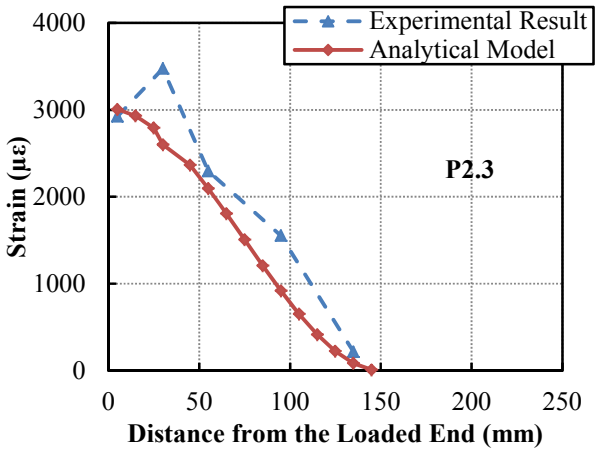
Experimental Result
Analytical Model
P2.3
Strain (με)
Distance from the Loaded End (mm)
0
1000
2000
3000
4000
0
50
100
150
200
250

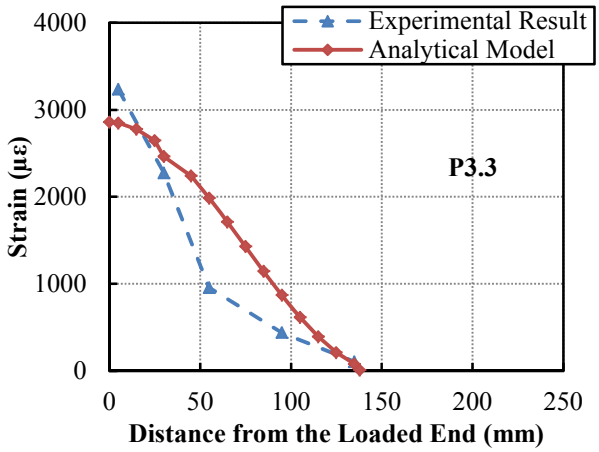
Experimental Result
Analytical Model
P3.3
Strain (με)
Distance from the Loaded End (mm)
0
1000
2000
3000
4000
0
50
100
150
200
250

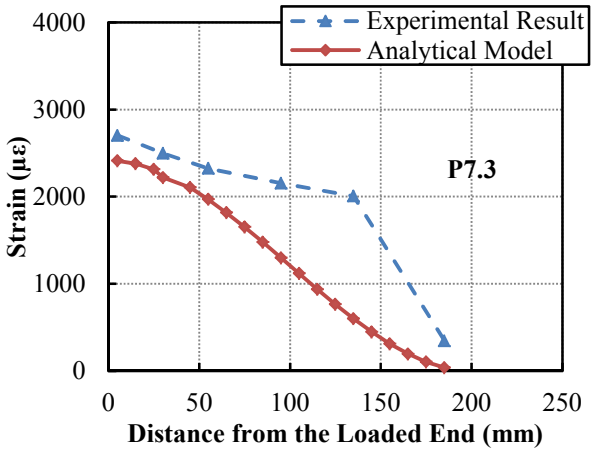
Experimental Result
Analytical Model
P7.3
Strain (με)
Distance from the Loaded End (mm)
0
1000
2000
3000
4000
0
50
100
150
200
250

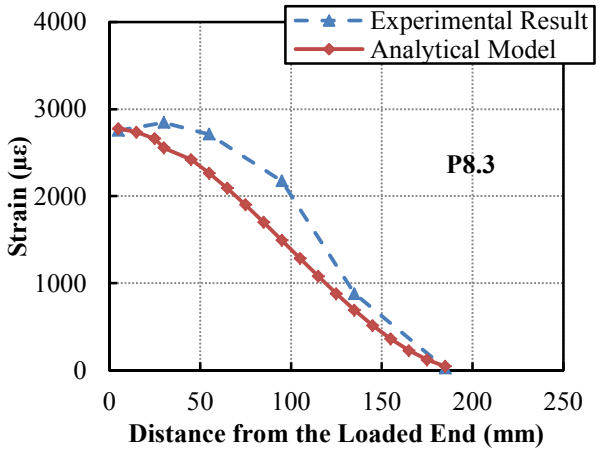
Experimental Result
Analytical Model
P8.3
Strain (με)
Distance from the Loaded End (mm)
0
1000
2000
3000
4000
0
50
100
150
200
250

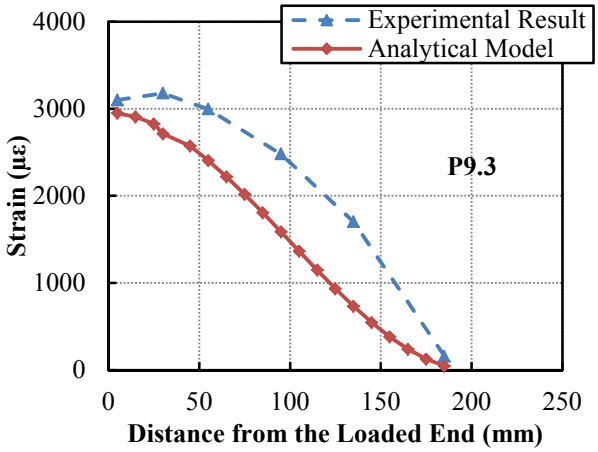
Experimental Result
Analytical Model
P9.3
Strain (με)
Distance from the Loaded End (mm)
0
1000
2000
3000
4000
0
50
100
150
200
250

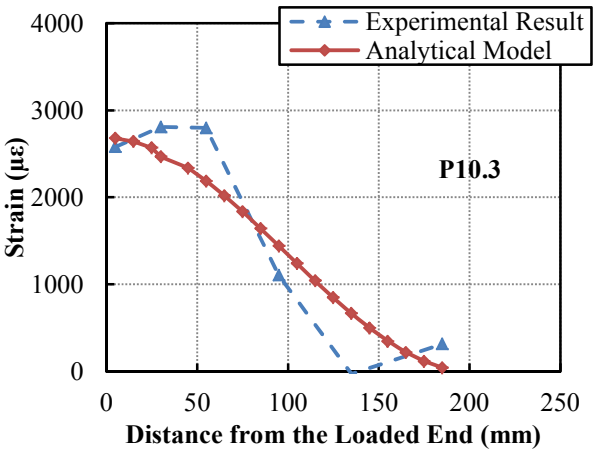
Experimental Result
Analytical Model
P10.3
Strain (με)
Distance from the Loaded End (mm)
0
1000
2000
3000
4000
0
50
100
150
200
250

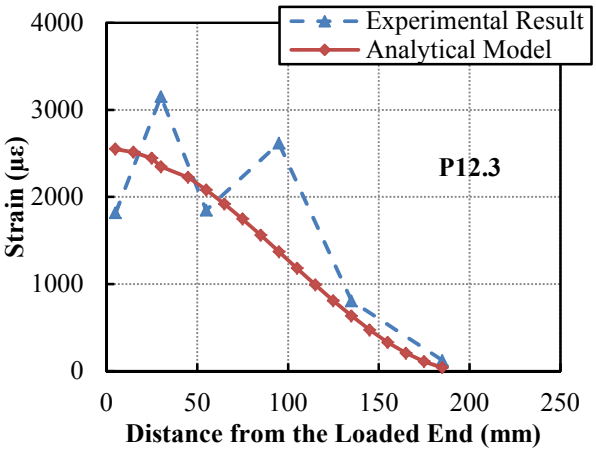
Experimental Result
Analytical Model
P12.3
Strain (με)
Distance from the Loaded End (mm)
0
1000
2000
3000
4000
0
50
100
150
200
250

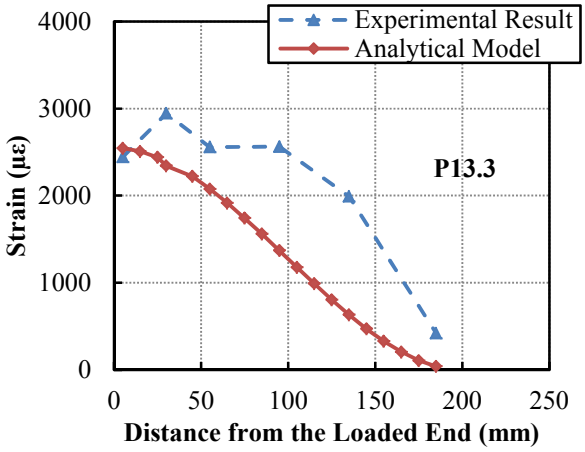
Experimental Result
Analytical Model
P13.3
Strain (με)
Distance from the Loaded End (mm)
0
1000
2000
3000
4000
0
50
100
150
200
250

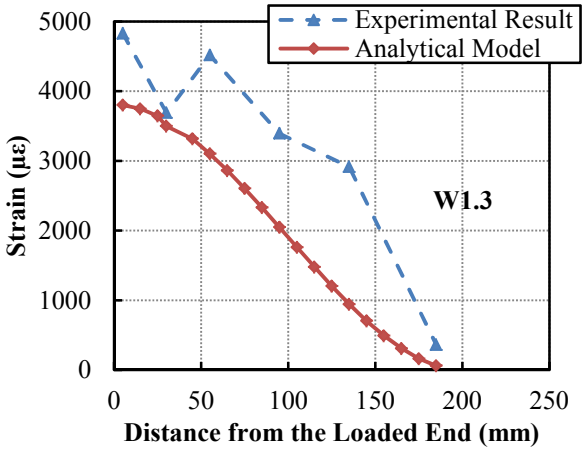
Experimental Result
Analytical Model
W1.3
Strain (με)
Distance from the Loaded End (mm)
0
1000
2000
3000
4000
5000
0
50
100
150
200
250

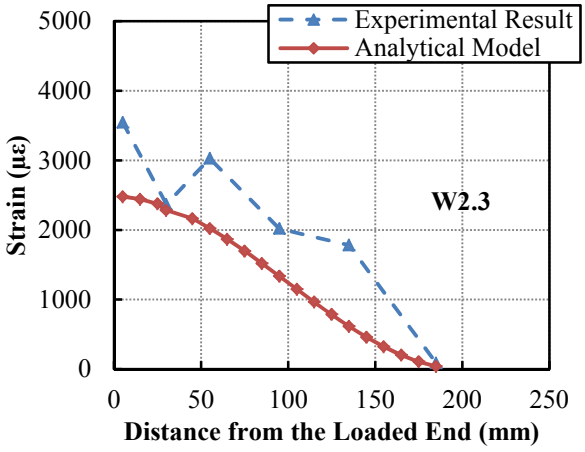
Experimental Result
Analytical Model
W2.3
Strain (με)
Distance from the Loaded End (mm)
0
1000
2000
3000
4000
5000
0
50
100
150
200
250

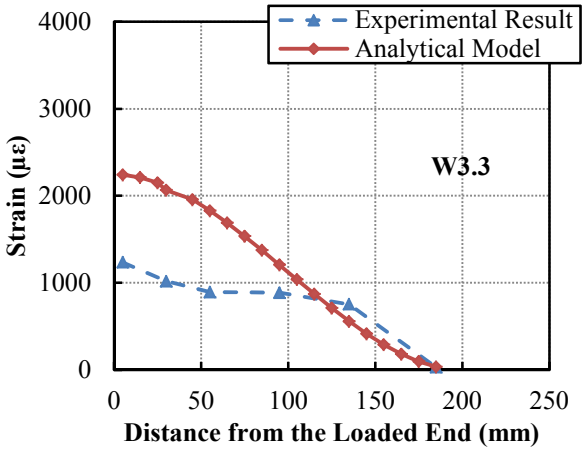
Experimental Result
Analytical Model
W3.3
Strain (με)
Distance from the Loaded End (mm)
0
1000
2000
3000
4000
0
50
100
150
200
250

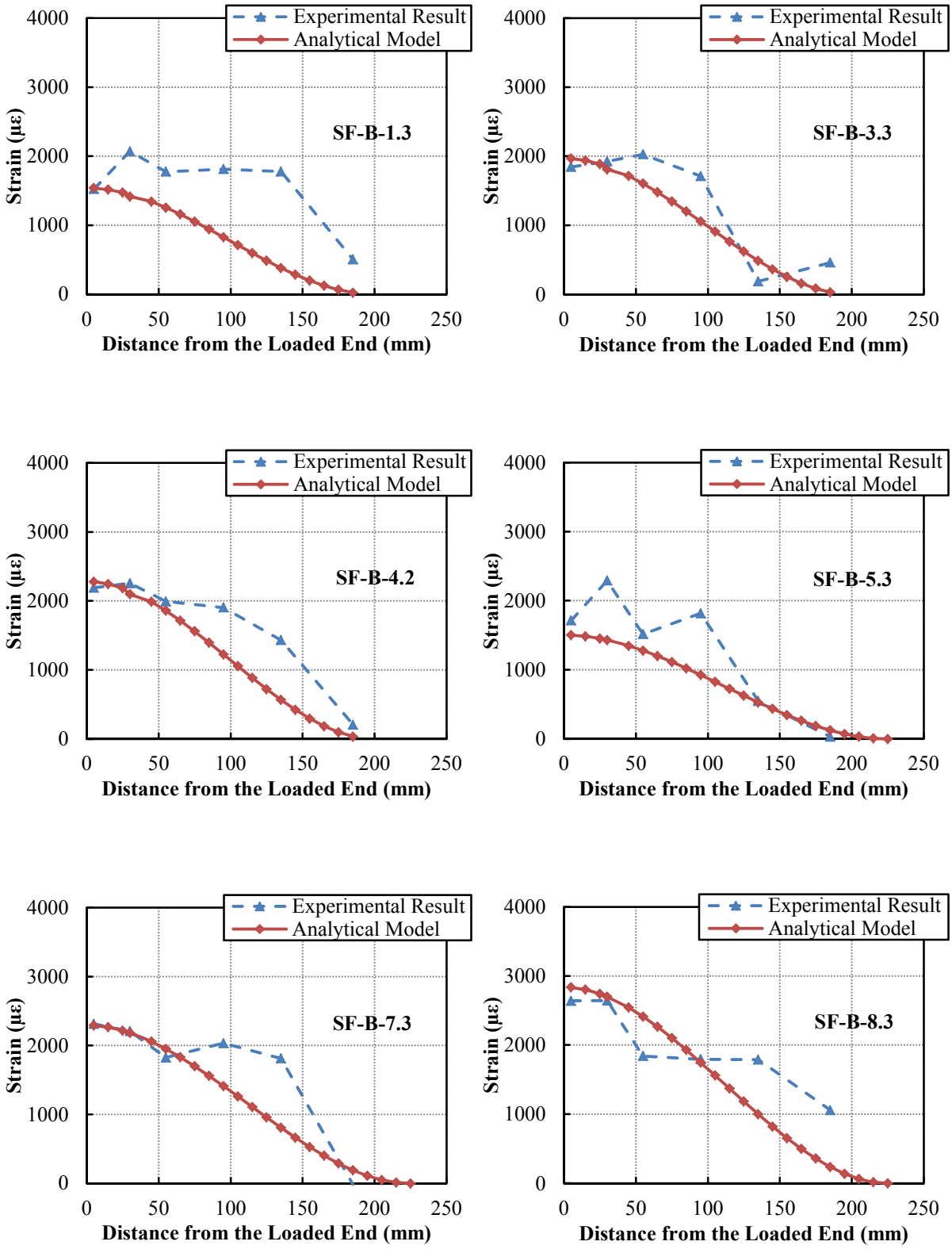

Figure 5-20. Analytical prediction of the strain distribution corresponding to the ultimate applied load (*Method B*).

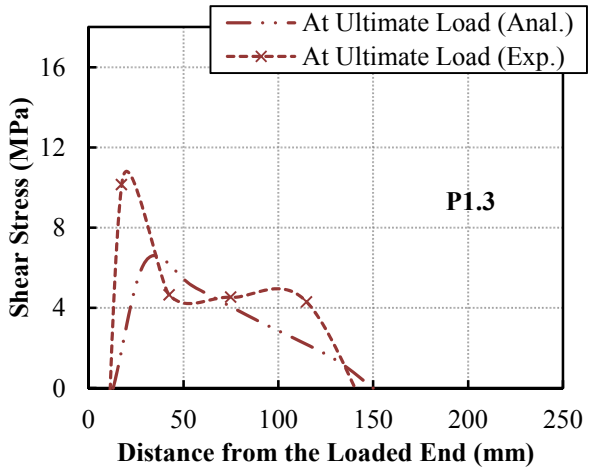
At Ultimate Load (Anal.)
At Ultimate Load (Exp.)
P1.3
Shear Stress (MPa)
Distance from the Loaded End (mm)

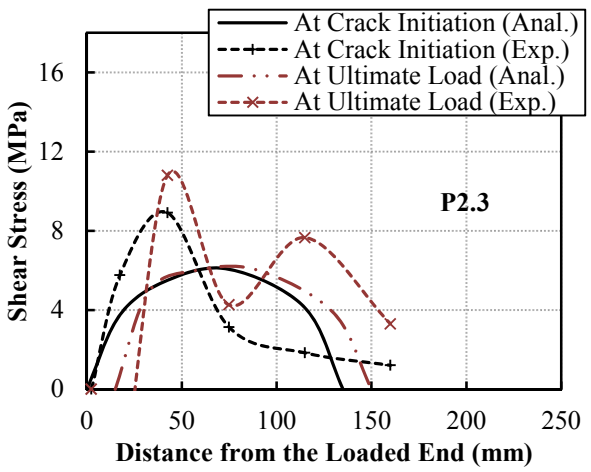
At Crack Initiation (Anal.)
At Crack Initiation (Exp.)
At Ultimate Load (Anal.)
At Ultimate Load (Exp.)
P2.3
Shear Stress (MPa)
Distance from the Loaded End (mm)

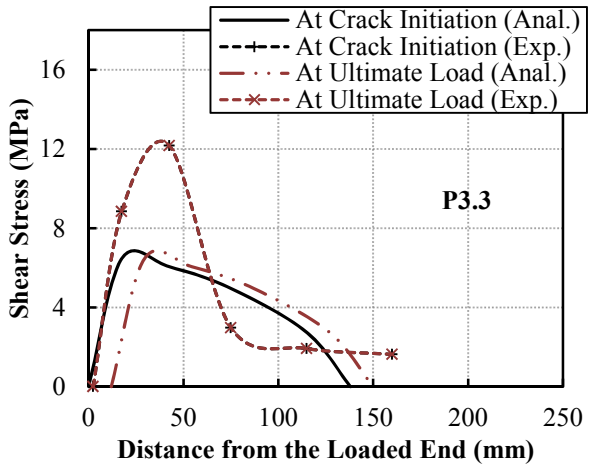
At Crack Initiation (Anal.)
At Crack Initiation (Exp.)
At Ultimate Load (Anal.)
At Ultimate Load (Exp.)
P3.3
Shear Stress (MPa)
Distance from the Loaded End (mm)

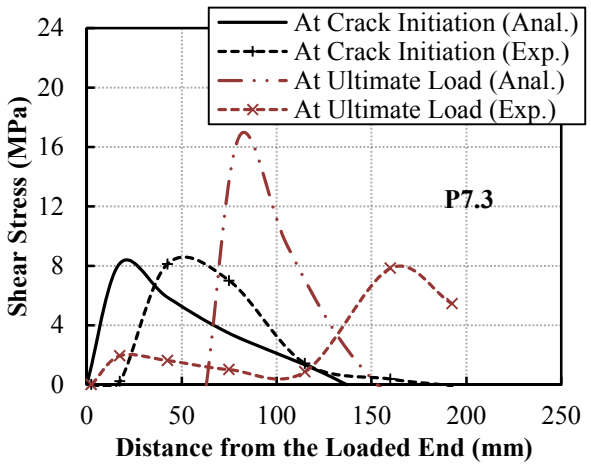
At Crack Initiation (Anal.)
At Crack Initiation (Exp.)
At Ultimate Load (Anal.)
At Ultimate Load (Exp.)
P7.3
Shear Stress (MPa)
Distance from the Loaded End (mm)

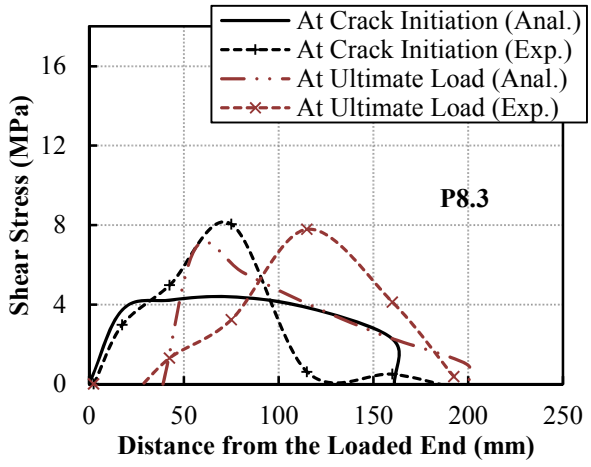
At Crack Initiation (Anal.)
At Crack Initiation (Exp.)
At Ultimate Load (Anal.)
At Ultimate Load (Exp.)
P8.3
Shear Stress (MPa)
Distance from the Loaded End (mm)

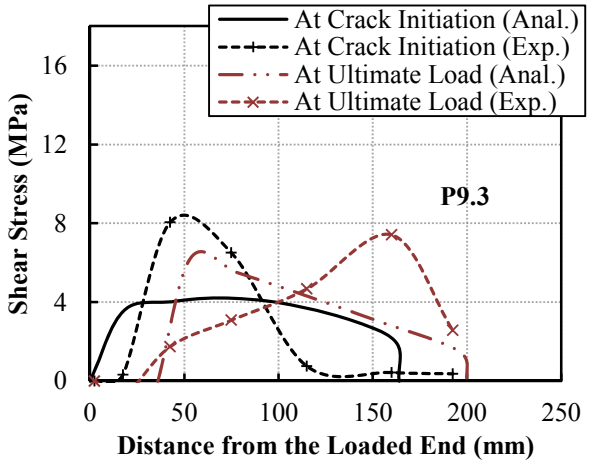
At Crack Initiation (Anal.)
At Crack Initiation (Exp.)
At Ultimate Load (Anal.)
At Ultimate Load (Exp.)
P9.3
Shear Stress (MPa)
Distance from the Loaded End (mm)

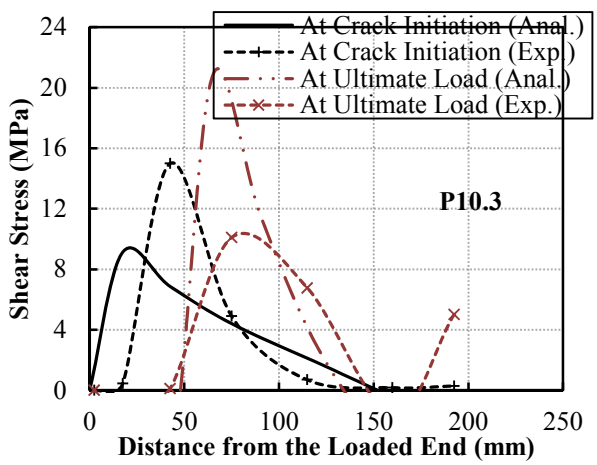
At Crack Initiation (Anal.)
At Crack Initiation (Exp.)
At Ultimate Load (Anal.)
At Ultimate Load (Exp.)
P10.3
Shear Stress (MPa)
Distance from the Loaded End (mm)

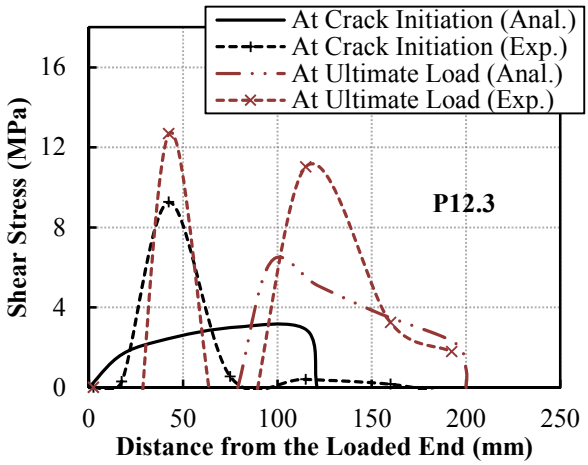
At Crack Initiation (Anal.)
At Crack Initiation (Exp.)
At Ultimate Load (Anal.)
At Ultimate Load (Exp.)
P12.3
Shear Stress (MPa)
Distance from the Loaded End (mm)

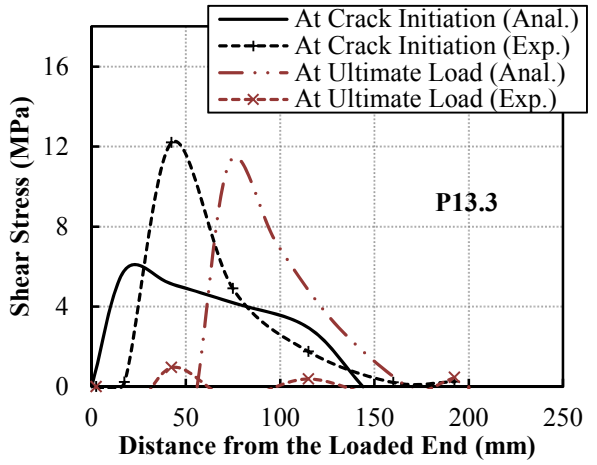
At Crack Initiation (Anal.)
At Crack Initiation (Exp.)
At Ultimate Load (Anal.)
At Ultimate Load (Exp.)
P13.3
Shear Stress (MPa)
Distance from the Loaded End (mm)

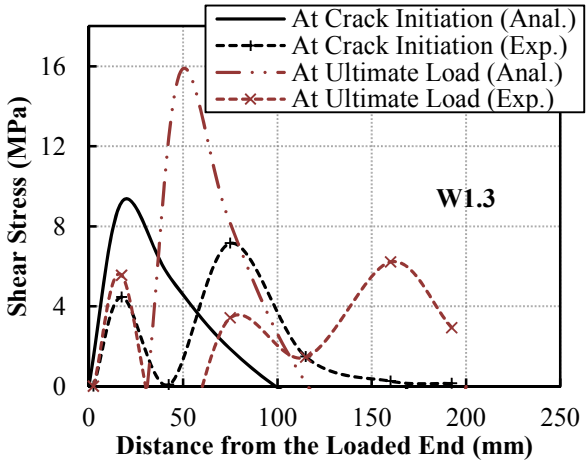
At Crack Initiation (Anal.)
At Crack Initiation (Exp.)
At Ultimate Load (Anal.)
At Ultimate Load (Exp.)
W1.3
Shear Stress (MPa)
Distance from the Loaded End (mm)

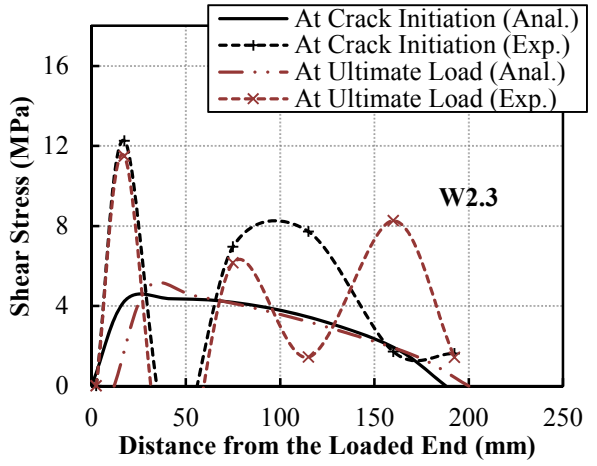
At Crack Initiation (Anal.)
At Crack Initiation (Exp.)
At Ultimate Load (Anal.)
At Ultimate Load (Exp.)
W2.3
Shear Stress (MPa)
Distance from the Loaded End (mm)

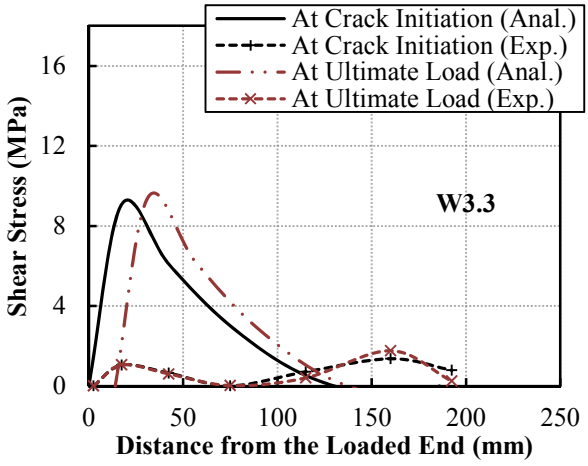
At Crack Initiation (Anal.)
At Crack Initiation (Exp.)
At Ultimate Load (Anal.)
At Ultimate Load (Exp.)
W3.3
Shear Stress (MPa)
Distance from the Loaded End (mm)

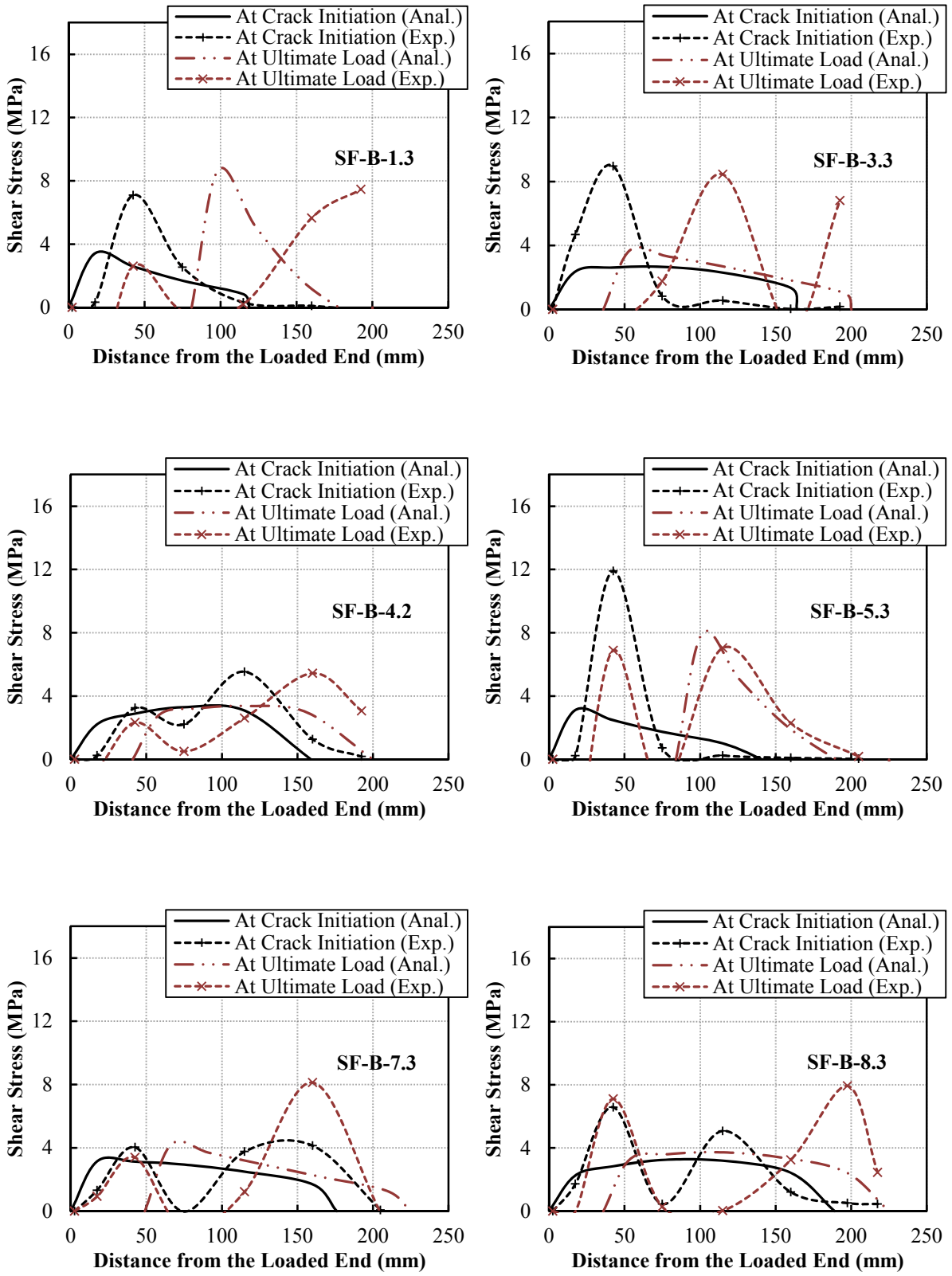

Figure 5-21. Experimental and analytical (*Method B*) distribution of the bond stress for the samples processed with different manufacturing techniques.

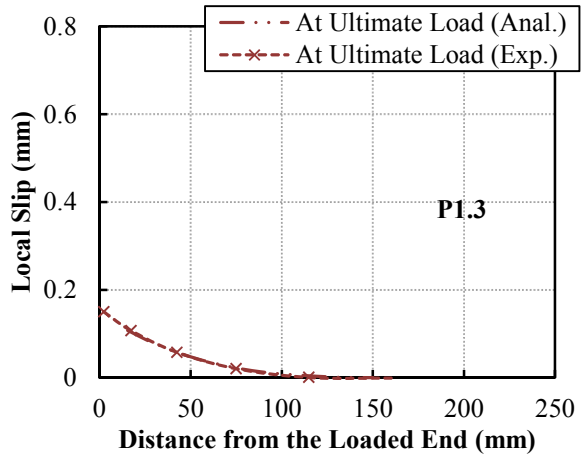
At Ultimate Load (Anal.)
At Ultimate Load (Exp.)
P1.3
Local Slip (mm)
Distance from the Loaded End (mm)

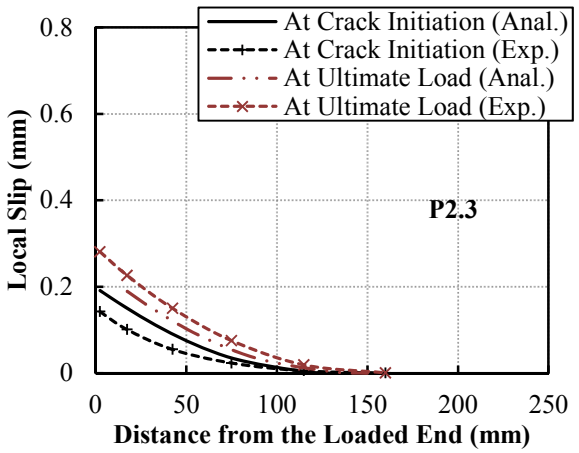
At Crack Initiation (Anal.)
At Crack Initiation (Exp.)
At Ultimate Load (Anal.)
At Ultimate Load (Exp.)
P2.3
Local Slip (mm)
Distance from the Loaded End (mm)

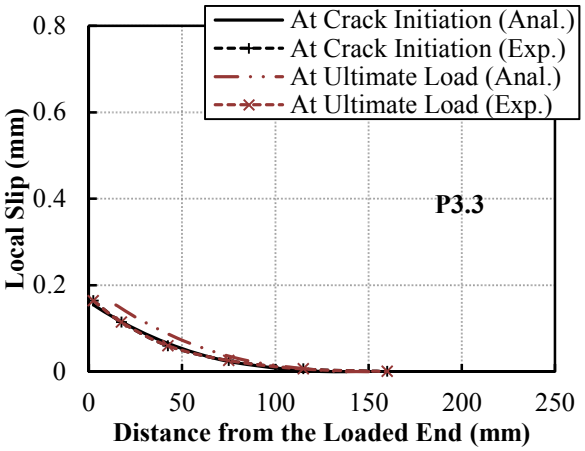
At Crack Initiation (Anal.)
At Crack Initiation (Exp.)
At Ultimate Load (Anal.)
At Ultimate Load (Exp.)
P3.3
Local Slip (mm)
Distance from the Loaded End (mm)

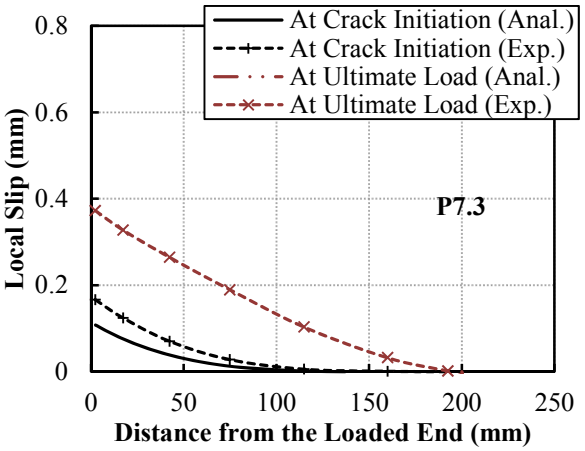
At Crack Initiation (Anal.)
At Crack Initiation (Exp.)
At Ultimate Load (Anal.)
At Ultimate Load (Exp.)
P7.3
Local Slip (mm)
Distance from the Loaded End (mm)

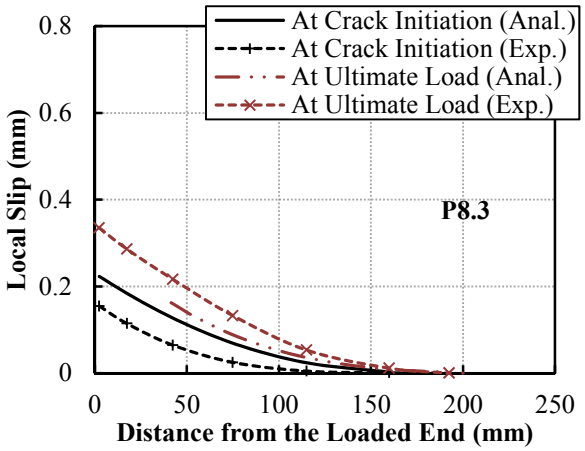
At Crack Initiation (Anal.)
At Crack Initiation (Exp.)
At Ultimate Load (Anal.)
At Ultimate Load (Exp.)
P8.3
Local Slip (mm)
Distance from the Loaded End (mm)

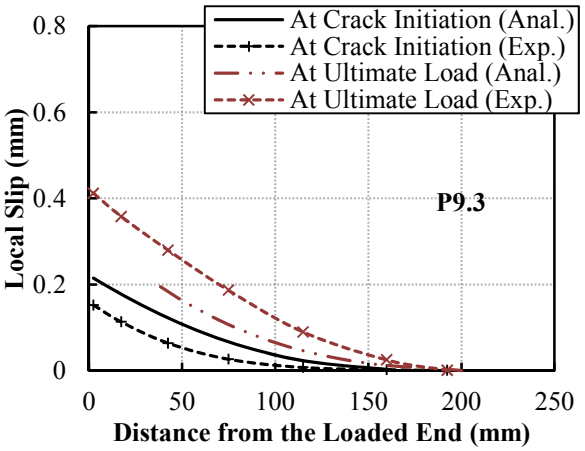
At Crack Initiation (Anal.)
At Crack Initiation (Exp.)
At Ultimate Load (Anal.)
At Ultimate Load (Exp.)
P9.3
Local Slip (mm)
Distance from the Loaded End (mm)

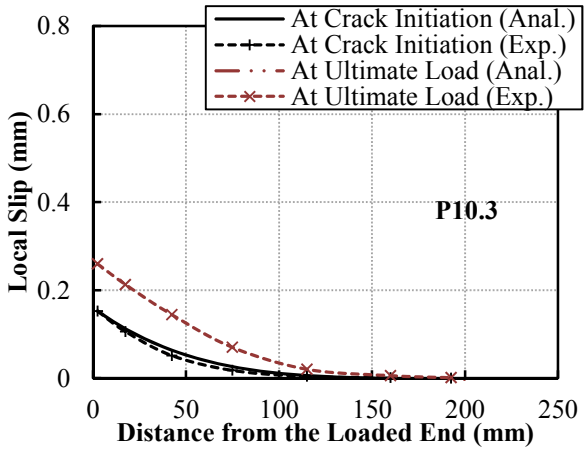
At Crack Initiation (Anal.)
At Crack Initiation (Exp.)
At Ultimate Load (Anal.)
At Ultimate Load (Exp.)
P10.3
Local Slip (mm)
Distance from the Loaded End (mm)
0
0.2
0.4
0.6
0.8
0
50
100
150
200
250

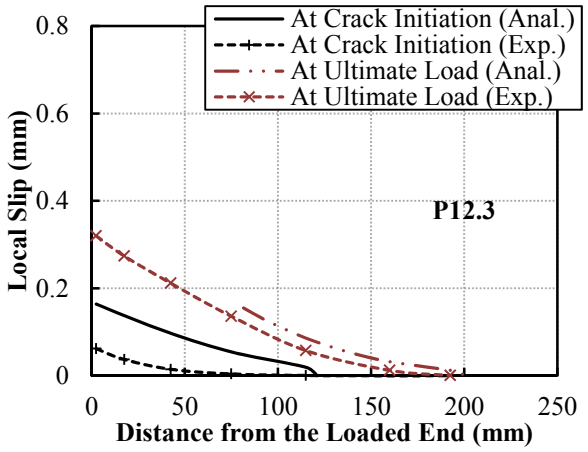
At Crack Initiation (Anal.)
At Crack Initiation (Exp.)
At Ultimate Load (Anal.)
At Ultimate Load (Exp.)
P12.3
Local Slip (mm)
Distance from the Loaded End (mm)
0
0.2
0.4
0.6
0.8
0
50
100
150
200
250

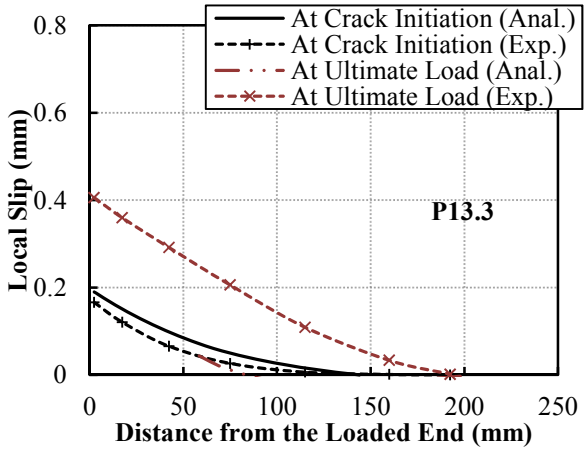
At Crack Initiation (Anal.)
At Crack Initiation (Exp.)
At Ultimate Load (Anal.)
At Ultimate Load (Exp.)
P13.3
Local Slip (mm)
Distance from the Loaded End (mm)
0
0.2
0.4
0.6
0.8
0
50
100
150
200
250

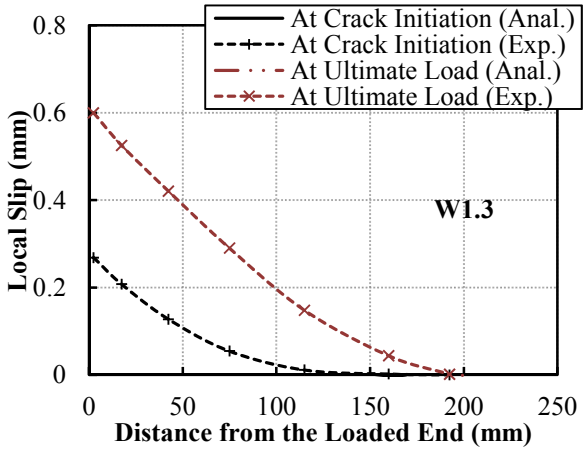
At Crack Initiation (Anal.)
At Crack Initiation (Exp.)
At Ultimate Load (Anal.)
At Ultimate Load (Exp.)
W1.3
Local Slip (mm)
Distance from the Loaded End (mm)
0
0.2
0.4
0.6
0.8
0
50
100
150
200
250

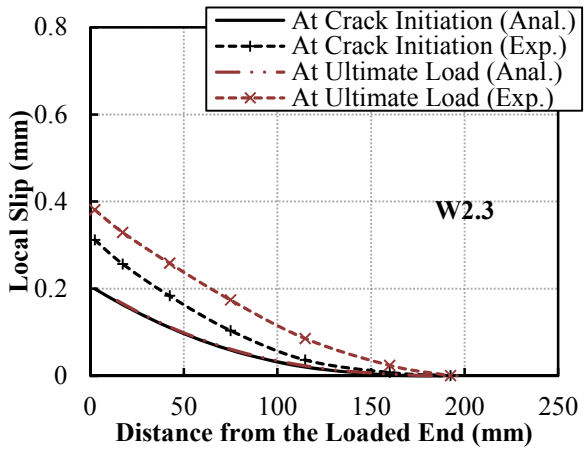
At Crack Initiation (Anal.)
At Crack Initiation (Exp.)
At Ultimate Load (Anal.)
At Ultimate Load (Exp.)
W2.3
Local Slip (mm)
Distance from the Loaded End (mm)
0
0.2
0.4
0.6
0.8
0
50
100
150
200
250

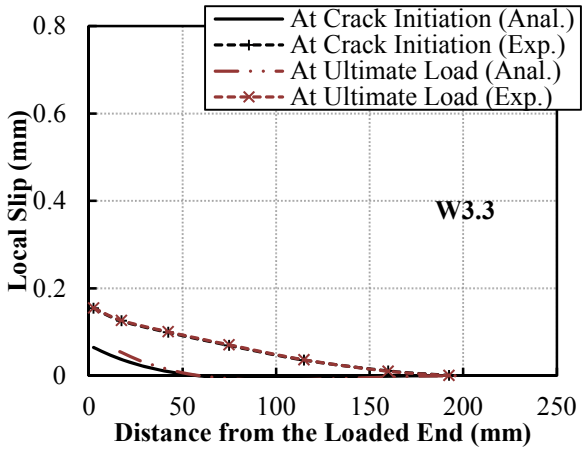
At Crack Initiation (Anal.)
At Crack Initiation (Exp.)
At Ultimate Load (Anal.)
At Ultimate Load (Exp.)
W3.3
Local Slip (mm)
Distance from the Loaded End (mm)
0
0.2
0.4
0.6
0.8
0
50
100
150
200
250

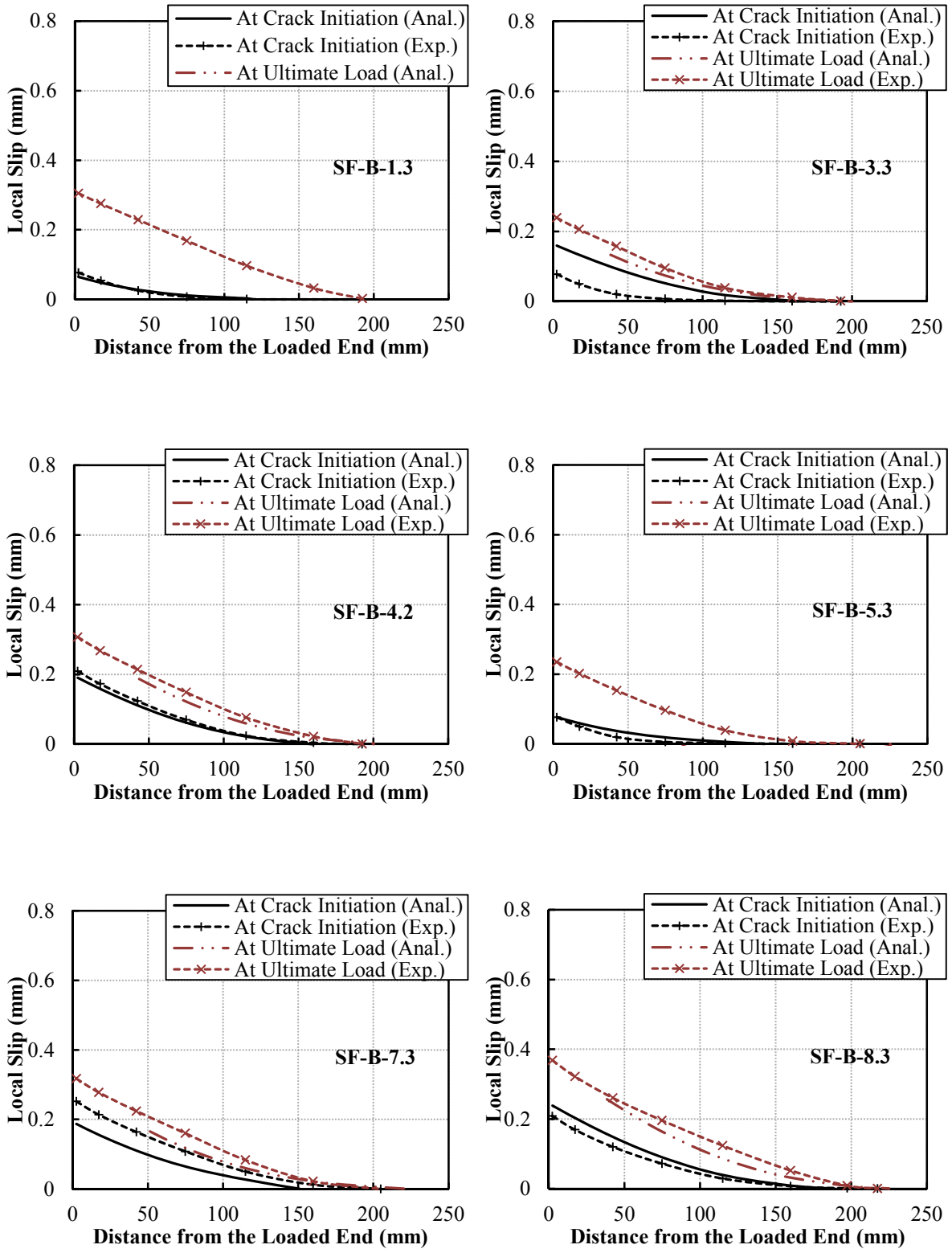

Figure 5-22. Comparison between the local slip values obtained from the experiments and the proposed model (*Method B*) for different processing techniques.

5.4.3. Comparison between the Proposed Models

Since the influence of the effective bond length is considered in *Method A*, this model is able to estimate the crack propagation along the bonded length with more precision. In addition in terms of the maximum shear stress, *Method A* provides more realistic estimation while *Method B* in most of the cases underestimates the values of τ_{max}. However, the predicted slip profiles calculated based on both methods are quite similar.

The bond-slip law is developed based on the FRP length in *method B*. In addition, the interface response is determined by an interface property factor in this model. Therefore, the properties of both adhesive and the FRP plate/laminate are considered in *Method B*. To make more convenient comparison between these two models, Appendix C presents the experimental results and analytical prediction of the strain, shear stress, and also slip profiles of the joints based on both *Method A* and *Method B*.

5.5. 2-D Nonlinear Finite Element Model of MSLS Specimens

In literature, finite element (FE) analysis of the bond between FRP and substrates have been undertaken in order to confirm the experimental results, verify and validate the proposed bond-slip models, or further comprehend the interfacial stress transfer mechanism (Barnes and Mays 2001). Since debonding in FRP/concrete bonded joints occurs very fast, capturing the interface fracture is difficult. Therefore, finite element analysis may assist to gain a better understanding about the debonding process.

Two main approaches have been implemented into the FE models to study the interface of adhesively bonded joints; discrete (local) or a continuum approach (Crocombe et al. 2006; Lu et al. 2005b). The former considers a layer of interface elements between two adherends and debonding is modelled by separation of these elements from each other. Cohesive crack models (CCM) may represent this approach which is discussed in section 2.6.3. This method can simulate the interfacial characteristics in conjunction with a proper bond-slip model. The second approach directly simulates the fracture of interface by considering appropriate constitutive models for materials. Crack band model (CBM) or non-local continuum damage mechanics can be categorized as continuum approaches. As mentioned in section 2.6.3, in crack band model, the fracture process zone is modelled within a band width in front of the crack where the inelastic deformations occur. In most cases, a fine mesh is required to achieve adequate response which imposes high computational cost to the FE model.

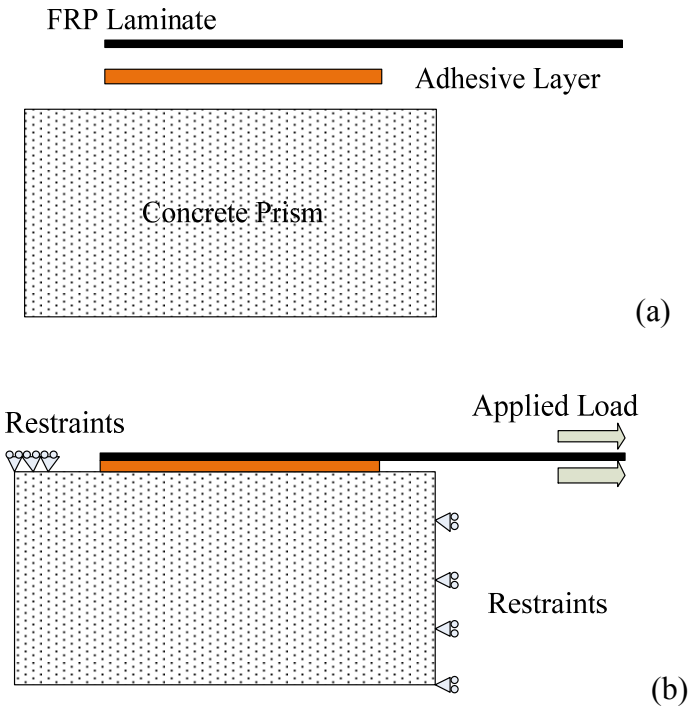

Figure 5-23. (a) Modelling of different parts and (b) boundary conditions of the simulated samples.

In this section, debonding mechanism of the FRP-to-concrete bonded joints is predicted numerically using Abaqus finite element analysis software (Abaqus/Standard). For this purpose, concrete blocks, adhesive layers and FRP laminates are modelled by three different parts (Figure 5-23a).

Nonlinearity has different sources:

- Material nonlinearity: in which the relationship between stress and strain is nonlinear.
- Boundary nonlinearity: when the boundary conditions change during the analysis.
- Geometric nonlinearity: when the magnitude of the displacement affects the overall response of the structure. This can occur by large deflections/rotations, snap through, or initial stress/load stiffening.

According to the MSLS test set-up, boundary conditions are prescribed in the models (Figure 5-23). Because of material and geometric nonlinearity occurrence, samples are analysed by modified Riks method. This method employs an additional unknown load magnitude and solves the problem for loads and displacement simultaneously. The current load is defined by summation of the initial load and the load increment;

$$F = F_{ini} + \psi(F_{ref} - F_{ini}) \quad (5\text{-}101)$$

where F_{int}, ψ, and F_{ref} are the initial load, load proportionality factor and the reference load vector, respectively.

Since stresses in the direction of the sample width are negligible, a two dimensional plane strain analysis of stresses can be performed to determine the interface behaviour in Abaqus (Figure 5-24). In this case, the strains of the interface are functions of planar coordinates alone, and out-of-plane normal and shear strains are zero. Therefore linear quadrilateral plane strain elements with reduced integration (CPE4R) are used to model the concrete, epoxy, and FRP. Elements with reduced integration apply a lower-order integration to form the stiffness matrix.

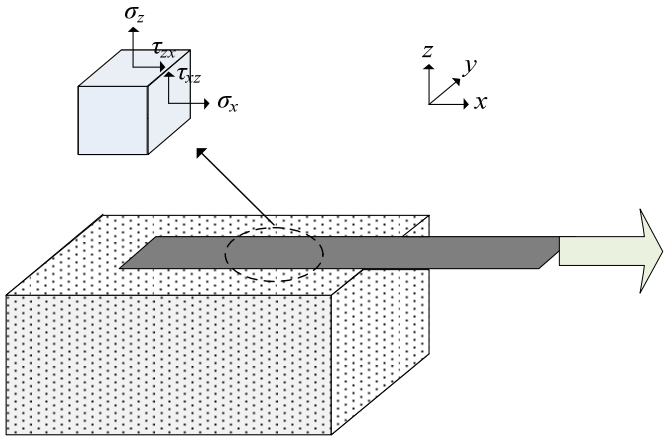

Figure 5-24. Application of plain strain elements in modells.

5.6. Constitutive Behaviour of Materials

The behaviour of the sections is introduced in the FE model by several constitutive laws which are as follows;

5.6.1. Concrete

Concrete damage plasticity (CDP) model is used to define the behaviour of the concrete. The CDP model can provide useful properties, including the softening behaviour in tension and the different yield strengths in tension and compression, with the initial yield stress in compression being nearly 10 times higher than the initial yield stress in tension.

Abaqus applies the yield surface of Lubliner et al. (1989) and Lee and Fenves (1998) to determine the behaviour of the concrete and the state of failure or damage under multiaxial stress. In this model, a scalar damaged elasticity controls the stress-strain relations:

$$\sigma = (1 - D)K_0^{el} : (\varepsilon - \varepsilon^{pl}) \qquad 5\text{-}102$$

where, K_0^{el} and K^{el} are the initial (undamaged) and the degraded elasticity matrices, respectively. D is the scalar stiffness degradation variable which is specified in the range of zero to one for undamaged and fully damaged materials, respectively. The stiffness degradation is isotropic and governed by a set of hardening variables (equivalent plastic strains, $\tilde{\varepsilon}^{pl}$) which control the evolution of the yield surface, the degradation of the elastic stiffness and the effective stress. Hardening variable is defined by stress condition, tension or compression (Figure 5-25 and Figure 5-26);

$$\tilde{\varepsilon}^{pl} = \begin{bmatrix} \tilde{\varepsilon}_t^{pl} \\ \tilde{\varepsilon}_c^{pl} \end{bmatrix} \qquad 5\text{-}103$$

where subscripts t and c represent tension and compression states, respectively.

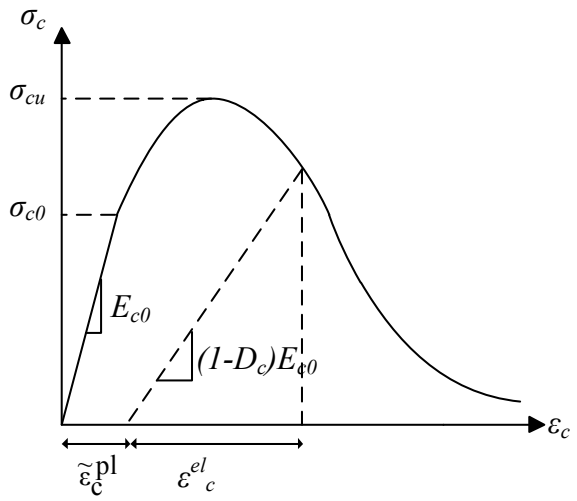

Figure 5-25. Definition of the compressive behaviour parameters in CDP model.

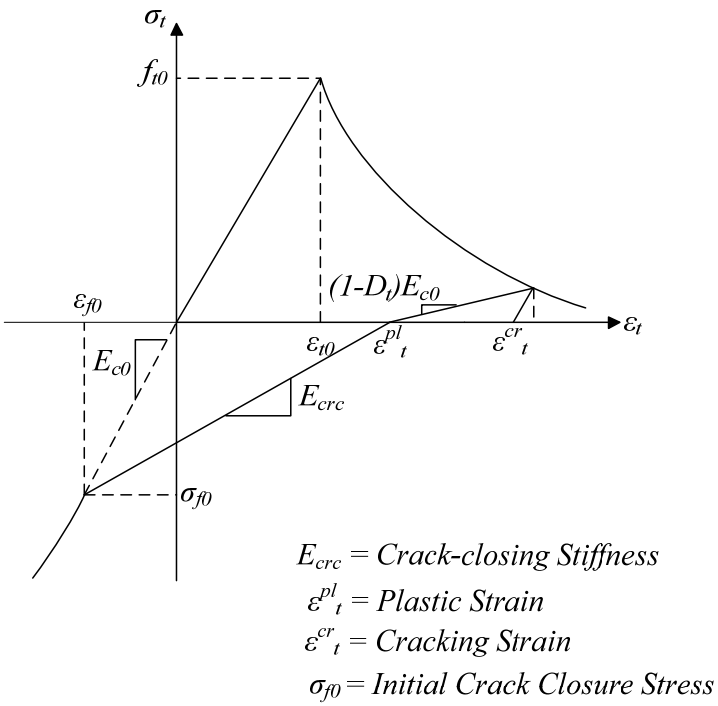

Figure 5-26. Definition of the tensile behaviour parameters in CDP model.

The stress-strain relation proposed by Kent and Park (1971) is employed to model the compressive behaviour of the unconfined concrete in FE analysis. Kent and Park (1971) relation is a generalized form of the Hognestad (1951) equation (Figure 5-27a);

$$\sigma_c = f_c^{'}\left[\frac{2\varepsilon_c}{\varepsilon_{c0}} - (\frac{\varepsilon_c}{\varepsilon_{c0}})^2\right] \quad \text{ascending part} \quad 5\text{-}104$$

$$\sigma_c = f_c^{'}[1 - Z(\varepsilon_c - \varepsilon_{c0})] \quad \text{descending part} \quad 5\text{-}105$$

$$Z = \frac{0.5}{\varepsilon_{50u} - \varepsilon_{c0}} \quad 5\text{-}106$$

$$\varepsilon_{50u} = \frac{3 + 0.29 f_c^{'}}{145 f_c^{'} - 1000} \quad 5\text{-}107$$

In above equation f'_c is in MPa and ε_{50u} expresses the strain corresponding to the stress equal to 50% of the maximum concrete strength.

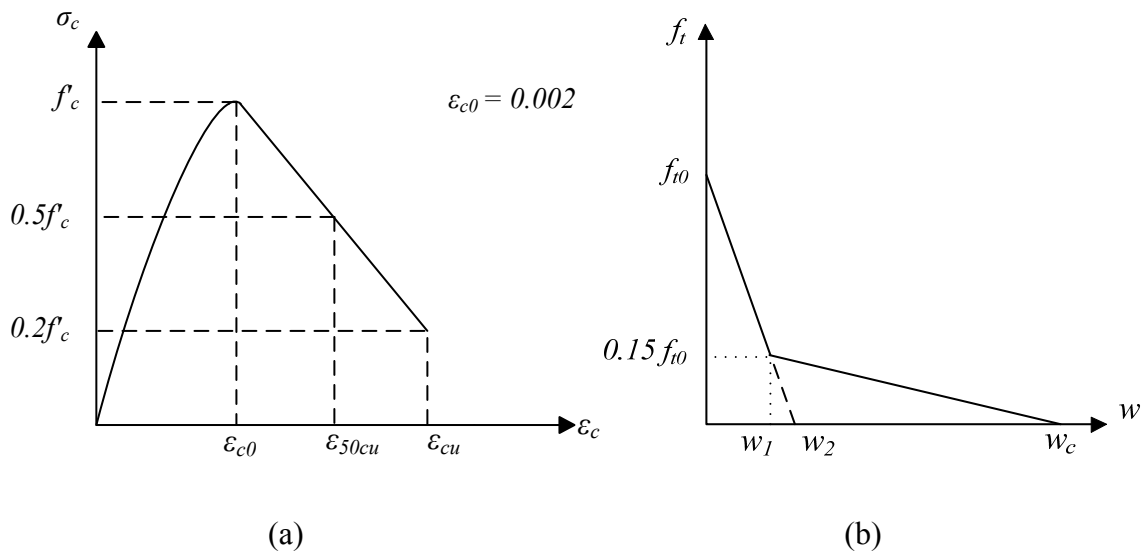

Figure 5-27. (a) Concrete compressive behaviour and (b) stress-crack opening displacement diagram of the concrete.

The post-failure (after cracking) behaviour of the concrete can be modelled by tension stiffening which enables the model to carry tension even after cracking of the concrete. This response may be considered by either post-failure stress-strain relation (σ_t-ε_t) or a fracture energy cracking criterion. In the later method, the tensile behaviour can be characterized as a function of cracking displacement (Figure 5-27b). Parameters of this figure can be defined by relations proposed in CEB-FIP Model Code 1990 (1991);

$$f_{t0} = 1.4\left(\frac{f'_{cm}}{10}\right)^{2/3} \qquad 5\text{-}108$$

$$f_{t1} = 0.15 f_{t0} \qquad 5\text{-}109$$

$$w_1 = \frac{1.7 G_f}{f_{t0}} \qquad 5\text{-}110$$

$$w_c = \frac{3.3 G_f}{f_{t1}} \qquad 5\text{-}111$$

G_f is the fracture energy of the size effect model corresponding to the area under the initial tangent of the stress-separation curve and is not sensitive to the structure size and shape. On

the other hand, G_F determines the area under the entire stress-deflection curve of the specimen and is highly dependent on the specimen size and geometry (Bažant and Becq-Giraudon 2002). The relationship between G_f and G_F can be expressed as (Bažant and Becq-Giraudon 2002);

$$G_F = 2.5G_f \tag{5-112}$$

$$G_f = \alpha_0 (\frac{f_{cm}^{'}}{0.051})^{0.46} (1 + \frac{d_a}{11.27})^{0.22} (\frac{w}{c})^{-0.30} \tag{5-113}$$

d_a, w, and c are the maximum aggregate size, water and cement weight, respectively. α_0 is 1.44 for crushed angular aggregates. It is noteworthy to mention that $f_{cm}^{'}$ in Eq. 5-113 is the mean compressive strength of concrete cylinders with dimension of 150×300 mm. Since in the present research $f_{cm}^{'}$ is obtained from compressive strength tests on the cylinders with standard dimensions of 200×100 mm (Chapter 3), results are required to be converted to the case of 150×300 mm. Therefore, the equation proposed by Mansur and Islam (2002) is employed;

$$(f_{cm}^{'})_{150\times300} = 0.98(f_{cm}^{'})_{100\times200} - 3.49 \tag{5-114}$$

5.6.2. FRP Laminate and Adhesive

The behaviour of the FRP laminates/sheets is assumed linear up to the failure (Figure 5-28). Properties of FRP, which is obtained from tensile tests and presented in Chapter 3, are introduced to the FE model. In addition, the elastic and plastic material properties of the epoxies are assigned as reported in Chapter 3.

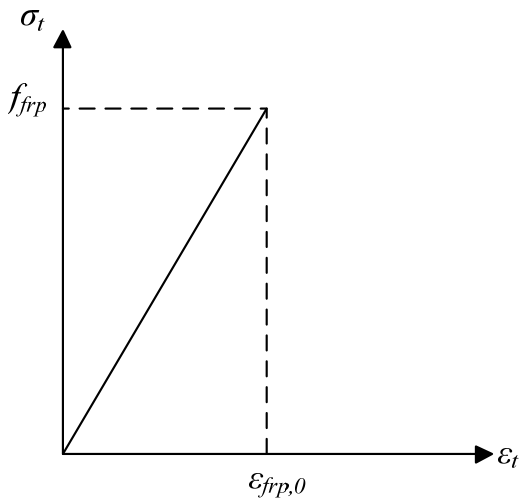

Figure 5-28. FRP stress vs strain behaviour.

5.7. Modelling of the Interface

Interface between FRP/epoxy and also epoxy/concrete is modelled with mesh tie constraints which connects the nodes from each surface in a way that both nodes have the same displacements in different directions. When the distance between the node on the slave and the master surfaces is less than a specific position tolerance criterion, two nodes are constrained to each other. In this case since both surfaces are deformable, the surface with coarser mesh is considered as the master surface.

5.8. FE Results

In order to reduce dependency of the FE results to element/mesh sizes, different mesh configurations (mesh refinement) are tested. Based on the FE analysis after mesh refinements, predicted applied load versus global slip at the loaded end and also applied load versus strain profile at the position of the second strain gauges are compared with the experimental results in Figure 5-29 and Figure 5-30, respectively. These curves show that finite element model can successfully simulate the interface behaviour in adhesively bonded joints.

In Figure 5-29, the predicted load-slip relationship for all of the samples is quite similar to the experimental results. The load increases linearly with increase in slip and after a certain stage shows nonlinear behaviour with further increase and the curve then tends to become plateau until failure. Post-nonlinear stage for samples shows the same trend in each series.

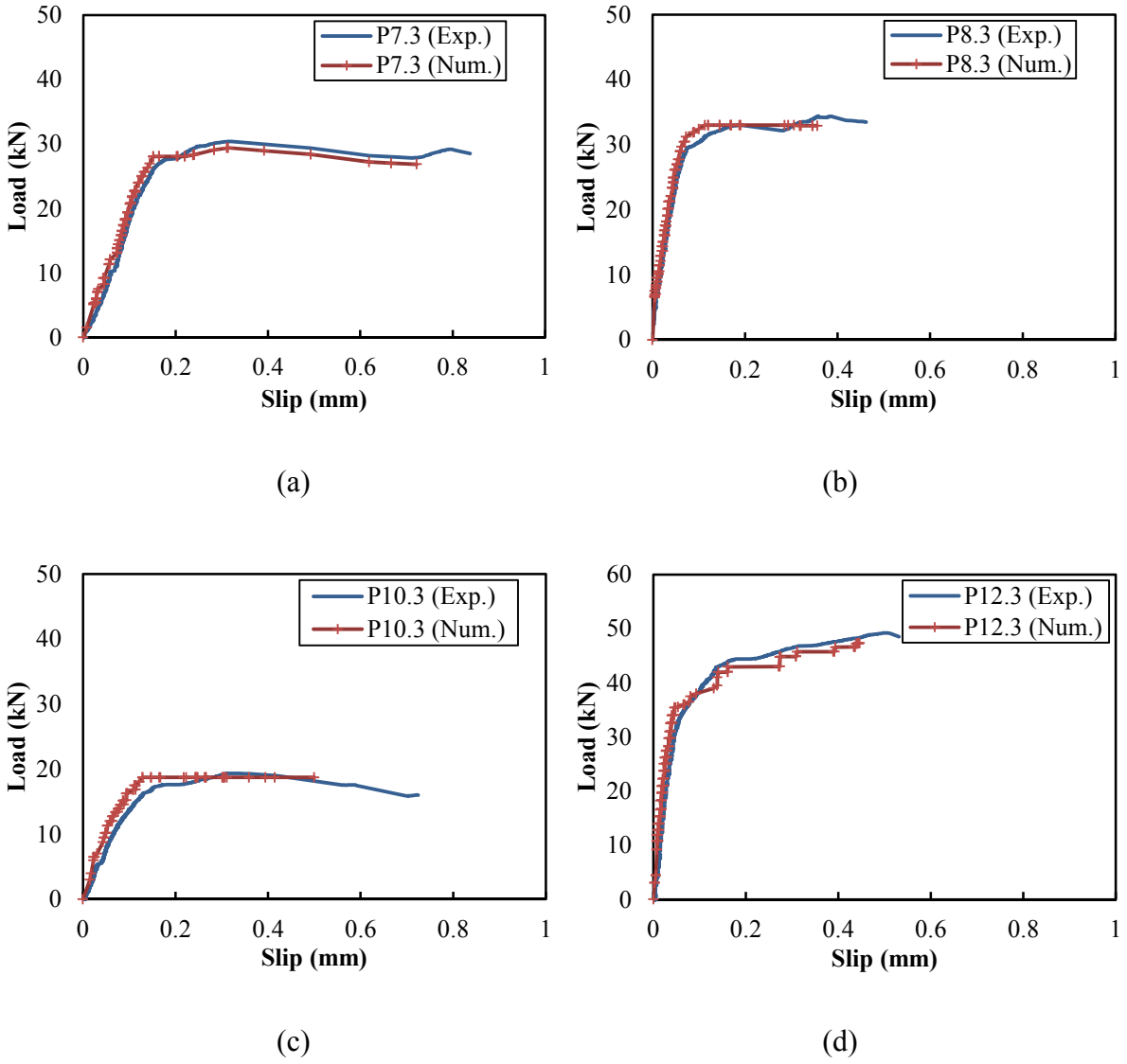

Figure 5-29. Experimental and numerical results of the load vs slip curves for MSLS specimens.

Load versus strain values of the interface at different locations along the bondline is presented in Figure 5-30. Similar to the experimental results, load-strain curve at each location consists of three stages: linear, nonlinear (post linear) and plateau (post nonlinear) sections. The load increases sharply with small change in strain values up to the formation of micro-cracks. Around the macro-crack initiation stage, the load-strain behaviour tends to be plateau and the strains of the interface rapidly increase without noticeable increase in load.

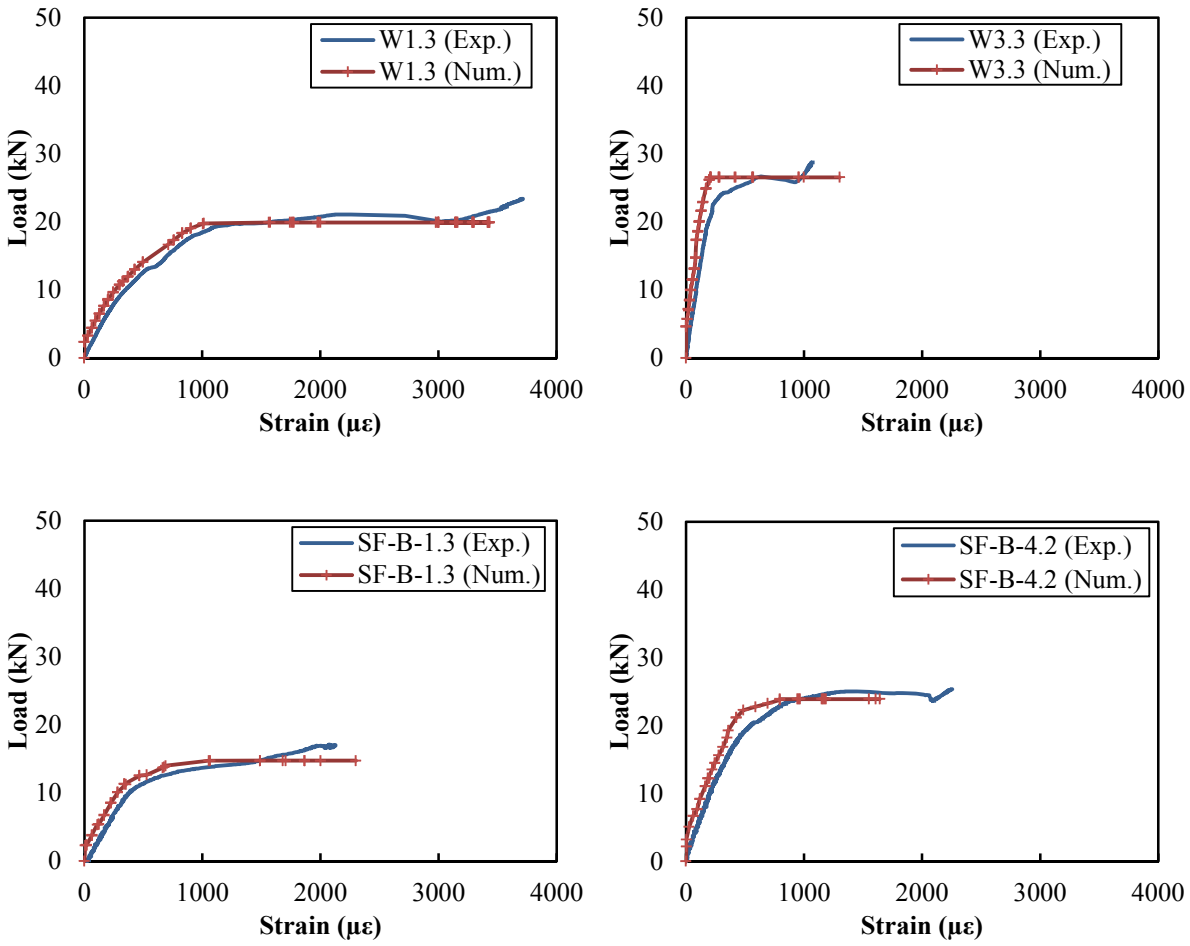

Figure 5-30. Experimental and numerical results of the load vs strain curves for MSLS specimens.

5.9. Summary

To attain a suitable strengthening system for concrete structures, adequate stress distribution between externally bonded fibre reinforced polymer (FRP) materials and the substrate is required. Several studies have been done and models have been proposed to estimate the interfacial behaviour in adhesively bonded joints. However, the bond characteristics are still not been fully understood.

With the growing application of the FRP in strengthening of the structures and in order to be able to sufficiently model the strengthened structure behaviour, the need for a generic bond-slip relationship is increasing. Therefore in this chapter, a new approach was developed for determination of the interface characteristics in the adhesively bonded joints. Based on this approach, a differential equation is proposed to estimate the local and global strain

profile of the joints. Further a continuously differentiable function is presented for deduction of bond stress along the interface.

Generally, the bond-slip models reported in the literature have been derived using the experimental results, or by indirect analytical approaches based on the regression of experimental data, or by finite element analysis. Therefore, bond-slip relationships show large scatter of results due to the variation and precision of data and cannot be extended to different types of the FRP processing techniques.

For analytically or numerically derived models the majority of the existing bond stress models apply sophisticated factors determined based on test data which can vary from one experiment to the other. Hence, exclusive features of the present investigation are that the bond characteristics are developed only based on boundary conditions of the joints and determined in accordance with the values of applied load at each stage and properties of the adherends and adhesive. These aspects of the proposed model contribute to overcome the instability of the bond stress function and application of the proposed model to different types of FRP manufacturing techniques.

According to the boundary conditions of the joints, two different methods are developed in this research (*Method A* and *Method B*). The properties of the FRP, applied load and the effective bond length are considered for determination of the bond behaviour in *Method A*. On the other hand, the interface response in *Method B* is characterised by an interface property factor, λ, FRP length, slip and applied load at the loaded end of the FRP. The interface property factor is dependent on the adhesive shear stiffness and also the FRP stiffness. Therefore, *Method B* considers the properties of the adherends and the adhesive for estimation of the bond behaviour.

Comparing the strain, shear stress, and slip profiles as well as the maximum applied load of the experimental and analytical predictions based on both methods indicate that the models are capable of prediction of the interface behaviour with satisfactory precision. The crack propagation along the bonded length can be estimated in a more efficient way with *Method A*. this is due to the fact that the influence of the effective bond length is considered in this method. In addition, the maximum shear stress estimated by *Method A* correlates better with the experimental results while it is underestimated by *Method B*. The predicted slip profiles calculated based on both methods are quite similar.

The interfacial fracture energy is an important factor for determination of the fracture mechanism and bond-slip response in adhesively bonded joints. Therefore in this research, the interfacial fracture energy is determined using the FRP stiffness and the strain at the

loaded face or the maximum shear stress. Comparison between experimental and analytical results shows that the proposed analytical equations can precisely estimate G_F.

The correlation between the fracture energy and the interface parameters showed that the fracture energy increases with thicker bondline while it decreases with higher FRP-to-concrete width ratio. It can be concluded from the results that there is no correlation between the fracture energy and the depth of intermediate crack debonding, D. Since the depth of IC debonding is related to the concrete properties therefore, unlike the models in which the interface response is solely determined by the concrete characteristics, other parameters of the joints (such as properties of FRP and adhesive layer) rather than just the concrete are required.

Finally, the interface behaviour of the joints was modelled in Abaqus finite element software. Comparing FE and experimental results indicate that by employment of proper constitutive behaviour for materials, the bond behaviour can be successfully predicted by FE models.

CHAPTER 6

CONCLUSIONS AND RECOMMENDATIONS

Considering the growing popularity of fibre reinforced polymer (FRP) materials in the strengthening of structures, new methods of FRP application are required to achieve more reliable FRP repairing systems with higher quality. Although extensive experimental and analytical studies have been carried out to characterize the interfacial behaviour, the application of the new FRP manufacturing techniques in strengthening of structures requires further investigation in the domain of intermediate-induced crack debonding. In addition, the state-of-the-art review of the existing constitutive interface laws reveals that the development of an efficient and sound analytical model is imperative to predict the bond behaviour of the joints manufactured with different processing methods.

This research has investigated the bond behaviour between the FRP and concrete substrates processed with different types of FRP manufacturing techniques. In achieving this objective, an extensive literature review was performed and a new modified single lap shear (MSLS) test set-up was proposed in order to minimise the experimental errors. During MSLS tests, several factors which influence the interface behaviour (specifically the bondline thickness) are studied. The interfacial performance of the FRP-to-concrete bonded joints is compared for different processing techniques (e.g. pultrusion, wet lay-up, HVBO, and VARI). To compare the characteristics of the joints fabricated with the various processing techniques, a specific criterion, called equalisation of the processing techniques, is used.

A new analytical approach was presented in the thesis to determine different characteristics of the joints. Based on the boundary conditions, two distinctive methods (*Method A* and *Method B*) are proposed to predict the bond-slip relationships and interfacial fracture energy. Comparing with the MSLS test's results, it was concluded that the proposed analytical methods are capable to predict the interfacial behaviour between the FRP and the concrete substrates with satisfactory precision.

6.1. Conclusions

Based on the main findings of this research, following conclusions can be derived:

6.1.1. Modified Single Lap Shear Tests

The interfacial behaviour of adhesively bonded joints processed with different types of manufacturing techniques was studied in this research. For this purpose, over 100 concrete blocks were cast and tested with the modified single lap shear test set-up. In addition, concrete compression and FRP tensile tests were carried out to define the properties of the concrete and the FRP materials, respectively. The effect of different factors on the bond behaviour was investigated for each processing technique through several test series. The parameters considered were concrete surface tensile strength (f'_{cst}), initial unbonded length (IUL), FRP bonded length (L_{frp}), FRP-to-concrete width ratio (w_r), bondline thickness (t_{bl}), surface treatment methods, and FRP processing techniques. Based on the developed MSLS test set-up, the bond-slip behaviour was captured directly from the loaded end. The significance of this method is more noticeable when the interface subjected to the unexpected out of plane stresses. Therefore, more accurate and reliable results can be achieved in terms of interfacial responses (global and local slips and shear stresses).

Concrete Surface Tensile Strength

Results of direct pull-off tests indicated that the correlation between the concrete surface tensile strength (f'_{cst}) and the interface response of the joints was inconsistent, while the maximum load and slip at the maximum applied load slightly increased with higher f'_{cst} for HVBO samples, they decreased for the pultruded specimens. A reason for this disassociation can be explained by the fracture mechanism occurring in MSLS tests. The failure of the interface in MSLS tests is mainly due to in plane shear mode II while mode I governs the direct pull-off tests.

Initial Unbonded Length

Studying the effect of the initial unbonded length on the bond behaviour of the joints revealed that longer IUL leads to higher maximum applied loads. For samples with no initial unbonded length the failure occurred with a rapid and partial propagation of the macro-crack

along the bonded region which accompanied with splitting of the concrete from the front side of the prisms. In addition, the local bond-slip relationships of the samples with proper initial gap consisted of ascending and descending branches while the ones with no IUL did not show the descending branch of the curve. Therefore, a sufficient initial unbonded length at the front side of the joint may contribute to distribution of the loads through the interface and finally achieve higher shear stresses while the fracture occurs inside a thin layer of the concrete under the bonded area.

FRP Bonded Length

The existence of the effective bond length (EBL) is proven in literature however the effect of different processing techniques on this parameter has not been investigated. Therefore, in the current research the effective bond length of the samples processed with different techniques was obtained using two methods, explicit and implicit. The EBL based on the explicit method is defined by the interpolation of the maximum applied load for different bonded lengths. In the implicit method, the strain distribution profiles along the bonded length are investigated to determine the EBL. In this model, it is defined as the distance between the points corresponding to 99% and 1% of the strain at the loaded end when the strain profile at the loaded face tends to become plateau. The effective bond length was determined for pultruded, wet lay-up and VARI samples based on the implicit method. Results indicated that wet lay-up has the longest effective bond length (around 180 mm) in comparison with other processing techniques (which was around 150 mm). In addition, the EBL is longer for the samples with thicker bondlines. However this increase stops after a specific bondline thickness.

FRP-to-concrete Width Ratio

With increase in the FRP-to-concrete width ratio, the maximum load carrying capacity increased. This may be attributed to the distribution of shear stresses over a larger area of the bond. The maximum shear stress increased for samples with wider FRP while the maximum local slip decreased. The same pattern was observed for the global slips corresponding to the maximum and ultimate loads. Depth of the intermediate crack debonding also increased with higher FRP-to-concrete width ratio. It indicates that wider joints show brittle behaviour compared with the samples with lower w_r.

Load-strain curves of the samples showed three distinctive stages: linear, nonlinear (post linear) and plateau (post nonlinear) sections. The load increased sharply with small change in strain values until the post linear stage. When the macro-crack initiated inside the interface, the load-strain behaviour became plateau and the strains of the interface rapidly increased without noticeable increase in load.

For the samples with W_{frp} = 80 mm, the strain along the bondline increased even after the initiation of the macro-crack. Since the concrete is a heterogeneous material consisting of aggregates and cement paste, micro-cracking occurs beneath the bondline in different directions. When the macro-crack initiates, it will cross micro-cracks and in order to continue its propagation toward the free end it requires to open the micro-cracks and releases energy. Therefore depending on the fact that the macro-crack crosses a longitudinal or a transverse micro-crack, the energy which is required to open a unit area of the crack differs. In samples with higher FRP-to-concrete width ratio, macro-crack can propagate over a larger area compared with the narrower w_r and change direction corresponding to the micro-cracks along its way to the free end of FRP. The same logic may explain the higher initial stiffness of the load-slip curves in the samples with wider FRP.

Bondline Thickness

The effect of the bondline thickness on the interface behaviour (e.g. the global load-slip curves, strain profiles, local bond-slip curves, and also shear stress and local slip profiles along the bonded length) of the samples processed with different manufacturing techniques such as pultruded, wet lay-up, HVBO, and VARI was investigated. Considering the nonlinear analysis of the load-slip responses, a new concept called optimum bondline thickness was proposed. By increasing the bondline thickness, the maximum applied load increases. However, the increase is not consistent and after a certain amount of bondline thickness, no increase in the load is observed. This phenomenon can be addressed by the stress states and also the physical and chemical interactions between FRP, adhesive and substrate.

The effect of bond thickness on the maximum load carrying capacity of the joints has not been considered in the past researches. Therefore, a relationship was suggested to predict the maximum load based on the bondline thickness for samples manufactured with different processing techniques. The samples with thicker bondline showed a softer behaviour in terms of load-global slip response. This response may be attributed to the surface condition of the substrate. When the bondline thickness decreases, the effect of the concrete surface condition

on the interfacial behaviour increases. Therefore, a thin bondline cannot sufficiently restrain the initiated cracks at the linear stage of the load-slip response. Since one of the major purposes in strengthening of concrete members is binding the emerged cracks on the substrate and preventing them from further growth during the initial stages of loading, the higher the initial stiffness of the strengthening method, the better. In addition, as the adhesive thickness increased, the slip at both maximum and ultimate load stages increased while the depth of intermediate crack debonding decreased. Therefore, with higher bondline thickness, the more ductile joint can be achieved.

Surface Treatment

To engage the interface element in a proper load transferring system of the joint, surface treatment is required to be carried out on the substrate by proper methods prior to the FRP attachment. Surface preparation aimed at removing the top layer of the mortar under the bonded region which contributes to the transmission of the interfacial stresses into the substrate with more proper mechanism. This may assist the bonded joints to withstand higher amount of loads. Therefore in this research, the effect of different surface preparation techniques (such as diamond grinding, abrasive belt sanding, water blasting, and sandblasting considering different levels of aggregate exposure) on the interface behaviour was investigated.

Comparing the load-slip curves of the samples treated with diamond grinding cup wheel and the abrasive belt sanding, diamond grinding cup wheel led to the softer initial stiffness and higher ultimate slips while later slightly decreased the maximum load of the joints. In general, the load-slip curves of the samples prepared with diamond grinding cup wheel were linear until failure. This may be caused by the formation of microscopic cracks during the surface treatment and loss of the bond between the aggregates and mortar under the bonded area. In addition from the long term performance perspective, these micro-cracks are prone to the environmental effects which can finally lead to the bond degradation. According to these facts, it may be advisable to use abrasive belt sanding as surface treatment method prior to the FRP attachment instead of grinding.

Water blasting and sandblasting methods were compared in the next series of the tests. The maximum load carrying capacity of the samples prepared with sandblasting was higher especially when the bondline thickness increased. The global slips at the maximum load and ultimate load stages were higher in the samples prepared with sandblasting. Since the

aggregate exposure for two methods was identical, surface treatment with sandblasting may contribute to a more appropriate interfacial behaviour.

In another attempt, MSLS results showed that the interface mostly experiences higher maximum applied load, slip at the maximum applied load and also the maximum shear stresses along the bonded length in the samples prepared with sandblasting compared with abrasive belt sanding method. Finally, the effect of aggregate exposure (medium and high) was investigated. Considering that larger area of the FRP is bonded to the aggregates, the maximum applied load and shear stresses were higher in the samples treated with this method. Based on these results, it is advisable to employ sandblasting for removing the top mortar layer on the concrete substrates.

FRP Processing Techniques

The bond characteristics between the concrete substrate and the FRP processed with heated vacuum bag only or vacuum assisted resin infusion techniques were compared with the commonly used methods (wet lay-up and pultrusion). Tests provided further understanding regarding the interface behaviour of the adhesively bonded joints processed with advanced manufacturing methods. Although the load-slip profiles of the samples processed with different techniques were quite similar, HVBO samples showed lower load carrying capacity among the methods. This may be attributed to two reasons; first, the FRP stiffness of HVBO samples was outstandingly lower than others and second, the manufacturing process involved application of the heat to the concrete for curing of the resin while such heat may cause damages to the substrate. Therefore, further investigation is required to achieve a comprehensive understanding about the interface behaviour of the joints fabricated by HVBO technique.

Throughout the experiment, wet lay-up specimens had the lowest local strain values. Further investigation on the strain profile indicated that the effective bond length of the wet lay-up samples was longer (around 181 mm) than the others (147 mm for pultruded and 158 mm for VARI samples). Therefore in strengthening of the reinforced concrete structures with wet lay-up sheets, longer anchorage length is required to achieve the maximum basic debonding resistance. Considering the local bond-slip law of the specimens, wet lay-up specimen experienced lower shear stresses and local slip values.

Among the methods, samples processed with VARI technique showed more ductile behaviour in terms of the local slip. In addition, the type of failure in VARI and HVBO

processed samples (mainly cohesive failure) is similar to pultruded and wet lay-up systems. It indicates that the quality of the bond between fibres and adhesive and also between FRP and concrete is satisfactory in VARI and HVBO processed specimens.

According to these outcomes, advanced processing techniques such as heated vacuum bag only and vacuum assisted resin infusion can be successfully applied to achieve high quality of the bond in strengthening of the reinforced concrete structures

6.1.2. Analytical and Numerical Modelling of the Interface

A new analytical approach was developed to define the interfacial behaviour of the adhesively bonded joints. The strain profile of the interface was expressed by a non-linear continuously differentiable function. Solving the governing strain equations for different boundary conditions, two distinctive methods were proposed (*Method A* and *Method B*) to determine the interface characteristics (shear stress, slip and the fracture energy). *Method A* was developed based on the fixity of the strain while *Method B* is expanded based on the slip fixity at the free and loaded ends of the bonded region. Since the models were characterised solely based on boundary conditions of the joints, they can be applied to any type of the FRP processing techniques. Another advantage of the proposed models is that all of the interface characteristics are obtained from the value of the applied load at each stage and the properties of the adherends and adhesive. Therefore, the proposed methods were developed by adopting the parameters which are available in the lap shear tests, namely the applied load and the global slip. In addition, the interfacial fracture energy corresponding to the antisymmetric in-plane shear mode was determined using the FRP stiffness and the strain at the loaded face or the maximum local shear stress.

Since the influence of the effective bond length is considered in *Method A*, this model is able to estimate the crack propagation along the bonded length with more precision. Considering the large amount of the concrete axial rigidity, the shear stress and slip profiles of the joints can be obtained based on an interface property factor, λ, applied load and slip at the loaded end in *Method B*. λ represents both the FRP axial stiffness and the shear stiffness of the adhesive layer. Therefore, *Method B* takes into account the properties of both adherends and adhesive to determine the bond-slip relationship.

Comparison between the analytical models and the experimental data indicated that the proposed analytical models can successfully estimate the interface behaviour of FRP-to-concrete bonded joints. To validate the proposed methods, different characteristics of the

joints, such as the maximum load carrying capacity, the strain, shear stress and slip profiles and also the fracture energy of the interface and the effective parameters were considered. It was attempted to assess the results of the proposed models for different processing techniques in all of the comparisons which showed the capability of the models in prediction of the bond behaviour of the joints with different fabrication methods.

Experimental results of the shear stress profile along the FRP bonded length showed that the magnitude of τ_{max} changes with the load level. Contrary to existing models which consider a constant shear stress, the proposed models in this research followed the experimental trend and were able to successfully capture the variation of the shear stress profile along the bonded length. Furthermore, the overall calculated value of the maximum shear stresses showed a good agreement with the experimental results.

Reviewing the literature points out that the bond-slip laws for the long joints (longer than effective bond length) may not be applicable to the short joints. However, comparison of the analytical and experimental slip profiles indicated that the developed models not only can predict the slip of the long joints but also are valid for the short joints (less than effective bond length).

The fracture energy obtained from analytical formulae was compared with the experimental observations corresponding to the first and second strain gauges. The analytical results showed closer agreement with the experimental ones at the second strain gauges. It may be due to the stress intensity at the loaded end of the bond. The correlation between the fracture energy and interface parameters showed that the fracture energy increases with thicker bondline while it decreases with higher FRP-to-concrete width ratio. Results showed that there is not a clear correlation between the depth of intermediate crack debonding and the fracture energy.

Two different relations, logarithmic and powered, are proposed for determination of the maximum shear stresses according to the fracture energy. Shear stress versus fracture energy curves indicated that the maximum shear stress may not increase constantly with the higher fracture energy. Therefore, the logarithmic equation is able to estimate the shape of increase in a more efficient way.

The interface behaviour of the joints was modelled in Abaqus finite element software. Concrete blocks, adhesive layers and FRP laminates were modelled by three different parts. Constitutive laws were used in order to introduce the materials behaviour in the FE model. Interface between FRP/epoxy and also epoxy/concrete was modelled with mesh tie constraints. Different mesh configurations were tested to reduce dependency of the FE results

to element/mesh sizes. Comparing FE and experimental results indicate that by employment of proper constitutive behaviour for materials, the bond behaviour can be successfully predicted by FE models.

6.2. Recommendations for Future Studies

The following recommendations can be made for future research:

- The experiments carried out in this study focused on the interface behaviour under the act of monotonic loads (constant increase). However the strengthened elements are mostly subjected to the cyclic loads during their life time. Therefore to examine the bond performance under such conditions, fatigue tests are required to be performed on the FRP-to-concrete bonded joints and establish appropriate fatigue crack propagation models.
- The bond performance of new processing techniques needs to be examined via full-scale beam tests. It can provide a data-base to study the advantages and shortcomings of these techniques in strengthening of the structures.
- The analytical models which are proposed in this research are subjected to some simplifications (e.g. assuming zero local slip at the free end, obtaining the effective bond length from the experimental results or neglecting the elongation of the FRP). Author suggests that these parameters are included in development of the future models.
- During the single lap shear test, bending stresses are imposed to the plate. Therefore, SLS test does not replicate pure shear mode II. However, to develop the analytical model, the effect of these out of plane stresses is ignored. Therefore, it is advisable that these effects are considered for development of the future models.
- For further validation, the proposed analytical models can be implemented into a finite element package and perform the parametric study in order to investigate the interface behaviour under different conditions.

REFERENCES

Abaqus/Standard "*User's Manual."* Version 6.11 edn, Dassault Systemes Simulia Corp., Providence, RI, USA.

Abdel Baky, H., Ebead, U. A. and Neale, K. W. (2012). "Nonlinear micromechanics-based bond–slip model for FRP/concrete interfaces." *Engineering Structures*, 39(0), 11-23.

Abraham, D., Matthews, S. and McIlhagger, R. (1998). "A comparison of physical properties of glass fibre epoxy composites produced by wet lay-up with autoclave consolidation and resin transfer moulding." *Composites Part A: Applied Science and Manufacturing*, 29(7), 795-801.

ACI 440.2R-08 (2008). "*Guide for the design and construction of externally bonded FRP system for strengthening concrete structures."* MCP 2005. ACI. , Michigan (USA).

ACI 440R-96 (1996). "*State-of-the-Art report on fiber reinforced plastic (FRP) reinforcement for concrete structures."* American Concrete Institute, Detroit, Michigan.

Agius, S. L., Magniez, K. J. C. and Fox, B. L. (2013). "Cure behaviour and void development within rapidly cured out-of-autoclave composites." *Composites Part B: Engineering*, 47(0), 230-7.

Alampalli, S., O'Connor, J. and Yannotti, A. P. (2002). "Fiber reinforced polymer composites for the superstructure of a short-span rural bridge." *Composite Structures*, 58(1), 21-7.

Alampalli, S., O'Connor, J. and Yannotti, A. (2000). "*Design fabrication construction, and testing of an FRP superstructure."* New York State Department of Transportation.

Ali, M., Oehlers, D. and Bradford, M. (2001). "Shear Peeling of Steel Plates Bonded to Tension Faces of RC Beams." *Journal of Structural Engineering*, 127(12), 1453-9.

Alms, J. B., Glancey, J. L. and Advani, S. G. (2010). "Mechanical properties of composite structures fabricated with the vacuum induced preform relaxation process." *Composite Structures*, 92(12), 2811-6.

Arduini, M., Tommaso, A. D. and Nanni, A. (1997). "Brittle failure in FRP plate and sheet bonded beams." *ACI Structural Journal*, 94(4), 363-70.

ASTM C39/C39M-09a (2009). "*Standard test method for compressive strength of cylindrical concrete specimens."* ASTM International, West Conshohocken, PA.

ASTM C1583-04 (2009). "*Standard test method for tensile strength of concrete surfaces and the bond strength or tensile strength of concrete repair and overlay materials by direct tension (pull-off method)."* ASTM International, West Conshohocken, PA.

ASTM D3039/D3039M (2008). "*Standard test method for tensile properties of polymer matrix composite materials."* ASTM International, West Conshohocken, PA.

ASTM Standard D5573-99 (2012). "*Standard practice for classifying failure modes in fiber-reinforced-plastic (FRP) joints."* West Conshohocken, PA.

Åström (1997). "*Manufacturing of polymer composites."* London, UK, Chapman & Hall.

Au, C. and Büyüköztürk, O. (2006). "Debonding of FRP plated concrete: A tri-layer fracture treatment." *Engineering Fracture Mechanics*, 73(3), 348-65.

Bader, M. G. (2002). "Selection of composite materials and manufacturing routes for cost-effective performance." *Composites Part A: Applied Science and Manufacturing*, 33(7), 913-34.

Bakis, C., Bank, L., Brown, V., Cosenza, E., Davalos, J., Lesko, J., Machida, A., Rizkalla, S. and Triantafillou, T. (2002). "Fiber-Reinforced Polymer Composites for Construction—State-of-the-Art Review." *Journal of Composites for Construction*, 6(2), 73-87.

Bank, L. C. (2006). "*Composites for construction : structural design with FRP materials*." John Wiley & Sons, Inc., Hoboken, New Jersey.

Barnes, R. A. and Mays, G. C. (2001). "The transfer of stress through a steel to concrete adhesive bond." *International Journal of Adhesion and Adhesives*, 21(6), 495-502.

Bažant, Z. P. and Becq-Giraudon, E. (2002). "Statistical prediction of fracture parameters of concrete and implications for choice of testing standard." *Cement and Concrete Research*, 32(4), 529-56.

Bazant, Z. P. and Planas, J. (1997). "*Fracture and size effect in concrete and other quasibrittle materials*." CRC Press.

Bilotta, A., DI Ludovico, M. and Nigro, E. (2009). "Influence of effective bond length on FRP-concrete debonding under monotonic and cyclic actions." FRPRCS-9, Sydney, Australia.

Bizindavyi, L. and Neale, K. W. (1999). "Transfer lengths and bond strengths for composites bonded to concrete." *Journal of Composites for Construction*, 3(4), 153-60.

Boey, F. Y. C. (1990). "Reducing the void content and its variability in polymeric fibre reinforced composite test specimens using a vacuum injection moulding process." *Polymer Testing*, 9(6), 363-77.

Böger, L., Wichmann, M. H. G., Meyer, L. O. and Schulte, K. (2008). "Load and health monitoring in glass fibre reinforced composites with an electrically conductive nanocomposite epoxy matrix." *Composites Science and Technology*, 68(7–8), 1886-94.

Boyd, S. W., Winkle, I. E. and Day, A. H. (2004). "Bonded butt joints in pultruded GRP panels—an experimental study." *International Journal of Adhesion and Adhesives*, 24(3), 263-75.

Brosens, K. and Van Gemert, D. (1998). "Plate end shear design for external CFRP laminates." Fracture Mechanics of Concrete Structures (FRAMCOS-3), Germany, 1793-804.

Brouwer, W. D., van Herpt, E. C. F. C. and Labordus, M. (2003). "Vacuum injection moulding for large structural applications." *Composites Part A: Applied Science and Manufacturing*, 34(6), 551-8.

Calabrese, L. and Valenza, A. (2003). "The effect of a liquid CTBN rubber modifier on the thermo-kinetic parameters of an epoxy resin during a pultrusion process." *Composites Science and Technology*, 63(6), 851-60.

Camli, U. S. and Binici, B. (2007). "Strength of carbon fiber reinforced polymers bonded to concrete and masonry." *Construction and Building Materials*, 21(7), 1431-46.

Canning, L., Hollaway, L. and Thorne, A. M. (1999). "An investigation of the composite action of an FRP/concrete prismatic beam." *Construction and Building Materials*, 13(8), 417-26.

Cao, S., Chen, J., Pan, J. and Sun, N. (2007). "ESPI Measurement of Bond-Slip Relationships of FRP-Concrete Interface." *Journal of Composites for Construction*, 11(2), 149-60.

Carlone, P., Palazzo, G. S. and Pasquino, R. (2007). "Pultrusion manufacturing process development: Cure optimization by hybrid computational methods." *Computers & Mathematics with Applications*, 53(9), 1464-71.

Carpinteri, A., Cornetti, P., Lacidogna, G. and Paggi, M. (2009). "Towards a Unified Approach for the Analysis of Failure Modes in FRP-Retrofitted Concrete Beams." *Advances in Structural Engineering*, 12(0), 715-29.

Causse, P., Ruiz, E. and Trochu, F. (2012). "Spring-in behavior of curved composites manufactured by Flexible Injection." *Composites Part A: Applied Science and Manufacturing*, 43(11), 1901-13.

CEB-FIP (2001). "*Externally bonded FRP reinforcement for RC structures."* Technical Report Bulletin 14, Geneva, Switzerland.

CEB-FIP Model Code 1990 (1991). "*Design Code."* Thomas Telford Services Ltd, London.

Cender, T. A., Simacek, P. and Advani, S. G. (2013). "Resin film impregnation in fabric prepregs with dual length scale permeability." *Composites Part A: Applied Science and Manufacturing*, 53(0), 118-28.

Centea, T. and Hubert, P. (2012). "Modelling the effect of material properties and process parameters on tow impregnation in out-of-autoclave prepregs." *Composites Part A: Applied Science and Manufacturing*, 43(9), 1505-13.

Chajes, M. J., Finch Jr, W. W., Januszka, T. F. and Thomson Jr, T. A. (1996). "Bond and force transfer of composite material plates bonded to concrete." *ACI Structural Journal*, 93(2), 208-17.

Chalmers, D. W. (1991). "Experience in design and production of FRP marine structures." *Marine Structures*, 4(2), 93-115.

Chen, G., Teng, J. and Chen, J. (2011). "Finite-Element Modeling of Intermediate Crack Debonding in FRP-Plated RC Beams." *Journal of Composites for Construction*, 15(3), 339-53.

Chen, G. M., Chen, J. F. and Teng, J. G. (2007). "Behaviour of FRP-to-concrete interfaces between two adjacent cracks in FRP-plated concrete memebrs: A numerical investigation." Asia-Pacific Conference on FRP in Structures (APFIS 2007), Hong Kong, China, 683-8.

Chen, J. and Teng, J. (2001). "Anchorage Strength Models for FRP and Steel Plates Bonded to Concrete." *Journal of Structural Engineering*, 127(7), 784-91.

Cornetti, P. and Carpinteri, A. (2011). "Modelling the FRP-concrete delamination by means of an exponential softening law." *Engineering Structures*, 33(6), 1988-2001.

Coronado, C. A. and Lopez, M. M. (2006). "Sensitivity analysis of reinforced concrete beams strengthened with FRP laminates." *Cement and Concrete Composites*, 28(1), 102-14.

Correia, N. C., Robitaille, F., Long, A. C., Rudd, C. D., Šimáček, P. and Advani, S. G. (2005). "Analysis of the vacuum infusion moulding process: I. Analytical formulation." *Composites Part A: Applied Science and Manufacturing*, 36(12), 1645-56.

Crocombe, A. D., Hua, Y. X., Loh, W. K., Wahab, M. A. and Ashcroft, I. A. (2006). "Predicting the residual strength for environmentally degraded adhesive lap joints." *International Journal of Adhesion and Adhesives*, 26(5), 325-36.

Dagher, H. J., Bannon, D. J., Davids, W. G., Lopez-Anido, R. A., Nagy, E. and Goslin, K. (2012). "Bending behavior of concrete-filled tubular FRP arches for bridge structures." *Construction and Building Materials*, 37(0), 432-9.

Dai, J., Ueda, T. and Sato, Y. (2005). "Development of the Nonlinear Bond Stress-Slip Model of Fiber Reinforced Plastics Sheet-Concrete Interfaces with a Simple Method." *Journal of Composites for Construction*, 9(1), 52-62.

Dai, J., Ueda, T. and Sato, Y. (2006). "Unified Analytical Approaches for Determining Shear Bond Characteristics of FRP-Concrete Interfaces through Pullout Tests." *Journal of Advanced Concrete Technology*, 4(1), 133-45.

Daken, H. H., Ismail, A. A. and Rashed, F. (1994). "Productivity improvement and resin-waste reduction in composites wet lay-up facilities." *Journal of Materials Processing Technology*, 41(1), 1-21.

Davies, L. W., Day, R. J., Bond, D., Nesbitt, A., Ellis, J. and Gardon, E. (2007). "Effect of cure cycle heat transfer rates on the physical and mechanical properties of an epoxy matrix composite." *Composites Science and Technology*, 67(9), 1892-9.

Dawood, M., Ballew, W. and Seiter, J. (2011). "Enhancing the resistance of composite sandwich panels to localized forces for civil infrastructure and transportation applications." *Composite Structures*, 93(11), 2983-91.

De Lorenzis, L., Miller, B. and Nanni, A. (2001). "Bond of FRP laminates to concrete." *ACI Materials Journal*, 98(3), 256-64.

Deka, L. J., Bartus, S. D. and Vaidya, U. K. (2009). "Multi-site impact response of S2-glass/epoxy composite laminates." *Composites Science and Technology*, 69(6), 725-35.

DO, E. (1997). "*Fiber placement."* Cincinnati: Cininnati Machine.

Dodkins, A. R., Shenoi, R. A. and Hawkins, G. L. (1994). "Design of joints and attachments in FRP ships' structures." *Marine Structures*, 7(2–5), 365-98.

Drakonakis, V. M., Seferis, J. C. and Doumanidis, C. C. (2013). "Curing Pressure Influence of Out-of-Autoclave Processing on Structural Composites for Commercial Aviation." *Advances in Materials Science and Engineering*, 2013(14.

Edwards, K. L. (1998). "An overview of the technology of fibre-reinforced plastics for design purposes." *Materials & Design*, 19(1–2), 1-10.

EN ISO 527-5 (2009). "*Plastics- Determination of tensile properties."* Part 5: Test conditions for unidirectional fibre-reinforced plastic composites.

Ferracuti, B., Savoia, M. and Mazzotti, C. (2007). "Interface law for FRP–concrete delamination." *Composite Structures*, 80(4), 523-31.

Foster, S. J. and Khomwan, N. (2005). "Determination of bond stress versus slip for externally bonded FRP from standardised bond strength tests." Proceedings of the

International Symposium on Bond Behaviour of FRP in Structures (BBFS 2005), Hong Kong, China, 85-90.

Garschke, C., Weimer, C., Parlevliet, P. P. and Fox, B. L. (2012). "Out-of-autoclave cure cycle study of a resin film infusion process using in situ process monitoring." *Composites Part A: Applied Science and Manufacturing*, 43(6), 935-44.

Gorthala, R., Roux, J. A., Vaughan, J. G. and Donti, R. P. (1994). "Comparison of Processing Parameters for Pultruded Graphite/Epoxy and Fiberglass/Epoxy: A Heat Transfer and Curing Model." *Journal of Reinforced Plastics and Composites*, 13(4), 288-300.

Grande, E., Imbimbo, M. and Sacco, E. (2011). "Bond behaviour of CFRP laminates glued on clay bricks: Experimental and numerical study." *Composites Part B: Engineering*, 42(2), 330-40.

Grant, L. D. R., Adams, R. D. and da Silva, L. F. M. (2009). "Experimental and numerical analysis of single-lap joints for the automotive industry." *International Journal of Adhesion and Adhesives*, 29(4), 405-13.

Griffith, A. A. (1921). "*The phenomena of rupture and flow in solids."*

Grunenfelder, L. K., Centea, T., Hubert, P. and Nutt, S. R. (2013). "Effect of room-temperature out-time on tow impregnation in an out-of-autoclave prepreg." *Composites Part A: Applied Science and Manufacturing*, 45(0), 119-26.

Gunes, O., Lau, D., Tuakta, C. and Büyüköztürk, O. (2013). "Ductility of FRP–concrete systems: Investigations at different length scales." *Construction and Building Materials*, 49(915-25.

Guo, Z. G., Cao, S. Y., Sun, W. M. and Lin, X. Y. (2005). "Experimental study on bond stress-slip behaviour between FRP sheets and concrete." Proceedings of the International Symposium on Bond Behaviour of FRP in Structures (BBFS 2005), 77-83.

Gupta, N. and Sundaram, R. (2009). "Fiber optic sensors for monitoring flow in vacuum enhanced resin infusion technology (VERITy) process." *Composites Part A: Applied Science and Manufacturing*, 40(8), 1065-70.

Harries, K. A. and Kim, Y. J. (2012). "Predictive response of notched steel beams repaired with cfrp strips including bond-slip behavior." *International Journal of Structural Stability and Dynamics*, 12(01), 1-21.

Hashim, S. A. (2009). "Strength of resin-coated-adhesive-bonded double lap-shear pultrusion joints at ambient temperature." *International Journal of Adhesion and Adhesives*, 29(3), 294-301.

Hayes, B. S., Gilbert, E. N. and Seferis, J. C. (2000). "Scaling complications of dual temperature cure resin prepreg systems in airplane part manufacture." *Composites Part A: Applied Science and Manufacturing*, 31(7), 717-25.

Hayward, J. S. and Harris, B. (1990). "The effect of vacuum assistance in resin transfer moulding." *Composites Manufacturing*, 1(3), 161-6.

HB 305 (2008). "*Design handbook for RC structures retrofitted with FRP and metal plates: beams and slabs."* Standards Australia, 476, Sydney, NSW 2001, Australia.

Hejll, A., Täljsten, B. and Motavalli, M. (2005). "Large scale hybrid FRP composite girders for use in bridge structures—theory, test and field application." *Composites Part B: Engineering*, 36(8), 573-85.

Hernández, S., Sket, F., Molina-Aldareguı´a, J. M., González, C. and Llorca, J. (2011). "Effect of curing cycle on void distribution and interlaminar shear strength in polymer-matrix composites." *Composites Science and Technology*, 71(10), 1331-41.

Hillerborg, A., Modéer, M. and Petersson, P. E. (1976). "Analysis of crack formation and crack growth in concrete by means of fracture mechanics and finite elements." *Cement and Concrete Research*, 6(6), 773-81.

Himmel, N. and Bach, C. (2006). "Cyclic fatigue behavior of carbon fiber reinforced vinylester resin composites manufactured by RTM and VARI." *International Journal of Fatigue*, 28(10), 1263-9.

Hognestad, E. (1951). "*A study on combined bending and axial load in reinforced concrete members."* Univ. of Illinois Engineering Experiment Station, Univ. of Illinois at Urbana-Champaign, IL.

Hollaway, L. (1994). "*Handbook of polymer composites for engineering.*" Woodhead Publishing Ltd., Cambridge, England, 338.

ICRI/ACI (1999). "*Concrete Repair Manual."* International Concerete Repair Institute and American Concrete Institute, Detroit, MI.

Irwin, G. R. (1957). "Analysis of stresses and strain near the end of a crack traversing a plate." *Trans. ASME. Ser. E: J. Appl. Mech.*, 24(3), 361-4 (1957), "Discussion," J. Appl. Mech., 25, No. 2, 299-303.

Iwashita, K., Wu, Z., Ishikawa, T., Hamaguchi, Y. and Suzuki, T. (2007). "Bonding and debonding behavior of FRP sheets under fatigue loading." *Advanced Composite Materials*, Volume 16(1), 31-44.

Jarry, E. and Shenoi, R. A. (2006). "Performance of butt strap joints for marine applications." *International Journal of Adhesion and Adhesives*, 26(3), 162-76.

Kalamkarov, A. L., Fitzgerald, S. B. and MacDonald, D. O. (1999). "The use of Fabry Perot fiber optic sensors to monitor residual strains during pultrusion of FRP composites." *Composites Part B: Engineering*, 30(2), 167-75.

Karbhari, V. M. and Zhao, L. (2000). "Use of composites for 21st century civil infrastructure." *Computer Methods in Applied Mechanics and Engineering*, 185(2–4), 433-54.

Kent, D. C. and Park, R. (1971). "Flexural members with confined concrete." *Journal of the Structural Division, Proc. of the American Society of Civil Engineers*, 97(ST7), 1969-90.

Kim, Y. J. and Harries, K. A. (2011). "Fatigue behavior of damaged steel beams repaired with CFRP strips." *Engineering Structures*, 33(5), 1491-502.

Kin Loch, A. J. and Shaw, S. J. (1981). "The Fracture Resistance of a Toughened Epoxy Adhesive." *The Journal of Adhesion*, 12(1), 59-77.

Kratz, J. and Hubert, P. (2011). "Processing out-of-autoclave honeycomb structures: Internal core pressure measurements." *Composites Part A: Applied Science and Manufacturing*, 42(8), 1060-5.

Kratz, J. and Hubert, P. (2013). "Anisotropic air permeability in out-of-autoclave prepregs: Effect on honeycomb panel evacuation prior to cure." *Composites Part A: Applied Science and Manufacturing*, 49(0), 179-91.

Krenchel, H. (1964). "*Fibre Reinforcement*." Akademisk Forlag, Copenhagen.

Kulshreshtha, A. K. and Vasile, C. (2002). "*Handbook of Polymer Blends and Composites*." vol. 2, Liquid moulding process, Smithers Rapra Technology.

Kumar, S., Murthy Reddy, K. V. V. S., Kumar, A. and Rohini Devi, G. (2013). "Development and characterization of polymer–ceramic continuous fiber reinforced functionally graded composites for aerospace application." *Aerospace Science and Technology*, 26(1), 185-91.

Lameiras, R., Barros, J., Valente, I. B. and Azenha, M. (2013). "Development of sandwich panels combining fibre reinforced concrete layers and fibre reinforced polymer connectors. Part I: Conception and pull-out tests." *Composite Structures*, 105(0), 446-59.

Lee and Fenves (1998). "Plastic-Damage Model for Cyclic Loading of Concrete Structures." *Journal of Engineering Mechanics*, 124(8), 892-900.

Lee, C.-L. and Wei, K.-H. (2000). "Resin transfer molding (RTM) process of a high performance epoxy resin. II: Effects of process variables on the physical, static and dynamic mechanical behavior." *Polymer Engineering & Science*, 40(4), 935-43.

Liu, K. and Wu, Y.-F. (2012). "Analytical identification of bond–slip relationship of EB-FRP joints." *Composites Part B: Engineering*, 43(4), 1955-63.

López-González, J., Fernández-Gómez, J. and González-Valle, E. (2012). "Effect of Adhesive Thickness and Concrete Strength on FRP-Concrete Bonds." *Journal of Composites for Construction*, 16(6), 705-11.

Lu, X. Z., Teng, J. G., Ye, L. P. and Jiang, J. J. (2005a). "Bond–slip models for FRP sheets/plates bonded to concrete." *Engineering Structures*, 27(6), 920-37.

Lu, X. Z., Ye, L. P., Teng, J. G. and Jiang, J. J. (2005b). "Meso-scale finite element model for FRP sheets/plates bonded to concrete." *Engineering Structures*, 27(564-75.

Lubliner, J., Oliver, J., Oller, S. and Oñate, E. (1989). "A plastic-damage model for concrete." *International Journal of Solids and Structures*, 25(3), 299-326.

Lukaszewicz, D. H. J. A., Potter, K. D. and Eales, J. (2013). "A concept for the in situ consolidation of thermoset matrix prepreg during automated lay-up." *Composites Part B: Engineering*, 45(1), 538-43.

Lukaszewicz, D. H. J. A., Ward, C. and Potter, K. D. (2012). "The engineering aspects of automated prepreg layup: History, present and future." *Composites Part B: Engineering*, 43(3), 997-1009.

Mansur, M. and Islam, M. (2002). "Interpretation of Concrete Strength for Nonstandard Specimens." *Journal of Materials in Civil Engineering*, 14(2), 151-5.

Mazzotti, C., Savoia, M. and Ferracuti, B. (2008). "An experimental study on delamination of FRP plates bonded to concrete." *Construction and Building Materials*, 22(7), 1409-21.

McGeorge, D., Echtermeyer, A. T., Leong, K. H., Melve, B., Robinson, M. and Fischer, K. P. (2009). "Repair of floating offshore units using bonded fibre composite materials." *Composites Part A: Applied Science and Manufacturing*, 40(9), 1364-80.

McIlhagger, A., Brown, D. and Hill, B. (2000). "The development of a dielectric system for the on-line cure monitoring of the resin transfer moulding process." *Composites Part A: Applied Science and Manufacturing*, 31(12), 1373-81.

Menta, V., Vuppalapati, R., Chandrashekhara, K., Schuman, T. and Sha, J. (2013). "Elevated-temperature vacuum-assisted resin transfer molding process for high performance aerospace composites." *Polymer International*, 62(10), 1465-76.

Mier, J. G. M. v. (2012). "*Concrete fracture: a multiscale approach*." CRC Press.

Monroy Aceves, C., Sutcliffe, M. P. F., Ashby, M. F., Skordos, A. A. and Rodríguez Román, C. (2012). "Design methodology for composite structures: A small low air-speed wind turbine blade case study." *Materials & Design*, 36(0), 296-305.

Morales, G., Barrena, M. I., Salazar, J. M. G. d., Merino, C. and Rodríguez, D. (2010). "Conductive CNF-reinforced hybrid composites by injection moulding." *Composite Structures*, 92(6), 1416-22.

Morrison, C. E. and Bader, M. G. (1989). "Computer modelling of resin flow during laminate cure." *Composites*, 20(1), 9-13.

Nakaba, K., Kanakubo, T., Furuta, T. and Yoshizawa, H. (2001). "Bond Behavior between Fiber-Reinforced Polymer Laminates and Concrete." *ACI Structural Journal*, 98(3), 359-67.

NCHRP Report 514 (2004). "*Bonded repair and retrofit of concrete structures using FRP composites."* Transportation Research Board, Washington, D.C.

Nehdi, M., El Damatty, A. and Rahimi, R. (2003). "Investigation on lap-joint behaviour of GFRP plates bonded to silica fume and rice husk ash concrete." *International Journal of Adhesion and Adhesives*, 23(4), 323-33.

Neubauer, U. and Rostasy, F. S. (1997). "Desing aspects of concrete structures strengthened with externally bonded CFRP plates." Proceedings of 7th International Conference on Structural Faults and Repairs, Edinburgh, Scotland, 109-18.

Nisar, J. A. and Hashim, S. A. (2010). "Meso-scale laminate adhesive joints for pultrusions." *International Journal of Adhesion and Adhesives*, 30(8), 763-73.

O'Mahoney, D. C., Katnam, K. B., O'Dowd, N. P., McCarthy, C. T. and Young, T. M. (2013). "Taguchi analysis of bonded composite single-lap joints using a combined interface–adhesive damage model." *International Journal of Adhesion and Adhesives*, 40(0), 168-78.

O'Guin, M. C. (1991). "*The complete guide to activity-based costing*." Prentice Hall.

Odler, I. and Rößler, M. (1985). "Investigations on the relationship between porosity, structure and strength of hydrated Portland cement pastes. II. Effect of pore structure and of degree of hydration." *Cement and Concrete Research*, 15(3), 401-10.

Oehlers, D. J. (2006). "FRP Plates Adhesively Bonded to Reinforced Concrete Beams: Generic Debonding Mechanisms." *Advances in Structural Engineering*, 9(6), 737-50.

Oehlers, D. J., Park, S. M. and Mohamed Ali, M. S. (2003). "A structural engineering approach to adhesive bonding longitudinal plates to RC beams and slabs." *Composites Part A: Applied Science and Manufacturing*, 34(9), 887-97.

Ombres, L. (2010). "Prediction of intermediate crack debonding failure in FRP-strengthened reinforced concrete beams." *Composite Structures*, 92(2), 322-9.

Pan, J. and Leung, C. K. Y. (2007). "Effect of Concrete Composition on FRP/Concrete Bond Capacity." *Journal of Composites for Construction*, 11(6), 611-8.

Perera, R., Recuero, A., Diego, A. D. and López, C. (2004). "Adherence analysis of fiber-reinforced polymer strengthened RC beams." *Computers & Structures*, 82(23–26), 1865-73.

Pešić, N. and Pilakoutas, K. (2003). "Concrete beams with externally bonded flexural FRP-reinforcement: analytical investigation of debonding failure." *Composites Part B: Engineering*, 34(4), 327-38.

Poodts, E., Minak, G. and Zucchelli, A. (2013). "Impact of sea-water on the quasi static and fatigue flexural properties of GFRP." *Composite Structures*, 97(0), 222-30.

Popovics, S. (1973). "A numerical approach to the complete stress-strain curve of concrete." *Cement and Concrete Research*, 3(583-99.

Rider, A. N., Wang, C. H. and Cao, J. (2011). "Internal resistance heating for homogeneous curing of adhesively bonded repairs." *International Journal of Adhesion and Adhesives*, 31(3), 168-76.

Savoia, M., Ferracuti, B. and Mazzotti, C. (2003). "Nonlinear bond-slip law for FRP-concrete interface." FRPRCS-6, Singapore, 163-72.

Schubel, P. J. (2012). "Cost modelling in polymer composite applications: Case study – Analysis of existing and automated manufacturing processes for a large wind turbine blade." *Composites Part B: Engineering*, 43(3), 953-60.

Seemann WH (1990). "*Plastic transfer molding techniques for the production of fiber reinforced plastic structures."* US Patent No. 4902,215.

Seracino, R. (2001). "Axial intermediate crack debonding of plates glued to concrete surfaces." FRP Composites in Civil Engineering (CICE 2001), Hong Kong, 365-72.

Seracino, R., Raizal Saifulnaz, M. R. and Oehlers, D. J. (2007). "Generic Debonding Resistance of EB and NSM Plate-to-Concrete Joints." *Journal of Composites for Construction*, 11(1), 62-70.

Serbescu, A., Guadagnini, M. and Pilakoutas, K. (2013). "Standardised double-shear test for determining bond of FRP to concrete and corresponding model development." *Composites Part B: Engineering*, 55(0), 277-97.

Sevkat, E. and Brahimi, M. (2011). "The bearing strength of pin loaded woven composites manufactured by vacuum assisted resin transfer moulding and hand lay-up techniques." *Procedia Engineering*, 10(0), 153-8.

Shi, Z. (2009). "*Crack analysis in structural concrete: theory and applications*." Butterworth-Heinemann.

Silva-Muñoz, R. A. and Lopez-Anido, R. A. (2009). "Structural health monitoring of marine composite structural joints using embedded fiber Bragg grating strain sensors." *Composite Structures*, 89(2), 224-34.

Silva, F. J. G., Ferreira, F., Ribeiro, M. C. S., Castro, A. C. M., Castro, M. R. A., Dinis, M. L. and Fiúza, A. (2013). "Optimizing the energy consumption on pultrusion process." *Composites Part B: Engineering*, 0).

Smith, S. T. and Teng, J. G. (2001). "Interfacial stresses in plated beams." *Engineering Structures*, 23(7), 857-71.

Smith, S. T. and Teng, J. G. (2002a). "FRP-strengthened RC beams. I: review of debonding strength models." *Engineering Structures*, 24(4), 385-95.

Smith, S. T. and Teng, J. G. (2002b). "FRP-strengthened RC beams. II: assessment of debonding strength models." *Engineering Structures*, 24(4), 397-417.

Subramaniam, K. V., Carloni, C. and Nobile, L. (2007). "Width effect in the interface fracture during shear debonding of FRP sheets from concrete." *Engineering Fracture Mechanics*, 74(4), 578-94.

Taib, A. A., Boukhili, R., Achiou, S., Gordon, S. and Boukehili, H. (2006). "Bonded joints with composite adherends. Part I. Effect of specimen configuration, adhesive thickness, spew

fillet and adherend stiffness on fracture." *International Journal of Adhesion and Adhesives*, 26(4), 226-36.

Taljsten, B. (1997). "Defining anchor lengths of steel and CFRP plates bonded to concrete." *Adhesion and Adhesives*, 17(4), 319-27.

Täljsten, B. (1996). "Strengthening of concrete prisms using the plate-bonding technique." *International Journal of Fracture*, 82(3), 253-66.

Täljsten, B. and Elfgren, L. (2000). "Strengthening concrete beams for shear using CFRP-materials: evaluation of different application methods." *Composites Part B: Engineering*, 31(2), 87-96.

Tang, Y., Ye, L., Zhang, Z. and Friedrich, K. (2013). "Interlaminar fracture toughness and CAI strength of fibre-reinforced composites with nanoparticles – A review." *Composites Science and Technology*, 86(0), 26-37.

Tapeinos, I. G., Miaris, A., Mitschang, P. and Alexopoulos, N. D. (2012). "Carbon nanotube-based polymer composites: A trade-off between manufacturing cost and mechanical performance." *Composites Science and Technology*, 72(7), 774-87.

Tavares, S. S., Caillet-Bois, N., Michaud, V. and Månson, J. A. E. (2010a). "Non-autoclave processing of honeycomb sandwich structures: Skin through thickness air permeability during cure." *Composites Part A: Applied Science and Manufacturing*, 41(5), 646-52.

Tavares, S. S., Michaud, V. and Månson, J. A. E. (2010b). "Assessment of semi-impregnated fabrics in honeycomb sandwich structures." *Composites Part A: Applied Science and Manufacturing*, 41(1), 8-15.

Teoh, K. J. and Hsiao, K.-T. (2011). "Improved dimensional infidelity of curve-shaped VARTM composite laminates using a multi-stage curing technique – Experiments and modeling." *Composites Part A: Applied Science and Manufacturing*, 42(7), 762-71.

Ueda, T. and Dai, J. (2005). "Interface bond between FRP sheets and concrete substrates: properties, numerical modeling and roles in member behaviour." *Progress in Structural Engineering and Materials*, 7(1), 27-43.

Ueda, T. and Dai, J. G. (2004). "New shear bond model for FRP–concrete interface–from modeling to application." Proc. Proceedings of the 2nd International Conference on FRP Composites in Civil Engineering - CICE 2004, Adelaide, Australia, 69-81.

Ueda, T., Sato, Y. and Asano, Y. (1999). "Experimental study on bond strength of continuous carbon fiber sheet." Proc. 4th international symposium on fiber reinforced polymer reinforcement for reinforced concrete structures, 407–16.

Wang, J. (2007). "Cohesive zone model of FRP-concrete interface debonding under mixed-mode loading." *International Journal of Solids and Structures*, 44(20), 6551-68.

Williams, C., Summerscales, J. and Grove, S. (1996). "Resin Infusion under Flexible Tooling (RIFT): a review." *Composites Part A: Applied Science and Manufacturing*, 27(7), 517-24.

Witik, R. A., Gaille, F., Teuscher, R., Ringwald, H., Michaud, V. and Månson, J.-A. E. (2012). "Economic and environmental assessment of alternative production methods for composite aircraft components." *Journal of Cleaner Production*, 29–30(0), 91-102.

Wong, R. S. Y. and Vecchio, F. J. (2003). "Towards modeling of reinforced concrete members with externally bonded fiber-reinforced polymer composites." *ACI Structural Journal*, 100(1), 47-55.

Woo, S.-K. and Lee, Y. (2010). "Experimental Study on Interfacial Behavior of CFRP-Bonded Concrete." *KSCE Journal of Civil Engineering*, 14(3), 385-93.

Wu, Z., Li, W. and Sakuma, N. (2006). "Innovative externally bonded FRP/concrete hybrid flexural members." *Composite Structures*, 72(3), 289-300.

Wu, Z., Yuan, H. and Niu, H. (2002). "Stress transfer and fracture propagation in different kinds of adhesive joints." *Journal of Engineering Mechanics*, Vol. 128(No. 5), 562–73.

Xia, S. H. and Teng, J. G. (2005). "Behaviour of FRP-to-concrete bonded joints." Proceedings of the International Symposium on Bond Behaviour of FRP in Structures (BBFS 2005), Hong Kong, 411-8.

Xiao, J., Li, J. and Zha, Q. (2004). "Experimental study on bond behavior between FRP and concrete." *Construction and Building Materials*, 18(10), 745-52.

Xie, M. and Karbhari, V. M. (1998). "Peel Test for Characterization of Polymer Composite/Concrete Interface." *Journal of Composite Materials*, 32(21), 1894-913.

Xu, W. and Wei, Y. (2012). "Strength and interface failure mechanism of adhesive joints." *International Journal of Adhesion and Adhesives*, 34(0), 80-92.

Xu, W. and Wei, Y. (2013). "Influence of adhesive thickness on local interface fracture and overall strength of metallic adhesive bonding structures." *International Journal of Adhesion and Adhesives*, 40(0), 158-67.

Yang, D.-S., Hong, S.-N. and Park, S.-K. (2007). "Experimental observation on bond-slip behavior between concrete and CFRP plate." *International Journal of Concrete Structures and Materials*, 1(1), 37-43.

Yang, Z. J., Chen, J. F. and Proverbs, D. (2003). "Finite element modelling of concrete cover separation failure in FRP plated RC beams." *Construction and Building Materials*, 17(1), 3-13.

Yao, J., Teng, J. G. and Chen, J. F. (2005). "Experimental study on FRP-to-concrete bonded joints." *Composites Part B: Engineering*, 36(2), 99-113.

Yarema, S. Y. (1996). "On the contribution of G. R. Irwin to fracture mechanics." *Materials Science*, 31(5), 617-23.

Yuan, H., Teng, J. G., Seracino, R., Wu, Z. S. and Yao, J. (2004). "Full-range behavior of FRP-to-concrete bonded joints." *Engineering Structures*, 26(5), 553-65.

Yuan, H., Wu, Z. and Yoshizawa, H. (2001). "Theoretical Solutions on interfacial stress transfer of externally bonded steel/composite plates." *Journal of Structural Mechanics and Earthquake Engineering JSCE*, 18(1), 27-39.

Zadražil, T., Vodák, F. and Kapičková, O. (2004). "Effect of temperature and age of concrete on strength-porosity relation." *Acta Polytechnica*, 44(1), 53-6.

Zainuddin, S., Hosur, M. V., Zhou, Y., Kumar, A. and Jeelani, S. (2010). "Durability study of neat/nanophased GFRP composites subjected to different environmental conditioning." *Materials Science and Engineering: A*, 527(13–14), 3091-9.

Zhang, J., Guo, Q. and Fox, B. L. (2009). "Study on thermoplastic-modified multifunctional epoxies: Influence of heating rate on cure behaviour and phase separation." *Composites Science and Technology*, 69(7–8), 1172-9.

Zhang, K., Gu, Y., li, M. and Zhang, Z. (2014). "Effect of rapid curing process on the properties of carbon fiber/epoxy composite fabricated using vacuum assisted resin infusion molding." *Materials & Design*, 54(624-31.

Zhao, M., Dong, Y., Zhao, Y., Tennant, A. and Ansari, F. (2007). "Monitoring of Bond in FRP Retrofitted Concrete Structures." *Journal of Intelligent Material Systems and Structures*, 18(853-60.

Zhou, S., Wang, Z., Zhou, J. and Wu, X. (2013). "Experimental and numerical investigation on bolted composite joint made by vacuum assisted resin injection." *Composites Part B: Engineering*, 45(1), 1620-8.

Zhou, Y.-W., Wu, Y.-F. and Yun, Y. (2010). "Analytical modeling of the bond–slip relationship at FRP-concrete interfaces for adhesively-bonded joints." *Composites Part B: Engineering*, 41(6), 423-33.

Zhu, J., Chandrashekhara, K., Flanigan, V. and Kapila, S. (2004). "Manufacturing and mechanical properties of soy-based composites using pultrusion." *Composites Part A: Applied Science and Manufacturing*, 35(1), 95-101.

APPENDIX A

TENSILE TESTS RESULTS ON FRP COMPOSITES

A.1. Pultruded-A

General		
Date of test	27.06.2012	
Date of laminate construction	15.06.2012	
Type of fibre	Kor-CLS 0814 (TORAYCA T700S)	No of layers:
	FAW of one fibre (gsm):	Total FAW (gsm):
Type of resin	Kor-CPA	
Laminate construction method	Pultruded-A	
Cure history	Time (day): ---	Temp (°C): ---
	Heating cure temp (°C): N.A.	Duration (day): N.A.
	vacuum pressure: N.A.	
Test room condition	Temp(°C): ---	Humidity (%): ---
Testing speed (mm/min)	2	
Specimen prep. method	Diamond blade saw machine	
Tapping method	Aluminium plate	Thickness (mm): ---
Referred test standard	ASTM D3039-08	

Test specimen detail									
Specimen ID	FRP Thickness, t_{frp} (mm) *			FRP Width, W_{frp} (mm) *			Ave. Thick. (mm)	Ave. Width (mm)	Sectional area (mm^2)
	1	2	3	1	2	3			
1	1.44	1.44	1.44	15.02	15.03	14.86	1.44	14.97	21.54
4	1.42	1.42	1.42	15.44	15.23	15.04	1.42	15.23	21.65
5	1.44	1.43	1.44	15.63	15.38	15.34	1.44	15.45	22.16
7	1.42	1.42	1.42	15.53	15.49	15.39	1.42	15.47	21.98
9	1.44	1.43	1.43	14.80	14.93	14.76	1.43	14.83	21.26
Average	1.43	1.43	1.43	15.28	15.21	15.08	1.43	15.19	21.72
SD#	0.01	0.01	0.01	0.35	0.24	0.28	0.01	0.29	0.36
CoV#	0.01	0.01	0.01	0.02	0.015	0.02	0.01	0.02	0.02

* Measured value three times within test region (i.e. between grips)
# SD = Standard deviation, CoV = Coefficient of variation

Test Results						
Specimen ID	Max. load (N)	Max. stress (MPa)	Elastic modulus^ (MPa)	Strain@ Max. Load (%)	Strain@ Break (%)	Failure mode^
1	60722	2819	153382	1.74	2.57	XMV
4	67304	3109	161756	1.88	2.43	XMV
5	60668	2737	158231	1.76	2.24	XMV
7	55355	2518	165903	1.53	1.53	XMV
9	64948	3054	153657	1.96	1.96	XMV
Average	61799	2847	158586	1.77	2.15	XMV
SD#	4588	241	5364	0.16	0.41	
CoV#	0.07	0.09	0.03	0.09	0.19	

^ According to the referred test standard

A.2. Pultruded-B

General		
Date of test	27.06.2012	
Date of laminate construction	15.06.2012	
Type of fibre	SikaCarboDur-S1214	Type of fibre
	FAW of one fibre (gsm):	
Type of resin	Sikadur-30	
Laminate construction method	Pultruded-B	
Cure history	Time (day): ---	Cure history
	Heating cure temp (°C): N.A.	
	vacuum pressure: N.A.	
Test room condition	Temp(°C): ---	Test room condition
Testing speed (mm/min)	2	
Specimen prep. method	Diamond blade saw machine	
Tapping method	Aluminium plate	Tapping method
Referred test standard	ASTM D3039-08	

Test specimen detail									
Specimen ID	FRP Thickness, t_{frp} (mm) *			FRP Width, W_{frp} (mm) *			Ave. Thick. (mm)	Ave. Width (mm)	Sectional area (mm^2)
	1	2	3	1	2	3			
2	1.45	1.46	1.45	14.48	14.40	14.48	1.45	14.46	21.01
4	1.45	1.44	1.45	14.21	14.77	14.33	1.45	14.44	20.89
5	1.43	1.43	1.43	15.69	15.47	15.27	1.43	15.48	22.16
9	1.44	1.44	1.44	14.06	14.16	14.53	1.44	14.25	20.53
10	1.46	1.46	1.47	14.13	13.91	13.81	1.46	13.95	20.41
Average	1.45	1.45	1.45	14.51	14.54	14.49	1.45	14.51	21.00
SD#	0.01	0.01	0.01	0.68	0.61	0.52	0.01	0.58	0.70
CoV#	0.01	0.01	0.01	0.05	0.04	0.04	0.01	0.04	0.03

* Measured value three times within test region (i.e. between grips)
# SD = Standard deviation, CoV = Coefficient of variation

Test Results						
Specimen ID	Max. load (N)	Max. stress (MPa)	Elastic modulus^ (MPa)	Strain@ Max. Load (%)	Strain@ Break (%)	Failure mode^
2	68452	3259	159944	1.95	1.95	XMV
4	68368	3272	164753	1.83	2.07	XMV
5	64850	2926	172754	1.83	1.97	XMV
9	66273	3227	167011	1.73	2.14	XMV
10	64571	3164	161412	1.81	2.15	XMV
Average	66503	3170	165175	1.83	2.06	XMV
SD#	1857	142	5062	0.08	0.09	
CoV#	0.03	0.05	0.03	0.04	0.05	

^ According to the referred test standard

A.3. Wet Lay-up

General		
Date of test	27.06.2012	
Date of laminate construction	10.06.2012	
Type of fibre	SikaWrap-230 C	Type of fibre
	FAW of one fibre (gsm):	
Type of resin	Sikadur-330	
Laminate construction method	Wet lay-up	
Cure history	Time (day): 17	Cure history
	Heating cure temp (°C): N.A.	
	vacuum pressure: N.A.	
Test room condition	Temp(°C): ---	Test room condition
Testing speed (mm/min)	2	
Specimen prep. method	Diamond blade saw machine	
Tapping method	Aluminium plate	Tapping method
Referred test standard	ASTM D3039-08	

Test specimen detail									
Specimen ID	FRP Thickness, t_{frp} (mm) *			FRP Width, W_{frp} (mm) *			Ave. Thick. (mm)	Ave. Width (mm)	Sectional area (mm^2)
	1	2	3	1	2	3			
3	0.52	0.52	0.52	15.67	15.38	15.96	0.52	15.67	8.15
6	0.52	0.52	0.52	15.39	15.34	15.40	0.52	15.38	8.00
10	0.52	0.52	0.52	15.37	15.40	15.49	0.52	15.42	8.02
11	0.52	0.52	0.52	15.07	14.83	15.07	0.52	14.99	7.79
12	0.52	0.52	0.52	15.08	14.62	14.70	0.52	14.80	7.70
Average	0.52	0.52	0.52	15.32	15.11	15.32	0.52	15.25	7.93
SD#	0.0	0.0	0.0	0.25	0.37	0.47	0.0	0.35	0.16
CoV#	0.0	0.0	0.0	0.02	0.02	0.03	0.0	0.02	0.02

* Measured value three times within test region (i.e. between grips)
# SD = Standard deviation, CoV = Coefficient of variation

Test Results						
Specimen ID	Max. load (N)	Max. stress (MPa)	Elastic modulus^ (MPa)	Strain@ Max. Load (%)	Strain@ Break (%)	Failure mode^
3	30191	3705	237144	1.53	1.53	M(LA)MV
6	32797	4101	232968	1.68	1.68	M(AS)GM
10	31770	3963	230984	1.61	1.61	LAV
11	32227	4135	234256	1.69	1.69	LVV
12	30424	3954	235707	1.64	1.64	SGM
Average	31482	3972	234256	1.63	1.63	
SD#	1135	169.80	2388	0.06	0.06	
CoV#	0.04	0.04	0.01	0.04	0.04	

^ According to the referred test standard

A.4. VARI-A

General		
Date of test	27.06.2012	
Date of laminate construction	---	
Type of fibre	Kor-CFW600 (TORAYCA T700S)	Type of fibre
	FAW of one fibre (gsm):	
Type of resin	Rimr 135 + Rimh 134	
Laminate construction method	VARI-A	
Cure history	Time (day): ---	Cure history
	Heating cure temp (°C): N.A.	
	vacuum pressure (kPa): 90	
Test room condition	Temp(°C): ---	Test room condition
Testing speed (mm/min)	2	
Specimen prep. method		
Tapping method	Aluminium plate	Tapping method
Referred test standard	ASTM D3039-08	

Test specimen detail									
Specimen ID	FRP Thickness, t_{frp} (mm) *			FRP Width, W_{frp} (mm) *			Ave. Thick. (mm)	Ave. Width (mm)	Sectional area (mm^2)
	1	2	3	1	2	3			
1	1.01	1.01	1.01	15.92	16.04	16.08	1.01	16.01	16.14
5	1.01	1.01	1.01	15.98	15.88	15.87	1.01	15.91	16.03
7	1.01	1.01	1.01	16.04	16.09	16.21	1.01	16.12	16.25
10	1.01	1.01	1.01	15.55	15.42	15.38	1.01	15.45	15.58
11	1.01	1.01	1.01	15.95	16.08	16.21	1.01	16.08	16.21
Average	1.01	1.01	1.01	15.89	15.90	15.95	1.01	15.91	16.04
SD#	0.00	0.00	0.00	0.19	0.28	0.35	0.00	0.27	0.27
CoV#	0.00	0.00	0.00	0.01	0.02	0.02	0.00	0.02	0.02

* Measured value three times within test region (i.e. between grips)
# SD = Standard deviation, CoV = Coefficient of variation

Test Results						
Specimen ID	Max. load (N)	Max. stress (MPa)	Elastic modulus^ (MPa)	Strain@ Max. Load (%)	Strain@ Break (%)	Failure mode^
1	43677	2706	223415	1.43	1.47	SMU
5	41654	2570	216317	1.32	1.32	SMU
7	35524	2187	232995	1.35	1.35	SMU
10	46031	2955	223579	1.36	1.45	SMU
11	36062	2225	228449	1.27	1.27	SMU
Average	40590	2529	224951	1.35	1.37	
SD#	4648	326	6240	0.06	0.09	
CoV#	0.12	0.13	0.03	0.04	0.06	

^ According to the referred test standard

A.5. VARI-B

General		
Date of test	27.06.2012	
Date of laminate construction	---	
Type of fibre	Kor-CFW600 (TORAYCA T700S)	Type of fibre
	FAW of one fibre (gsm):	
Type of resin	Daron ZW7567	
Laminate construction method	VARI-B	
Cure history	Time (day): ---	Cure history
	Heating cure temp (°C): N.A.	
	vacuum pressure (kPa): 90	
Test room condition	Temp(°C):	Test room condition
Testing speed (mm/min)	2	
Specimen prep. method		
Tapping method	Aluminium plate	Tapping method
Referred test standard	ASTM D3039-08	

Test specimen detail									
Specimen ID	FRP Thickness, t_{frp} (mm) *			FRP Width, W_{frp} (mm) *			Ave. Thick. (mm)	Ave. Width (mm)	Sectional area (mm^2)
	1	2	3	1	2	3			
1	0.99	0.99	0.99	15.45	15.18	15.41	0.99	15.35	15.15
2	0.99	0.99	0.99	15.27	14.93	14.91	0.99	15.04	14.84
7	0.99	0.99	0.99	15.45	15.79	15.38	0.99	15.54	15.34
9	0.99	0.99	0.99	15.06	15.06	15.46	0.99	15.19	15.00
10	0.99	0.99	0.99	15.18	15.33	15.54	0.99	15.35	15.15
Average	0.99	0.99	0.99	15.20	15.30	15.39	0.99	15.29	15.09
SD#	0.00	0.00	0.00	0.15	0.29	0.11	0.00	0.19	0.19
CoV#	0.00	0.00	0.00	0.01	0.02	0.01	0.00	0.01	0.01

* Measured value three times within test region (i.e. between grips)
# SD = Standard deviation, CoV = Coefficient of variation

Test Results						
Specimen ID	Max. load (N)	Max. stress (MPa)	Elastic modulus^ (MPa)	Strain@ Max. Load (%)	Strain@ Break (%)	Failure mode^
1	31416	2074	227708	0.96	0.96	SMU
	30486	2054	210886	1.13	1.13	SMU
7	31050	2025	229708	0.93	1.72	SMU
9	28431	1896	228350	0.92	0.92	SMU
10	29543	1950	227410	1.05	1.12	SMU
Average	30185	2000	224812	1.00	1.17	
SD#	1209	74.70	7835	0.09	0.32	
CoV#	0.04	0.04	0.04	0.09	0.27	

^ According to the referred test standard

APPENDIX B

MODIFIED SINGLE LAP SHEAR TEST RESULTS

B.1. Load-slip Graphs

B.1.1. Pultruded Specimens

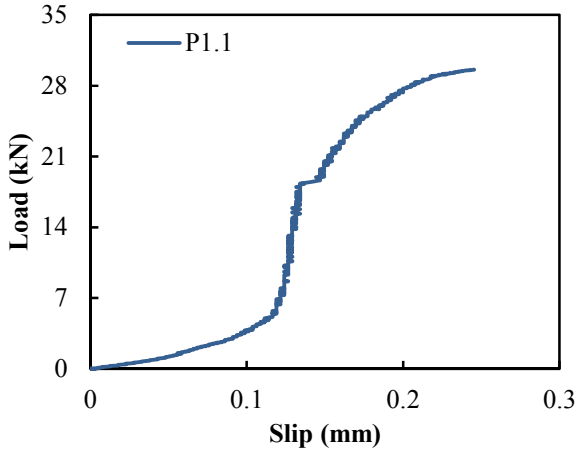

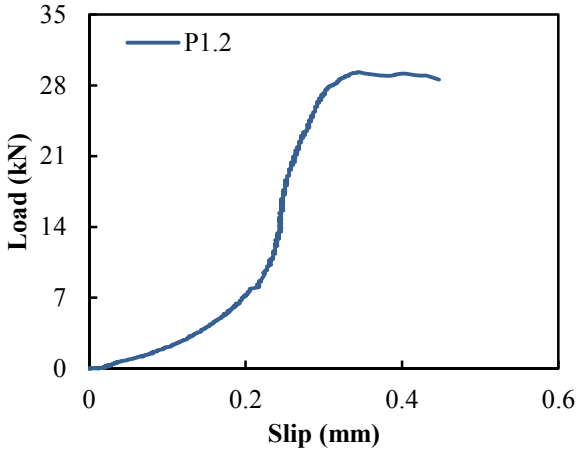

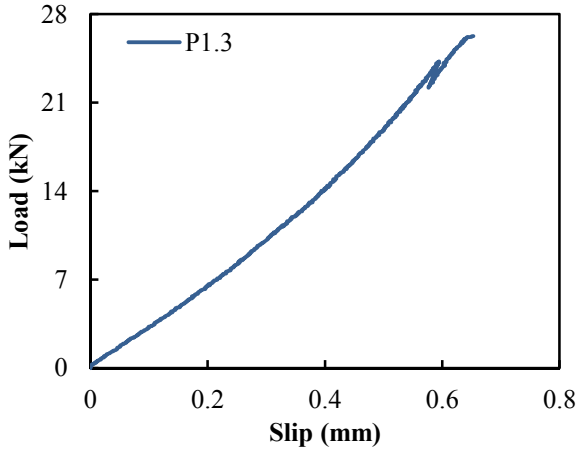

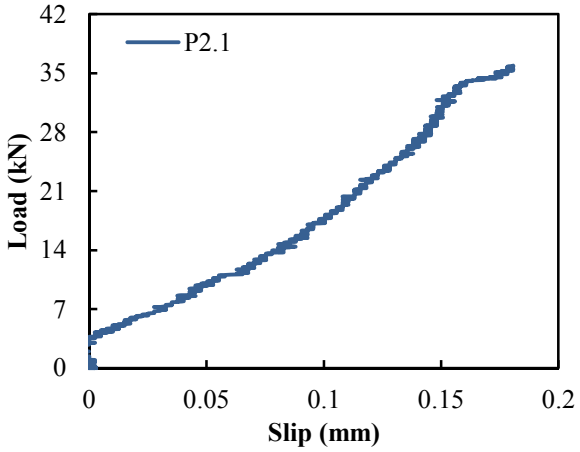

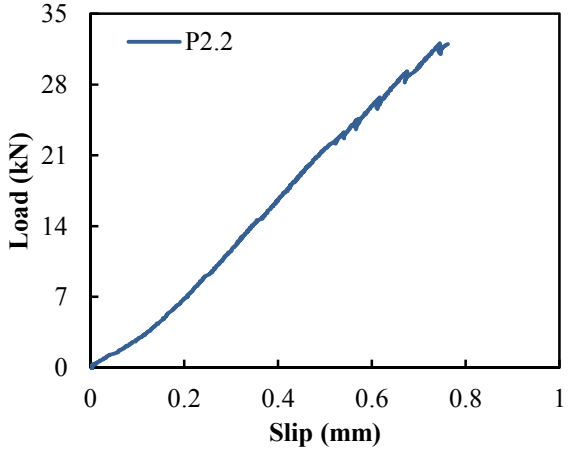

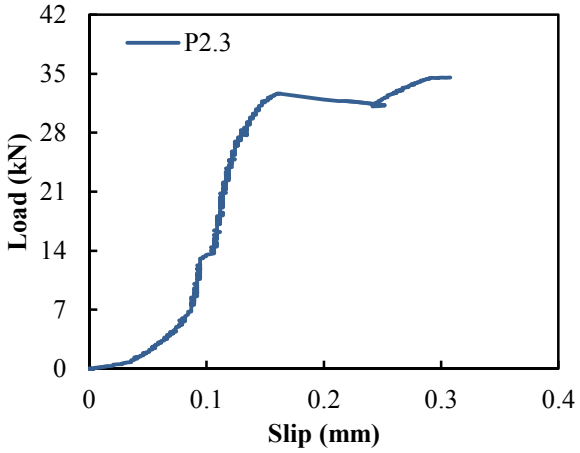

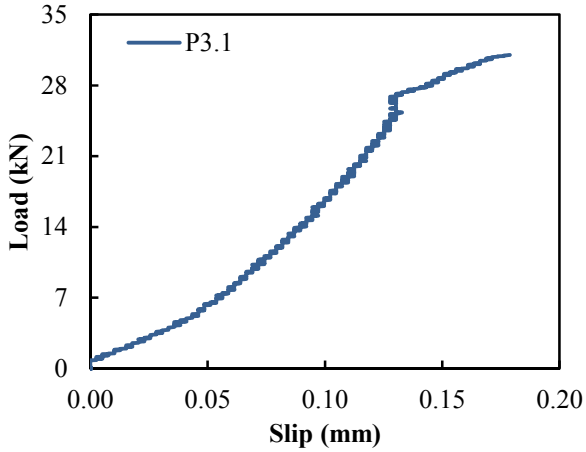
P3.1
Load (kN)
Slip (mm)
0
7
14
21
28
35
0.00
0.05
0.10
0.15
0.20

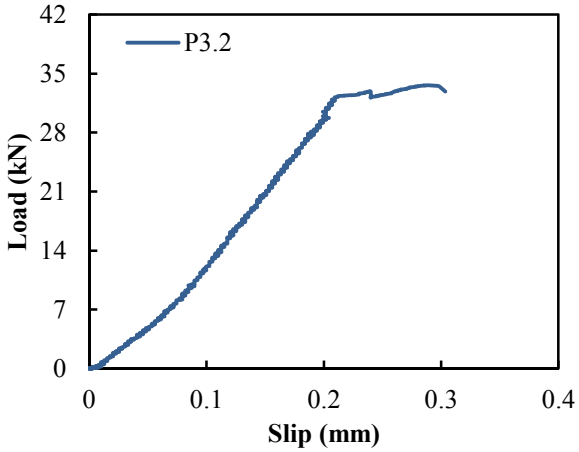
P3.2
Load (kN)
Slip (mm)
0
7
14
21
28
35
42
0
0.1
0.2
0.3
0.4

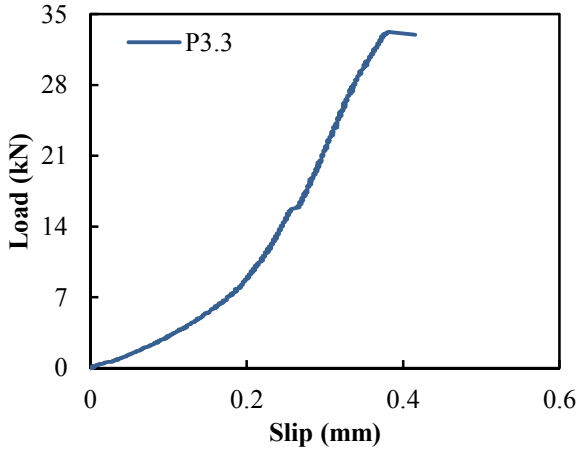
P3.3
Load (kN)
Slip (mm)
0
7
14
21
28
35
0
0.2
0.4
0.6

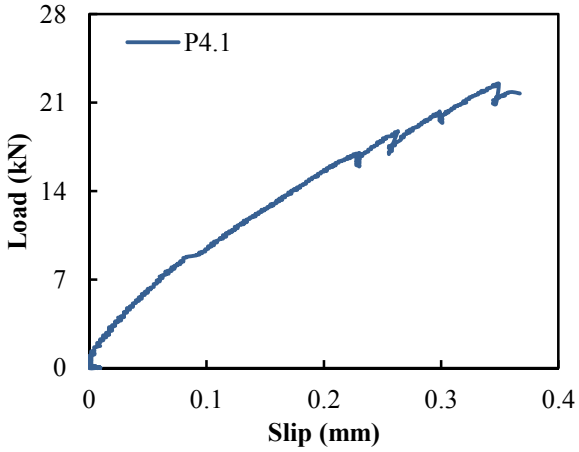
P4.1
Load (kN)
Slip (mm)
0
7
14
21
28
0
0.1
0.2
0.3
0.4

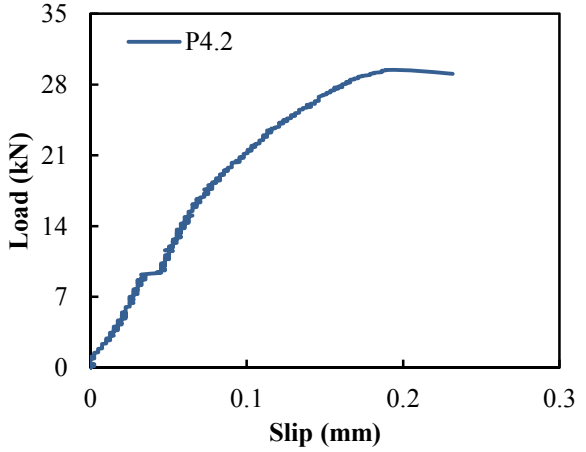
P4.2
Load (kN)
Slip (mm)
0
7
14
21
28
35
0
0.1
0.2
0.3

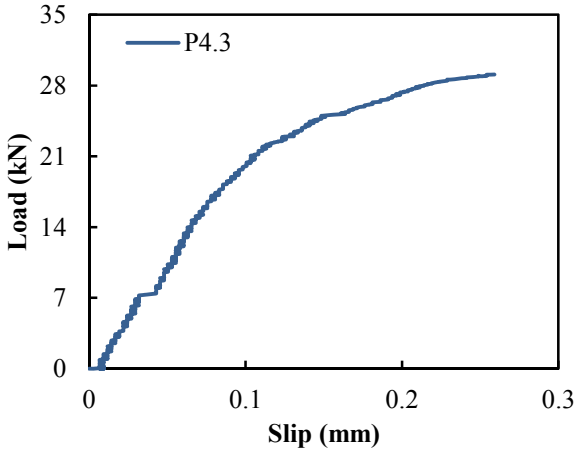
P4.3
Load (kN)
Slip (mm)
0
7
14
21
28
35
0
0.1
0.2
0.3

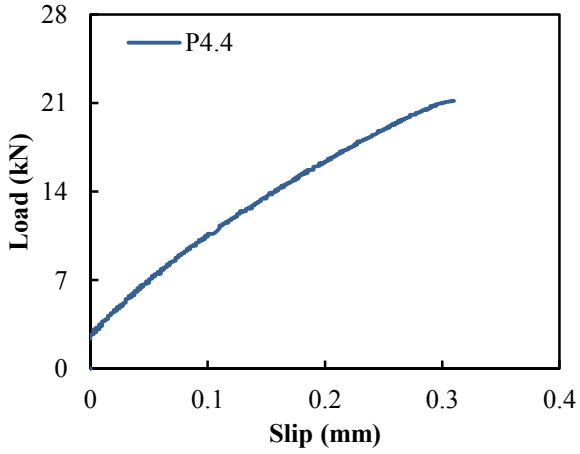
P4.4
Load (kN)
Slip (mm)
0
7
14
21
28
0
0.1
0.2
0.3
0.4

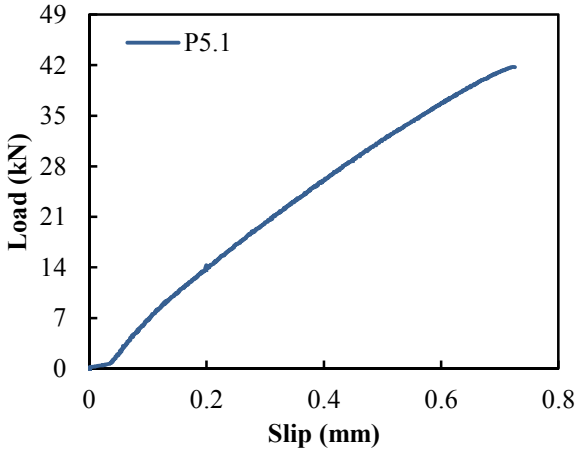
P5.1
Load (kN)
Slip (mm)
0
7
14
21
28
35
42
49
0
0.2
0.4
0.6
0.8

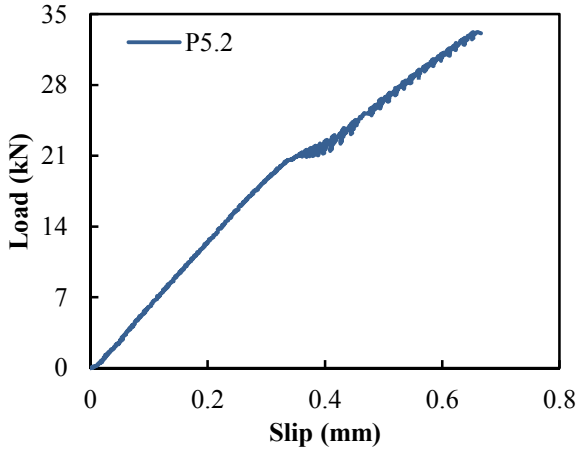
P5.2
Load (kN)
Slip (mm)
0
7
14
21
28
35
0
0.2
0.4
0.6
0.8

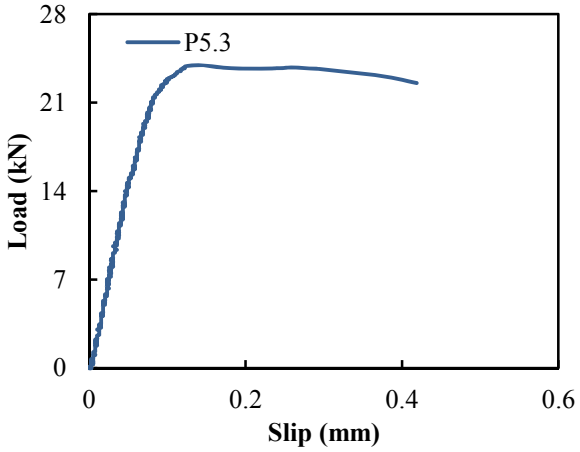
P5.3
Load (kN)
Slip (mm)
0
7
14
21
28
0
0.2
0.4
0.6

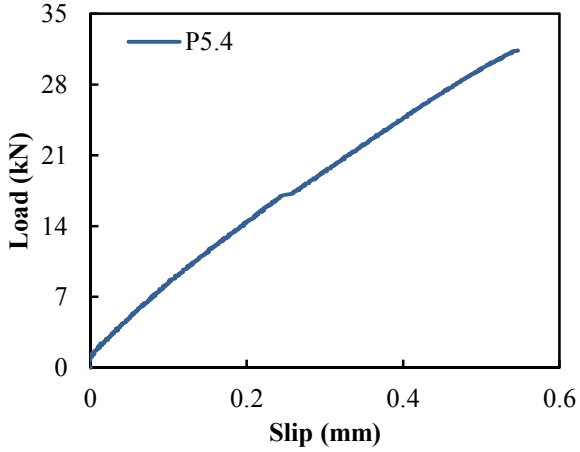
P5.4
Load (kN)
Slip (mm)
0
7
14
21
28
35
0
0.2
0.4
0.6

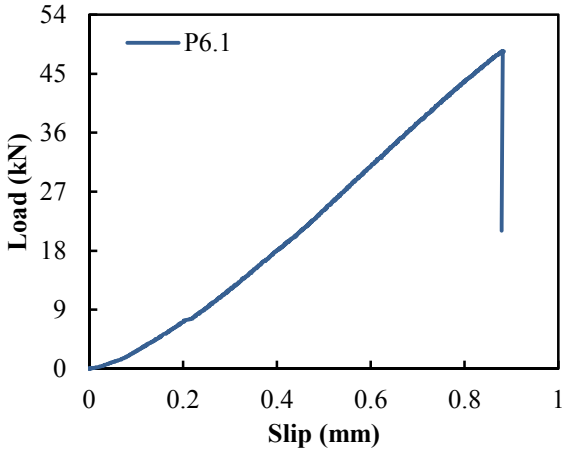
P6.1
Load (kN)
Slip (mm)
0
9
18
27
36
45
54
0
0.2
0.4
0.6
0.8
1

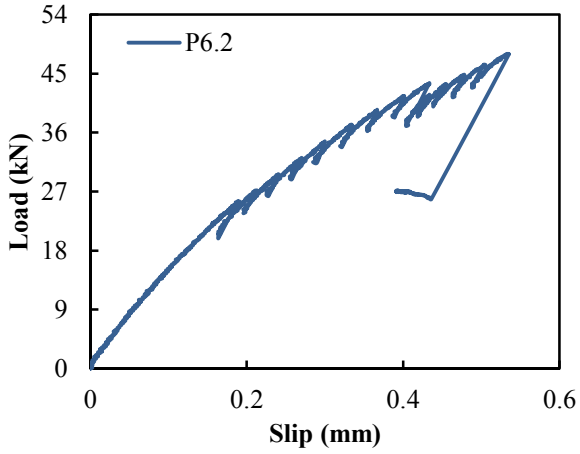
P6.2
Load (kN)
Slip (mm)
0
9
18
27
36
45
54
0.2
0.4
0.6

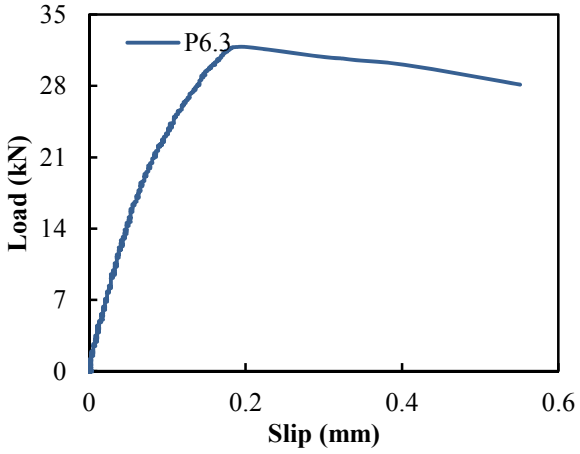
P6.3
Load (kN)
Slip (mm)
0
7
14
21
28
35
0.2
0.4
0.6

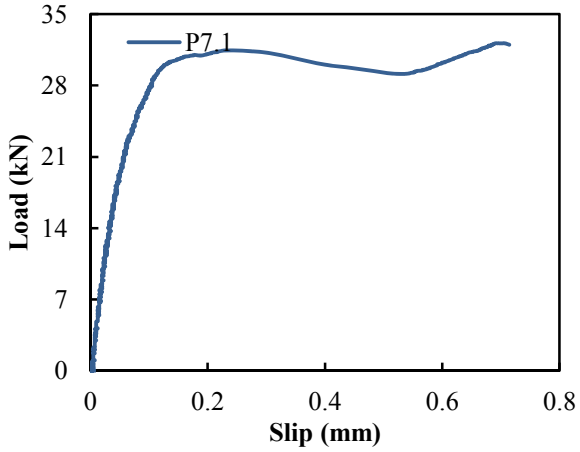
P7.1
Load (kN)
Slip (mm)
0
7
14
21
28
35
0.2
0.4
0.6
0.8

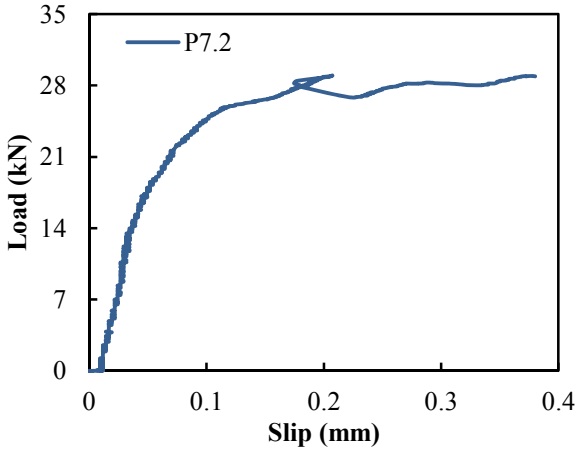
P7.2
Load (kN)
Slip (mm)
0
7
14
21
28
35
0.1
0.2
0.3
0.4

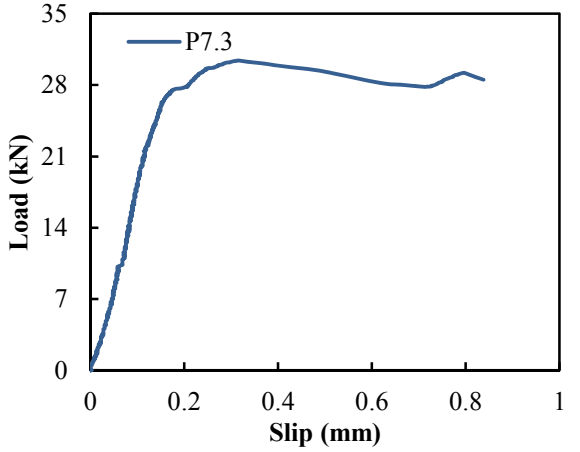
P7.3
Load (kN)
Slip (mm)
0
7
14
21
28
35
0.2
0.4
0.6
0.8
1

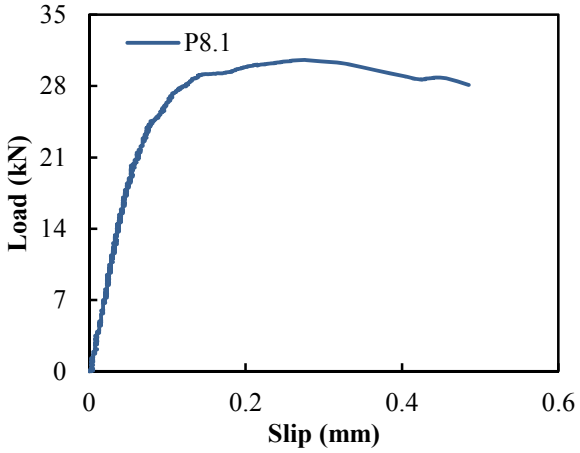
P8.1
Load (kN)
Slip (mm)
0
7
14
21
28
35
0.2
0.4
0.6

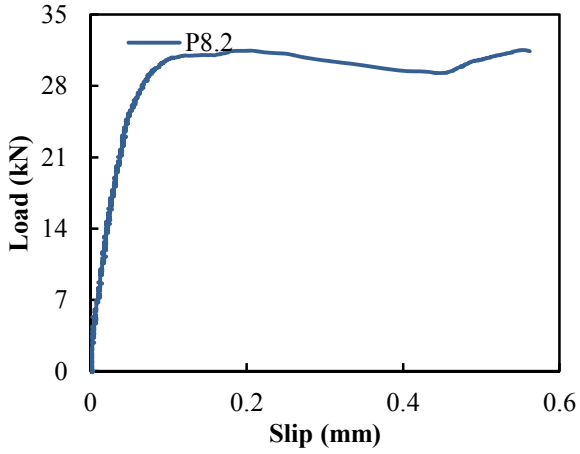
P8.2
Load (kN)
Slip (mm)
0
7
14
21
28
35
0
0.2
0.4
0.6

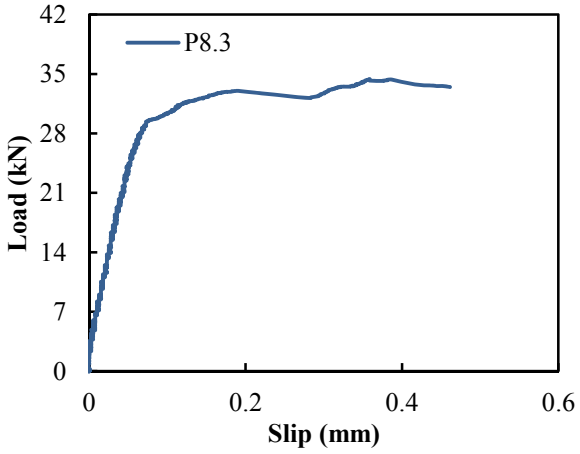
P8.3
Load (kN)
Slip (mm)
0
7
14
21
28
35
42
0
0.2
0.4
0.6

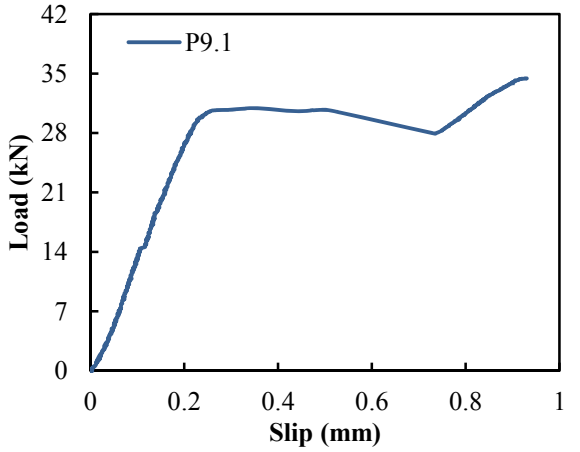
P9.1
Load (kN)
Slip (mm)
0
7
14
21
28
35
42
0
0.2
0.4
0.6
0.8
1

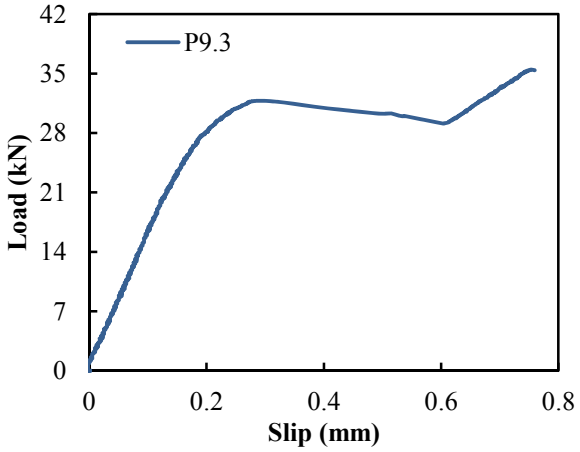
P9.3
Load (kN)
Slip (mm)
0
7
14
21
28
35
42
0
0.2
0.4
0.6
0.8

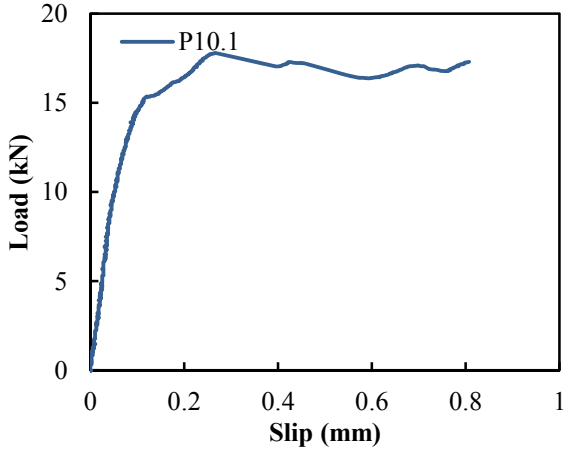
P10.1
Load (kN)
Slip (mm)
0
5
10
15
20
0
0.2
0.4
0.6
0.8
1

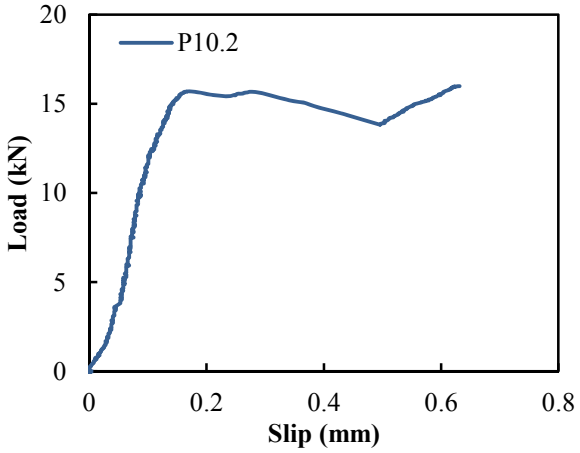
P10.2
Load (kN)
Slip (mm)
0
5
10
15
20
0
0.2
0.4
0.6
0.8

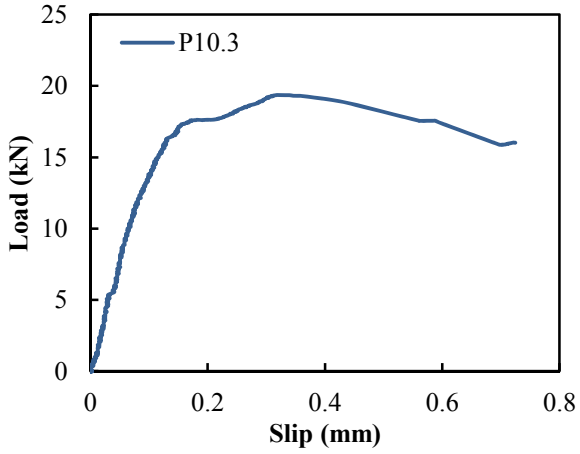
P10.3
Load (kN)
Slip (mm)
0
5
10
15
20
25
0
0.2
0.4
0.6
0.8

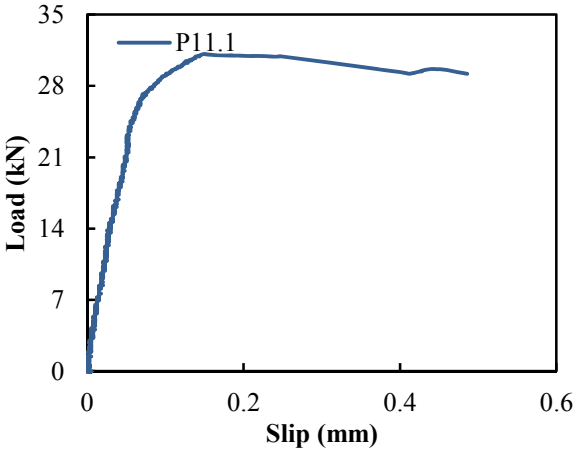
P11.1
Load (kN)
Slip (mm)
0
7
14
21
28
35
0
0.2
0.4
0.6

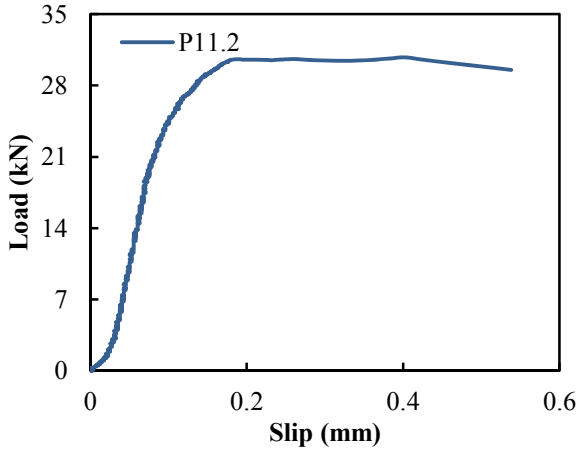
P11.2
Load (kN)
Slip (mm)
0
7
14
21
28
35
0
0.2
0.4
0.6

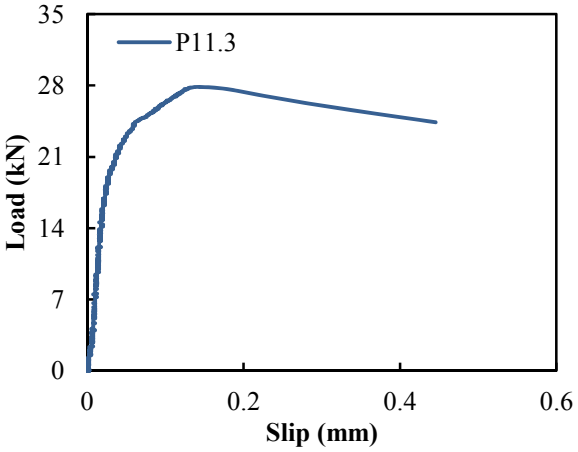
P11.3
Load (kN)
Slip (mm)
0
7
14
21
28
35
0
0.2
0.4
0.6

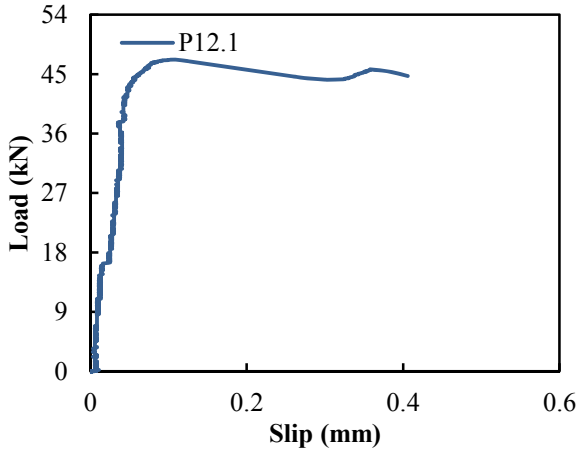
P12.1
Load (kN)
Slip (mm)
0
9
18
27
36
45
54
0
0.2
0.4
0.6

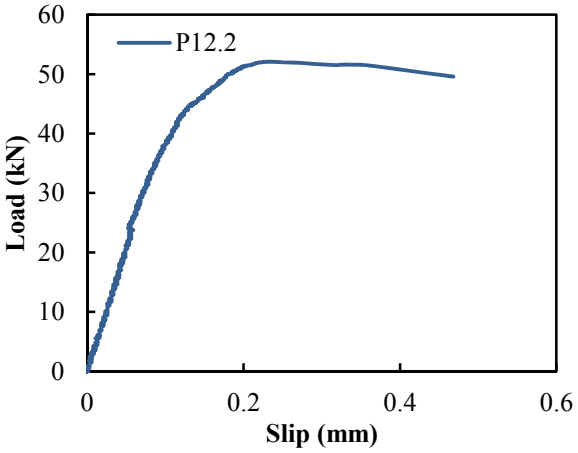
P12.2
Load (kN)
Slip (mm)
0
10
20
30
40
50
60
0
0.2
0.4
0.6

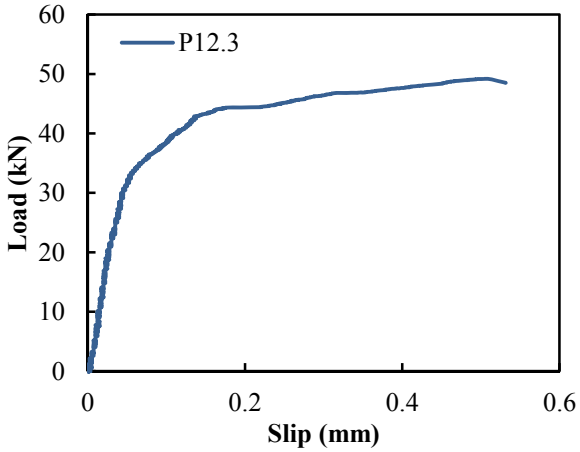
P12.3
Load (kN)
Slip (mm)
0
10
20
30
40
50
60
0
0.2
0.4
0.6

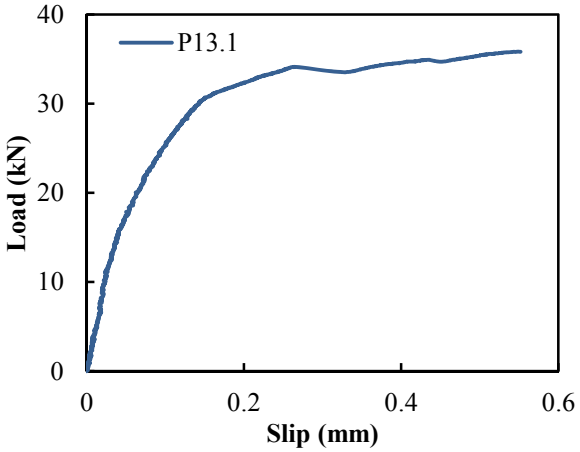
P13.1
Load (kN)
Slip (mm)
0
10
20
30
40
0
0.2
0.4
0.6

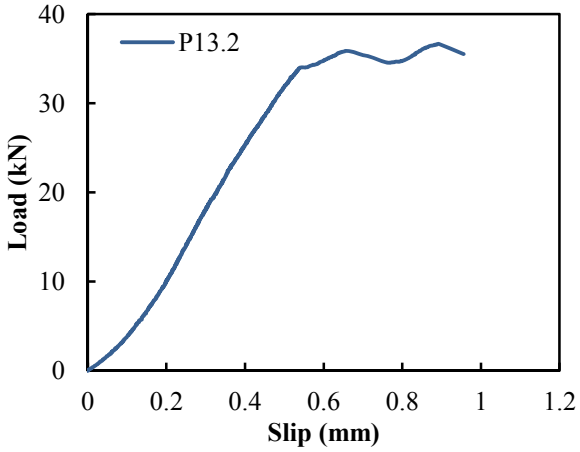
P13.2
Load (kN)
Slip (mm)
0
10
20
30
40
0
0.2
0.4
0.6
0.8
1
1.2

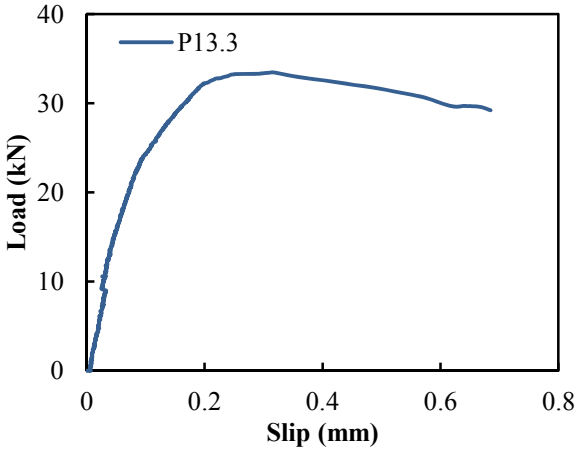
P13.3
Load (kN)
Slip (mm)
0
10
20
30
40
0
0.2
0.4
0.6
0.8

B.1.2. Wet Lay-up Specimens

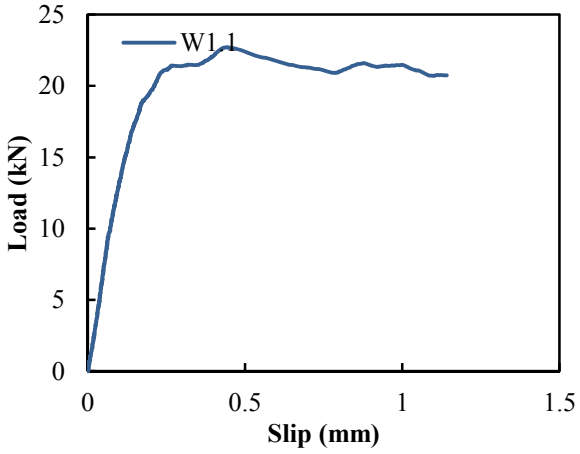

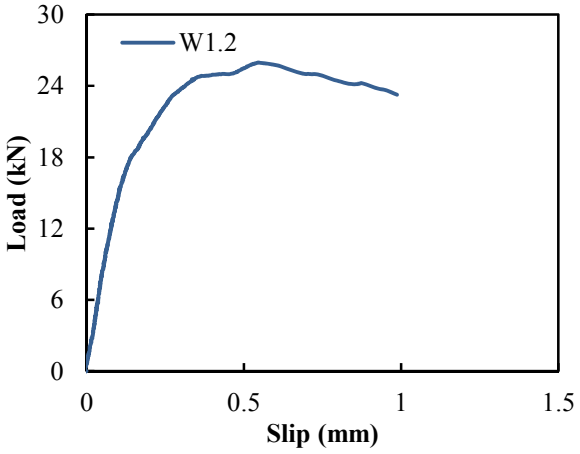

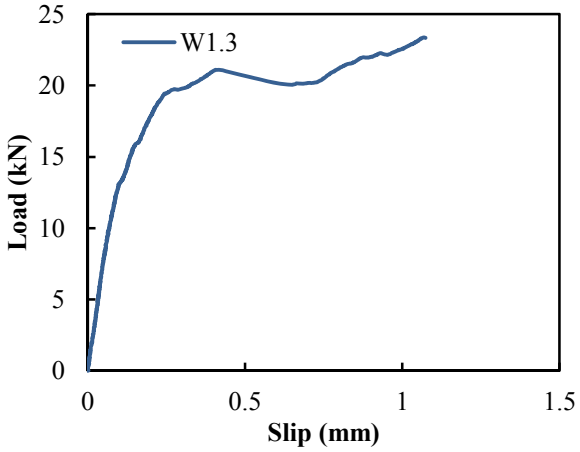

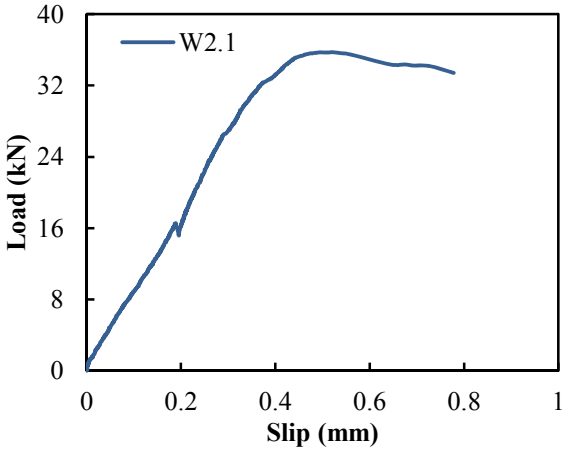

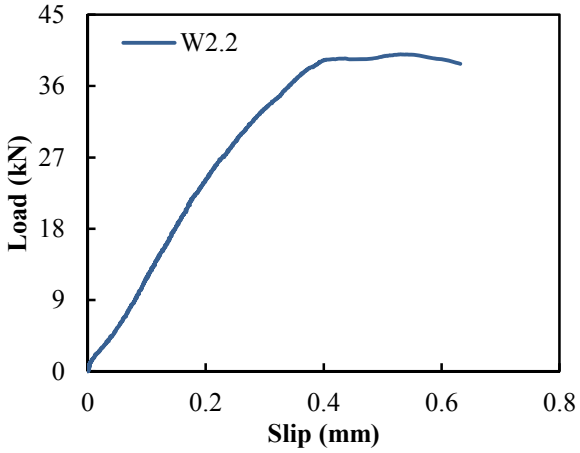

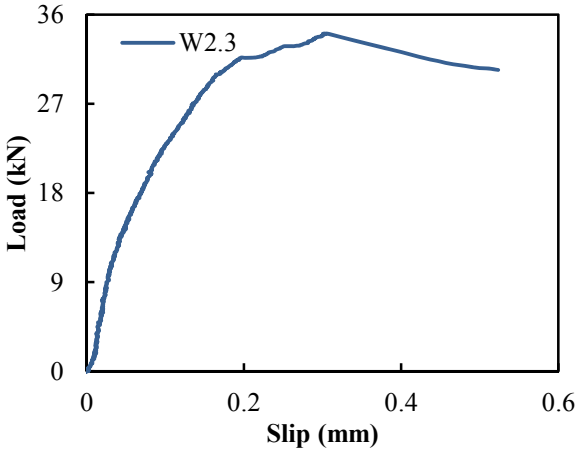

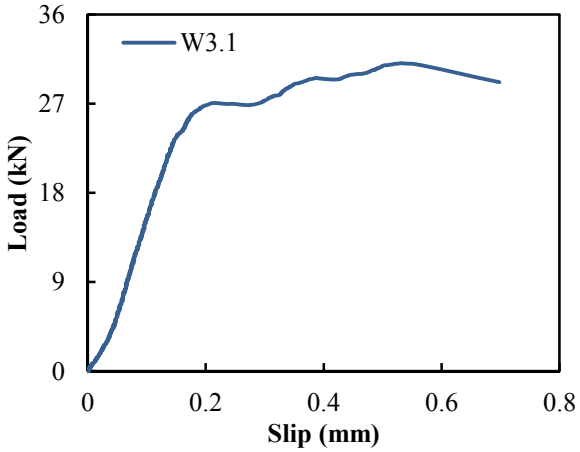
W3.1
Load (kN)
Slip (mm)
0
9
18
27
36
0
0.2
0.4
0.6
0.8

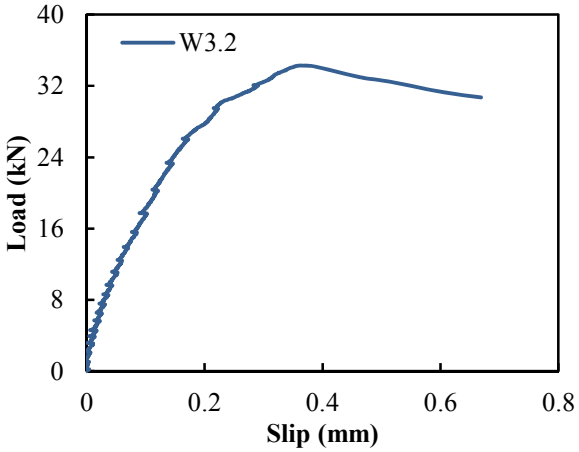
W3.2
Load (kN)
Slip (mm)
0
8
16
24
32
40
0
0.2
0.4
0.6
0.8

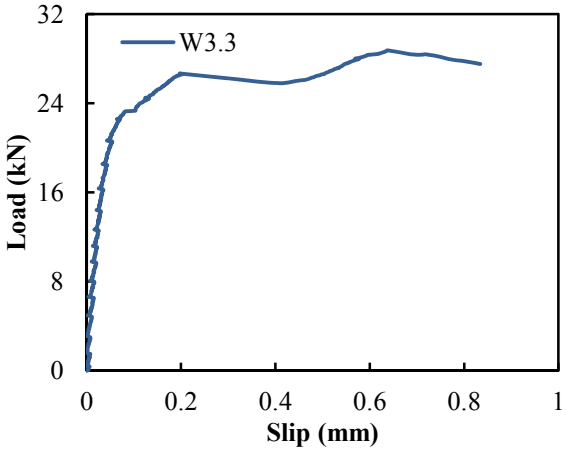
W3.3
Load (kN)
Slip (mm)
0
8
16
24
32
0
0.2
0.4
0.6
0.8
1

B.1.3. VARI Specimens

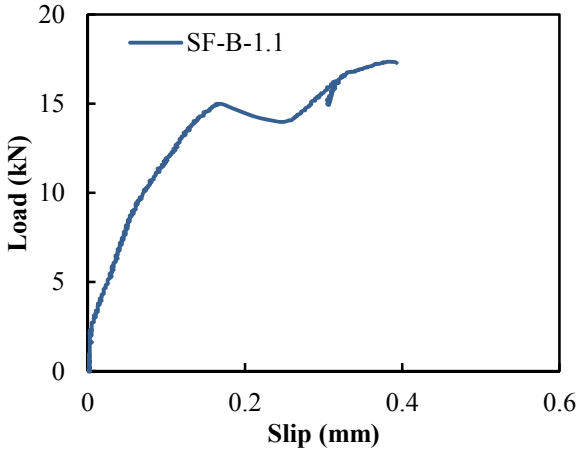

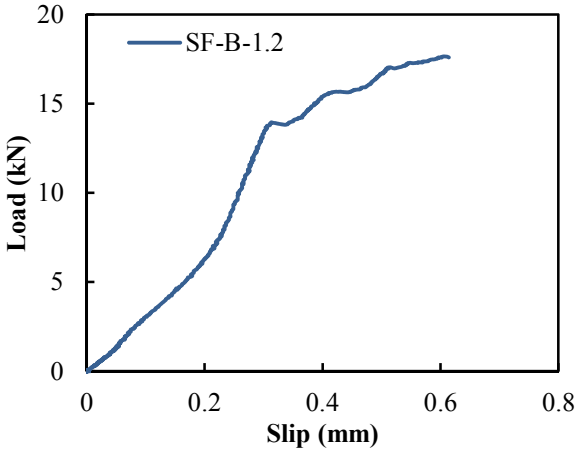

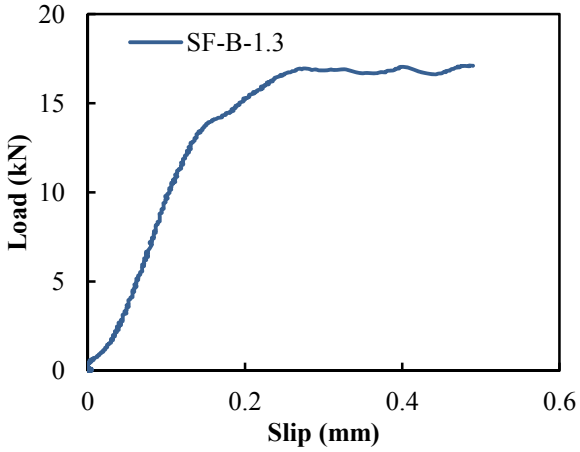

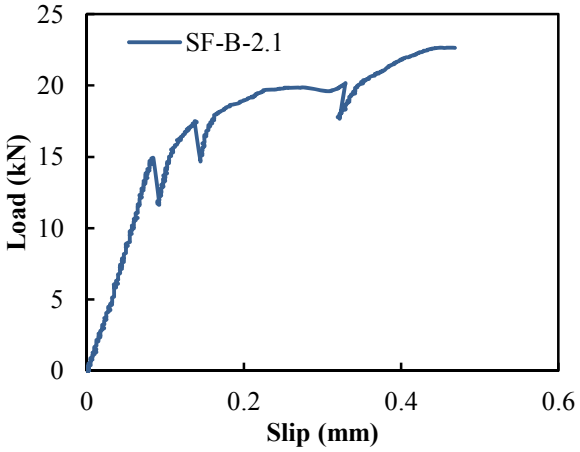

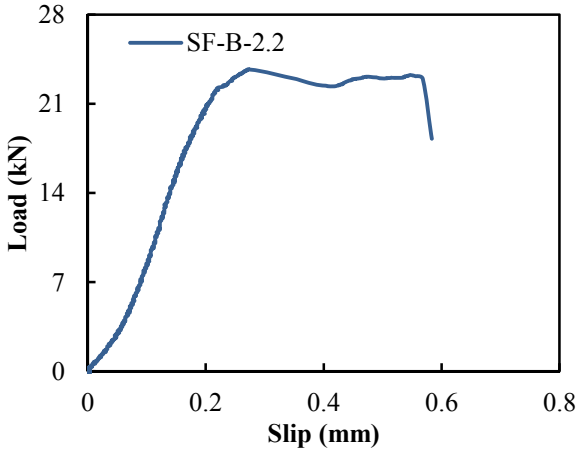

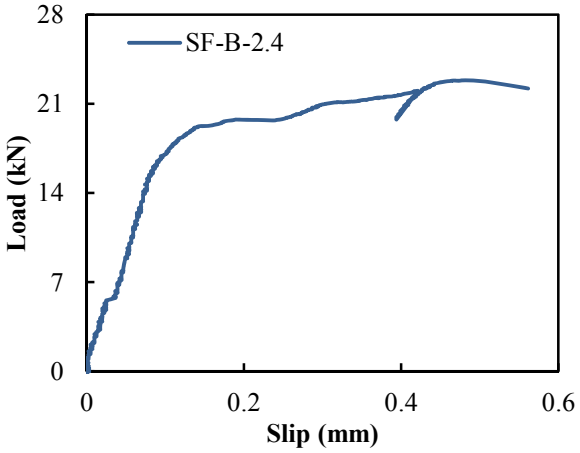

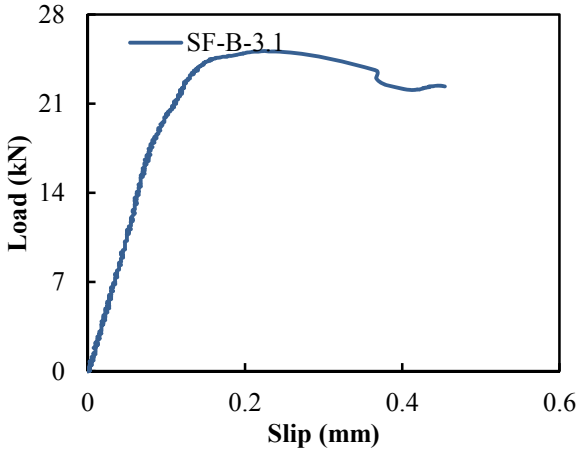
SF-B-3.1
Load (kN)
Slip (mm)
0
7
14
21
28
0.2
0.4
0.6

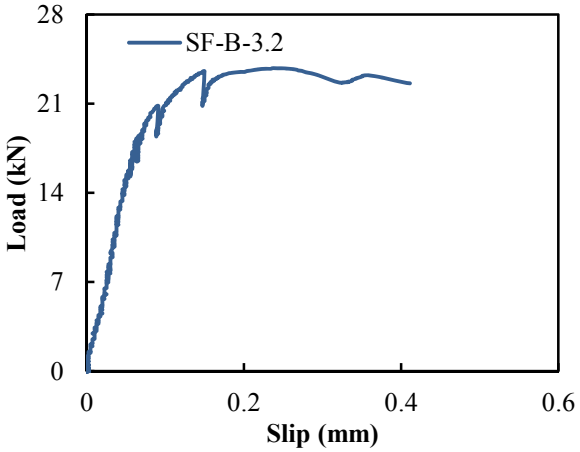
SF-B-3.2
Load (kN)
Slip (mm)
0
7
14
21
28
0.2
0.4
0.6

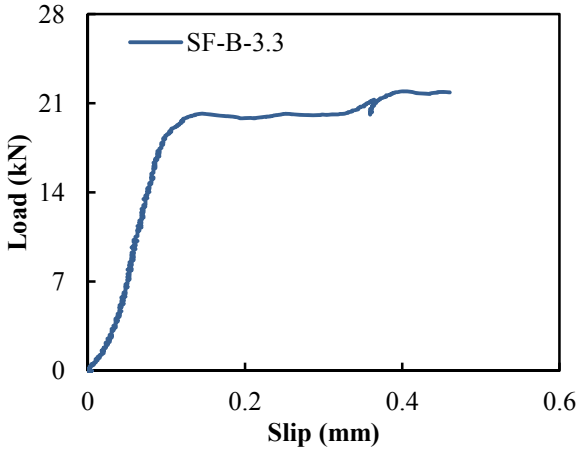
SF-B-3.3
Load (kN)
Slip (mm)
0
7
14
21
28
0.2
0.4
0.6

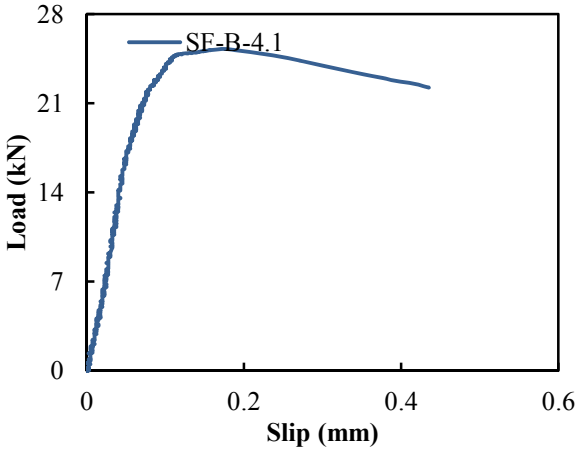
SF-B-4.1
Load (kN)
Slip (mm)
0
7
14
21
28
0.2
0.4
0.6

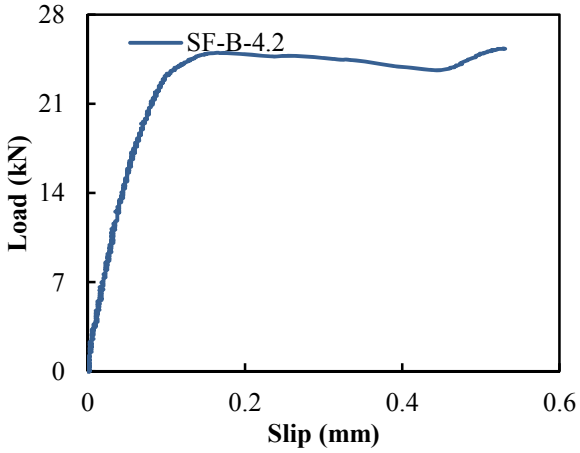
SF-B-4.2
Load (kN)
Slip (mm)
0
7
14
21
28
0.2
0.4
0.6

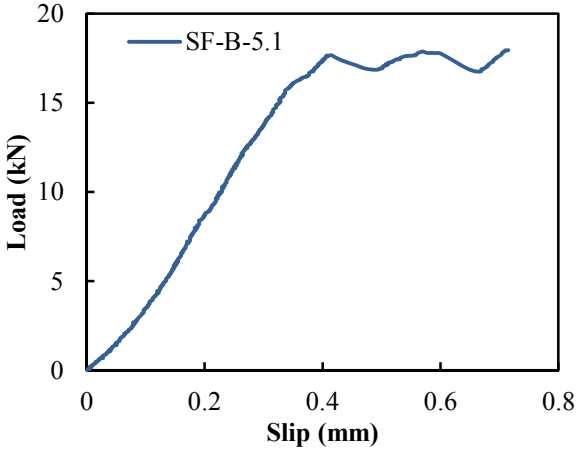
SF-B-5.1
Load (kN)
Slip (mm)
0
5
10
15
20
0.2
0.4
0.6
0.8

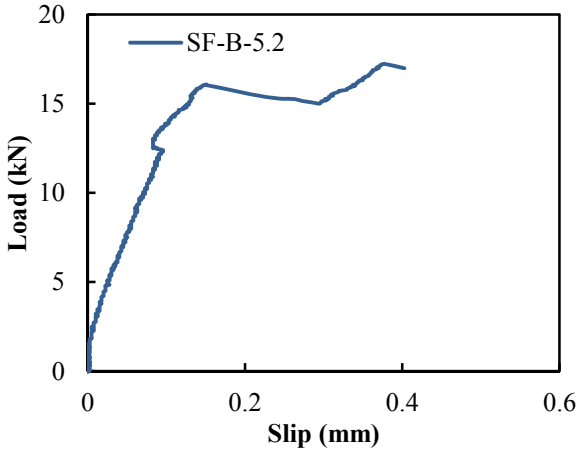
SF-B-5.2
Load (kN)
Slip (mm)
0
5
10
15
20
0
0.2
0.4
0.6

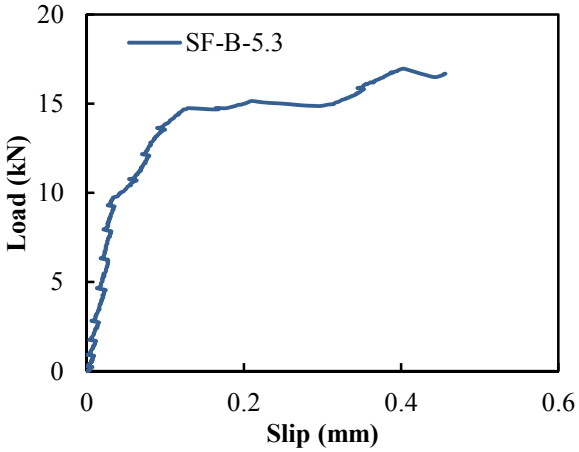
SF-B-5.3
Load (kN)
Slip (mm)
0
5
10
15
20
0
0.2
0.4
0.6

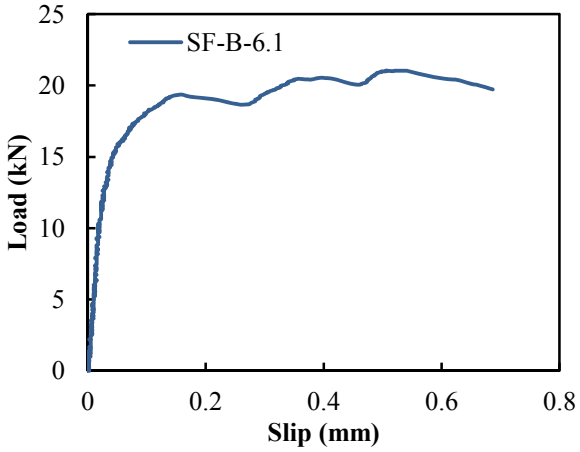
SF-B-6.1
Load (kN)
Slip (mm)
0
5
10
15
20
25
0
0.2
0.4
0.6
0.8

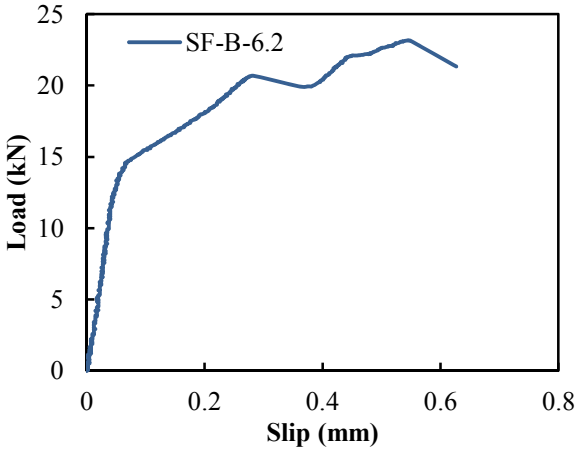
SF-B-6.2
Load (kN)
Slip (mm)
0
5
10
15
20
25
0
0.2
0.4
0.6
0.8

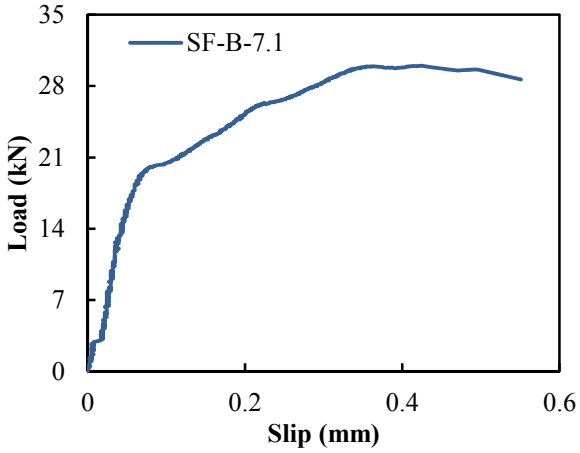
SF-B-7.1
Load (kN)
Slip (mm)
0
7
14
21
28
35
0
0.2
0.4
0.6

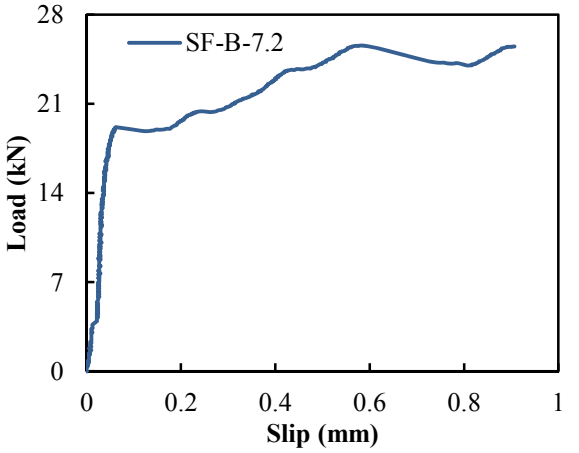
SF-B-7.2
Load (kN)
Slip (mm)
0
7
14
21
28
0
0.2
0.4
0.6
0.8
1

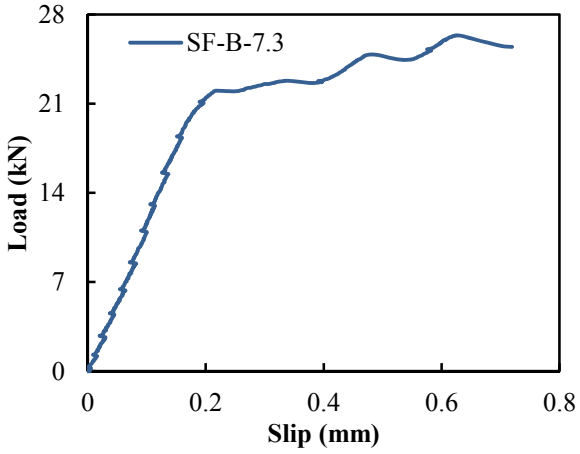
SF-B-7.3
Load (kN)
Slip (mm)
0
7
14
21
28
0
0.2
0.4
0.6
0.8

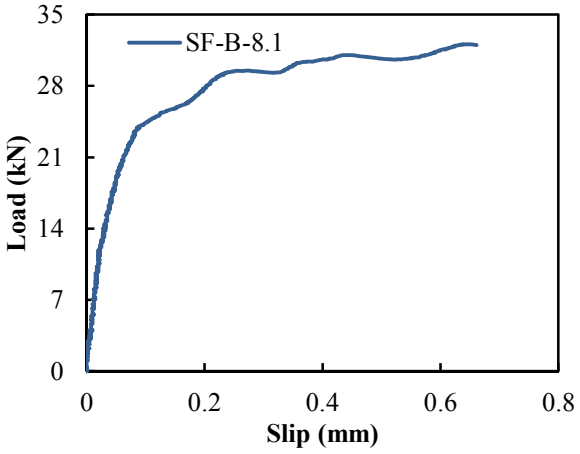
SF-B-8.1
Load (kN)
Slip (mm)
0
7
14
21
28
35
0
0.2
0.4
0.6
0.8

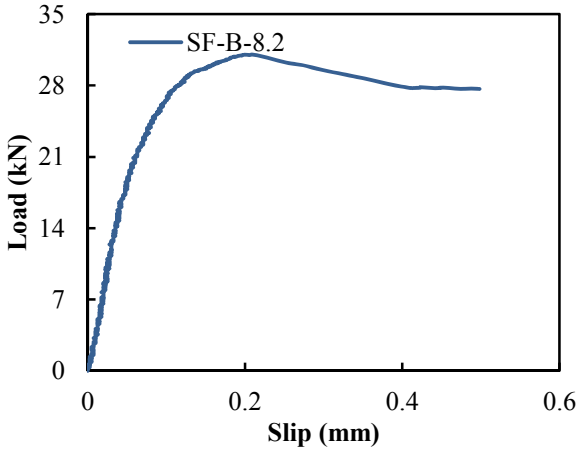
SF-B-8.2
Load (kN)
Slip (mm)
0
7
14
21
28
35
0
0.2
0.4
0.6

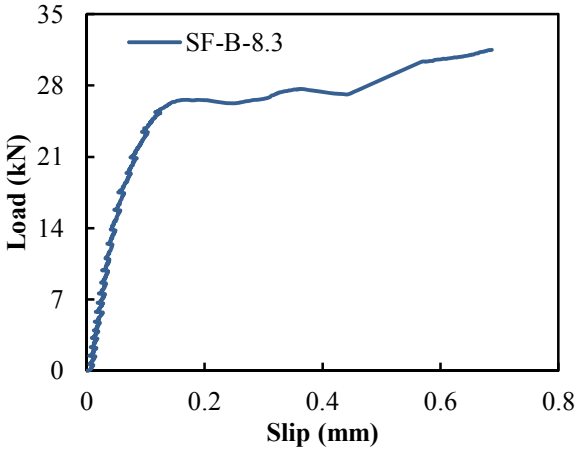
SF-B-8.3
Load (kN)
Slip (mm)
0
7
14
21
28
35
0
0.2
0.4
0.6
0.8

APPENDIX C

COMPARISON BETWEEN THE PROPOSED ANALYTICAL MODELS

C.1. Strain Profiles

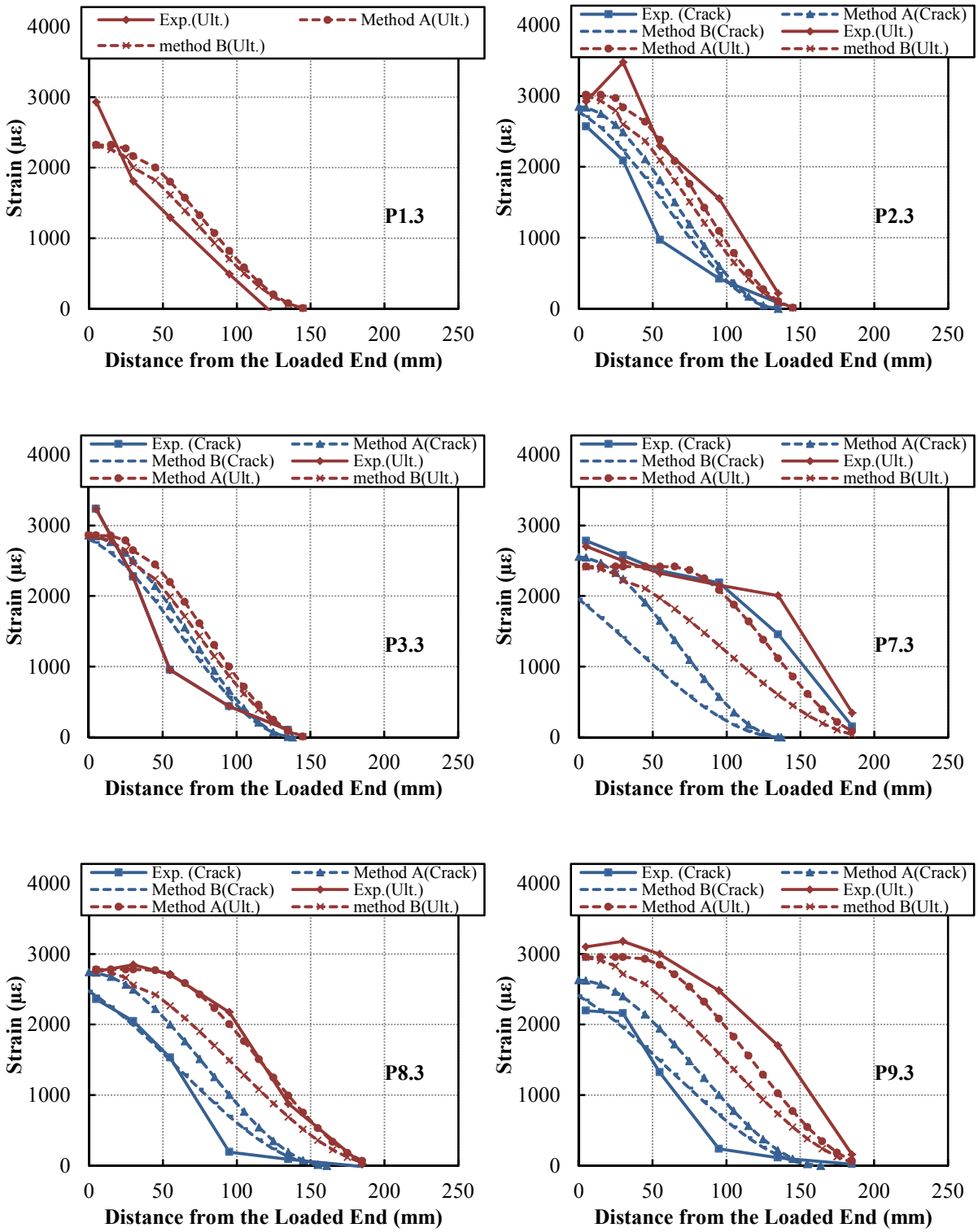

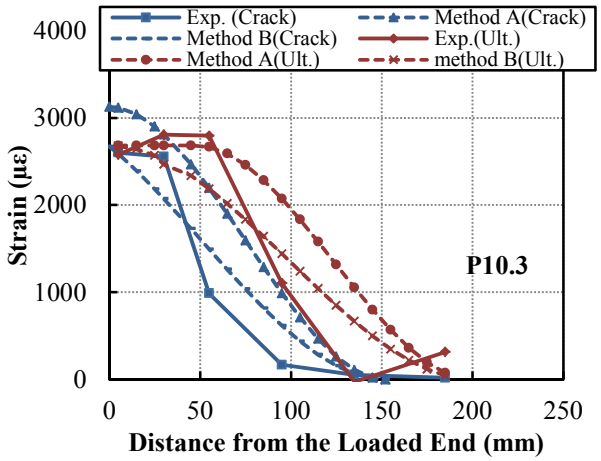
Exp. (Crack)
Method A(Crack)
Method B(Crack)
Exp.(Ult.)
Method A(Ult.)
method B(Ult.)
Strain (με)
Distance from the Loaded End (mm)
P10.3

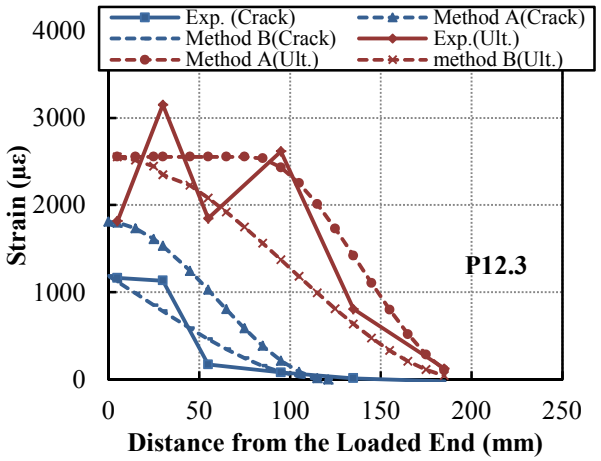
Exp. (Crack)
Method A(Crack)
Method B(Crack)
Exp.(Ult.)
Method A(Ult.)
method B(Ult.)
Strain (με)
Distance from the Loaded End (mm)
P12.3

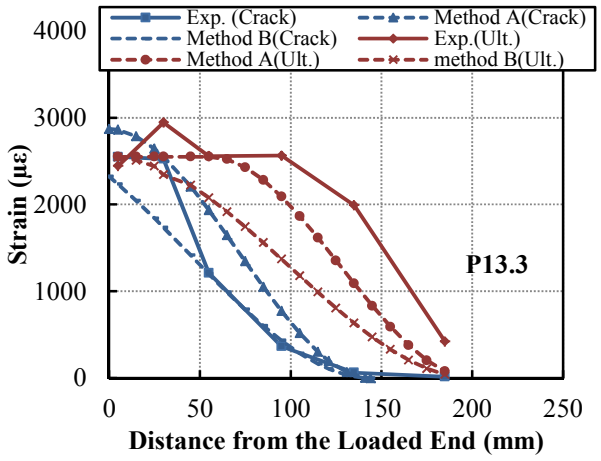
Exp. (Crack)
Method A(Crack)
Method B(Crack)
Exp.(Ult.)
Method A(Ult.)
method B(Ult.)
Strain (με)
Distance from the Loaded End (mm)
P13.3

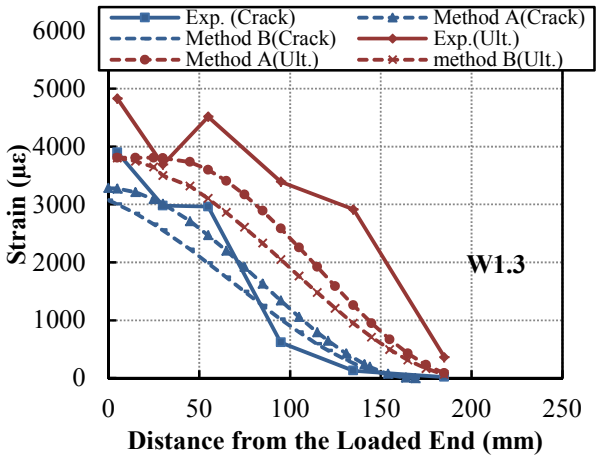
Exp. (Crack)
Method A(Crack)
Method B(Crack)
Exp.(Ult.)
Method A(Ult.)
method B(Ult.)
Strain (με)
Distance from the Loaded End (mm)
W1.3

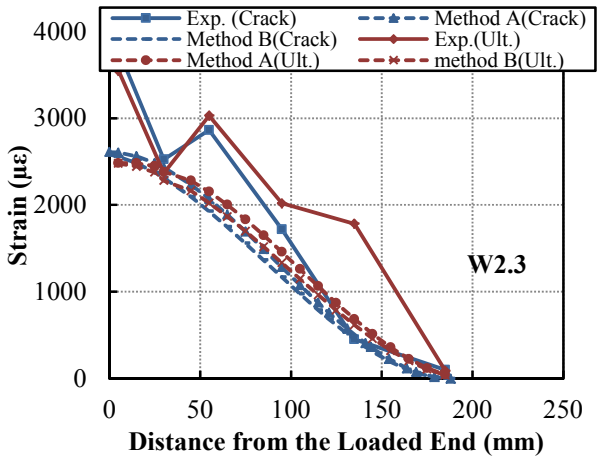
Exp. (Crack)
Method A(Crack)
Method B(Crack)
Exp.(Ult.)
Method A(Ult.)
method B(Ult.)
Strain (με)
Distance from the Loaded End (mm)
W2.3

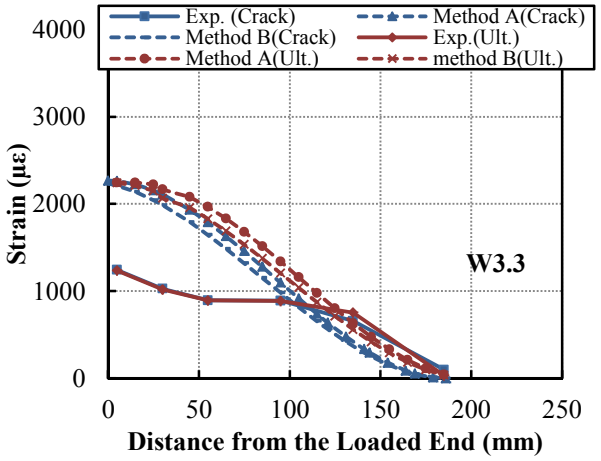
Exp. (Crack)
Method A(Crack)
Method B(Crack)
Exp.(Ult.)
Method A(Ult.)
method B(Ult.)
Strain (με)
Distance from the Loaded End (mm)
W3.3

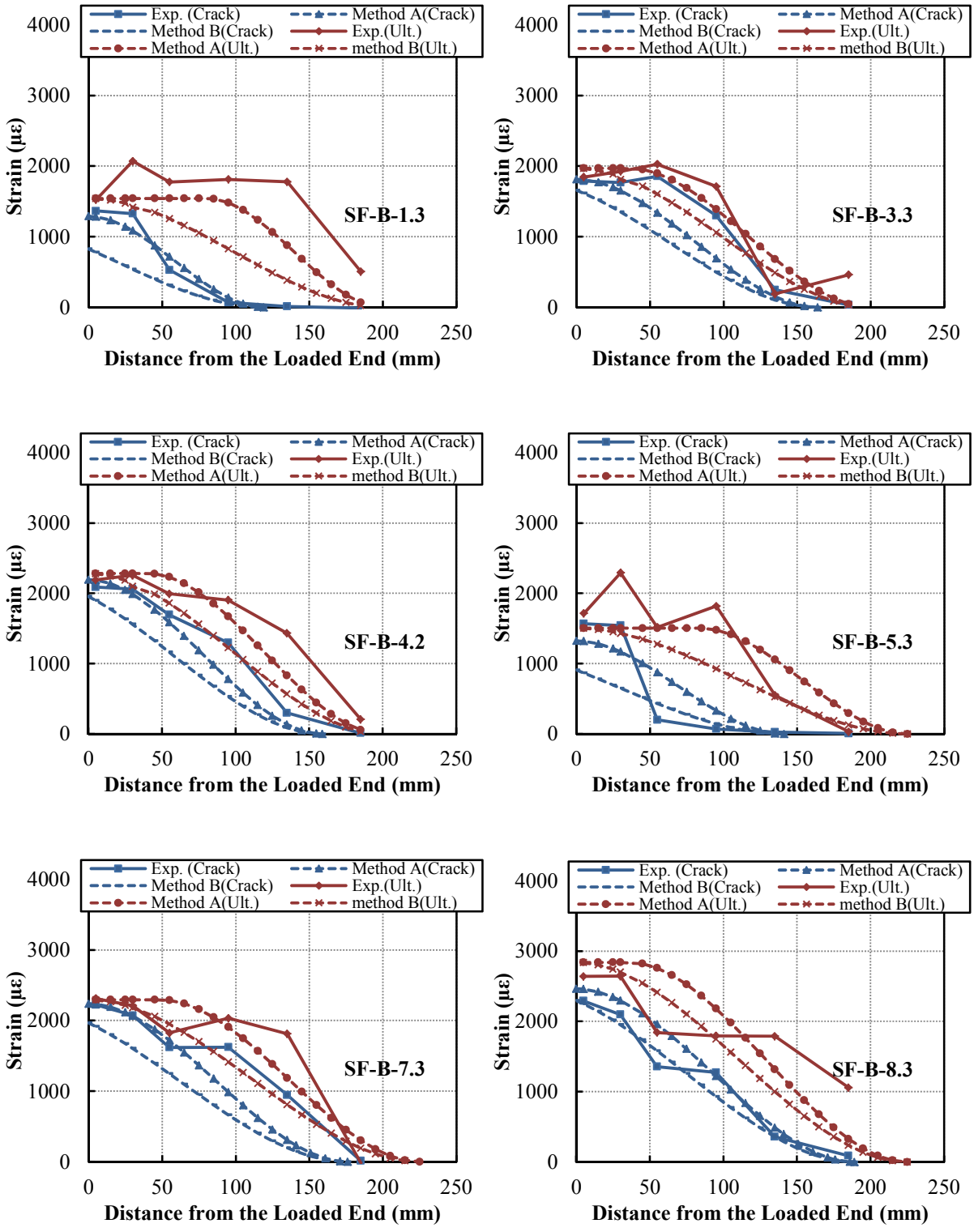
Exp. (Crack)
Method A(Crack)
Method B(Crack)
Exp.(Ult.)
Method A(Ult.)
method B(Ult.)
Strain (με)
Distance from the Loaded End (mm)
SF-B-1.3
SF-B-3.3
SF-B-4.2
SF-B-5.3
SF-B-7.3
SF-B-8.3

C.2. Shear Stress Profiles

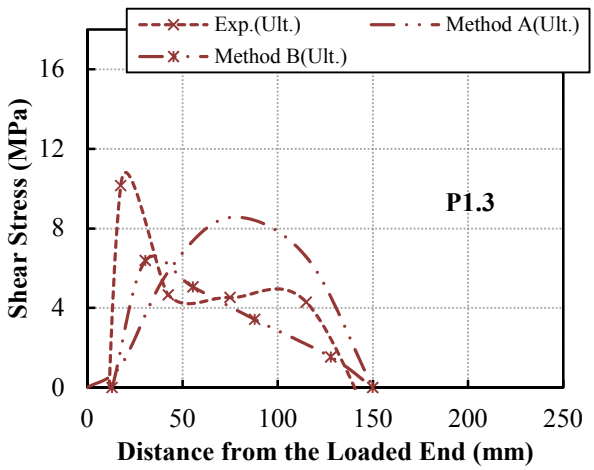

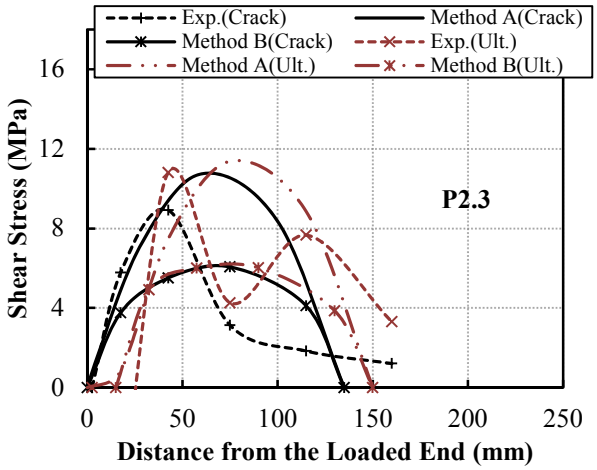

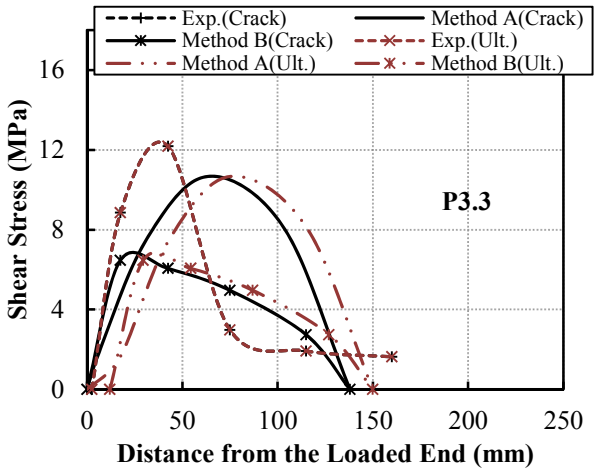

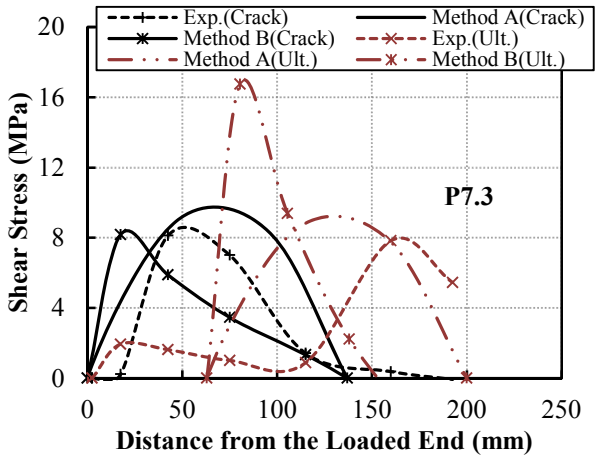

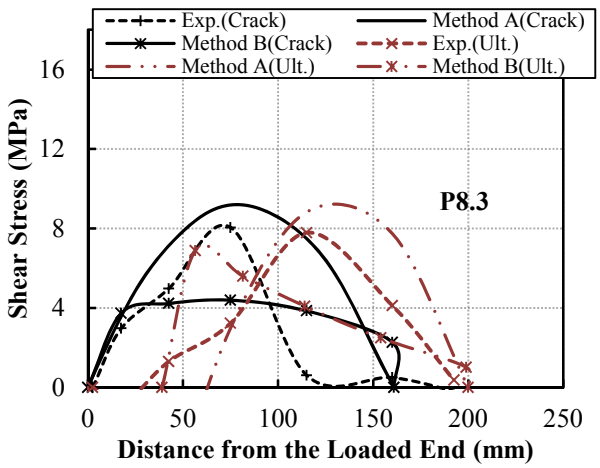

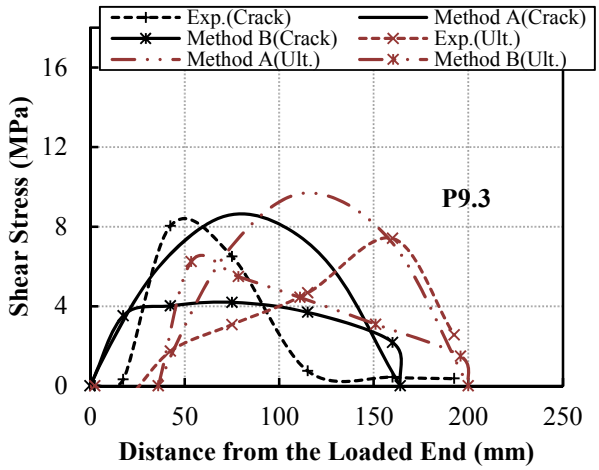

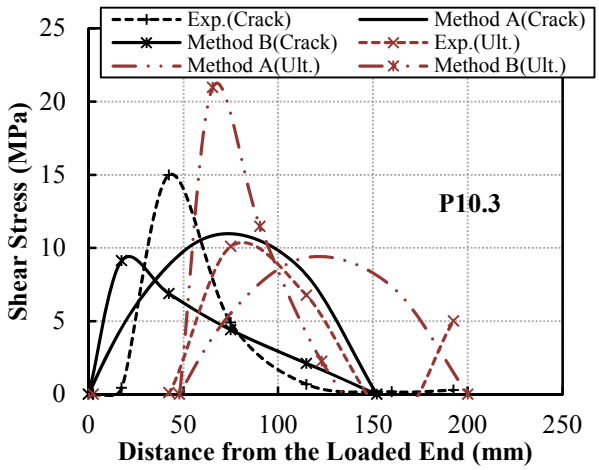
Exp.(Crack)
Method A(Crack)
Method B(Crack)
Exp.(Ult.)
Method A(Ult.)
Method B(Ult.)
P10.3
Shear Stress (MPa)
Distance from the Loaded End (mm)

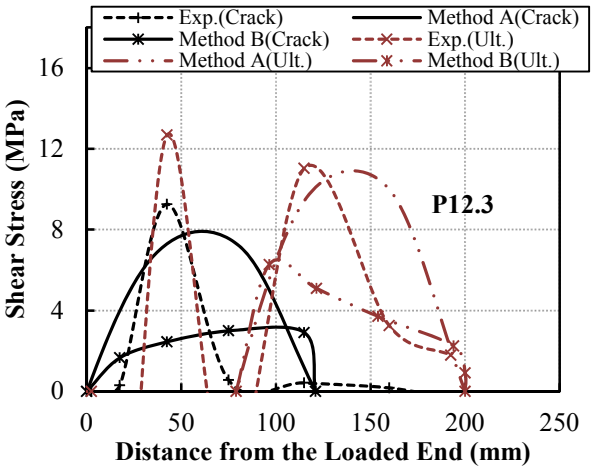
Exp.(Crack)
Method A(Crack)
Method B(Crack)
Exp.(Ult.)
Method A(Ult.)
Method B(Ult.)
P12.3
Shear Stress (MPa)
Distance from the Loaded End (mm)

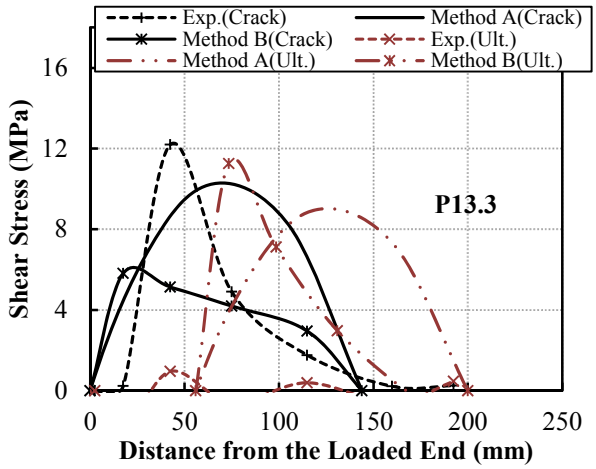
Exp.(Crack)
Method A(Crack)
Method B(Crack)
Exp.(Ult.)
Method A(Ult.)
Method B(Ult.)
P13.3
Shear Stress (MPa)
Distance from the Loaded End (mm)

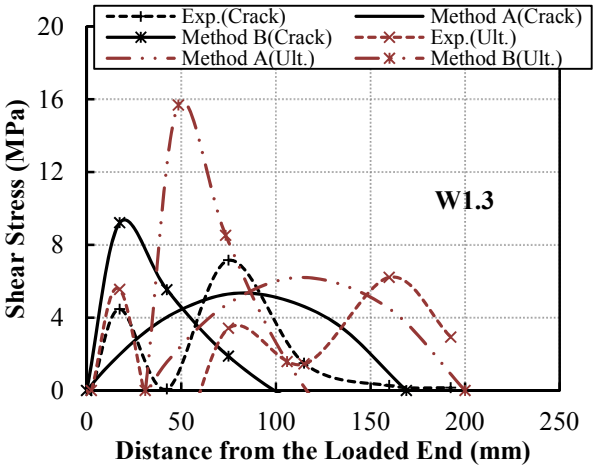
Exp.(Crack)
Method A(Crack)
Method B(Crack)
Exp.(Ult.)
Method A(Ult.)
Method B(Ult.)
W1.3
Shear Stress (MPa)
Distance from the Loaded End (mm)

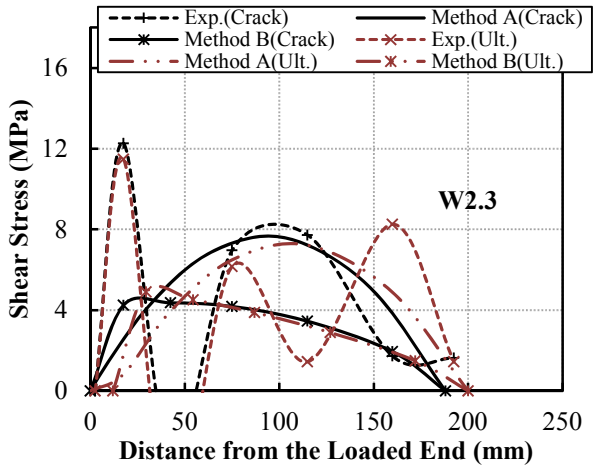
Exp.(Crack)
Method A(Crack)
Method B(Crack)
Exp.(Ult.)
Method A(Ult.)
Method B(Ult.)
W2.3
Shear Stress (MPa)
Distance from the Loaded End (mm)

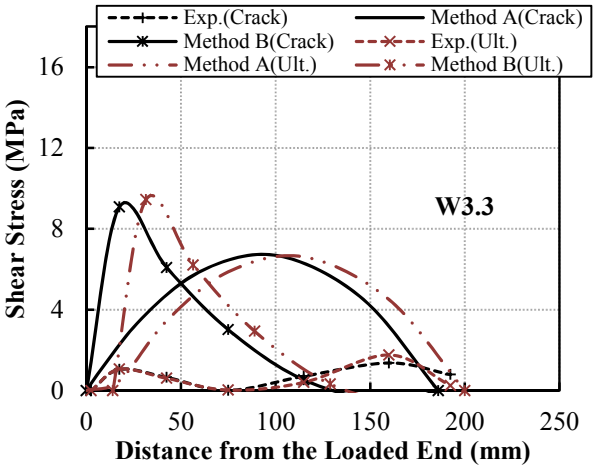
Exp.(Crack)
Method A(Crack)
Method B(Crack)
Exp.(Ult.)
Method A(Ult.)
Method B(Ult.)
W3.3
Shear Stress (MPa)
Distance from the Loaded End (mm)

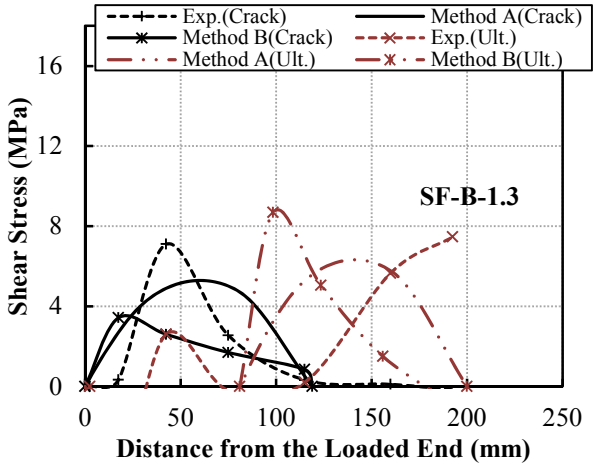
Exp.(Crack)
Method A(Crack)
Method B(Crack)
Exp.(Ult.)
Method A(Ult.)
Method B(Ult.)
SF-B-1.3
Shear Stress (MPa)
Distance from the Loaded End (mm)

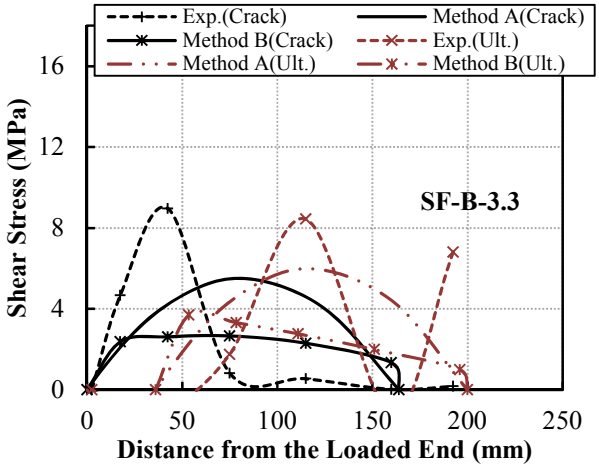
Exp.(Crack)
Method A(Crack)
Method B(Crack)
Exp.(Ult.)
Method A(Ult.)
Method B(Ult.)
SF-B-3.3
Shear Stress (MPa)
Distance from the Loaded End (mm)

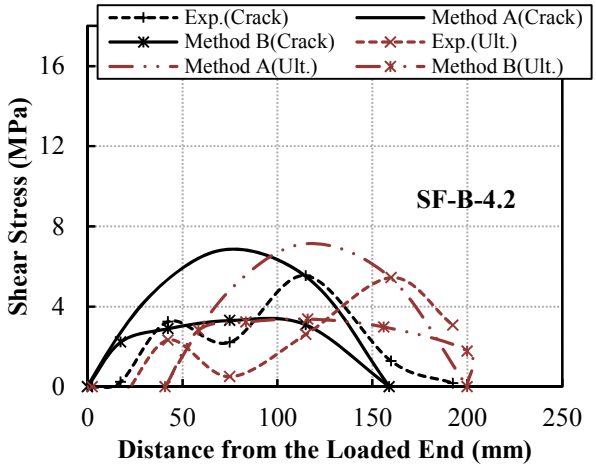
Exp.(Crack)
Method A(Crack)
Method B(Crack)
Exp.(Ult.)
Method A(Ult.)
Method B(Ult.)
SF-B-4.2
Shear Stress (MPa)
Distance from the Loaded End (mm)

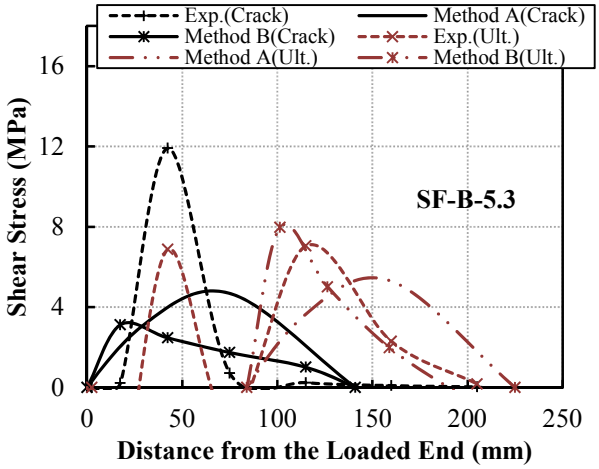
Exp.(Crack)
Method A(Crack)
Method B(Crack)
Exp.(Ult.)
Method A(Ult.)
Method B(Ult.)
SF-B-5.3
Shear Stress (MPa)
Distance from the Loaded End (mm)

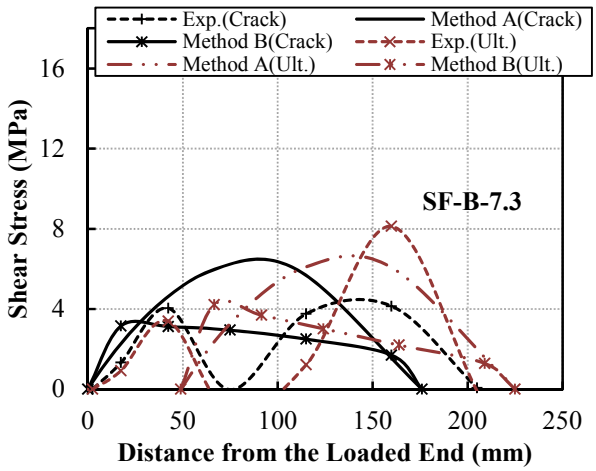
Exp.(Crack)
Method A(Crack)
Method B(Crack)
Exp.(Ult.)
Method A(Ult.)
Method B(Ult.)
SF-B-7.3
Shear Stress (MPa)
Distance from the Loaded End (mm)

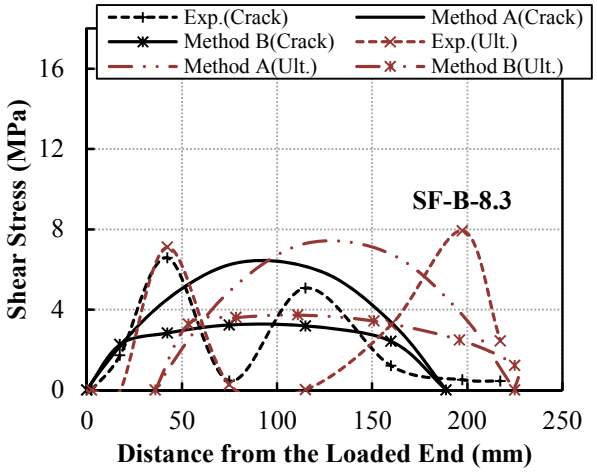
Exp.(Crack)
Method A(Crack)
Method B(Crack)
Exp.(Ult.)
Method A(Ult.)
Method B(Ult.)
SF-B-8.3
Shear Stress (MPa)
Distance from the Loaded End (mm)

C.3. Slip Profiles

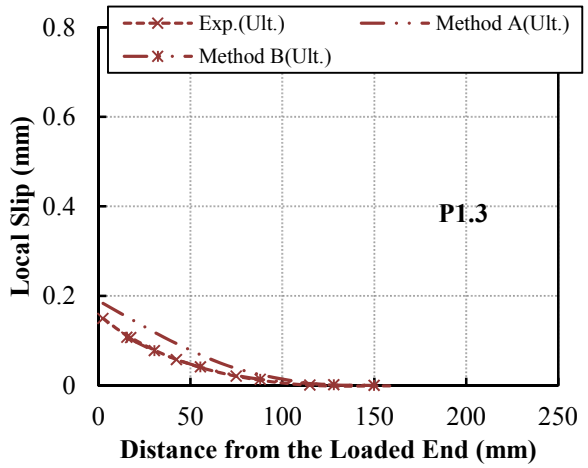

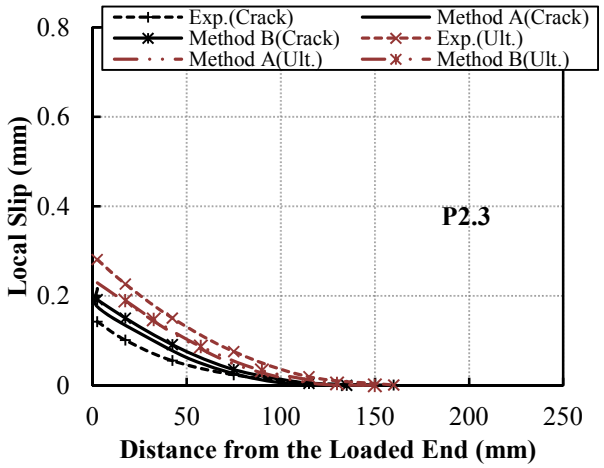

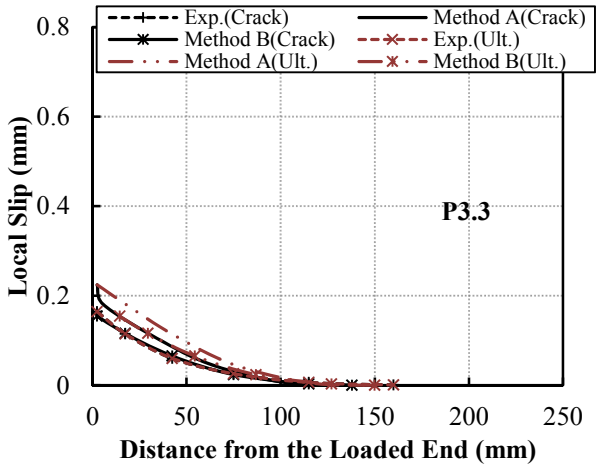

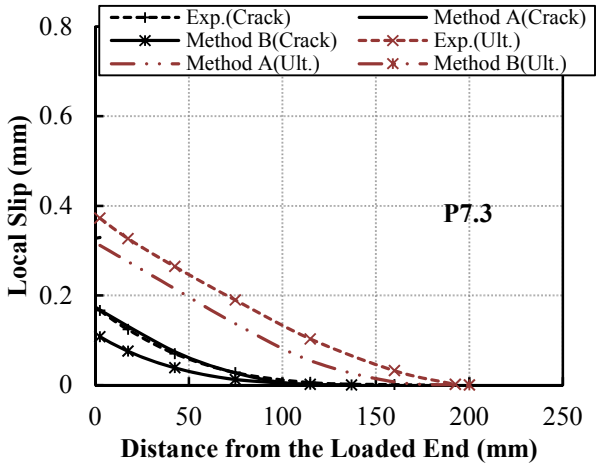

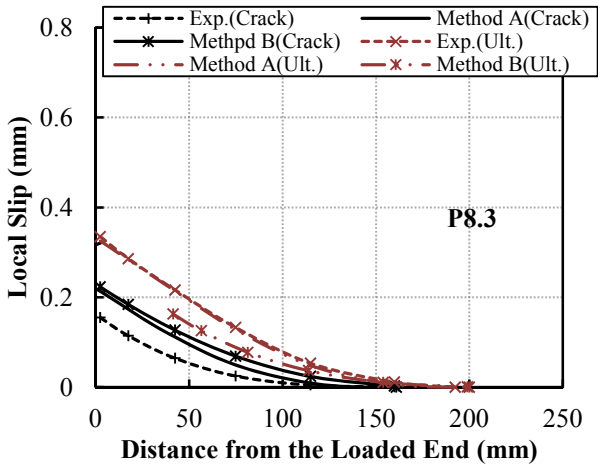

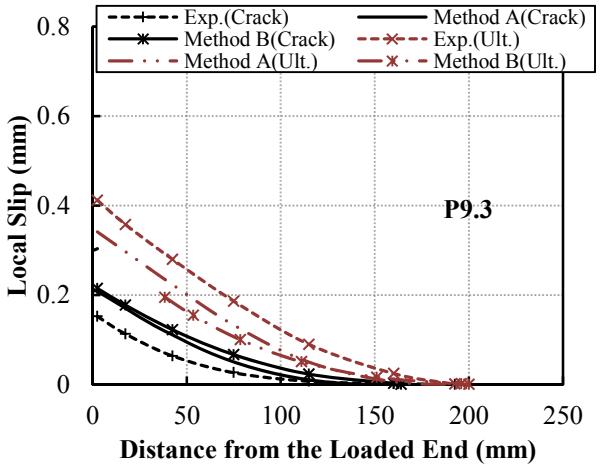

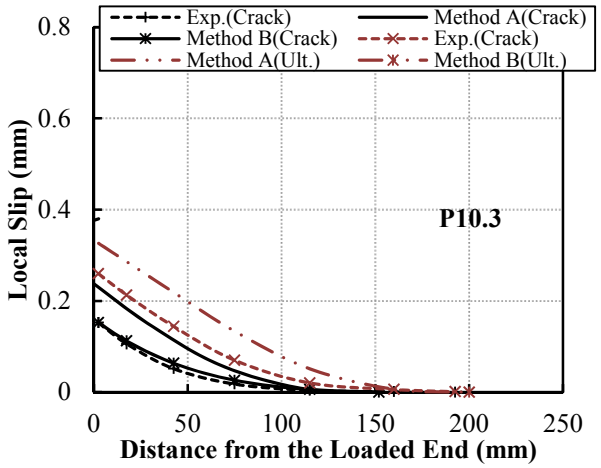
Exp.(Crack)
Method A(Crack)
Method B(Crack)
Exp.(Crack)
Method A(Ult.)
Method B(Ult.)
P10.3
Local Slip (mm)
Distance from the Loaded End (mm)

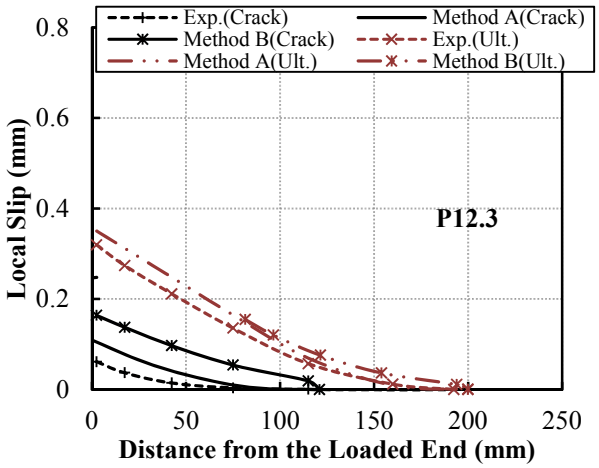
Exp.(Crack)
Method A(Crack)
Method B(Crack)
Exp.(Ult.)
Method A(Ult.)
Method B(Ult.)
P12.3
Local Slip (mm)
Distance from the Loaded End (mm)

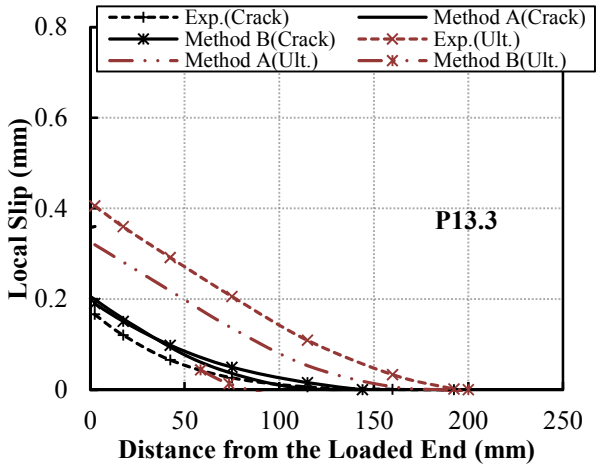
Exp.(Crack)
Method A(Crack)
Method B(Crack)
Exp.(Ult.)
Method A(Ult.)
Method B(Ult.)
P13.3
Local Slip (mm)
Distance from the Loaded End (mm)

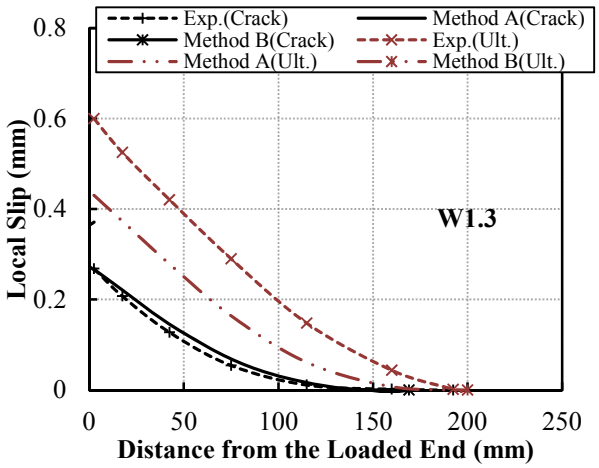
Exp.(Crack)
Method A(Crack)
Method B(Crack)
Exp.(Ult.)
Method A(Ult.)
Method B(Ult.)
W1.3
Local Slip (mm)
Distance from the Loaded End (mm)

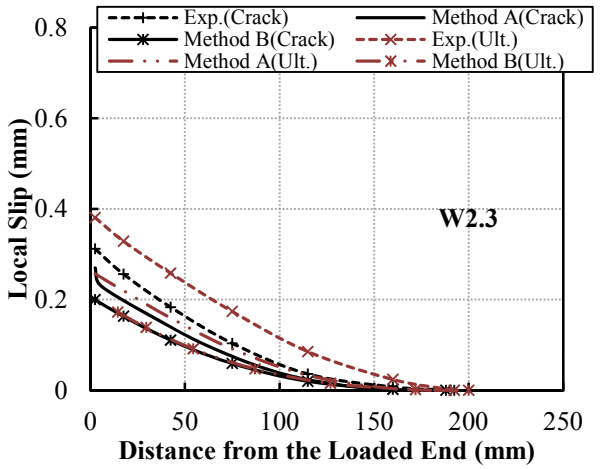
Exp.(Crack)
Method A(Crack)
Method B(Crack)
Exp.(Ult.)
Method A(Ult.)
Method B(Ult.)
W2.3
Local Slip (mm)
Distance from the Loaded End (mm)

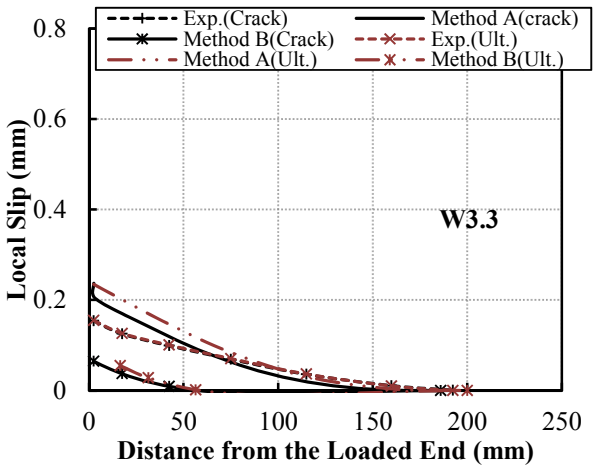
Exp.(Crack)
Method A(crack)
Method B(Crack)
Exp.(Ult.)
Method A(Ult.)
Method B(Ult.)
W3.3
Local Slip (mm)
Distance from the Loaded End (mm)

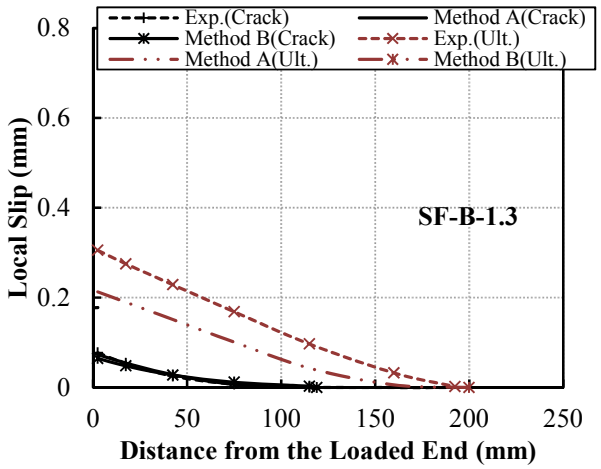
Exp.(Crack)
Method A(Crack)
Method B(Crack)
Exp.(Ult.)
Method A(Ult.)
Method B(Ult.)
SF-B-1.3
Local Slip (mm)
Distance from the Loaded End (mm)
0
0.2
0.4
0.6
0.8
0
50
100
150
200
250

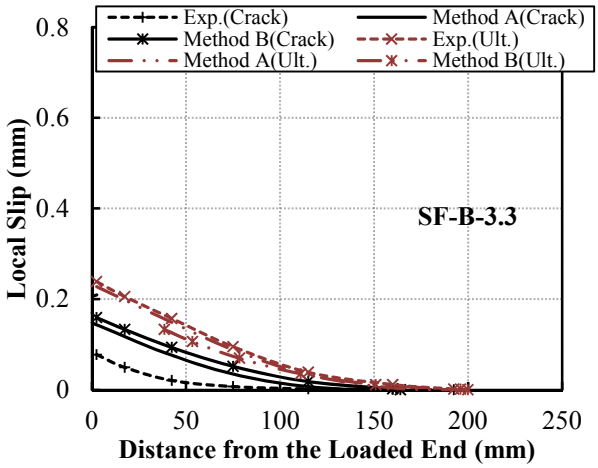
Exp.(Crack)
Method A(Crack)
Method B(Crack)
Exp.(Ult.)
Method A(Ult.)
Method B(Ult.)
SF-B-3.3
Local Slip (mm)
Distance from the Loaded End (mm)
0
0.2
0.4
0.6
0.8
0
50
100
150
200
250

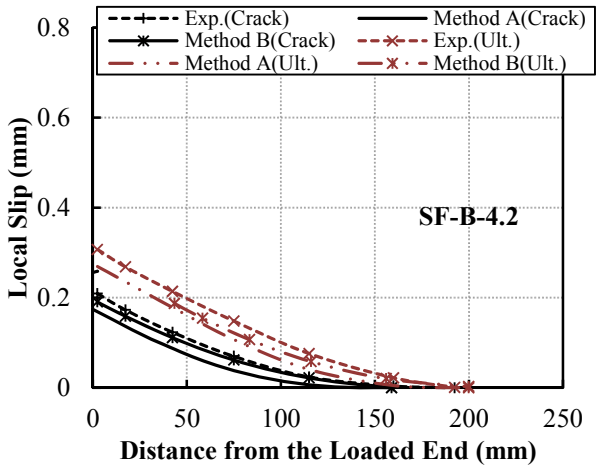
Exp.(Crack)
Method A(Crack)
Method B(Crack)
Exp.(Ult.)
Method A(Ult.)
Method B(Ult.)
SF-B-4.2
Local Slip (mm)
Distance from the Loaded End (mm)
0
0.2
0.4
0.6
0.8
0
50
100
150
200
250

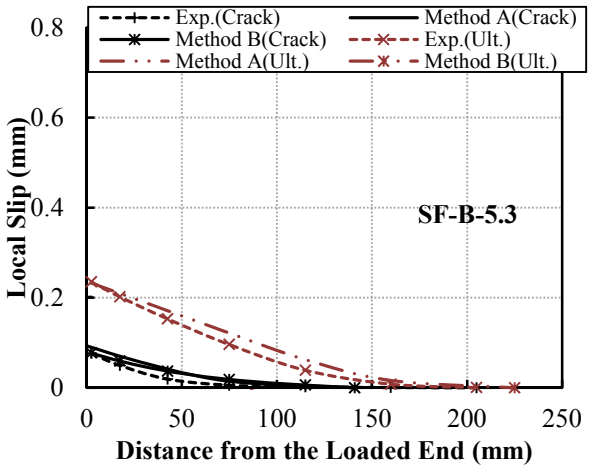
Exp.(Crack)
Method A(Crack)
Method B(Crack)
Exp.(Ult.)
Method A(Ult.)
Method B(Ult.)
SF-B-5.3
Local Slip (mm)
Distance from the Loaded End (mm)
0
0.2
0.4
0.6
0.8
0
50
100
150
200
250

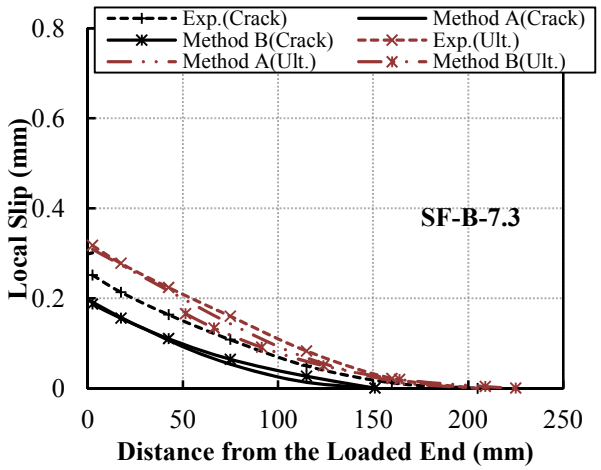
Exp.(Crack)
Method A(Crack)
Method B(Crack)
Exp.(Ult.)
Method A(Ult.)
Method B(Ult.)
SF-B-7.3
Local Slip (mm)
Distance from the Loaded End (mm)
0
0.2
0.4
0.6
0.8
0
50
100
150
200
250

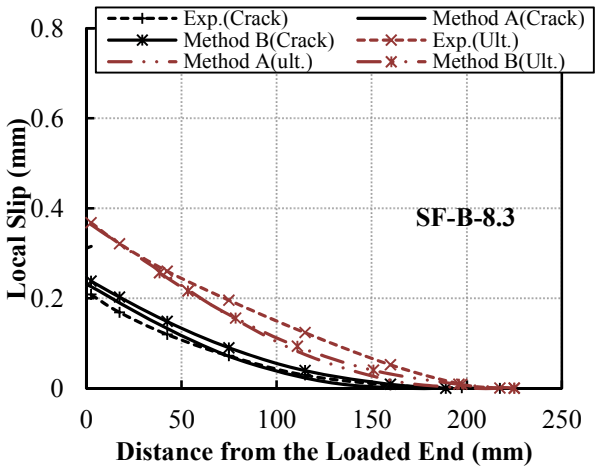
Exp.(Crack)
Method A(Crack)
Method B(Crack)
Exp.(Ult.)
Method A(ult.)
Method B(Ult.)
SF-B-8.3
Local Slip (mm)
Distance from the Loaded End (mm)
0
0.2
0.4
0.6
0.8
0
50
100
150
200
250